UNIVERSITY OF OKLAHOMA

GRADUATE COLLEGE

MODELING OF INTEGRAL ABUTMENT BRIDGES CONSIDERING SOIL-STRUCTURE INTERACTION EFFECTS

A DISSERTATION

SUBMITTED TO THE GRADUATE FACULTY

in partial fulfillment of the requirements for the

Degree of

DOCTOR OF PHILOSOPHY

By

DANIEL KRIER
Norman, Oklahoma
2009

MODELING OF INTEGRAL ABUTMENT BRIDGES CONSIDERING SOIL-STRUCTURE INTERACTION EFFECTS

A DISSERTATION APPROVED FOR THE
SCHOOL OF CIVIL ENGINEERING AND ENVIRONMENTAL SCIENCE

BY

Dr. K.K. Muraleetharan, Co-Chair

Dr. K.D. Mish, Co-Chair

Dr. G.A. Miller

Dr. L.W. White

Dr. L.M. Taylor

Dedicated to My Parents

ACKNOWLEDGEMENT

I would like to express my sincere thanks to Dr. K.K. Muraleetharan for all he has done for me over the past few years. From helping me with a research project as an undergraduate to the completion of this degree, he has been nothing but supportive. He has served as a wonderful teacher and mentor to me, and spent countless hours working to help me develop as a researcher, student, and human being. I thank him for his help to me in all forms. I thank Drs. G.A. Miller and L.W. White for serving on my committee. I would like to thank Dr. K.D. Mish for his invaluable guidance throughout this process. Observing his many talents and tremendous knowledge has made me want to become a better thinker and push myself to learn in many areas. I would like to thank Dr. L.M. Taylor for his advice and support, which has been supremely helpful. I thank Colin Potter of ANATECH Corp. for countless instances of support with computational issues. I also thank Dr. N. Ravichandran for his friendship and infinite patience with me as I struggled early in my research.

I thank the Graduate Assistance in Areas of National Need (GAANN) Fellowship, the National Science Foundation (NSF) GK-12 Fellowship, and the Oklahoma Transportation Center (Project No. OTCREOS7-1-37) for the financial support that made my attendance of graduate school possible.

I also want to thank the long string of teachers and mentors who have contributed to my learning over the years. There are too many to name, but their interest in my success is greatly appreciated. I also thank my family for the encouragement, care, and love I have received.

TABLE OF CONTENTS

Acknowledgement……...…………………………………………………………...iv
Table of Contents……..………………………………………………….……....v
List of Tables……...………………………………………………..………...viii
List of Figures……..…………………………………...……………………...ix
Abstract……...………………………………………...…….………………...xiii
1. Introduction 1
   1.1 General 1
   1.2 Modeling 3
   1.3 Finite Element Technology 4
   1.4 Computational Framework... 4
   1.5 Objectives... 5
   1.6 Dissertation Layout 5
2. Literature Review 6
   2.1 Integral Abutment Bridges 6
   2.2 Current Practices 8
   2.3 Skewed IABs... 9
   2.4 Soil-Structure Interaction 11
   2.5 Instrumentation Projects.. 12
   2.6 Important Loading Cases 14
3. Finite Element Technology 15
   3.1 Soil Element.. 15
      3.1.1 Governing Equations 15
      3.1.2 Linear Elastic Constitutive Model.. 20
      3.1.3 Bounding Surface Constitutive Model for Clays 21
      3.1.4 Bounding Surface Constitutive Model for Sands............................... 22
   3.2 Beam Element 25
      3.2.1 Stiffness Matrix 26
      3.2.2 Mass Matrix.. 32
      3.2.3 Damping Matrix 33
      3.2.4 Thermal Loading 33
      3.2.5 Element Transformation... 36
      3.2.6 Nonlinear EI 38

3.3 Plate Element.. 46
    3.3.1 Stiffness Matrix 47
    3.3.2 Numerical Integration.. 53
    3.3.3 Mass Matrix.. 55
    3.3.4 Damping Matrix 56
    3.3.5 Thermal Loading 56
    3.3.6 Element Transformation.. 59
    3.3.7 Hourglassing... 62
3.4 Numerical Integration 67
    3.4.1 Time Integration Scheme... 67
    3.4.2 Ramped Loading... 70
4. Soil-Structure Interaction 76
4.1 Linear Problems 76
    4.1.1 Beams on Elastic Foundation 76
    4.1.2 Linear SSI Example Problem 77
4.2 Soil-Pile Interaction in a Soft Clay 91
    4.2.1 Nonlinear SSI Example Problem.. 91
5. Thermal Modeling 102
5.1 Linear Temperature Distribution.. 102
5.2 Skewed Plates Subjected to Thermal Loading 104
5.3 Assemblies of Elements 113
6. TeraGrande Modeling.. 118
6.1 General 118
    6.1.1 Explicit Dynamics 118
    6.1.2 ANATECH Concrete Model 119
    6.1.3 Concrete Cracking 120
    6.1.4 Reinforcement Modeling... 121
    6.1.5 Tied Contact 122
6.2 Prestressed Girder Modeling... 123
6.3 Superstructure Model 127
6.4 Thermal Analysis 130
    6.4.1 Temperature Increase 130

6.4.2 Temperature Decrease 133
6.4.3 Blast Loading 136
7. TeraDysac Modeling 140
7.1 Problem Description 140
7.2 Soil Properties 142
7.3 Structural Properties 143
7.3.1 Weighted Average Example 144
7.3.2 Set-Up for Plane Strain Analysis 145
7.3.3 Set-Up for 3D Analysis 146
7.4 Applied Thermal Loading 148
7.4.1 Validation Technique 149
7.5 Linear Elastic Analysis 151
7.5.1 Temperature Increase 154
7.5.2 Temperature Decrease 157
7.6 Bounding Surface Analysis 160
7.6.1 Bounding Surface Properties 160
7.6.2 Temperature Increase 163
7.6.3 Temperature Decrease 165
7.7 Three-Dimensional Analysis 166
8. Conclusions 171
8.1 General 171
8.2 Recommendations 174
References........ 182

LIST OF TABLES

Table 3.1: Bounding Surface Model Parameters for Speswhite Kaolin 22
Table 3.2: Bounding Surface Model Parameters 24
Table 3.3: Integration Points on the Master Element 53
Table 7.1: Young’s Modulus as a Function of N-Value (NAVFAC 1986).................... 142
Table 7.2: Element Blocks by Color.. 152
Table 7.3: Bounding Surface Properties for Sand Layers... 162
Table 7.4: Results and Error Estimates for Heating Analysis 164
Table 7.5: Results and Error Estimates for Cooling Analysis 166

LIST OF FIGURES

Figure 1.1: Schematic Drawing of a Traditional Bridge 2
Figure 1.2: Schematic Drawing of an Integral Abutment Bridge 3
Figure 2.1: Skew Angle Depiction 10
Figure 2.2: Obtuse and Acute Corners in IABs 10
Figure 3.1: Soil-Fluid Mixture 15
Figure 3.2: Bounding Surface Representation (Clayey Soils) 21
Figure 3.3: Bounding Surface Representation (Sands) 23
Figure 3.4: Beam Element Nodal Variables 25
Figure 3.5: Beam Element Coordinate Transformation 25
Figure 3.6: Temperature Distribution for Beams 34
Figure 3.7: Local Coordinate System for Beam Element 36
Figure 3.8: X-Axis Directions for Beam Element 37
Figure 3.9: Typical Moment-Curvature Relationship for a Beam 39
Figure 3.10: Piece-wise Approximation of the Moment-Curvature Curve for a Beam 40
Figure 3.11: Bending Stiffness vs. Bending Moment for a Beam 40
Figure 3.12: Example Beam Geometry 41
Figure 3.13: Stress Distribution at Yield 42
Figure 3.14: Stress Distribution After Yield 43
Figure 3.15: Stress Distribution at Ultimate Moment 44
Figure 3.16: Moment-Curvature Relationship for the Example Beam 44
Figure 3.17: Nonlinear EI Example Problem Layout 45
Figure 3.18: EI-Moment Relationship for the Example Beam 45
Figure 3.19: Plate Element Nodal Variables 47
Figure 3.20: Plate Element Layout 50
Figure 3.21: Plate Element Coordinate Transformation 53
Figure 3.22: Temperature Distribution for Plates 56
Figure 3.23: Middle Chords for Plate Element 60
Figure 3.24: Local Coordinate System for Plate Element 61
Figure 3.25: w-Hourglassing Mode 63
Figure 3.26: Problem Set-Up for Hourglassing Example 65
Figure 3.27: Deformed Shape for Corner-Supported Plate (No Hourglass Stiffness) 65
Figure 3.28: Deformed Shape for Corner-Supported Plate with Hourglass Stiffness 66
Figure 3.29: Simply-Supported Set-Up for Hourglassing Example 67
Figure 3.30: Deformed Shape for Simply-Supported Plate (No Hourglass Stiffness) 67
Figure 3.31: Ramped Loading 70
Figure 3.32: Cantilever Beam Problem Demonstrating Minor Oscillation 71
Figure 3.33: Nodal Displacement-Time History for Cantilever Beam Tip 71
Figure 3.34: Soil-Structure Interaction Problem Demonstrating Oscillation 72
Figure 3.35: Nodal Displacement-Time History (Full Mass) 73
Figure 3.36: Nodal Displacement-Time History (Full Mass, Extended Ramp) 73
Figure 3.37: Nodal Displacement-Time History (10% Mass) 74
Figure 3.38: Nodal Displacement-Time History (Zero Mass) 74
Figure 4.1: Beam on Elastic Foundation 76
Figure 4.2: Problem Set-Up 77

Figure 4.3: Point Load Applied to Axial Bar 79
Figure 4.4: Finite Element Set-Up for Point Load Analysis 79
Figure 4.5: Beam Displacement (Winkler vs. Vesic) 81
Figure 4.6: Beam Rotation (Winkler vs. Vesic) 81
Figure 4.7: Beam Shear Force (Winkler vs. Vesic) 82
Figure 4.8: Beam Bending Moment (Winkler vs. Vesic) 82
Figure 4.9: Elastic Beam Analysis Set-Up 83
Figure 4.10: Euler-Bernoulli Beam Displacement Comparison 84
Figure 4.11: Euler-Bernoulli Beam Rotation Comparison 84
Figure 4.12: Finite Element Model Set-Up for Linear Soil-Structure Analysis 85
Figure 4.13: Beam Displacement (Vesic vs. TeraDysac) 86
Figure 4.14: Beam Rotation (Vesic vs. TeraDysac) 86
Figure 4.15: Beam Shear Force (Vesic vs. TeraDysac) 87
Figure 4.16: Beam Bending Moment (Vesic vs. TeraDysac) 87
Figure 4.17: TeraDysac Linear SSI Analysis Deformed Shape 88
Figure 4.18: Beam Displacement (Vesic vs. TeraDysac – 3D) 89
Figure 4.19: Beam Rotation (Vesic vs. TeraDysac – 3D) 89
Figure 4.20: Beam Shear Force (Vesic vs. TeraDysac – 3D) 90
Figure 4.21: Beam Bending Moment (Vesic vs. TeraDysac – 3D) 90
Figure 4.22: Nonlinear SSI Example Set-Up 91
Figure 4.23: Problem Set-Up for Nonlinear SSI TeraDysac Analysis 92
Figure 4.24: Loading and Node Sets for Nonlinear SSI TeraDysac Analysis 92
Figure 4.25: Initial Vertical Stress State Contours (kPa) 93
Figure 4.26: Deviator Stress-Strain Curve at 20 m Depth 94
Figure 4.27: Stress Paths at 20 m Depth 94
Figure 4.28: p-y Curves Obtained from LPILE 95
Figure 4.29: Soil Contribution to Nodal Force 96
Figure 4.30: Free Body Diagram of the Center Node 96
Figure 4.31: p-y Curves Obtained from TeraDysac 97
Figure 4.32: p-y Curve Comparison 97
Figure 4.33: Pile Deflection Comparison for Nonlinear SSI Analysis 98
Figure 4.34: Pile Rotation Comparison for Nonlinear SSI Analysis 99
Figure 4.35: Pile Shear Force Comparison for Nonlinear SSI Analysis 99
Figure 4.36: Pile Bending Moment Comparison for Nonlinear SSI Analysis 99
Figure 4.37: Pore Water Pressure Contours (kPa) 101
Figure 4.38: Pore Water Pressure-Time History (kPa, s) 101
Figure 5.1: Deformed Shape (No Gradient) 102
Figure 5.2: Curvature Depiction (Positive Gradient) 102
Figure 5.3: Curvature Depiction (Negative Gradient) 103
Figure 5.4: Finite Element Mesh for Gradient Analysis 103
Figure 5.5: Deformed Shape for Gradient Analysis 104
Figure 5.6: Square Test Plate Set-Up 105
Figure 5.7: Square Plate Corner Forces 105
Figure 5.8: Rhombus Plate Set-Up 106
Figure 5.9: Rhombus Plate Corner Forces 106
Figure 5.10. Rectangular Plate Set-Up 107

Figure 5.11: Rectangular Plate Corner Forces 108
Figure 5.12: Rectangular Plate (Deformed Shape) 109
Figure 5.13: Parallelogram Plate Set-Up 110
Figure 5.14: Parallelogram Plate Corner Forces 110
Figure 5.15: Skewed IAB Deck Idealization Highlighting Corner Forces 111
Figure 5.16: Skewed Plate with Corner Connections 112
Figure 5.17: Corner-Connecting Beams 112
Figure 5.18: 100 Element Plate for Mesh Assembly 113
Figure 5.19: 10 Element Beam for Mesh Assembly 114
Figure 5.20: Beam and Plate Mesh Assembly 115
Figure 5.21: Deformed Shape (Both Element Blocks Heated) 116
Figure 5.22: Deformed Shape (Plate Element Block Heated Only) 116
Figure 5.23: Deformed Shape (Beam Element Block Heated Only) 117
Figure 6.1: Compressive Stress-Strain Curve (Pa) 120
Figure 6.2: Tensile Stress-Strain Curve (Pa) 120
Figure 6.3: Concrete Stress-Strain Diagram 121
Figure 6.4: Bridge Girder Mesh 122
Figure 6.5: Tied Contact Between Mesh Instances 123
Figure 6.6: Prestressed Tendons in Bridge Girder 123
Figure 6.7: Girder End Caps 124
Figure 6.8: Loading Amplitudes for Girder Analysis 124
Figure 6.9: Important Node Sets for Girder Analysis 125
Figure 6.10: Crack Pattern at 0.15 s 125
Figure 6.11: Crack Pattern at 0.6 s 125
Figure 6.12: Midspan Displacement-Time History from Girder Analysis 126
Figure 6.13: Minnesota IAB Model (Piers and Pier Piles Included) 127
Figure 6.14: Pier Piles (Above Grade) Mesh 128
Figure 6.15: Minnesota IAB Superstructure Model (Rebar Shown) 128
Figure 6.16: Superstructure Interior Nodes 129
Figure 6.17: Superstructure End Node Set 129
Figure 6.18: Superstructure Crack Pattern for Temperature Increase 130
Figure 6.19: Girder Crack Pattern for Temperature Increase 131
Figure 6.20: Strain Contours for Temperature Increase 132
Figure 6.21: Strain Contours for Temperature Increase (Close-Up) 132
Figure 6.22: Deck Schematic at Pier Locations 133
Figure 6.23: Bridge Deck Stress (Pa) Contours for Temperature Decrease 134
Figure 6.24: Stress (Pa) Contours Viewed from Beneath Bridge 134
Figure 6.25: Deck Crack Pattern for Temperature Decrease 135
Figure 6.26: Deck Compressive Stress-Strain Curve (Pa) 135
Figure 6.27: Blast Pressure (Pa) vs. Time (s) 137
Figure 6.28: Blast Pressure (Pa) vs. Distance (m) 137
Figure 6.29: Superstructure Pressure (Pa) 6 ms After Blast Initiation 137
Figure 6.30: Superstructure Deformed Shape at 0.15 s (Magnified by 15) 138
Figure 6.31: Bridge Deck Crack Pattern 138
Figure 6.32: Bridge Girders Crack Pattern 139
Figure 7.1: Concrete IAB (Photo Courtesy of Huang et al. 2004) 140

Figure 7.2: Elevation View of Minnesota IAB 141
Figure 7.3: Transverse Section (Through Deck)... 141
Figure 7.4: Soil Stratigraphy with Used E/N Ratios 143
Figure 7.5: Cross-Section Pier Piles Above Grade 144
Figure 7.6: Bridge Details at Pier Locations 147
Figure 7.7: 3D TeraDysac Superstructure Model 147
Figure 7.8: Temperature Gradient (Sunny Summer Day, After Huang et al. 2004)....... 148
Figure 7.9: Temperature Gradient (Cloudy Winter Day, After Huang et al. 2004) 149
Figure 7.10: Superstructure Temperature Input (Heating) 150
Figure 7.11: 2D IAB Finite Element Model 151
Figure 7.12: Element Block View 152
Figure 7.13: Structure Assembly at Abutment 153
Figure 7.14: Junction Undeformed and Deformed Shapes 153
Figure 7.15: Boundary Nodes for 2D Analysis 154
Figure 7.16: IAB Deformed Shape for Temperature Increase 154
Figure 7.17: Abutment and Abutment Pile Displacement for Temperature Increase..... 155
Figure 7.18: Developed Pore Water Pressure (kPa) During Temperature Increase 157
Figure 7.19: IAB Deformed Shape for Temperature Decrease 158
Figure 7.20: Abutment and Abutment Pile Displacement for Temperature Decrease ... 158
Figure 7.21: Developed Pore Water Pressure (kPa) During Temperature Decrease 159
Figure 7.22: Soil Profile Composition (Nevada Sand and Speswhite Kaolin) 161
Figure 7.23: Initial Stress State (kPa) for Bounding Surface Analysis.......................... 163
Figure 7.24: Abutment and Abutment Pile Deformation Comparison 164
Figure 7.25: Bounding Surface Pore Pressure Development (kPa)............................... 165
Figure 7.26: Abutment and Abutment Pile Deformation Comparison 166
Figure 7.27: 3D Superstructure Model (Non-Skewed).. 167
Figure 7.28: Plan View of 3D Superstructure Models... 168
Figure 7.29: Abutment Deformations from 3D Analyses.. 169
Figure 7.30: 3D Superstructure Corner Forces 170
Figure 8.1: Full 3D Minnesota IAB Model 176
Figure 8.2: Full 3D Minnesota Bridge Model (Skewed) 176
Figure 8.3: 3D Reduced Model (Skewed IAB) 177
Figure 8.4: Elevation View of 3D Reduced Model (Skewed IAB) 177
Figure 8.5: Element Block Composition for Nonlinear Pile Analysis........................... 179

ABSTRACT

Soil-structure interaction problems are both highly interesting and highly complex. To model soil-structure interaction problems accurately, the constitutive parts (i.e. foundations, soils, and superstructures) must be considered. Implementing the finite element technology necessary to analyze soil-structure interactions problems is a significant task. In this work, structural elements were added to the soil analysis computer program TeraDysac (Muraleetharan et al. 2003, Ravichandran 2005) and the soil-structure interaction in integral abutment bridges (IABs) was studied. IABs are a form of bridge where the superstructure ends are cast integrally with the abutments. The abutments, which are supported on piles in weak-axis bending move into and away from the backfill soils when the bridge deck undergoes thermal loading. These bridges provide numerous advantages to traditional bridges including reduced maintenance, simpler bridge hardware, and better water-tightness. However, because the superstructure movement is not accommodated with rollers or bearing pads like in traditional bridges, a complex soil-structure interaction problem emerges.

Three-dimensional (3D) Timoshenko beam elements and Reissner-Mindlin plate elements were developed. The merging of soil and structural elements allows bridge models to be developed that consider all of the components of an actual bridge in a realistic manner. In addition to the structural elements, a thermal loading scheme and a nonlinear beam bending stiffness (EI) scheme were also developed. In IABs, the abutment piles sometimes yield and hence enter a nonlinear range, so a nonlinear EI application may be important. Both linear elastic and bounding surface soil models were considered in this work to model the stress-strain behavior of soils.

Several soil-structure interaction problems were analyzed in this work. Beams on elastic foundations were studied and comparisons were made between analytical results and the solutions obtained from a TeraDysac finite element analysis. A nonlinear soil-structure interaction analysis using TeraDysac with a bounding surface clay model is compared with results obtained from LPILE (ENSOFT 2007), which uses a $p-y$ approach.

To test and validate the developed finite element technology, results from the field instrumentation of an IAB in Minnesota were used (see Huang et al. 2004). Two thermal events were studied in this work, a heating event during the summer and a temperature drop during the winter. The IAB used for the validation has a zero skew angle. A series of two-dimensional (2D) analyses were used to study the bridge behavior. A method for obtaining the approximate 2D structural properties is discussed. A 3D analysis comparing the Minnesota IAB superstructure (no skew) and a skewed version of the same superstructure is presented. A non-uniform abutment movement and stress distribution in the backfill soils in the skewed example show the importance of a 3D analysis when IABs are skewed.

The reinforced concrete behavior at the bridge site was studied in detail using the finite element program TeraGrande (ANATECH 2005). TeraGrande models the rebar accurately and uses a smeared crack concrete model. Significant nonlinear behavior (e.g. cracking) was not seen for the thermally-induced abutment movements. Therefore, the developed linear structural elements were deemed acceptable for the IAB analyses performed in this work.

1. Introduction

1.1 General

Bridges present a challenge for both structural and geotechnical engineers. The desirable characteristics of a bridge include simple construction, minimal maintenance, smooth riding for users (including transition areas over abutments and bents), water-tightness, and long service lives. Bridges are interesting soil-structure interaction problems because cyclic loading due to heating and cooling causes the superstructure to move relative to foundation soils. Generally speaking, these movements are small, but can be quite important from an engineering standpoint.

Traditional bridges (see Figure 1.1) accommodate cyclic loading with the following components: simply-supported girders, roller supports at intermediate bents, and expansion joints at approach slabs. These components allow for expansion and contraction of the roadway during thermal loading cycles without developing significant loads in the superstructure. The major pitfalls of traditional bridges include: rough riding for users (specifically over the bridge abutments), poor water-tightness, leakage through joints, corrosion of bearings and girders, freezing of trapped water in joints, and high levels of required maintenance.

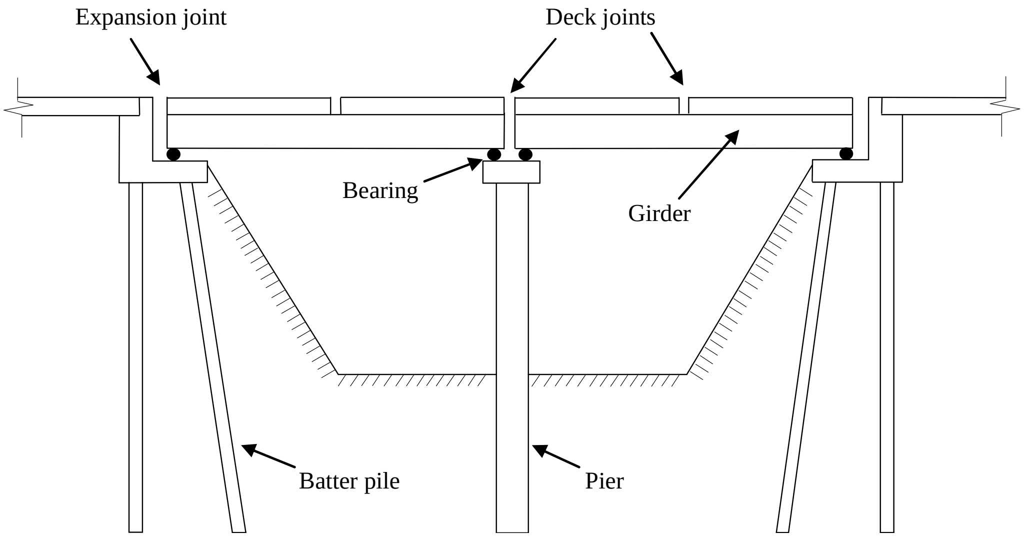

Figure 1.1: Schematic Drawing of a Traditional Bridge

In an integral abutment bridge (IAB), there is continuity in the bridge system (see Figure 1.2). These systems have numerous advantages over traditional bridges. Namely, the girder-supporting hardware is simpler, less maintenance is required, and construction is easier. Today, IAB systems can be found in almost every state. These systems are superior to traditional bridges in several areas, but are not fully pursued because there are still uncertainties with respect to their behavior and design (see Chapter 2). A typical IAB system consists of the following components: a bridge superstructure (consisting of the roadway deck, abutments, piers, girders, parapet walls), drilled shafts and pile foundations, and select fill and native soils. The bridge superstructure is generally a reinforced concrete deck sitting on pre-stressed concrete girders or heavy duty steel sections. The piers are typically resting on drilled shaft foundations, while the abutments are located on driven steel H-piles in weak-axis bending. The abutments move due to thermal effects in IABs as opposed to traditional bridges where rollers and expansion joints allow the bridge deck to move, but the abutments remain stationary.

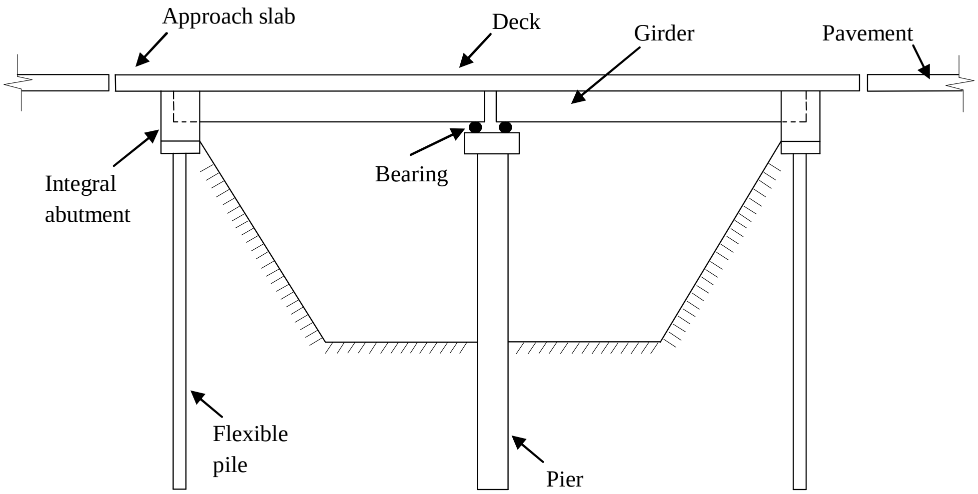

Figure 1.2: Schematic Drawing of an Integral Abutment Bridge

1.2 Modeling

To study the behavior of IAB systems, modeling that considers soil, structure, and their interaction needs to be done. Underlying and backfill soils in IAB systems need to be modeled accurately. A soil model accounting for the complexities inherent to soils, namely solid, liquid, and gas constituents, hysteresis, plastic deformation, pore water pressure development, anisotropy, and load- and time-dependence is desirable. A structural model which can account for the relevant behavior of the superstructure (i.e. the girders and deck) and the foundation (i.e. the piles and drilled shafts) is also needed. Coupling soil and structural models provides a basis for modeling IAB behavior accurately. Once the finite element technology is in place and validated against instrumented results, then many different bridge geometries, foundation designs, and loading scenarios can be simulated to gain insight into IAB performance during various events.

1.3 Finite Element Technology

Analytical solutions for real world problems are often impossible to obtain. So mathematical models are formed and numerical techniques are used to find approximate solutions. For example, the finite element and finite difference methods can be used to solve governing differential equations and find numerical approximations. TeraDysac (Muraleetharan et al. 2003, Ravichandran 2005) is a fully-coupled soil analysis code with considerations for pore water and pore air pressure and soil nonlinearity. Bounding surface plasticity soil models (Dafalias and Herrmann 1982, Yogachandran 1991) are available in addition to a linear elastic constitutive model. This work consists of adding a Timoshenko beam element and a Reissner-Mindlin plate element to the TeraDysac computer code. Also, the capability to model thermal events is developed. Coupling beams, plates, and soil elements in a finite element model allow for a user to simulate real-world systems. Though this work focuses on IABs, the technology developed can be extended to other systems (e.g. buildings and their foundations, port facilities, and offshore oil rigs).

1.4 Computational Framework

Models of complex systems such as an IAB require a high number of finite elements, sometimes on the order of hundreds of thousands to obtain accurate results. This means that big problems can not be analyzed on single processor personal computers. Even medium sized problems may take days or even weeks to analyze on a single processor machine. In practice, this is unacceptable, so parallel computing must be used. Dividing a large problem up into smaller parts and then using a different processor to analyze each part allows for a significant decrease in computational time. In this work, the parallel processing capabilities available within the TeraScale framework (ANATECH 2001) were utilized.

1.5 Objectives

The objectives of this work include the following:

1. Develop and implement structural elements (beams and plates) in TeraDysac.
2. Knowing that foundation elements (i.e. driven piles) can go beyond yielding in some IAB systems, implement an algorithm to account for this behavior.
3. Develop thermal loading capabilities in the finite element code.
4. Analyze IAB systems (soil and superstructure) for various thermal load cases and validate the results against instrumented field studies.
5. Use an external nonlinear finite element application, TeraGrande (ANATECH 2005) to verify that linear assumptions for superstructure elements are acceptable for this work.
6. Gain insight into IAB performance and design.

1.6 Dissertation Layout

This dissertation is organized into 8 chapters. Chapter 2 provides a literature review considering previous and relevant work to the field of IAB modeling. Chapter 3 discusses all of the relevant finite element technology. Chapter 4 deals with soil-structure interaction. Modeling thermal events is discussed in Chapter 5. Chapter 6 contains the TeraGrande finite element analyses which substantiate the use of linear structural elements in TeraDysac. Chapter 7 provides all of the TeraDysac results and comparisons with monitored field studies. Chapter 8 contains concluding remarks and suggestions for future work.

2. Literature Review

2.1 Integral Abutment Bridges

In traditional bridges, structural releases are provided in bridges to permit thermal expansion and contraction. These joints lead to water-tightness problems. Water runoff into newly opened deck joints can cause extensive damage. Water corrodes the underlying steel elements (girders, supports, connection hardware, etc). Water can also damage the concrete and expose reinforcing steel and subsequently corrode that. This problem is magnified in states subject to heavy snow storms, where sodium chloride and calcium chloride are commonly used in de-icing applications. The emergence of joint problems came in the 1960s as traffic loads increased in speed, volume, and weight. The cost of maintenance or replacement of expansion joints is a considerable portion of the total money spent by state Departments of Transportation (DOTs) every year. Joints and bearings in traditional bridges have emerged as major sources of bridge maintenance problems (Wolde-Tinsae and Greimann 1988).

In an IAB, there are no rollers or simple supports at the abutments. Instead, the girder ends are cast integrally with the abutment, hence the terminology integral abutment bridge. These bridges have been commissioned for some time. States like Ohio, Oregon, and South Dakota have been employing IABs since the 1930s (Hassiotis and Roman 2005). IABs have shown to be better from a fiscal standpoint than traditional bridges. They generally have a lower construction cost and much lower life cycle costs because of minimal maintenance. Retrofitting traditional bridges with IAB features has also been shown to be cost effective (Nickerson 1996).

In IABs, the thermal loading causes bending in the piles supporting the abutments. Flexibility at the abutment is provided by the use of a stub abutment supported by a single row of piles in weak-axis bending. In some cases, piles are placed in predrilled holes and then filled with sandy material. Approach slabs are usually poured behind integral abutments in order to prevent compaction of backfill soils by traffic loading and offer a smooth transition to the bridge (Arockiasamy et al. 2004).

A numerical study conducted by Yang et al. (1985) investigated the effect predrilled oversized holes have on abutment pile response. A finite element model of beam-column elements and nonlinear soil springs was used for the study. The work revealed that oversized holes, especially holes drilled to significant depths did much to alleviate overstressing the steel H-piles used under the abutment. Piles without oversized holes in harder materials such as stiff clay or compacted fill were shown to develop plastic hinges much quicker for prescribed transverse tip displacement than their counterparts with predrilled holes.

IABs have proven to be economical and effective in eliminating joint maintenance issues, but they are not without problems. When the bridge expands and contracts during thermal loading, soil at the interface is disturbed. Ground subsidence adjacent to abutments (under approach slabs) has been observed. Subsidence behind the abutment wall can cause structural problems in the approach slab if bending loads are significant as vehicles pass over the slab. In the long term, these bridges can cause a buildup of lateral earth pressures on the abutments due to the soil-mechanics phenomenon known as ratcheting (Horvath 2004).

In some cases, special additions are made to IAB systems to alleviate high pressures behind the abutments and high stresses in the abutment piles. A field experiment was conducted in North Dakota which addressed this matter (Jorgenson 1983). A 137 m IAB with concrete box girders was instrumented and monitored for a period of one year. 10 cm thick strips of compressible pressure relief material were placed in a slot between the abutments and the granular backfill. 5 cm layers of the material were placed on both sides of the abutment pile webs. These piles were in oversized holes filled with sand. These methods were shown to be effective in this case, as little yielding of the abutment piles was observed and plastic hinges did not form.

2.2 Current Practices

IABs have been in use for many years, but there still is no comprehensive design procedure. Each state highway department manages its own integral abutment program and establishes guidelines with regard to design and construction. Not having an organized design and construction procedure leads to variation in the analysis, design, and construction practices of IABs between states (Arockiasamy et al. 2004).

An excellent survey on current practices in the United States and Canada was conducted by Kunin and Alampalli (2000). The responses from 39 states and Canadian provinces provided insight into the differences in IAB design and construction practices. With the exception of one state, the opinion of the bridges was positive. Due to some expensive repair operations on bridge approaches, Arizona did not recommend IAB use. Most agencies were found to use AASHTO recommendations for temperature variation according to their region and the following formula to calculate the estimated bridge thermal movement:

$$\Delta L = \alpha \Delta T L \tag{2.1}$$

where α is the coefficient of linear thermal expansion of the superstructure, ΔT is the temperature change, and L is the bridge length. Passive soil pressure was commonly used behind the abutments, but some states use an active and passive combination. Three agencies reported not considering earth pressure in their designs. A majority of the responses revealed that skew effects are not considered with respect to soil pressure. A significant number of agencies (almost half) design piles solely for axial loads. The $p-y$ program LPILE (ENSOFT 2007) was used by some of the agencies for their pile design. In addition to soil nonlinearity, LPILE can consider structural nonlinearity (e.g. loss of bending stiffness in the piles).

2.3 Skewed IABs

A skewed IAB is one in which the abutments are not perpendicular to the roadway centerline (see Figure 2.1). A comprehensive survey of highway departments in all 50 states was conducted to determine design practices and performance of skewed IABs (Greimann et al. 1983). This survey revealed 26 states were using skewed IABs, but designing them primarily based on local experience. No theoretical or computational methods were used in most of the designs. There was noticeable variation in the practices from state to state, including abutment pile orientation and the use of batter piles for certain skew angles.

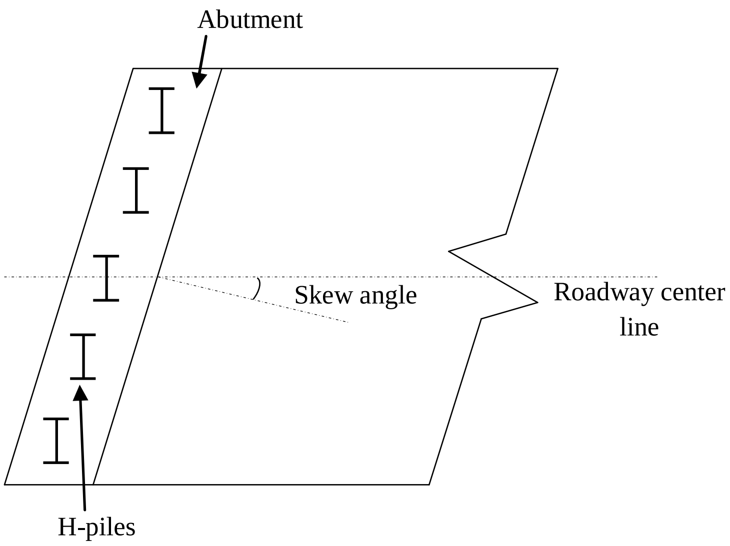

Figure 2.1: Skew Angle Depiction

A field experiment on a Maine IAB with a 20° skew angle showed the backfill pressure behind the abutments is affected by skew angle (Sandford and Elgaaly 1993). Pressure cells were mounted behind abutments to monitor skew effects. The study lasted for 33 months and revealed that the backfill behind the obtuse corners of IABs experienced significantly higher pressure (more than double in some locations) than the backfill behind the acute corners. Figure 2.2 depicts the obtuse and acute angles in an IAB.

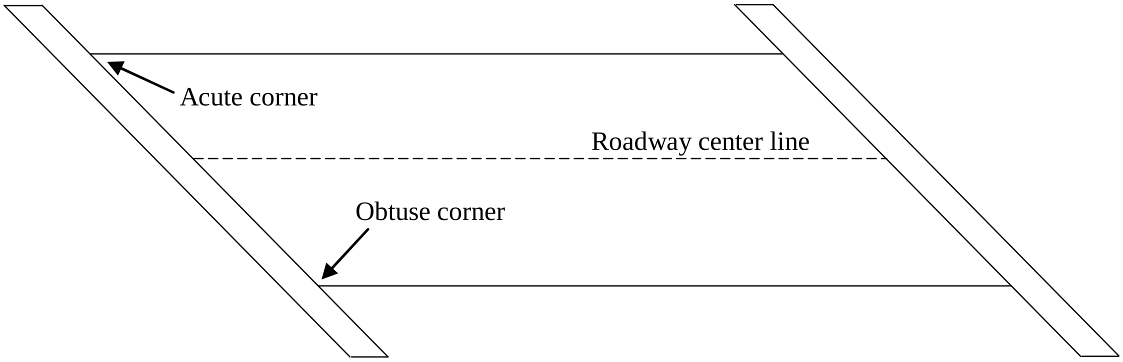

Figure 2.2: Obtuse and Acute Corners in IABs

Alampalli and Yannotti (1998) performed an in-service evaluation of IABs in New York. IABs were graded based on the New York State DOT condition rating scale for bridges. Bridge ratings were lower for both steel and concrete superstructures when the IABs were skewed. Greater skew angles were linked to poorer ratings according to their work.

A recommendation of a maximum bridge skew angle of 30° was made pending further study. In a paper by Comstock and Dagher (1993), rearranging the longitudinal reinforcement in the bridge was shown to delay cracking in the deck near the abutment walls. By placing more steel in the obtuse corners, the bending moment and shear force capacities in the obtuse corners of the bridge were increased. This delayed cracking in the obtuse corners and ultimately led to a more uniform crack pattern across the deck.

In a study conducted by Steinberg et al. (2004) on two Ohio skewed semi-integral abutment bridges, the forces developed in the wingwalls were found to be significant. It was recommended that these forces be considered in the design process, as opposed to designing the wingwalls simply as retaining walls. A subsequent finite element analysis showed the reaction at the wingwalls to increase with bridge skew angle.

2.4 Soil-Structure Interaction

In analyzing soil-structure interaction problems, sometimes interface elements are used in finite element programs to simulate behavior at the interface. The important phenomena at the interface are relative slipping and shear resistance (tangential behavior) and bearing and gapping (normal behavior). Two dimensional (2D) elements or 'Zero Thickness Elements' have been around for years (e.g. Goodman et al. 1968, Beer 1985). Zero thickness elements using a Mohr-Coulomb failure criterion have been shown to model interface behavior of retaining walls with good accuracy, but numerical stability issues emerge in some problems (Day and Potts 1994). Three dimensional (3D) elements with a finite thickness or 'Thin-Layer Elements' have also been used to model soil-structure interfaces (e.g. Desai et al. 1984). These elements require a constitutive model for implementation. Usually experiments and simple lab tests are performed on the soil and the interface (e.g. a direct shear test between concrete and clay) to obtain various parameters such as the normal and tangential stiffness. Another approach models the structure and soil separately, but uses constraint equations to maintain compatibility of force and displacement between the two. This so-called ‘Hybrid Method’ can accommodate the relevant modes at the interface and also has been shown to be more numerically stable than the above methods because there are no vastly different magnitudes of numbers in the stiffness matrix (Lai and Booker 1991). This work will use tied contact between shared soil and structure nodes. Although this procedure has its limitations, the coupling of soil and structural elements is a good first step to modeling soil-structure interaction. The development of an interface element to be used in conjunction with this work may need to be pursued later. However, for the small displacements in the IAB modeling for thermal effects considered here, tied contact should be acceptable.

2.5 Instrumentation Projects

There have been numerous IAB instrumentation projects in the literature (e.g. Fennema et al. 2005 and Sandford et al. 2006). Fennema et al. instrumented and analyzed a three-span bridge (52.4 m bridge length, zero skew angle) in Pennsylvania. The project examined several uncertainties of IAB design, performed field-monitoring, and analyzed the bridge with three levels of numerical modeling. The analysis levels included laterally loaded pile models using commercially available software, 2D single bent models, and 3D finite element models. Multilinear spring stiffnesses were developed through a sequence of linear regressions to fit $p - y$ curves at depths corresponding to locations of soil springs defined in the bridge structural analysis model. The instrument data from the bridge site was used to refine the numerical models. The models were then used to predict IAB behavior of other Pennsylvania bridges of similar construction.

A field monitoring effort during the construction of an IAB in Maine (30 m bridge length, 35° skew angle) revealed bending stresses from dead loads are quite important (Sandford et al. 2006). Some agencies explicitly calculate bending effects, but many neglect dead load bending in piles. This monitoring effort revealed stresses from bending by abutment rotation due to dead load should be included in the design process. If the bridge is skewed, bending in piles perpendicular to the centerline should also be computed.

Major work has been done in the field of IAB instrumentation, monitoring, and analysis through the University of Minnesota (see Huang et al. 2004). An IAB located in Rochester, Minnesota (65.6 m bridge length, zero skew angle) was monitored from the beginning of construction through several years of service. More than 180 instruments, including tiltmeters, strain gauges, and pressure cells, were installed in and around the bridge during construction to monitor loading effects. Various weather recording devices were also set up at the bridge site to monitor temperature and solar radiation. The primary movement of the abutment was found to be a horizontal translation to accommodate superstructure expansion and contraction due to seasonal changes. There was a net inward movement of the abutments over time. An extensive numerical study was also performed. The numerical modeling showed that the $p-y$ method could simulate soil-pile interaction reasonably well. The work provided good insight into IAB performance and a wealth of results from instrumentation, some of which will be used to validate the proposed finite element code.

An IAB instrumentation effort is currently underway in Lawton, Oklahoma (64.3 m bridge length, 10° skew angle). The Oklahoma Transportation Center project (No. OTCREOS7-1-37) will provide data including weather information, abutment translation, rotation, pile curvature, and earth pressure. Skewed IABs are typically not built in Oklahoma, so the project results will help determine the course for the skewed IAB program in Oklahoma.

2.6 Important Loading Cases

There are many factors to be considered when designing these complicated systems. Static, live, cyclic, and dynamic loading scenarios are all possible. Because of the size and weight of highway bridges, the effect of gravity loading alone is an important load case. As discussed previously, thermal loading is of major importance in IABs. In a paper by Paul et al. (2005), the thermal forces developed in prestressed girder IABs were found to be comparable in magnitude to those caused by live load. Their work showed the largest thermally induced superstructure forces to be found near the abutments. After studying several parameters that influence thermal loading, they concluded that bridge length and abutment height strongly influence thermal forces. Taller abutments have a larger cross-sectional area exposed to the backfill soil, so upon bridge expansion there is a greater passive soil resistance leading to higher superstructure forces. In addition to traffic loads and creep of the superstructure, earthquakes and blast loading may also need consideration.

3. Finite Element Technology

3.1 Soil Element

3.1.1 Governing Equations

The soils modeled in this work are assumed to be saturated (i.e. there is no air in the soil), but capabilities exist to model unsaturated soils in TeraDysac (see Ravichandran 2005). The governing equations are written in standard indicial notation below. See Muraleetharan et al. (1994) for further reference to the formulation of the governing equations. Tensile normal stresses and strains are assumed positive. Porewater pressure, h, is assumed positive in compression. The following equations apply to a representative unit volume of the soil-water mixture, see Figure 3.1.

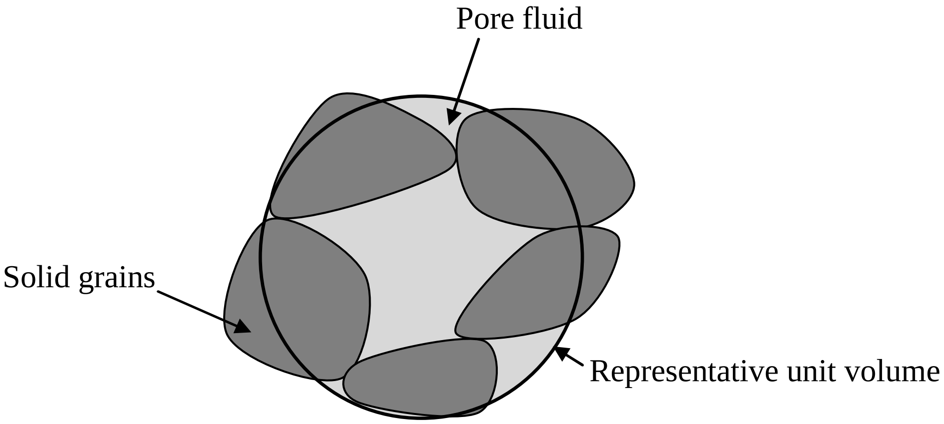

Figure 3.1: Soil-Fluid Mixture

The equation of motion for the grain-fluid mixture is given by:

$$\sigma_{ij,i} + \rho g_j - (1 - n)\rho_s \ddot{u}_j - n\rho_f \left(\ddot{u}_j + \frac{\ddot{w}_j}{n}\right) = 0 \tag{3.1}$$

where σ_{ij} is the total stress tensor, u_i is the displacement of the soil skeleton, ρ_s is the density of the solid grains, ρ_f is the density of the pore fluid, g_i is the body force per unit volume (generally, gravitational acceleration), n is the porosity of the mixture, w_i is the average displacement of the fluid relative to the soil skeleton such that $\dot{w}_i$ is the Darcy velocity. The density of the mixture, ρ, is given by Equation 3.2.

$$\rho = (1 - n)\rho_s + n\rho_f \tag{3.2}$$

The porosity is related to the void ratio e through:

$$n = \frac{e}{1+e} \tag{3.3}$$

Using Equation 3.2, the Equation 3.1 can be rewritten as follows:

$$\sigma_{ij,i} + \rho g_j - \rho \ddot{u}_j - \rho_f \ddot{w}_j = 0 \tag{3.4}$$

The equation of motion for a unit volume of pore fluid is given by Equation 3.5.

$$\dot{w}_i = -k_{ij}^{*}\left[h_{,j} - \rho_f g_j + \rho_f\left(\ddot{u}_j + \frac{\ddot{w}_j}{n}\right)\right] \tag{3.5}$$

Conservation of mass for the solid-fluid mixture is given by:

$$\dot{\epsilon}_{ii} = -\dot{w}_{i,i} - \left(\frac{n}{K_f} + \frac{1-n}{K_s}\right)\dot{h} + \frac{1-n}{3}\delta_{ij}\frac{\dot{\sigma}'_{ij}}{K_s} \tag{3.6}$$

where ϵ_{ij} is the strain tensor for the soil skeleton, K_f is the bulk modulus of the pore fluid (typically on the order of 10^5 – 10^6 kPa), K_s is the bulk modulus of the solid grains (typically on the order of 10^{10} – 10^{20} kPa), and δ_{ij} is the Kronecker delta. Due to the magnitude of K_s, the compression of the solid grains due to inter-granular pressure (the last term on the right-hand side of Equation 3.6) is essentially zero. Therefore, this term will be omitted from this point further. The combined bulk modulus, Γ, can be found by evaluating Equation 3.7.

$$\frac{1}{\Gamma} = \frac{n}{K_f} + \frac{1-n}{K_s} \tag{3.7}$$

Therefore, Equation 3.6 can be rewritten as follows:

$$\dot{\epsilon}_{ii} = -\dot{w}_{i,i} - \frac{\dot{h}}{\Gamma} \qquad (3.8)$$

The equation used for classical small-strain kinematics is given by Equation 3.9.

$$\epsilon_{ij} = \frac{1}{2}(u_{i,j} + u_{j,i}) \qquad (3.9)$$

A large deformation formulation is also available in TeraDysac (see Ravichandran 2005). The effective stress, total stress minus pore fluid pressure, for the soil skeleton is given by Equation 3.10.

$$\sigma'_{ij} = \sigma_{ij} - h\delta_{ij} \qquad (3.10)$$

The fourth-rank tensor D_{ijkl} holds the various elastoplastic moduli. The relationship given by Equation 3.11 is sufficiently general to accommodate any constitutive relationship describing the effective stress-strain relationship of the soil skeleton. The last term on the right-hand side includes the rate of change of strain-independent stresses.

$$\dot{\sigma}'_{ij} = D_{ijkl}\dot{\epsilon}_{kl} + \dot{\sigma}'_{ij_0} \qquad (3.11)$$

The boundary conditions applied on the soil boundaries are given in the form of Equations 3.12 and 3.13.

$$\dot{T}_j = \dot{\sigma}_{ij}\nu_i \ \text{ or } \ \dot{u}_j \text{ given} \qquad (3.12)$$

$$\dot{Q} \ \text{ or } \ \dot{h} \text{ given} \qquad (3.13)$$

where ν_i is the unit normal and Q is the fluid flow rate across the boundary. The total displacement of the fluid is given by:

$$U_i = u_i + \frac{w_i}{n} \qquad (3.14)$$

The final forms of the governing equations are given in Equations 3.15 and 3.16.

$$(1-n)\rho_s\ddot{u}_j - n^2 {k_{ij}^{*}}^{-1}\left(\dot{U}_i - \dot{u}_i\right) - \Gamma n(1-n)U_{i,ij} - \Gamma(1-n)^2 u_{i,ij}$$

$$-(1-n)\rho_s g_j - \sigma'_{ij,i} = 0 \qquad (3.15)$$

$$n\rho_f \ddot{U}_j - n^2 k_{ij}^{*^{-1}} \left(\dot{U}_i - \dot{u}_i\right) - \Gamma n^2 U_{i,ij} - \Gamma n(1-n) u_{i,ij} - n\rho_f g_j = 0 \tag{3.16}$$

Note:

$$u_i = N_J^u u_{Ji} \tag{3.17}$$

$$U_i = N_J^U U_{Ji} \tag{3.18}$$

where u_i is the nodal solid displacement and U_i is the nodal fluid displacement. Generally, the shape functions N_J^u and N_J^U are different, but in this work they are the same.

The bilinear shape functions are given by:

$$N_J(\xi,\eta) = \frac{1}{4}\left(1+\xi_J\xi\right)(1+\eta_J\eta) \tag{3.19}$$

no summation over J.

The governing equations can be written in matrix form as follows:

$$Ma + Cv + K_p d + p = f \tag{3.20}$$

$$a = \text{vector of nodal accelerations} = \begin{Bmatrix} \ddot{u}_{Ji} \\ \ddot{U}_{Ji} \end{Bmatrix} \tag{3.21}$$

$$v = \text{vector of nodal velocities} = \begin{Bmatrix} \dot{u}_{Ji} \\ \dot{U}_{Ji} \end{Bmatrix} \tag{3.22}$$

$$d = \text{vector of nodal displacements} = \begin{Bmatrix} u_{Ji} \\ U_{Ji} \end{Bmatrix} \tag{3.23}$$

In the definitions of a, v, and d, the indices I and J indicate node numbers and i and j are associated with the spatial coordinates of the displacement, velocity, or acceleration vector. The solution vectors a, v, and d are multiplied by the coefficient matrices M, C, and K_p, and the resultant inertial, damping, and stiffness force vectors are augmented by the internal and external load vectors p and f, respectively. The integrals are defined over elemental domains Ω_m, where m ranges over the number of elements (NE) and over boundary segments Φ_s, and where s ranges over the number of element sides (NS). The finite element matrices are defined by:

$$M = \text{mass matrix} = \begin{bmatrix} M_1 & 0 \\ 0 & M_2 \end{bmatrix} \tag{3.24}$$

$$M_1 = \sum_{m=1}^{NE} \int_{\Omega_m} N_I^u (1-n)\rho_s N_J^u \, d\Omega \tag{3.25}$$

$$M_2 = \sum_{m=1}^{NE} \int_{\Omega_m} N_I^U n\rho_f N_J^U \, d\Omega \tag{3.26}$$

$$C = \text{damping matrix} = \begin{bmatrix} C_1 & -C_2 \\ -C_2^T & C_3 \end{bmatrix} \tag{3.27}$$

$$C_1 = \sum_{m=1}^{NE} \int_{\Omega_m} N_I^u \left(n^2 k_{ij}^{*^{-1}}\right) N_J^u \, d\Omega \tag{3.28}$$

$$C_2 = \sum_{m=1}^{NE} \int_{\Omega_m} N_I^u \left(n^2 k_{ij}^{*^{-1}}\right) N_J^U \, d\Omega \tag{3.29}$$

$$C_3 = \sum_{m=1}^{NE} \int_{\Omega_m} N_I^U \left(n^2 k_{ij}^{*^{-1}}\right) N_J^U \, d\Omega \tag{3.30}$$

$$K_p = \text{pore fluid stiffness matrix} = \begin{bmatrix} K_1 & K_2 \\ K_2^T & K_3 \end{bmatrix} \tag{3.31}$$

$$K_1 = \sum_{m=1}^{NE} \int_{\Omega_m} N_{I,j}^u \Gamma (1-n)^2 N_{J,i}^u \, d\Omega \tag{3.32}$$

$$K_2 = \sum_{m=1}^{NE} \int_{\Omega_m} N_{I,j}^u \Gamma n(1-n)^2 N_{J,i}^U \, d\Omega \tag{3.33}$$

$$K_3 = \sum_{m=1}^{NE} \int_{\Omega_m} N_{I,j}^U \Gamma n^2 N_{J,i}^U \, d\Omega \tag{3.34}$$

$$p = \text{internal load vector} = \begin{Bmatrix} p_1 \\ 0 \end{Bmatrix} \tag{3.35}$$

$$p_1 = \sum_{m=1}^{NE} \int_{\Omega_m} N_{I,i}^u \sigma'_{ij} \, d\Omega \tag{3.36}$$

$$f = \text{applied load vector} = \begin{Bmatrix} f_1 \\ f_2 \end{Bmatrix} \tag{3.37}$$

$$f_1 = \sum_{m=1}^{NE} \int_{\Omega_m} N_I^u (1-n)\rho_s g_j d\Omega + \sum_{s=1}^{NS} \int_{\Phi_n} N_I^u \left(T_j + nhv_j\right)\rho_s g_j d\Phi \qquad (3.38)$$

$$f_2 = \sum_{m=1}^{NE} \int_{\Omega_m} N_I^U n\rho_f g_j d\Omega - \sum_{s=1}^{NS} \int_{\Phi_n} N_I^U nhv_j d\Phi \qquad (3.39)$$

The integration of the element matrices for the four node quadrilaterals is performed using a Gauss-Quadrature (2x2) or a Uniform Gradient (one-point selective reduced integration with Belytschko hourglass control) formulation. A detailed discussion of the Uniform Gradient element is discussed in Ravichandran (2005).

3.1.2 Linear Elastic Constitutive Model

In 3D, the constitutive model is given by:

$$\begin{bmatrix} \sigma_{11} \\ \sigma_{22} \\ \sigma_{33} \\ \sigma_{12} \\ \sigma_{23} \\ \sigma_{31} \end{bmatrix} = \frac{E}{(1+\nu)(1-2\nu)} \begin{bmatrix} (1-\nu) & \nu & \nu & 0 & 0 & 0 \\ \nu & (1-\nu) & \nu & 0 & 0 & 0 \\ \nu & \nu & (1-\nu) & 0 & 0 & 0 \\ 0 & 0 & 0 & \frac{(1-2\nu)}{2} & 0 & 0 \\ 0 & 0 & 0 & 0 & \frac{(1-2\nu)}{2} & 0 \\ 0 & 0 & 0 & 0 & 0 & \frac{(1-2\nu)}{2} \end{bmatrix} \begin{bmatrix} \epsilon_{11} \\ \epsilon_{22} \\ \epsilon_{33} \\ \epsilon_{12} \\ \epsilon_{23} \\ \epsilon_{31} \end{bmatrix} \qquad (3.40)$$

where E is Young's modulus and ν is Poisson's ratio.

The 2D model in TeraDysac uses a plane strain assumption, thus

$$\epsilon_{33} = \epsilon_{31} = \epsilon_{23} = 0 \qquad (3.41)$$

The constitutive relationship collapses to the following:

$$\begin{bmatrix} \sigma_{11} \\ \sigma_{22} \\ \sigma_{33} \\ \sigma_{12} \end{bmatrix} = \frac{E}{(1+\nu)(1-2\nu)} \begin{bmatrix} (1-\nu) & \nu & \nu & 0 \\ \nu & (1-\nu) & \nu & 0 \\ \nu & \nu & (1-\nu) & 0 \\ 0 & 0 & 0 & \frac{(1-2\nu)}{2} \end{bmatrix} \begin{bmatrix} \epsilon_{11} \\ \epsilon_{22} \\ \epsilon_{33} \\ \epsilon_{12} \end{bmatrix} \qquad (3.42)$$

3.1.3 Bounding Surface Constitutive Model for Clays

For clayey soils in TeraDysac, the constitutive model used is the one developed by Dafalias and Herrmann (1982, 1986). The model is based on the concept of the bounding surface in stress space (see Figure 3.2). The bounding surface is comprised of two ellipses and a hyperbola. The three-surface model yields a better description of the material response for heavily overconsolidated soil (Dafalias and Herrmann 1986). Inelastic deformations are allowed to occur for stress points within the bounding surface. A radial mapping rule is used to relate the actual stress point (I, J) to an “image” stress point on the bounding surface $(\bar{I}, \bar{J})$. The value of the plastic modulus depends on the distance between the actual stress point and the “image” stress point.

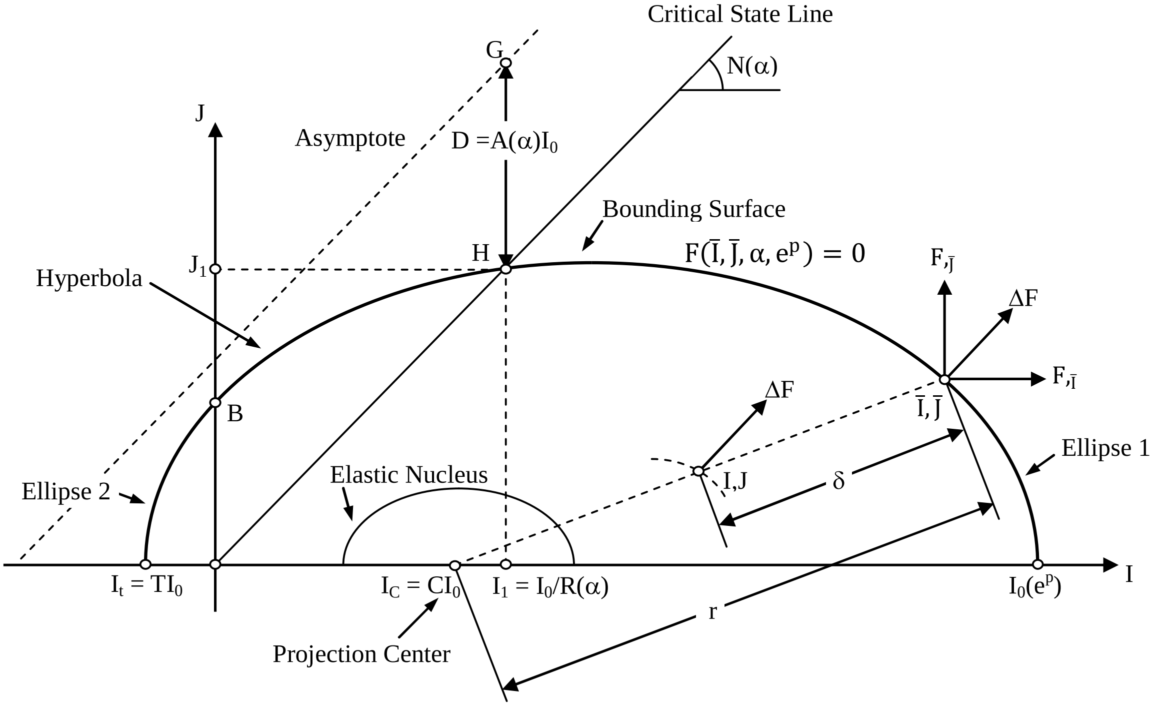

Figure 3.2: Bounding Surface Representation (Clayey Soils)

The bounding surface parameters for Speswhite Kaolin, the soft clay used in a later analysis, were determined from experimental results. The parameters (from Muraleetharan et al. 1994) are given in Table 3.1:

Table 3.1: Bounding Surface Model Parameters for Speswhite Kaolin

Property		**Value**
Liquid limit		69%
Plasticity index		31%
Specific gravity		2.62
Permeability (m/s)		$1.7*10^{-9}$
Traditional Model Parameters		
Slope of isotropic consolidation line on $e - \ln p'$ plot	λ	0.25
Slope of elastic rebound line on $e - \ln p'$ plot	κ	0.05
Slope of critical state line in $q - p'$ space (compression)	M_c	0.88
Ratio of extension to compression value of M	M_e/M_c	1.0
Poisson's ratio	ν	0.3
Bounding Surface Configuration Parameters		
Value of parameter defining ellipse 1 in compression	R_c	2.4
Value of parameter defining the hyperbola in compression	A_c	0.01
Parameter defining ellipse 2 (the tension zone)	T	0.01
Projection center parameter	C	0.0
Elastic nucleus parameter	S	1.0
Ratio of triaxial extension to triaxial compression value of A	A_e/A_c	1.2
Hardening Parameters		
Shape hardening parameter in triaxial compression	h_c	3.0
Ratio of triaxial extension to triaxial compression value of h	h_e/h_c	1.0
Shape hardening parameter on the I-axis	h_2	2.0
Notes:		
e = void ratio, $p' = (\sigma_1' + 2\sigma_3')/3$, $q = \sigma_1' - \sigma_3'$		

3.1.4 Bounding Surface Constitutive Model for Sands

A bounding surface constitutive model for sands developed by Yogachandran (1991) is available in TeraDysac. The model uses the theory first developed by Dafalias and Popov (1976). The important features of the model include: the allowance of plastic strains to occur within the bounding surface, a non-associative flow rule which more accurately describes the behavior of dense sands (e.g. dilation), and consideration of plastic strain during unloading which can help capture cyclic mobility and liquefaction. Figure 3.3 is a schematic of the bounding surface for sands. Two ellipses define the bounding surface and a plastic potential is used to define the incremental plastic strain direction.

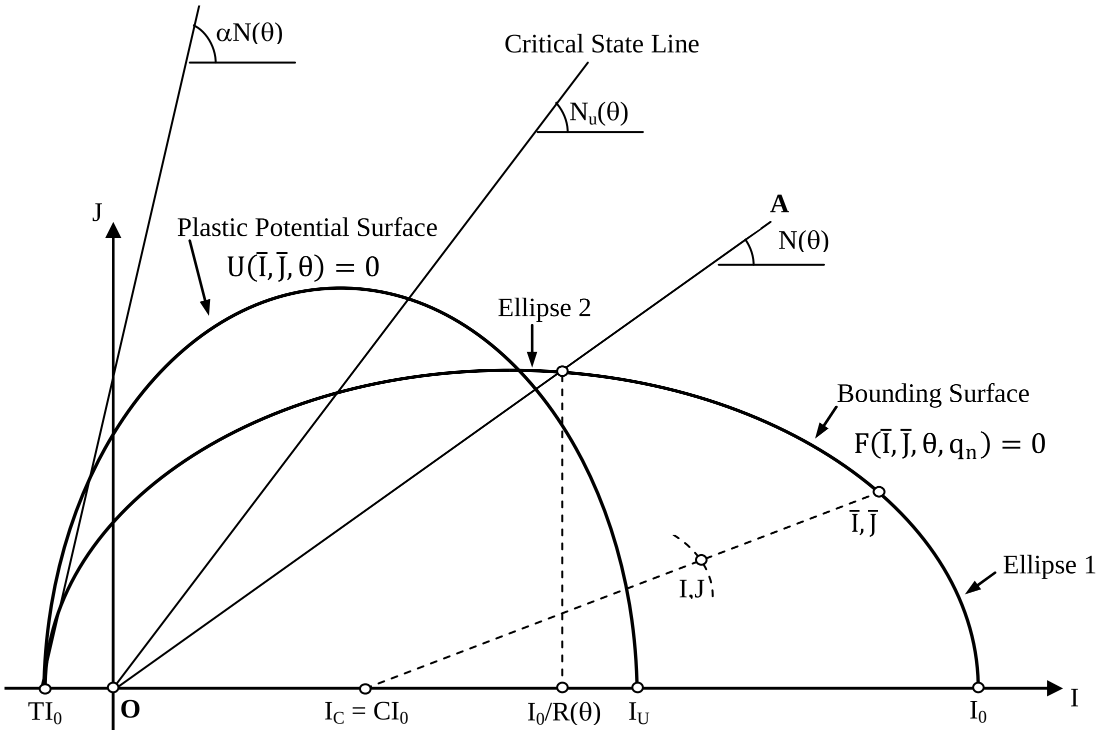

Figure 3.3: Bounding Surface Representation (Sands)

To calibrate the bounding surface parameters for sands a total of at least six laboratory tests should be performed (Yogachandran 1991). These tests include:

- isotropic or anisotropic (K_0) consolidation or drained compression test with both loading and unloading (one test)
- consolidated-undrained (preferably) or drained triaxial compression and extension tests, with pore water pressure measurements on specimens in loose and dense states (four tests)
- consolidated-undrained triaxial cyclic loading test with pore water pressure measurements (one test)

The model parameters for Nevada Sand with relative densities of 40 and 60% have been presented previously (see Muraleetharan 1995). They are used to guide the selection of bounding surface parameters for the Minnesota IAB analysis discussed in Chapter 7. Generally, only the parameters given in the two right hand columns of Table 3.2 require calibration.

Table 3.2: Bounding Surface Model Parameters

		All Sands	Nevada Sand (D_r = 40%)	Nevada Sand (D_r = 60%)
Traditional Model Parameters				
Slope of isotropic consolidation line on $e - \ln p'$ plot	λ	-	0.007	0.009
Slope of elastic rebound line on $e - \ln p'$ plot	κ	-	0.003	0.002
Poisson's ratio	ν	0.3	-	-
Bounding Surface Configuration Parameters				
Slope of line OA (Fig. 3) in $q - p'$ space (compression)	M_c	-	0.89	0.89
Ratio of extension to compression value of M	M_e/M_c	-	0.61	0.61
Value of R in triaxial compression	R_c	-	1.5	1.5
Ratio of extension to compression value of R	R_e/R_c	1.0	-	-
Related to gradient of ellipse 2 on I-axis	α	-	5.0	5.0
Projection center parameter	C	0.0	-	-
Tension zone parameter	T	0.005	-	-
Parameter defining the initial size of the bounding surface	I_0/I	-	1.0	1.5
Plastic Potential Surface Configuration Parameter				
Slope of critical state line (compression) in $q - p'$ space	$(M_u)_c$	-	1.33	1.44
Hardening Parameters During Loading				
Shape hardening parameter in triaxial compression	h_c	-	2.0	2.0
Ratio of triaxial extension to triaxial compression value of h	h_e/h_c	-	0.05	0.05
Shape hardening parameter on the I-axis	h_2	$(h_c + h_e)/2.0$	-	-
Hardening parameter	m	0.02	-	-
Deviatoric hardening parameter	β_0	1.0	-	-

Deviatoric hardening parameter	β_1	-	0.5	0.4
Hardening Parameters During Unloading				
Unloading hardening parameter	H_u	-	0.2	0.2
Unloading hardening parameter	γ_u	0.9	-	-
Additional Parameters				
Atmospheric pressure (kPa)	P_a	101.4	-	-
Transitional value of confining pressure	P_l	$P_a/3$	-	-

Notes:

e = void ratio,

$p' = (\sigma_1' + 2\sigma_3')/3,\ q = \sigma_1' - \sigma_3'$

3.2 Beam Element

A low order beam element has been developed for TeraDysac. The low order element is compatible with the four node soil quadrilaterals and eight node hexagonal soil elements, which have a linear variation of displacement between nodes. The line element has six degrees of freedom at each node (three displacements and three rotations). Figure 3.4 shows a typical element with nodal variables designated for the right node.

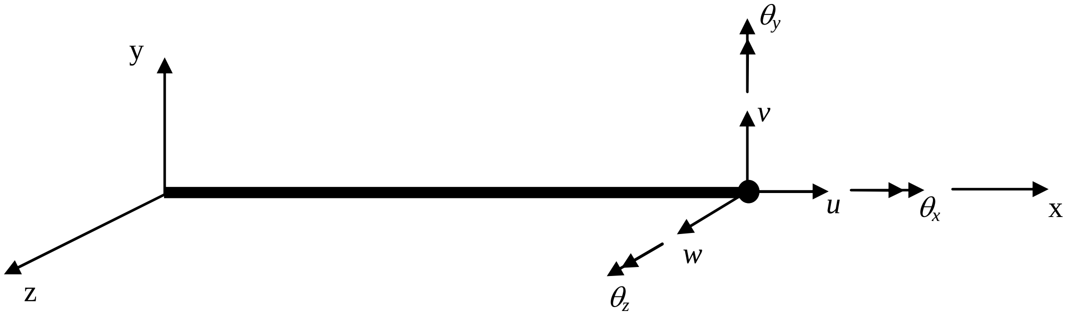

Figure 3.4: Beam Element Nodal Variables

Linear interpolation is used between the nodes. Figure 3.5 shows the coordinate transformation needed to interpolate nodal unknowns.

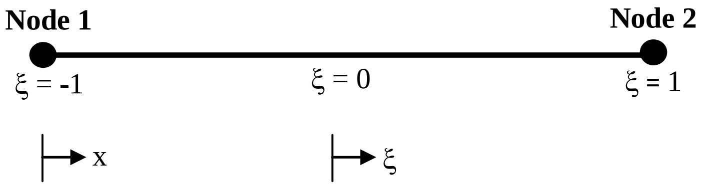

Figure 3.5: Beam Element Coordinate Transformation

x can be written as a function of ξ:

$$x = \frac{L}{2}(1 + \xi) \tag{3.43}$$

where L is the length of the beam.

The linear interpolation functions are:

$$N_1(\xi) = \frac{1}{2}(1 - \xi) \tag{3.44}$$

$$N_2(\xi) = \frac{1}{2}(1 + \xi) \tag{3.45}$$

The Jacobian is given by:

$$J = \frac{\partial x}{\partial \xi} = \frac{L}{2} \tag{3.46}$$

The inverse of the Jacobian is given by:

$$J^{-1} = \frac{2}{L} \tag{3.47}$$

3.2.1 Stiffness Matrix

Axial Stiffness

The displacement components for the element are given as follows:

$$u = u(x) = \sum_{i=1}^{2} N_i u_i \tag{3.48}$$

The axial strain in the beam is given by:

$$\epsilon = \frac{\partial u}{\partial x} \tag{3.49}$$

The constitutive relationship is given as follows:

$$\sigma = E\epsilon \tag{3.50}$$

where E is Young's modulus.

The total strain energy in the element is given as follows:

$$U = \frac{1}{2}\int_V \epsilon^T \sigma \, dV = \frac{1}{2}\int_V \epsilon^T E\epsilon \, dV \tag{3.51}$$

where V is the element volume. The 2x2 stiffness matrix, K_{axial}, can be found by minimizing the total strain energy. Denoting P_i as the axial force at node i and u_i as the displacement in x-direction at node i, the result is given as follows:

$$\begin{Bmatrix} P_1 \\ P_2 \end{Bmatrix} = \begin{bmatrix} \frac{EA}{L} & \frac{-EA}{L} \\ \frac{-EA}{L} & \frac{EA}{L} \end{bmatrix} \begin{Bmatrix} u_1 \\ u_2 \end{Bmatrix} \tag{3.52}$$

where A is the cross-sectional area of the beam.

Torsional Stiffness

The displacement components for the element are given as follows:

$$\theta_x = \theta_x(x) = \sum_{i=1}^{2} N_i \theta_{xi} \tag{3.53}$$

The shear strain in the beam is given by:

$$\gamma = r\frac{\partial \theta_x}{\partial x} \tag{3.54}$$

where r is the distance from the centroid of the beam.

The constitutive relationship is given as follows:

$$\tau = G\gamma \tag{3.55}$$

where G is the shear modulus of the beam.

The total strain energy in the element is given as follows:

$$U = \frac{1}{2}\int_V \gamma^T \tau \, dV = \frac{1}{2}\int_V \gamma^T G\gamma \, dV \tag{3.56}$$

The 2x2 stiffness matrix, $K_{torsional}$, can be found by minimizing the total strain energy. Denoting T_i as the torque at node i and θ_{xi} as the rotation about the x-axis at node i, the result is given as follows:

$$\begin{Bmatrix} T_1 \\ T_2 \end{Bmatrix} = \begin{bmatrix} \frac{GJ}{L} & \frac{-GJ}{L} \\ \frac{-GJ}{L} & \frac{GJ}{L} \end{bmatrix} \begin{Bmatrix} \theta_{x1} \\ \theta_{x2} \end{Bmatrix} \tag{3.57}$$

where J is the polar moment of inertia of the beam.

Bending Stiffness

Timoshenko beam theory (Timoshenko 1921) is used with reduced integration on the shear terms to develop the beam elements for TeraDysac. The reduced integration eliminates the shear locking problem that emerges for thin beams.

The displacement components for the element are given as follows:

$$v = v(x) = \sum_{i=1}^{2} N_i v_i \tag{3.58}$$

$$\theta_z = \theta_z(x) = \sum_{i=1}^{2} N_i \theta_{zi} \tag{3.59}$$

The total rotation of the plane originally normal to the neutral axis of the beam is given by:

$$\theta_z = \frac{dv}{dx} - \gamma \tag{3.60}$$

where v is transverse displacement, $\frac{dv}{dx}$ is the slope of the mid-surface, and γ is the constant shearing strain across the section.

Rearranging, the shear strain in the beam can be written as follows:

$$\gamma = \frac{dv}{dx} - \theta_z \tag{3.61}$$

Because the actual shearing stress and strain vary over the beam area, A, the shearing strain given above is an equivalent constant strain on a corresponding shear area, A_s. A constant, k is introduced to account for this.

$$k = \frac{A_s}{A} \tag{3.62}$$

The constitutive relationship is given as follows:

$$\tau = kG\gamma \tag{3.63}$$

where G is the shear modulus of the beam.

The bending strain in the beam is given by:

$$\epsilon_b = y\frac{\partial\theta_z}{\partial x} \tag{3.64}$$

where y is the distance above the neutral axis of the beam.

The constitutive relationship is given as follows:

$$\sigma_b = E\epsilon_b \tag{3.65}$$

where E is Young's modulus.

The total strain energy of the beam is given by:

$$U = \frac{1}{2}\int_V \ {\epsilon_b}^T \sigma_b \, dV + \frac{1}{2}\int_V \ \gamma^T \tau \, dV = \frac{1}{2}\int_V \ {\epsilon_b}^T E\epsilon_b \, dV + \frac{k}{2}\int_V \ \gamma^T G\gamma \, dV \tag{3.66}$$

The 4x4 stiffness matrix, $K_{bending}$, can be found by minimizing the total strain energy. Denoting V_{yi} as the shear force in the y-direction at node i, M_{zi} as the bending moment about the z-axis at node i, v_i as the displacement in the y-direction at node i, and θ_{zi} as the rotation about the z-axis at node i, the result is given as follows:

$$\begin{Bmatrix} V_{y1} \\ M_{z1} \\ V_{y2} \\ M_{z2} \end{Bmatrix} = \begin{bmatrix} \frac{GAk}{L} & \frac{GAk}{2} & \frac{-GAk}{L} & \frac{GAk}{2} \\ \frac{GAk}{2} & \frac{EI_z}{L} + \frac{GAkL}{4} & \frac{-GAk}{2} & \frac{-EI_z}{L} + \frac{GAkL}{4} \\ \frac{-GAk}{L} & \frac{-GAk}{2} & \frac{GAk}{L} & \frac{-GAk}{2} \\ \frac{GAk}{2} & \frac{-EI_z}{L} + \frac{GAkL}{4} & \frac{-GAk}{2} & \frac{EI_z}{L} + \frac{GAkL}{4} \end{bmatrix} \begin{Bmatrix} v_1 \\ \theta_{z1} \\ v_2 \\ \theta_{z2} \end{Bmatrix} \tag{3.67}$$

where I_z is the moment of inertia about the z-axis of beam.

The above relationship applies to bending of the beam in the x-y plane. An analogous formulation can be applied to obtain the bending stiffness in the z-x plane. The result is given by:

$$\begin{Bmatrix} V_{z1} \\ M_{y1} \\ V_{z2} \\ M_{y2} \end{Bmatrix} = \begin{bmatrix} \frac{GAk}{L} & \frac{-GAk}{2} & \frac{-GAk}{L} & \frac{-GAk}{2} \\ \frac{-GAk}{2} & \frac{EI_y}{L} + \frac{GAkL}{4} & \frac{GAk}{2} & \frac{-EI_y}{L} + \frac{GAkL}{4} \\ \frac{-GAk}{L} & \frac{GAk}{2} & \frac{GAk}{L} & \frac{GAk}{2} \\ \frac{-GAk}{2} & \frac{-EI_y}{L} + \frac{GAkL}{4} & \frac{GAk}{2} & \frac{EI_y}{L} + \frac{GAkL}{4} \end{bmatrix} \begin{Bmatrix} w_1 \\ \theta_{y1} \\ w_2 \\ \theta_{y2} \end{Bmatrix} \qquad (3.68)$$

where I_y is the moment of inertia about the y-axis of beam. Putting all of the components together yields the full stiffness matrix for the 3D beam element:

$$\begin{Bmatrix} P_1 \\ V_{y1} \\ V_{z1} \\ T_1 \\ M_{y1} \\ M_{z1} \\ P_2 \\ V_{y2} \\ V_{z2} \\ T_2 \\ M_{y2} \\ M_{z2} \end{Bmatrix} = \begin{bmatrix} \frac{EA}{L} & 0 & 0 & 0 & 0 & 0 & \frac{-EA}{L} & 0 & 0 & 0 & 0 & 0 \\ 0 & \frac{GAk}{L} & 0 & 0 & 0 & \frac{GAk}{2} & 0 & \frac{-GAk}{L} & 0 & 0 & 0 & \frac{GAk}{2} \\ 0 & 0 & \frac{GAk}{L} & 0 & \frac{-GAk}{2} & 0 & 0 & 0 & \frac{-GAk}{L} & 0 & \frac{-GAk}{2} & 0 \\ 0 & 0 & 0 & \frac{GJ}{L} & 0 & 0 & 0 & 0 & 0 & \frac{-GJ}{L} & 0 & 0 \\ 0 & 0 & \frac{-GAk}{2} & 0 & \frac{EI_y}{L}+\frac{GAkL}{4} & 0 & 0 & 0 & \frac{GAk}{2} & 0 & \frac{-EI_y}{L}+\frac{GAkL}{4} & 0 \\ 0 & \frac{GAk}{2} & 0 & 0 & 0 & \frac{EI_z}{L}+\frac{GAkL}{4} & 0 & \frac{-GAk}{2} & 0 & 0 & 0 & \frac{-EI_z}{L}+\frac{GAkL}{4} \\ \frac{-EA}{L} & 0 & 0 & 0 & 0 & 0 & \frac{EA}{L} & 0 & 0 & 0 & 0 & 0 \\ 0 & \frac{-GAk}{L} & 0 & 0 & 0 & \frac{-GAk}{2} & 0 & \frac{GAk}{L} & 0 & 0 & 0 & \frac{-GAk}{2} \\ 0 & 0 & \frac{-GAk}{L} & 0 & \frac{GAk}{2} & 0 & 0 & 0 & \frac{GAk}{L} & 0 & \frac{GAk}{2} & 0 \\ 0 & 0 & 0 & \frac{-GJ}{L} & 0 & 0 & 0 & 0 & 0 & \frac{GJ}{L} & 0 & 0 \\ 0 & 0 & \frac{-GAk}{2} & 0 & \frac{-EI_y}{L}+\frac{GAkL}{4} & 0 & 0 & 0 & \frac{GAk}{2} & 0 & \frac{EI_y}{L}+\frac{GAkL}{4} & 0 \\ 0 & \frac{GAk}{2} & 0 & 0 & 0 & \frac{-EI_z}{L}+\frac{GAkL}{4} & 0 & \frac{-GAk}{2} & 0 & 0 & 0 & \frac{EI_z}{L}+\frac{GAkL}{4} \end{bmatrix} \begin{Bmatrix} u_1 \\ v_1 \\ w_1 \\ \theta_{x1} \\ \theta_{y1} \\ \theta_{z1} \\ u_2 \\ v_2 \\ w_2 \\ \theta_{x2} \\ \theta_{y2} \\ \theta_{z2} \end{Bmatrix} \quad (3.69)$$

Denoting the 12x1 vector of forces and moments as f, the 12x12 stiffness matrix as K, and the 12x1 vector of displacements and rotations as u, Equation 3.69 can be rewritten as:

$$f = Ku \tag{3.70}$$

3.2.2 Mass Matrix

A consistent mass matrix is used which can be found by evaluating:

$$M_i = \rho A \int_{-1}^{1} \begin{Bmatrix} N_1(\xi) \\ N_2(\xi) \end{Bmatrix} \{N_1(\xi) \quad N_2(\xi)\} \frac{L}{2}\, d\xi \tag{3.71}$$

which yields:

$$M_i = \frac{\rho AL}{6} \begin{bmatrix} 2 & 1 \\ 1 & 2 \end{bmatrix} \tag{3.72}$$

where ρ is the density of the beam (units of $\frac{M}{L^3}$).

The 2x2 matrix above is applied to appropriate locations for each of the six degrees of freedom $\{u_i, v_i, w_i, \theta_{xi}, \theta_{yi}, \theta_{zi}\}$, resulting in a 12x12 mass matrix, M. On terms applied to nodal rotations, a characteristic length needs to be utilized in order to make the units consistent in the formulation. The characteristic length has been set as $\frac{L}{2}$. The full mass matrix is given by:

$$M = \frac{\rho A L}{6}\begin{bmatrix} 2 & 0 & 0 & 0 & 0 & 0 & 1 & 0 & 0 & 0 & 0 & 0 \\ 0 & 2 & 0 & 0 & 0 & 0 & 0 & 1 & 0 & 0 & 0 & 0 \\ 0 & 0 & 2 & 0 & 0 & 0 & 0 & 0 & 1 & 0 & 0 & 0 \\ 0 & 0 & 0 & L & 0 & 0 & 0 & 0 & 0 & \frac{L}{2} & 0 & 0 \\ 0 & 0 & 0 & 0 & L & 0 & 0 & 0 & 0 & 0 & \frac{L}{2} & 0 \\ 0 & 0 & 0 & 0 & 0 & L & 0 & 0 & 0 & 0 & 0 & \frac{L}{2} \\ 1 & 0 & 0 & 0 & 0 & 0 & 2 & 0 & 0 & 0 & 0 & 0 \\ 0 & 1 & 0 & 0 & 0 & 0 & 0 & 2 & 0 & 0 & 0 & 0 \\ 0 & 0 & 1 & 0 & 0 & 0 & 0 & 0 & 2 & 0 & 0 & 0 \\ 0 & 0 & 0 & \frac{L}{2} & 0 & 0 & 0 & 0 & 0 & L & 0 & 0 \\ 0 & 0 & 0 & 0 & \frac{L}{2} & 0 & 0 & 0 & 0 & 0 & L & 0 \\ 0 & 0 & 0 & 0 & 0 & \frac{L}{2} & 0 & 0 & 0 & 0 & 0 & L \end{bmatrix} \tag{3.73}$$

3.2.3 Damping Matrix

Rayleigh damping is used in the beam element formulation. The user is allowed to input both a mass proportional damping coefficient, r_1, and a stiffness proportional damping coefficient, r_2. Thus, the 12x12 damping matrix, C, is given as follows:

$$C = r_1 M + r_2 K \tag{3.74}$$

3.2.4 Thermal Loading

The thermal strain in a beam is given by:

$$\epsilon_{therm} = \alpha \Delta T \tag{3.75}$$

where α is the coefficient of linear thermal expansion and ΔT is the temperature change. The thermal loading formulation allows a linear temperature distribution between the top and bottom surfaces of the beam. Figure 3.6 depicts this relationship. A thermal gradient in the z-direction (through the width of the beam) is not considered. Przemieniecki (1968) can be consulted for further reference to the formulation.

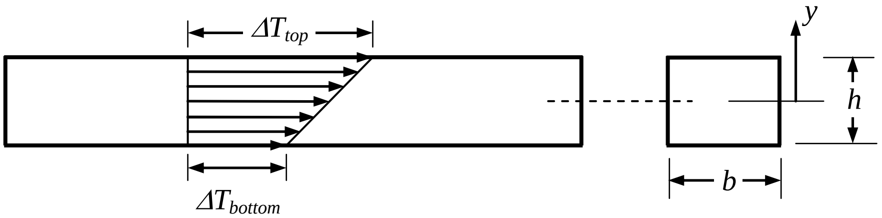

Figure 3.6: Temperature Distribution for Beams

where b is the beam width and h is the beam height.

Axial Loads

Due to the linear relationship between ΔT_{top} and ΔT_{bottom}, the temperature change along the middle surface ($y = 0$) is given by:

$$\Delta T_{mid} = \frac{1}{2}(\Delta T_{top} + \Delta T_{bottom}) \tag{3.76}$$

This temperature change results in axial loading. The thermal axial forces are found by evaluating the following:

$$f_{ta} = -\int_V \epsilon^T E\, \epsilon_{therm}\, dV = -EA\int_0^L \epsilon^T \alpha \Delta T_{mid} dx \tag{3.77}$$

The resulting forces are given by:

$$f_{ta} = \begin{Bmatrix} EA\alpha\Delta T_{mid} \\ -EA\alpha\Delta T_{mid} \end{Bmatrix} \tag{3.78}$$

Bending Moments

The gradient effect allows for curvature in the x-y plane to be introduced in the beam. The temperature change needs to be written as a function of vertical position (y) in the element to find thermal-induced bending moments.

$$\Delta T_{grad} = \Delta T_{mid} + \left(\frac{\Delta T_{top} - \Delta T_{bottom}}{h}\right) y \qquad (3.79)$$

The thermal-induced bending moments are found by evaluating the following:

$$f_{tb} = \int_V \epsilon_b^T E\, \epsilon_{therm}\, dV = Eb \int_0^L \int_{-h/2}^{h/2} \epsilon_b^T \alpha \Delta T_{grad}\, dy\, dx \qquad (3.80)$$

The resulting moments are given by:

$$f_{tb} = \begin{Bmatrix} 0 \\ \frac{-EAh\alpha}{12}(\Delta T_{top} - \Delta T_{bottom}) \\ 0 \\ \frac{EAh\alpha}{12}(\Delta T_{top} - \Delta T_{bottom}) \end{Bmatrix} \qquad (3.81)$$

Finally, the axial and bending effects can be combined into a single thermal load vector represented by:

$$f_{therm} = \begin{Bmatrix} EA\alpha\Delta T_{mid} \\ 0 \\ 0 \\ 0 \\ 0 \\ \frac{-EAh\alpha}{12}(\Delta T_{top} - \Delta T_{bottom}) \\ -EA\alpha\Delta T_{mid} \\ 0 \\ 0 \\ 0 \\ 0 \\ \frac{EAh\alpha}{12}(\Delta T_{top} - \Delta T_{bottom}) \end{Bmatrix} \qquad (3.82)$$

Now that thermal effects have been introduced, Equation 3.70 can be augmented:

$$f = Ku + f_{therm} \tag{3.83}$$

3.2.5 Element Transformation

Until this point, the beam formulation has only been discussed in terms of the local coordinate system. The assembled element equations are solved in the global coordinate system. To accommodate beams in any orientation, the local stiffness matrices need to be transformed into global stiffness matrices. Establishing the local coordinate system for the beam in $\mathbb{R}^3$ involves finding the direction cosines of the beam. In TeraDysac, a web vector establishes the strong and weak axes of the beam. The Gram-Schmidt process is used to establish the local coordinate system of the beam.

The local x-axis is defined by the coordinates of the nodes of the element. An initial web vector is furnished by the program. Unless the beam element is oriented within 5% of the global y-axis, the default initial web vector is given by $\langle 0,1,0 \rangle$. If the beam is effectively aligned with the global y-axis, the default initial web vector is given by $\langle 0,0,1 \rangle$. The Gram-Schmidt process is used to establish the final web vector. The final web vector is also the local y-axis. Crossing the local x-axis with the local y-axis yields the local z-axis. Figure 3.7 depicts the geometry involved in the process.

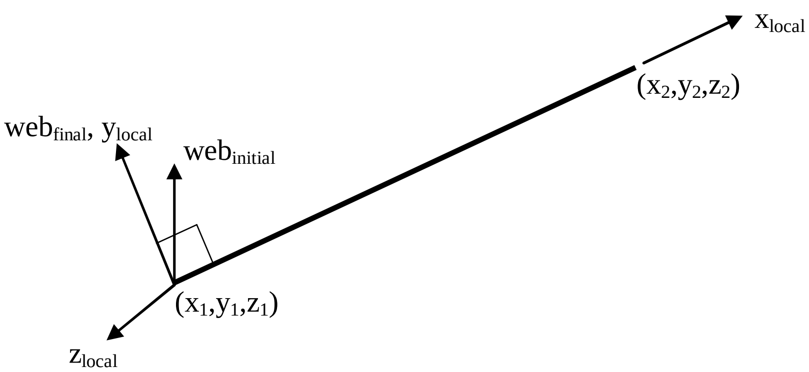

Figure 3.7: Local Coordinate System for Beam Element

The relationship between the local and global coordinate systems is defined by the direction cosines of the element. Figure 3.8 shows the relationship between a beam's local axis and the global coordinate system.

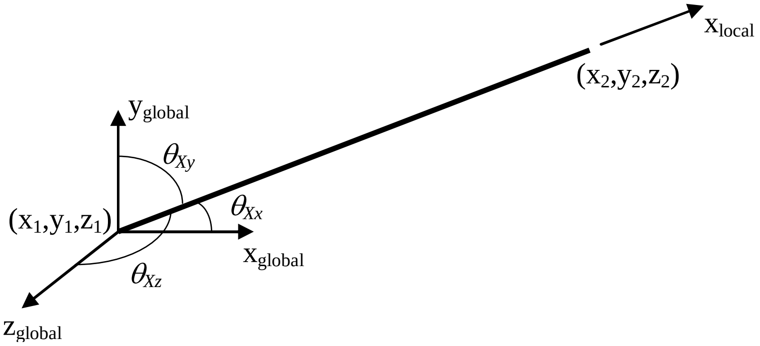

Figure 3.8: X-Axis Directions for Beam Element

The direction cosines are defined as follows:

$$x_{length} = x_2 - x_1 \tag{3.84}$$

$$y_{length} = y_2 - y_1 \tag{3.85}$$

$$z_{length} = z_2 - z_1 \tag{3.86}$$

$$length = (x_{length} + y_{length} + z_{length})^{1/2} \tag{3.87}$$

$$cosXx = \frac{x_{length}}{length} \tag{3.88}$$

$$cosXy = \frac{y_{length}}{length} \tag{3.89}$$

$$cosXz = \frac{z_{length}}{length} \tag{3.90}$$

The angles depicted in Figure 3.8 are given by the following:

$$\theta_{Xx} = cos^{-1}(cosXx) \tag{3.91}$$

$$\theta_{Xy} = cos^{-1}(cosXy) \tag{3.92}$$

$$\theta_{Xz} = cos^{-1}(cosXz) \tag{3.93}$$

Direction cosines for the local y-axis ($cosYx, cosYy, cosYz$) and the local z-axis ($cosZx, cosZy, cosZz$) are determined in a similar fashion. The matrix of direction cosines is given by:

$$\Theta = \begin{bmatrix} cosXx & cosXy & cosXz \\ cosYx & cosYy & cosYz \\ cosZx & cosZy & cosZz \end{bmatrix} \tag{3.94}$$

The local stiffness matrix for the beam element is a 12x12 matrix. Therefore, the transformation matrix for the beam is given by:

$$T = \begin{bmatrix} \Theta & 0 & 0 & 0 \\ 0 & \Theta & 0 & 0 \\ 0 & 0 & \Theta & 0 \\ 0 & 0 & 0 & \Theta \end{bmatrix} \tag{3.95}$$

Unknowns and forces in the local coordinate system can be written in the global coordinate system as follows:

$$\bar{u} = T^T u \tag{3.96}$$

$$\bar{f} = T^T f \tag{3.97}$$

$$\bar{f}_{therm} = T^T f_{therm} \tag{3.98}$$

Furthermore, the equation 3.83 can be re-written in the global coordinate system as follows:

$$\bar{f} = T^T K \, T\bar{u} + \bar{f}_{therm} \tag{3.99}$$

3.2.6 Nonlinear EI

Piles located at the abutments in IABs are usually oriented in weak-axis bending. These piles are intentionally flexible to accommodate the expansion and contraction of the roadway. In some IABs, abutment piles yield under certain loading situations. Plastic hinges may form in the region near the abutment (Hassiotis and Roman 2005). Therefore, an analysis considering Moment-Curvature behavior in the abutment piles may be needed in some cases.

A scheme for modeling beams in the nonlinear range has been developed for TeraDysac. The relationship between the bending moment in a beam and its curvature can be stated as follows:

$$\frac{M}{\phi} = EI \qquad (3.100)$$

where: M = bending moment
E = Young's modulus
I = beam moment of inertia
ϕ = curvature

While in the elastic range, this relationship is linear. However, at the onset of yield the relationship becomes nonlinear until it reaches a plastic state. Figure 3.9 shows a typical Moment-Curvature curve for a beam.

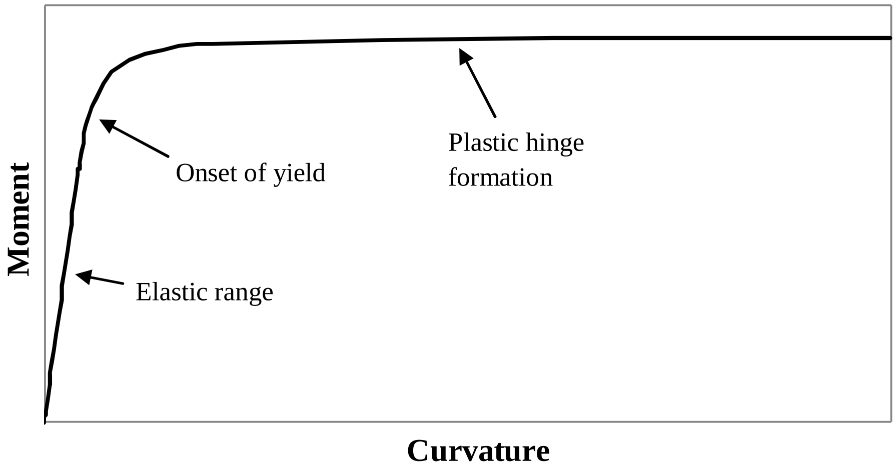

Figure 3.9: Typical Moment-Curvature Relationship for a Beam

A small piece of computer code controls the nonlinear EI application. The user must furnish the Moment-Curvature relationship to TeraDysac by specifying (Curvature, Moment) points. The slope between adjacent points is linear, so the input curve gets more accurate as more points are included. Figure 3.10 shows an example piece-wise curve.

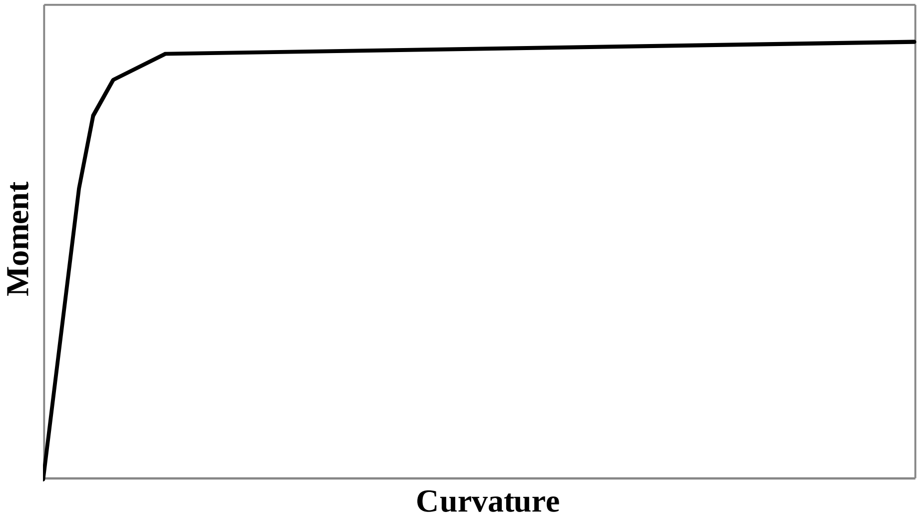

Figure 3.10: Piece-wise Approximation of the Moment-Curvature Curve for a Beam

The bending stiffness, EI of the beam is calculated as a function of the bending moment from the previous time step. In the linear range, EI doesn't change with bending moment (see Figure 3.11).

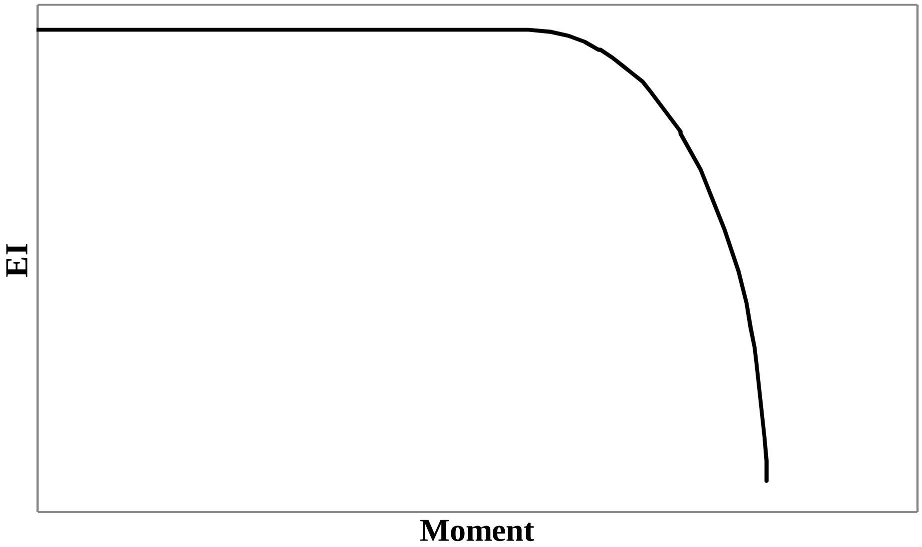

Figure 3.11: Bending Stiffness vs. Bending Moment for a Beam

Once the yield moment is reached in the section, the bending stiffness diminishes and must be updated. In this range, iteration occurs until the bending moment in the section and bending stiffness agree with Equation 3.100.

Example problem

To illustrate how to set-up a nonlinear beam analysis in TeraDysac, a simple example is carried out below. Beginning with section geometry and material properties, the nonlinear EI relationship is developed and then an analysis in TeraDysac is performed.

Consider a rectangular steel beam with the following geometry:

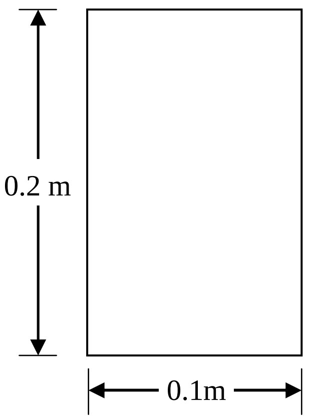

Figure 3.12: Example Beam Geometry

The beam properties are given here:

A = 0.02 m^2
I = 6.67 * 10^{-5} m^4
E = 200 * 10^6 kPa
f_y = 415 * 10^3 kPa
ν = 0.3
k = 5/6

where f_y is the yield stress and ν is Poisson's ratio. At yield, the stress diagram for the beam is given by Figure 3.13 with equivalent point loads, P, shown. The beam height is denoted by h and the beam width is denoted by b.

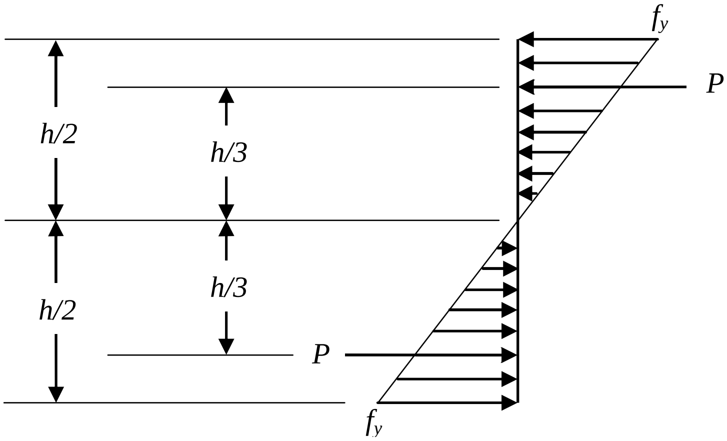

Figure 3.13: Stress Distribution at Yield

The equivalent point load on each half of the beam, P is given in Equation 3.101.

$$P = \frac{bhf_y}{4} \tag{3.101}$$

The moment at yield, M_y is given by Equation 3.102.

$$M_y = \frac{2Ph}{3} = \frac{f_y bh^2}{6} \tag{3.102}$$

The equation for bending stress in the beam (Equation 3.103) can also be rearranged to find the bending moment in the beam at the onset of yield.

$$f = \frac{Mc}{I} \tag{3.103}$$

For the rectangular section in this example,

$$c = \frac{h}{2} \tag{3.104}$$

$$I = \frac{bh^3}{12} \tag{3.105}$$

Making appropriate substitutions in Equation 3.103, Equation 3.102 can be obtained.

$$M = \frac{f_y \frac{bh^3}{12}}{\frac{h}{2}} = \frac{f_y bh^2}{6} = M_y \tag{3.106}$$

After the outer fibers in the beam yield, the stress diagram is given in Figure 3.14.

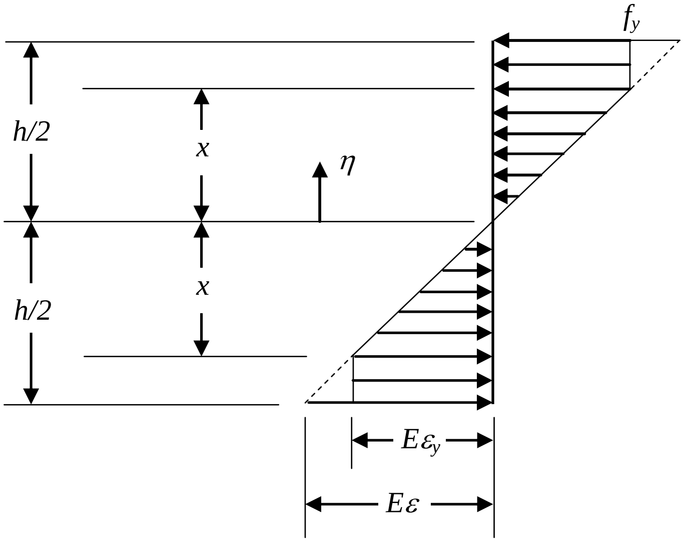

Figure 3.14: Stress Distribution After Yield

The stress, σ at a particular location above the neutral axis, η is given by Equation 3.107. The strain is related to the curvature, ϕ through Equation 3.108.

$$\sigma = E\epsilon = \frac{M\eta}{I} \quad (3.107)$$

$$\epsilon = \phi\eta \quad (3.108)$$

Using these equations, the yield strain can be found as follows:

$$\epsilon_y = \frac{\sigma_y}{E} = \frac{415*10^3 \text{ kPa}}{200*10^6 \text{ kPa}} = 0.002075 \frac{\text{m}}{\text{m}} \quad (3.109)$$

Using similar triangles, x from Figure 3.14 can be written as follows:

$$x = \frac{h}{2} - \frac{h}{2\epsilon}\left(\epsilon - \epsilon_y\right) \quad (3.110)$$

Applying equivalent point loads to represent the triangular and rectangular parts in Figure 3.14, the bending moment in the beam can be written as follows:

$$M = bf_y\left(\frac{h^2}{4} - \frac{x^2}{3}\right) \quad (3.111)$$

When the beam reaches the ultimate moment, the entire beam section has yielded. It is at this point where a plastic hinge forms. Figure 3.15 shows the stress distribution in a beam that has reached the ultimate moment.

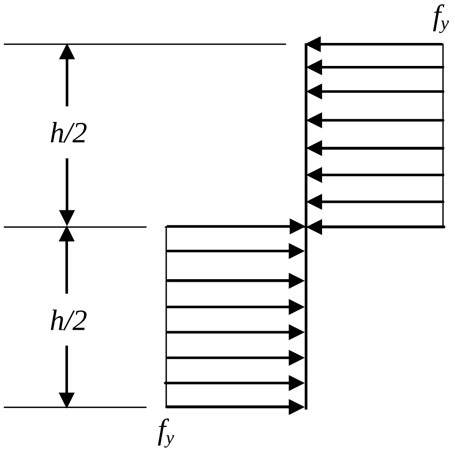

Figure 3.15: Stress Distribution at Ultimate Moment

The Moment-Curvature relationship for the example section is given in Figure 3.16. Developing the relationship for circular sections, reinforced concrete sections, and H-piles is more difficult, but must be done for an accurate nonlinear pile analysis.

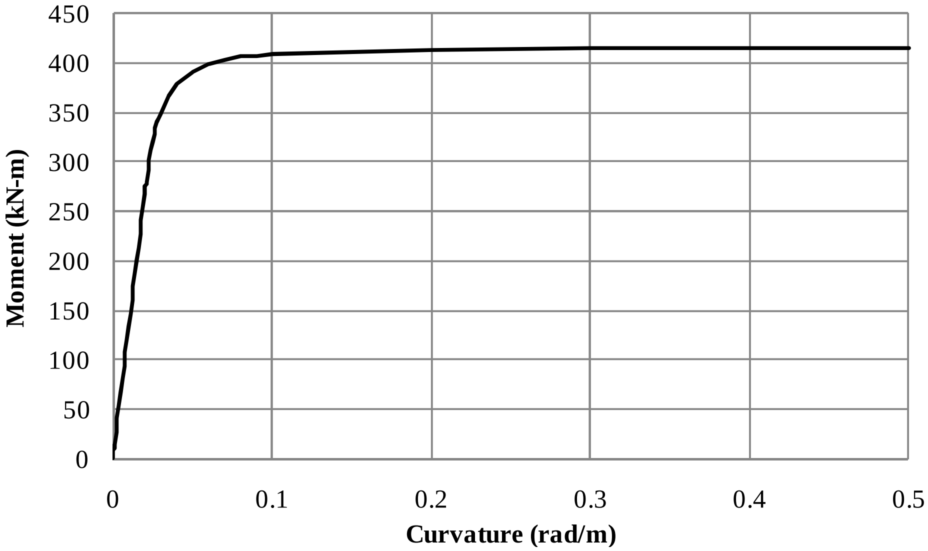

Figure 3.16: Moment-Curvature Relationship for the Example Beam

To illustrate the nonlinear *EI* beam application implemented in TeraDysac, an analysis of the example section was performed. Figure 3.17 shows the problem geometry and boundary conditions.

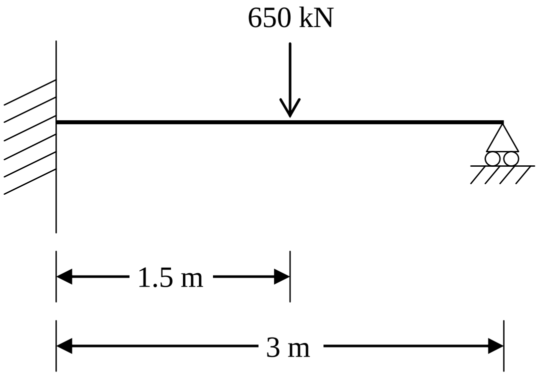

Figure 3.17: Nonlinear EI Example Problem Layout

The example section begins to yield at a bending moment of 276.67 kN-m. The loading given in Figure 3.17 forces the moment at midspan and at the rigid connection into the nonlinear range. The highest bending moment in the mesh is used to determine the bending stiffness. Figure 3.18 shows the relationship between the bending stiffness and moment for the example section. It is apparent that bending stiffness quickly diminishes after the moment reaches 300 kN-m. A plastic hinge forms in the section as EI tends to zero.

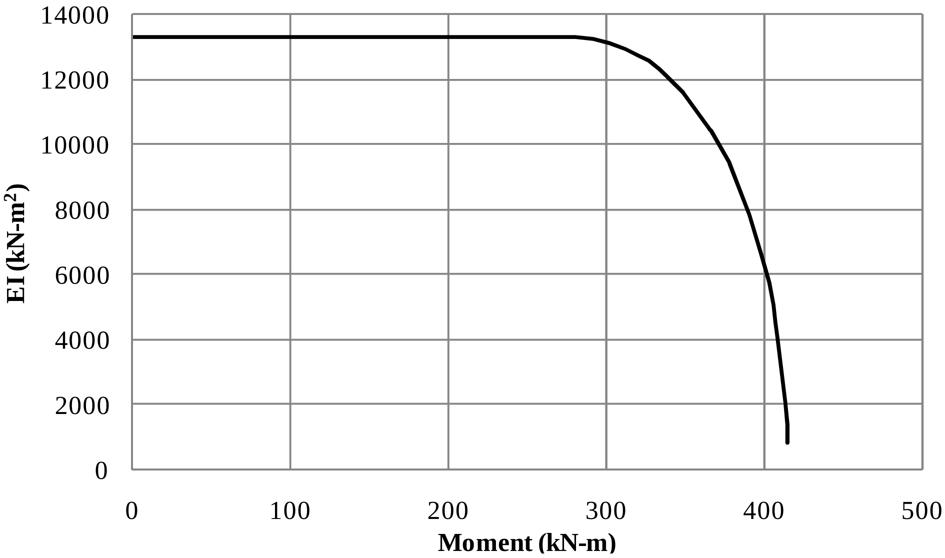

Figure 3.18: EI-Moment Relationship for the Example Beam

An 8-element mesh was used for the analysis. If the nonlinear EI feature is not used, TeraDysac gives a midpoint displacement of 0.011943 m. This is within 0.5% of the analytical solution given by Euler-Bernoulli beam theory. With the algorithm active, the displacement at the midpoint is 0.015059 m and the maximum bending moment in the section was found to be 366.06 kN-m.

As a check on the scheme, another analysis was performed. Knowing the maximum bending moment in the mesh is 366.06 kN-m, a value of EI of 10,492.38 kN-m^2 can be found (see Figure 3.18). Substituting this value of bending stiffness and re-running the problem without using the nonlinear EI feature should yield the same solution as when the feature was active previously. The obtained midpoint displacement is 0.015059 m which reveals that the algorithm is working properly.

3.3 Plate Element

A low order plate element has been developed for TeraDysac. The general quadrilateral element has six degrees of freedom at each node (three displacements and three rotations). Figure 3.19 shows a typical element with nodal variables designated for the upper-right node.

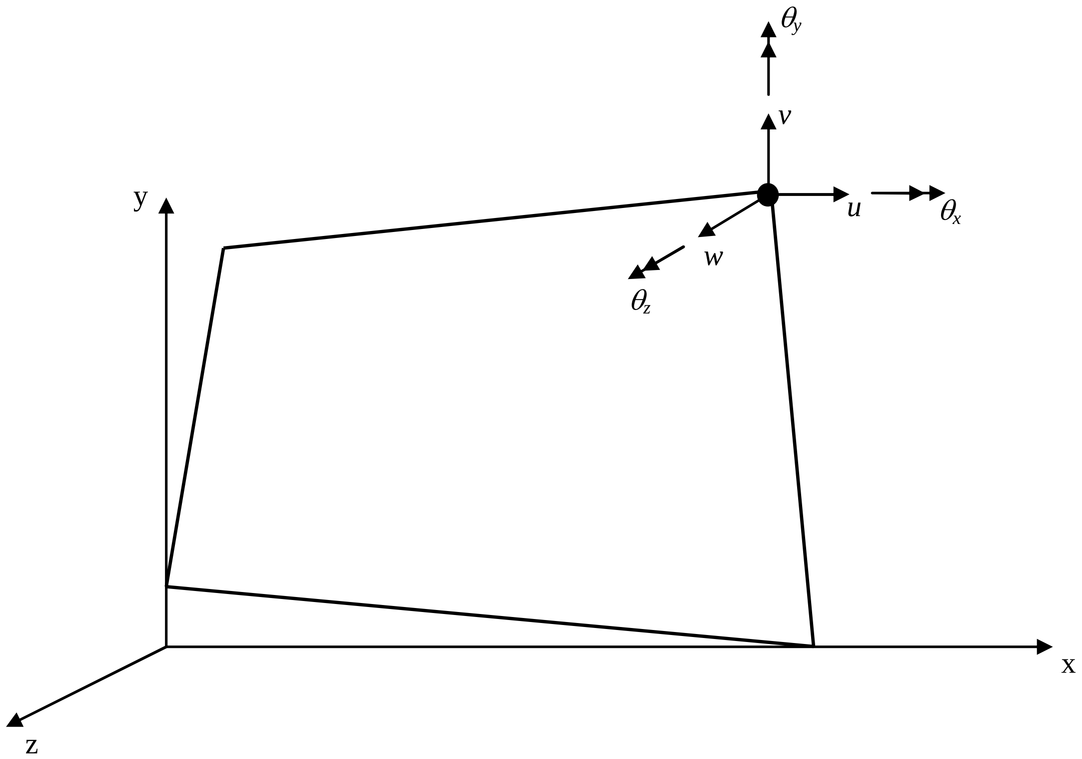

Figure 3.19: Plate Element Nodal Variables

The total stiffness matrix for the plate (24x24) is formed by coupling the in-plane and out-of-plane effects. Plane stress with a rotation penalty formulation is used to form the in-plane stiffness matrix (12x12). Reissner-Mindlin plate theory (Reissner 1945, Mindlin 1951) is used to develop the bending stiffness matrix (12x12).

3.3.1 Stiffness Matrix

In-Plane Stiffness

The in-plane effects of the plate deal with the in-plane displacements (two per node) and the in-plane rotations (one per node), yielding a total of 12 nodal unknowns. If one wished to neglect in-plane rotations for the quadrilateral element, plane stress alone could be used to develop an 8x8 in-plane stiffness matrix. However, for completeness (and for compatibility with beam elements which have a torsional component), the plate element will consider in-plane rotations at each node. To develop the 12x12 matrix for the in-plane stiffness, plane stress assumptions and a penalty formulation are utilized together. The nodal displacement in the x-direction is denoted by u, displacement in the y-direction is denoted by v, and rotation about the z-axis is denoted by θ_z. The penalty formulation penalizes the difference between the nodal rotation field θ_z, and the exact rotation due to u and v.

The penalty formulation is given by:

$$P_m\left[\theta_z - \frac{1}{2}\left(\frac{\partial v}{\partial x} - \frac{\partial u}{\partial y}\right)\right]^2 \tag{3.112}$$

The elemental strain, including plane stress and the in-plane rotation, is given below:

$$\epsilon = \begin{Bmatrix} e_{xx} \\ e_{yy} \\ e_{xy} \\ r \end{Bmatrix} = \begin{Bmatrix} \dfrac{\partial u}{\partial x} \\ \dfrac{\partial v}{\partial y} \\ \dfrac{\partial u}{\partial y} + \dfrac{\partial v}{\partial x} \\ \theta_z - \frac{1}{2}\left(\dfrac{\partial v}{\partial x} - \dfrac{\partial u}{\partial y}\right) \end{Bmatrix} \tag{3.113}$$

The constitutive relationship is given as:

$$\sigma = \begin{Bmatrix} \sigma_{xx} \\ \sigma_{yy} \\ \sigma_{xy} \\ \sigma_r \end{Bmatrix} = \frac{E}{1-\nu^2}\begin{bmatrix} 1 & \nu & 0 & 0 \\ \nu & 1 & 0 & 0 \\ 0 & 0 & \frac{1-\nu}{2} & 0 \\ 0 & 0 & 0 & \frac{1-\nu^2}{E}P_m \end{bmatrix}\begin{Bmatrix} e_{xx} \\ e_{yy} \\ e_{xy} \\ r \end{Bmatrix} \tag{3.114}$$

where E is Young's modulus and ν is Poisson's ratio. Setting P_m to 5% of Young's modulus did not severely distort the results from a truly plane stress case (P_m = 0.0), yet allowed compatibility with connecting beams undergoing torsion.

The strain-displacement matrix is given by:

$$D = \begin{bmatrix} \frac{\partial}{\partial x} & 0 & 0 \\ 0 & \frac{\partial}{\partial y} & 0 \\ \frac{\partial}{\partial y} & \frac{\partial}{\partial x} & 0 \\ \frac{1}{2}\frac{\partial}{\partial y} & -\frac{1}{2}\frac{\partial}{\partial x} & 1 \end{bmatrix} \tag{3.115}$$

The constitutive parameter matrix is given as:

$$C = \frac{E}{1-\nu^2}\begin{bmatrix} 1 & \nu & 0 & 0 \\ \nu & 1 & 0 & 0 \\ 0 & 0 & \frac{1-\nu}{2} & 0 \\ 0 & 0 & 0 & \frac{1-\nu^2}{E}P_m \end{bmatrix} \tag{3.116}$$

The displacement vector of unknowns for the element is given as follows:

$$d = \begin{Bmatrix} u(x,y) \\ v(x,y) \\ \theta_z(x,y) \end{Bmatrix} \tag{3.117}$$

The strain can be written in terms of the strain-displacement matrix and the displacement vector.

$$\epsilon = Dd \tag{3.118}$$

The total strain energy in the element is given as follows:

$$U = \frac{1}{2}\int_V \epsilon^T \sigma \, dV = \frac{1}{2}\int_V \epsilon^T C\epsilon \, dV = \frac{1}{2}\int_V [Dd]^T C[Dd] \, dV \tag{3.119}$$

where V is the element volume. The 12x12 stiffness matrix, $K_{in-plane}$, can be found by minimizing the total strain energy.

Bending Stiffness

Reissner-Mindlin plate theory is used to develop the bending effects for the plate element. The bending effects of the plate deal with the transverse displacements (one per node) and the rotations due to bending (two per node). The theory leads to a 12x12 stiffness matrix. The nodal displacement in the z-direction is denoted by w, rotation about the x-axis is denoted by θ_x, and rotation about the y-axis is denoted by θ_y. The subscript b is used to designate bending terms, while the subscript s is used to designate shear terms.

Bathe (1982) can be used for further reference to the formulation. Like Timoshenko beam theory, plane sections are assumed to remain plane, but not necessarily perpendicular to the neutral axis. Figure 3.20 shows the layout of the plate element used in the formulation.

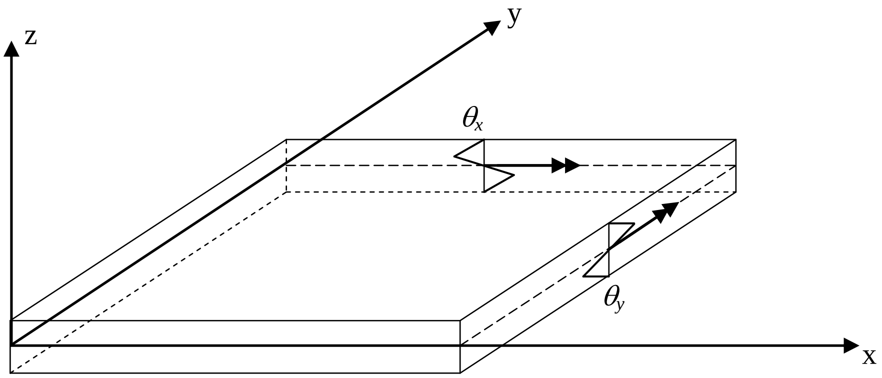

Figure 3.20: Plate Element Layout

The displacement components for the element are given as follows:

$$u = z\theta_y(x, y) \tag{3.120}$$

$$v = -z\theta_x(x, y) \tag{3.121}$$

$$w = w(x, y) \tag{3.122}$$

The bending strains, e_{xx}, e_{yy}, and e_{xy}, are assumed to vary linearly through the plate thickness:

$$\epsilon_b = \begin{Bmatrix} e_{xx} \\ e_{yy} \\ e_{xy} \end{Bmatrix} = z \begin{Bmatrix} \frac{\partial \theta_y}{\partial x} \\ -\frac{\partial \theta_x}{\partial y} \\ \frac{\partial \theta_y}{\partial y} - \frac{\partial \theta_x}{\partial x} \end{Bmatrix} \tag{3.123}$$

The transverse shear strains, e_{yz} and e_{zx}, are assumed constant through the plate thickness:

$$\epsilon_s = \begin{Bmatrix} e_{yz} \\ e_{zx} \end{Bmatrix} = \begin{Bmatrix} \frac{\partial w}{\partial y} - \theta_x \\ \frac{\partial w}{\partial x} + \theta_y \end{Bmatrix} \tag{3.124}$$

The constitutive relationships are given by:

$$\sigma_b = \begin{Bmatrix} \sigma_{xx} \\ \sigma_{yy} \\ \sigma_{xy} \end{Bmatrix} = \frac{E}{1-\nu^2} \begin{bmatrix} 1 & \nu & 0 \\ \nu & 1 & 0 \\ 0 & 0 & \frac{1-\nu}{2} \end{bmatrix} \begin{Bmatrix} e_{xx} \\ e_{yy} \\ e_{xy} \end{Bmatrix} \tag{3.125}$$

$$\sigma_s = \begin{Bmatrix} \sigma_{yz} \\ \sigma_{zx} \end{Bmatrix} = \frac{E}{2(1+\nu)} \begin{bmatrix} 1 & 0 \\ 0 & 1 \end{bmatrix} \begin{Bmatrix} e_{yz} \\ e_{zx} \end{Bmatrix} \tag{3.126}$$

The strain-displacement matrices are given by:

$$D_b = \begin{bmatrix} 0 & 0 & z\frac{\partial}{\partial x} \\ 0 & -z\frac{\partial}{\partial y} & 0 \\ 0 & -z\frac{\partial}{\partial x} & z\frac{\partial}{\partial y} \end{bmatrix} \tag{3.127}$$

$$D_s = \begin{bmatrix} \frac{\partial}{\partial y} & -1 & 0 \\ \frac{\partial}{\partial x} & 0 & 1 \end{bmatrix} \tag{3.128}$$

The constitutive parameter matrices are given by:

$$C_b = \frac{E}{1-\nu^2}\begin{bmatrix} 1 & \nu & 0 \\ \nu & 1 & 0 \\ 0 & 0 & \frac{1-\nu}{2} \end{bmatrix} \tag{3.129}$$

$$C_s = \frac{E}{2(1+\nu)}\begin{bmatrix} 1 & 0 \\ 0 & 1 \end{bmatrix} \tag{3.130}$$

The vector of unknowns for the element is given as follows:

$$d = \begin{Bmatrix} w(x,y) \\ \theta_x(x,y) \\ \theta_y(x,y) \end{Bmatrix} \tag{3.131}$$

The strains can be written in terms of the strain-displacement matrices and the displacement vector.

$$\epsilon_b = D_b d \tag{3.132}$$

$$\epsilon_s = D_s d \tag{3.133}$$

The total strain energy in the element is given as follows:

$$U = \frac{1}{2}\int_V \ {\epsilon_b}^T \sigma_b \, dV + \frac{k}{2}\int_V \ {\epsilon_s}^T \sigma_s \, dV = \frac{1}{2}\int_V \ {\epsilon_b}^T C_b \epsilon_b \, dV + \frac{k}{2}\int_V \ {\epsilon_s}^T C_s \epsilon_s \, dV =$$

$$\frac{1}{2}\int_V \ [D_b d]^T C_b [D_b d] \, dV + \frac{k}{2}\int_V \ [D_s d]^T C_s [D_s d] \, dV \tag{3.134}$$

where k is a constant to account for the actual shear stress distribution. The 12x12 stiffness matrix, $K_{bending}$, can be found by minimizing the total strain energy.

The total stiffness matrix is shaped by combining the in-plane and bending stiffness matrices.

$K_{in-plane}$ is a 12x12 matrix dealing with the following unknowns:

$\{u1, v1, \theta_{z1}, u2, v2, \theta_{z2}, u3, v3, \theta_{z3}, u4, v4, \theta_{z4}\}$.

$K_{bending}$ is a 12x12 matrix dealing with the following unknowns:

$\{w1, \theta_{x1}, \theta_{y1}, w2, \theta_{x2}, \theta_{y2}, w3, \theta_{x3}, \theta_{y3}, w4, \theta_{x4}, \theta_{y4}\}$.

Because the plate element is linear elastic, the matrices are independent of one another and can be combined to shape the complete stiffness matrix, K, a 24x24 matrix containing stiffness terms for all 24 degrees of freedom.

3.3.2 Numerical Integration

The plate element implemented is a general quadrilateral. Numerical integration is used to evaluate the element stiffness matrices. Figure 3.21 shows the coordinate transformation used for the numerical integration.

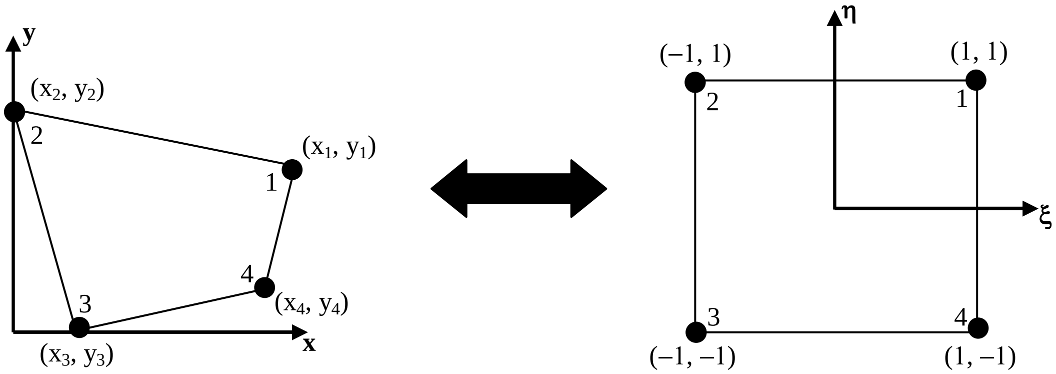

Figure 3.21: Plate Element Coordinate Transformation

The integration points on the master element are as follows:

Table 3.3: Integration Points on the Master Element

Node	ξ	η
1	$1/\sqrt{3}$	$1/\sqrt{3}$
2	$-1/\sqrt{3}$	$1/\sqrt{3}$
3	$-1/\sqrt{3}$	$-1/\sqrt{3}$
4	$1/\sqrt{3}$	$-1/\sqrt{3}$

In the bending stiffness matrix, reduced integration is used on the shear terms. These terms are evaluated at the origin of the master element (ξ = 0, η = 0).

The bilinear shape functions are given by:

$$N_1(\xi,\eta) = \tfrac{1}{4}(1+\xi)(1+\eta) \tag{3.135}$$

$$N_2(\xi,\eta) = \tfrac{1}{4}(1-\xi)(1+\eta) \tag{3.136}$$

$$N_3(\xi,\eta) = \tfrac{1}{4}(1-\xi)(1-\eta) \tag{3.137}$$

$$N_4(\xi,\eta) = \tfrac{1}{4}(1+\xi)(1-\eta) \tag{3.138}$$

The coordinate interpolations are stated as follows:

$$x = \textstyle\sum_{i=1}^{4} N_i x_i \tag{3.139}$$

$$y = \textstyle\sum_{i=1}^{4} N_i y_i \tag{3.140}$$

To evaluate the element stiffness matrices, strains (and subsequently derivatives of the coordinate transformations) are needed. They can be evaluated by using the Jacobian matrix given as follows:

$$J = \begin{bmatrix} \frac{\partial x}{\partial \xi} & \frac{\partial x}{\partial \eta} \\ \frac{\partial y}{\partial \xi} & \frac{\partial y}{\partial \eta} \end{bmatrix} \tag{3.141}$$

Partial differentiation with respect to x and y on the actual element is related to partial differentiation with respect to ξ and η on the master element through the following relationship:

$$\begin{Bmatrix} \frac{\partial}{\partial x} \\ \frac{\partial}{\partial y} \end{Bmatrix} = \begin{bmatrix} \frac{\partial \xi}{\partial x} & \frac{\partial \eta}{\partial x} \\ \frac{\partial \xi}{\partial y} & \frac{\partial \eta}{\partial y} \end{bmatrix} \begin{Bmatrix} \frac{\partial}{\partial \xi} \\ \frac{\partial}{\partial \eta} \end{Bmatrix} = [J^T]^{-1} \begin{Bmatrix} \frac{\partial}{\partial \xi} \\ \frac{\partial}{\partial \eta} \end{Bmatrix} \tag{3.142}$$

3.3.3 Mass Matrix

A consistent mass matrix is used which can be found by evaluating:

$$M_i = \rho h \int_{-1}^{1}\int_{-1}^{1} \begin{Bmatrix} N_1(\xi,\eta) \\ N_2(\xi,\eta) \\ N_3(\xi,\eta) \\ N_4(\xi,\eta) \end{Bmatrix} \{N_1(\xi,\eta) \;\; N_2(\xi,\eta) \;\; N_3(\xi,\eta) \;\; N_4(\xi,\eta)\} |J| \, d\xi \, d\eta \qquad (3.143)$$

which yields:

$$M_i = \frac{\rho h |J|}{9} \begin{bmatrix} 4 & 2 & 1 & 2 \\ 2 & 4 & 2 & 1 \\ 1 & 2 & 4 & 2 \\ 2 & 1 & 2 & 4 \end{bmatrix} \qquad (3.144)$$

where ρ is the density of the plate (units of $\frac{M}{L^3}$) and h is the plate thickness.

The 4x4 matrix above is applied to appropriate locations for each of the six degrees of freedom $\{u_i, v_i, w_i, \theta_{xi}, \theta_{yi}, \theta_{zi}\}$, resulting in a 24x24 mass matrix, M. On terms applied to nodal rotations, a characteristic length needs to be utilized in order to make the units consistent in the formulation. The characteristic length has been set as $\sqrt{|J|}$.

The identity matrix I is given by:

$$I = \begin{bmatrix} 1 & 0 & 0 \\ 0 & 1 & 0 \\ 0 & 0 & 1 \end{bmatrix} \qquad (3.145)$$

The full mass matrix is given by:

$$M = \frac{\rho h|J|}{9}\begin{bmatrix} 4I & 0 & 2I & 0 & I & 0 & 2I & 0 \\ 0 & 4\sqrt{|J|}I & 0 & 2\sqrt{|J|}I & 0 & \sqrt{|J|}I & 0 & 2\sqrt{|J|}I \\ 2I & 0 & 4I & 0 & 2I & 0 & I & 0 \\ 0 & 2\sqrt{|J|}I & 0 & 4\sqrt{|J|}I & 0 & 2\sqrt{|J|}I & 0 & \sqrt{|J|}I \\ I & 0 & 2I & 0 & 4I & 0 & 2I & 0 \\ 0 & \sqrt{|J|}I & 0 & 2\sqrt{|J|}I & 0 & 4\sqrt{|J|}I & 0 & 2\sqrt{|J|}I \\ 2I & 0 & I & 0 & 2I & 0 & 4I & 0 \\ 0 & 2\sqrt{|J|}I & 0 & \sqrt{|J|}I & 0 & 2\sqrt{|J|}I & 0 & 4\sqrt{|J|}I \end{bmatrix} \tag{3.146}$$

3.3.4 Damping Matrix

Rayleigh damping is used in the plate element formulation. The user is allowed to input both a mass proportional damping coefficient, r_1, and a stiffness proportional damping coefficient, r_2. Thus, the 24x24 damping matrix, C, is given as follows:

$$C = r_1 M + r_2 K \tag{3.147}$$

3.3.5 Thermal Loading

The thermal loading formulation allows a linear temperature distribution between the top and bottom surfaces of the plate. Figure 3.22 depicts this relationship.

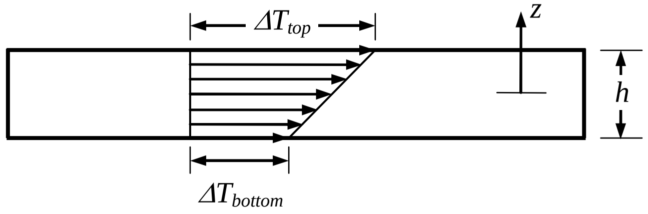

Figure 3.22: Temperature Distribution for Plates

where h is the plate thickness. The entire top of the plate is subjected to ΔT_{top} and the entire bottom of the plate is subjected to ΔT_{bottom}. Thus, there are only stresses and strains in the local x- and y-directions and there is no thermal induced shear stress.

The thermal stresses are represented by:

$$\sigma_{therm} = \frac{-E\alpha\Delta T}{1-\nu}\begin{Bmatrix} 1 \\ 1 \end{Bmatrix} \tag{3.148}$$

where α is the coefficient of linear thermal expansion and ΔT is the temperature change.

In-Plane Loads

Rewriting the strain in the element as:

$$\epsilon = \begin{Bmatrix} e_{xx} \\ e_{yy} \end{Bmatrix} = \begin{Bmatrix} \frac{\partial u}{\partial x} \\ \frac{\partial v}{\partial y} \end{Bmatrix} \tag{3.149}$$

The strain-displacement matrix is given by:

$$D = \begin{bmatrix} \frac{\partial}{\partial x} & 0 \\ 0 & \frac{\partial}{\partial y} \end{bmatrix} \tag{3.150}$$

The displacement vector of unknowns for the element is given as follows:

$$d = \begin{Bmatrix} u(x,y) \\ v(x,y) \end{Bmatrix} \tag{3.151}$$

The strain can be written in terms of the strain-displacement matrix and the displacement vector.

$$\epsilon = Dd \tag{3.152}$$

Due to the linear relationship between ΔT_{top} and ΔT_{bottom}, the temperature change along the middle surface (z = 0.0) is given by:

$$\Delta T_{mid} = \frac{1}{2}(\Delta T_{top} + \Delta T_{bottom}) \tag{3.153}$$

For the in-plane loading, the thermal stress can be rewritten as follows:

$$\sigma_{therm} = \frac{-E\alpha\Delta T_{mid}}{1-\nu}\begin{Bmatrix}1\\1\end{Bmatrix} \tag{3.154}$$

The thermal in-plane forces are found by evaluating the following:

$$f_{tip} = \int_V \ \epsilon^T \, \sigma_{therm} \, dV = h\int_A \ [Dd]^T \sigma_{therm} \, dA \tag{3.155}$$

where A is the in-plane element area. The resulting force vector is 8x1 and deals only with the unknowns:

$\{u1, v1, u2, v2, u3, v3, u4, v4\}$

Bending Moments

The gradient effect allows for curvature to be introduced in the plate. The temperature change needs to be written as a function of vertical position (z) in the element to find thermal-induced bending moments.

$$\Delta T_{grad} = \Delta T_{mid} + \left(\frac{\Delta T_{top} - \Delta T_{bottom}}{h}\right) z \tag{3.156}$$

For the out-of-plane loading, the thermal stress can be rewritten as follows:

$$\sigma_{therm} = \frac{-E\alpha\Delta T_{grad}}{1-\nu}\begin{Bmatrix}1\\1\end{Bmatrix} \tag{3.157}$$

The bending strains, e_{xx} and e_{yy}, vary linearly through the plate thickness:

$$\epsilon_b = \begin{Bmatrix} e_{xx} \\ e_{yy} \end{Bmatrix} = z\begin{Bmatrix} \frac{\partial\theta_y}{\partial x} \\ -\frac{\partial\theta_x}{\partial y} \end{Bmatrix} \tag{3.158}$$

The strain-displacement matrix is given by:

$$D_b = \begin{bmatrix} 0 & z\frac{\partial}{\partial x} \\ -z\frac{\partial}{\partial y} & 0 \end{bmatrix} \tag{3.159}$$

The vector of unknowns is given by:

$$d = \begin{Bmatrix} \theta_x(x,y) \\ \theta_y(x,y) \end{Bmatrix} \tag{3.160}$$

The strains can be written in terms of the strain-displacement matrices and the displacement vector.

$$\epsilon_b = D_b d \tag{3.161}$$

The thermal bending moments are found by evaluating the following:

$$f_{tbp} = \int_V \ \epsilon_b^T \, \sigma_{therm} \, dV = \int_A \ \int_{-h/2}^{h/2} [Dd]^T \sigma_{therm} \, dz \, dA \tag{3.162}$$

The resulting force vector is 8x1 and deals only in the unknowns:

$$\{ \theta_{x1}, \theta_{y1}, \theta_{x2}, \theta_{y2}, \theta_{x3}, \theta_{y3}, \theta_{x4}, \theta_{y4} \}$$

Finally, the axial and bending effects can be combined into a single thermal load vector represented as f_{therm}.

3.3.6 Element Transformation

Until this point, the plate formulation has only been discussed in terms of the local coordinate system. The assembled element equations are solved in the global coordinate system. To accommodate plates in any orientation, the local stiffness matrices need to be transformed into global stiffness matrices. Establishing the local coordinate system for the plate in $\mathbb{R}^3$ involves finding the direction cosines of the plate. The procedure to find the direction cosines is described below.

The first step is to find the chords which split the element into four parts. These chords will be referred to as x_{mc} and y_{mc}, the middle chords in the local x- and y-directions; they connect the midpoints of opposite element edges. Figure 3.23 shows this relationship.

The middle chords are found by evaluating the following:

$$x_{mc} = \frac{1}{2}\begin{Bmatrix} x_2 + x_3 - x_4 - x_1 \\ y_2 + y_3 - y_4 - y_1 \\ z_2 + z_3 - z_4 - z_1 \end{Bmatrix} \tag{3.163}$$

$$y_{mc} = \frac{1}{2}\begin{Bmatrix} x_3 + x_4 - y_2 - y_1 \\ y_3 + y_4 - y_2 - y_1 \\ z_3 + z_4 - z_2 - z_1 \end{Bmatrix} \tag{3.164}$$

The local z-axis is found by crossing the middle chord vectors. Depending on the plate orientation, the local z-axis is then crossed with the global x-axis or the global z-axis to find the local y-axis. Finally, the local y- and z-axes are crossed to find the local x-axis. Figure 3.24 illustrates the local coordinate system of the plate. All of these axes are unit vectors so the direction cosines are defined by the components of each vector in the global coordinate system.

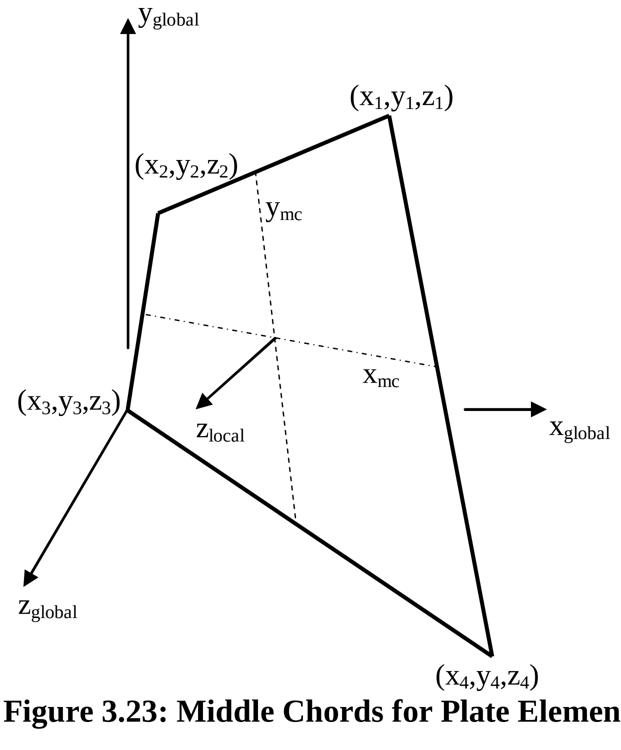

Figure 3.23: Middle Chords for Plate Element

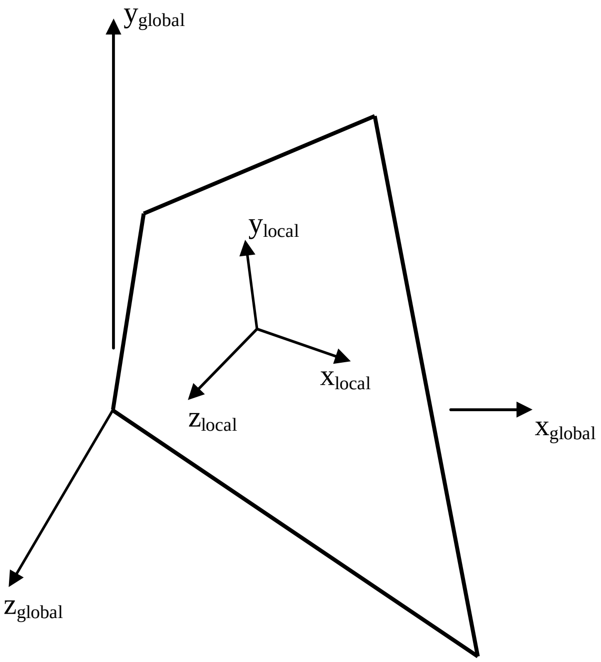

Figure 3.24: Local Coordinate System for Plate Element

The direction cosines for the local x-axis ($cosXx, cosXy, cosXz$), local y-axis ($cosYx, cosYy, cosYz$), and the local z-axis ($cosZx, cosZy, cosZz$) fill the matrix of direction cosines given by:

$$\Theta = \begin{bmatrix} cosXx & cosXy & cosXz \\ cosYx & cosYy & cosYz \\ cosZx & cosZy & cosZz \end{bmatrix} \tag{3.165}$$

The local stiffness matrix for the plate element is a 24x24 matrix. Therefore, the transformation matrix for the plate is given by:

$$T = \begin{bmatrix} \Theta & 0 & 0 & 0 & 0 & 0 & 0 & 0 \\ 0 & \Theta & 0 & 0 & 0 & 0 & 0 & 0 \\ 0 & 0 & \Theta & 0 & 0 & 0 & 0 & 0 \\ 0 & 0 & 0 & \Theta & 0 & 0 & 0 & 0 \\ 0 & 0 & 0 & 0 & \Theta & 0 & 0 & 0 \\ 0 & 0 & 0 & 0 & 0 & \Theta & 0 & 0 \\ 0 & 0 & 0 & 0 & 0 & 0 & \Theta & 0 \\ 0 & 0 & 0 & 0 & 0 & 0 & 0 & \Theta \end{bmatrix} \tag{3.166}$$

Denoting the 24x1 vector of forces and moments as f, the 24x24 stiffness matrix as K, and the 24x1 vector of displacements and rotations as u, the equations to be solved in the local coordinate system are defined as follows:

$$f = Ku + f_{therm} \tag{3.167}$$

The unknowns and forces in the global coordinate system can be written as follows:

$$\bar{u} = T^T u \tag{3.168}$$

$$\bar{f} = T^T f \tag{3.169}$$

$$\bar{f}_{therm} = T^T f_{therm} \tag{3.170}$$

Furthermore, Equation 3.167 can be re-written in the global coordinate system as follows:

$$\bar{f} = T^T K\, T\bar{u} + \bar{f}_{therm} \tag{3.171}$$

3.3.7 Hourglassing

The use of single point integration on the shear terms in the bending stiffness for the plate element can lead to hourglassing problems. Namely, in situations where no two adjacent nodes are restrained, hourglassing in the z-direction can occur. The nodal displacement in the z-direction is denoted by w, so this hourglassing mode is referred to as w-hourglassing. Figure 3.25 illustrates the w-hourglassing mode.

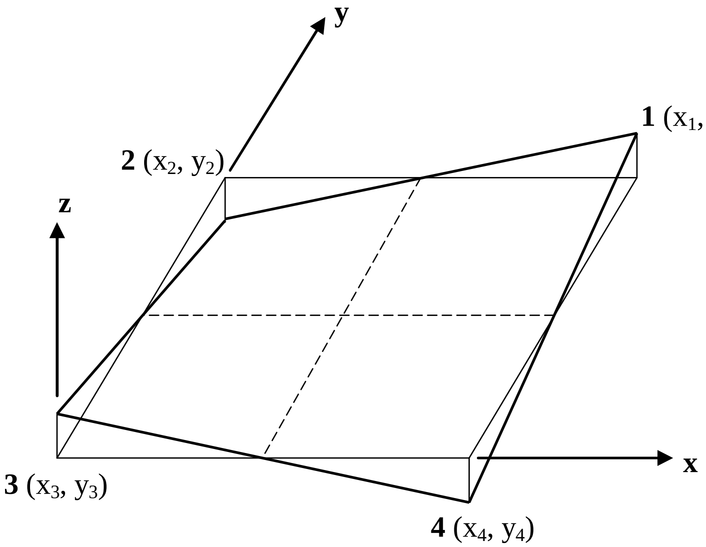

Figure 3.25: w-Hourglassing Mode

The stabilization scheme described by Belytschko and Tsay (1983) is used to supress the spurious mode. Using the node numbers given in Figure 3.25, the hourglass shape, h_w is given by the following displacement pattern in the z-direction:

$$h_w = \begin{Bmatrix} 1 \\ -1 \\ 1 \\ -1 \end{Bmatrix} \tag{3.172}$$

The coefficient for the hourglass matrix is given by:

$$c_{hg} = \frac{r_w k G t^3}{12\,A^2}\left(b_1^T b_1 + b_2^T b_2\right) \tag{3.173}$$

where r_w is a constant (~10^{-2}), k is the shear correction factor, G is the shear modulus, t is the element thickness, and A is the element area.

The vectors b_1 and b_2 are given by:

$$b_1 = \frac{1}{2}\begin{Bmatrix} y_2 - y_4 \\ y_3 - y_1 \\ y_4 - y_2 \\ y_1 - y_3 \end{Bmatrix} \tag{3.174}$$

$$b_2 = \frac{1}{2}\begin{Bmatrix} x_4 - x_2 \\ x_1 - x_3 \\ x_2 - x_4 \\ x_3 - x_1 \end{Bmatrix} \tag{3.175}$$

where x_i and y_i are the locations of the nodes in local x-y coordinate system. The element area is given by:

$$A = x^T b_1 = y^T b_2 \tag{3.176}$$

where:

$$x = \begin{Bmatrix} x_1 \\ x_2 \\ x_3 \\ x_4 \end{Bmatrix} \tag{3.177}$$

$$y = \begin{Bmatrix} y_1 \\ y_2 \\ y_3 \\ y_4 \end{Bmatrix} \tag{3.178}$$

The hourglass matrix is given by:

$$K_i^{hg} = c_{hg} h_w^T h_w = c_{hg}\begin{bmatrix} 1 & -1 & 1 & -1 \\ -1 & 1 & -1 & 1 \\ 1 & -1 & 1 & -1 \\ -1 & 1 & -1 & 1 \end{bmatrix} \tag{3.179}$$

The 4x4 matrix above is applied to appropriate locations for each of the transverse displacement degrees of freedom resulting in a 24x24 matrix hourglass stiffness matrix denoted by K^{hg}.

Hourglass Example

One case where w-hourglassing will emerge is a plate supported by corner nodes subjected to loading in the transverse direction. Consider a plate with the following properties: dimensions 5.0 m x 5.0 m x 0.05 m, $E = 3 * 10^6$ kPa, $\nu = 0.3$, $\rho = 0.1$ Mg/m^3, and $k = 5/6$. The plate corners are pinned and there is a concentrated load of 1 kN applied at the mesh center. Figure 3.26 shows the finite element mesh with the corner nodes highlighted.

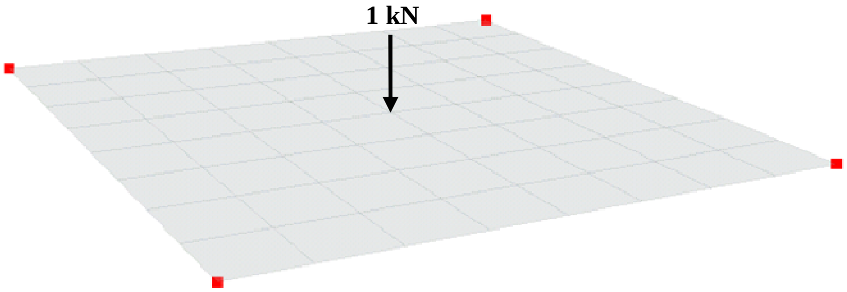

Figure 3.26: Problem Set-Up for Hourglassing Example

Two analyses were performed. The first sets r_w in hourglass stiffness coefficient equal to 0.0. Figure 3.27 shows the deformed shape of the plate (magnified by 10). It is apparent that severe hourglassing has occurred.

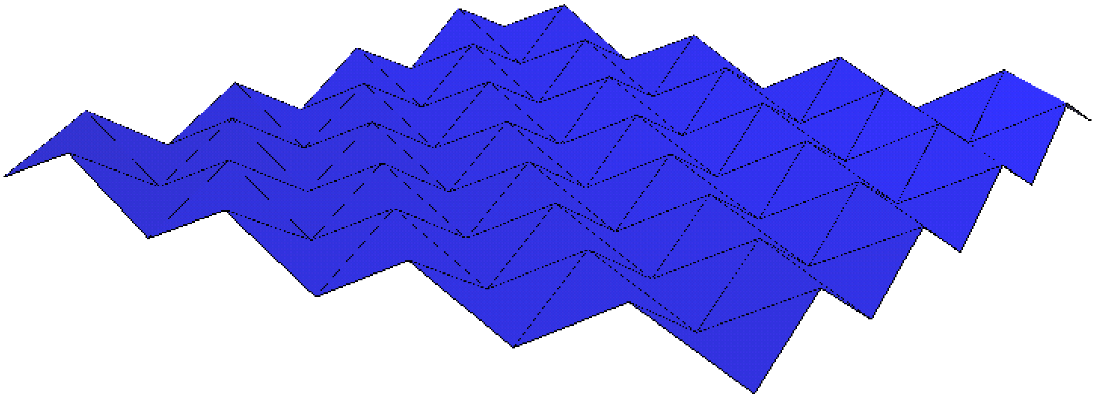

Figure 3.27: Deformed Shape for Corner-Supported Plate (No Hourglass Stiffness)

The second analysis sets r_w in hourglass stiffness coefficient equal to 0.01, as recommended by Belytschko and Tsay (1983). Figure 3.28 shows the deformed shape of the plate (magnified by 10).

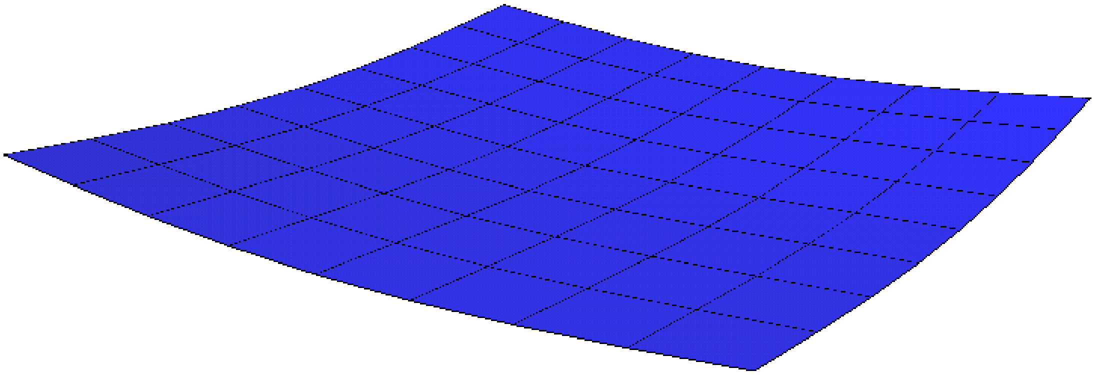

Figure 3.28: Deformed Shape for Corner-Supported Plate with Hourglass Stiffness

It is apparent that the hourglassing has been significantly reduced by incorporating the hourglass stiffness matrix. As a further check on the hourglass control scheme, the computed center deflection (w_{center} = 0.027892 m) of the plate is in good agreement with the thin plate theory (Kirchhoff 1850) solution and the obtained reaction at each corner is 0.25 kN (1/4 of the applied load, as expected). The TeraDysac displacement solution is within 0.9% of the 8x8 element Kirchhoff solution provided by ANSYS (2007). SHELL63 elements were used, which are four node quadrilaterals comprised of four overlaid triangles. The addition of the hourglass stiffness has curtailed the hourglassing and not distorted the results. Setting r_w to 0.01 for future problems is recommended as it has a negligible effect on the solution and ensures that hourglassing is contained.

This hourglassing mode only appears for some problems and loading conditions. For example, the same plate geometry, material properties, and loading applied, but with the transverse displacement at every edge node fixed does not show hourglassing. An analysis was run with r_w = 0.0. Figures 3.29 and 3.30 show the undeformed and deformed (magnified by 10) meshes.

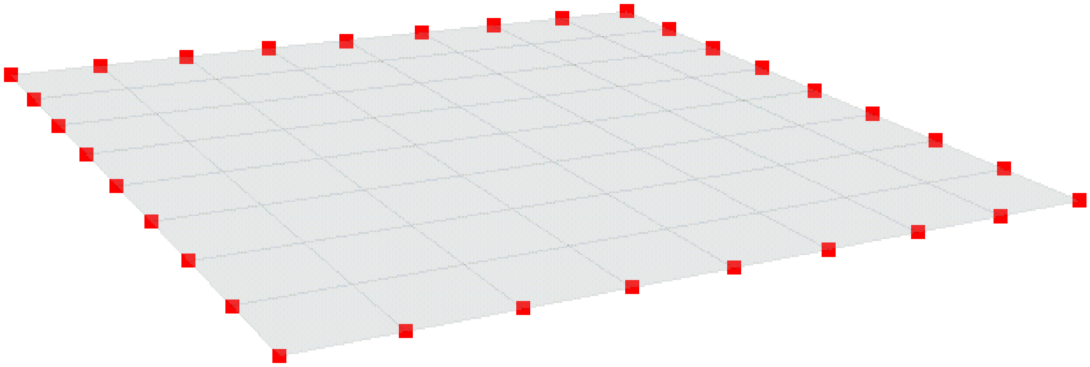

Figure 3.29: Simply-Supported Set-Up for Hourglassing Example

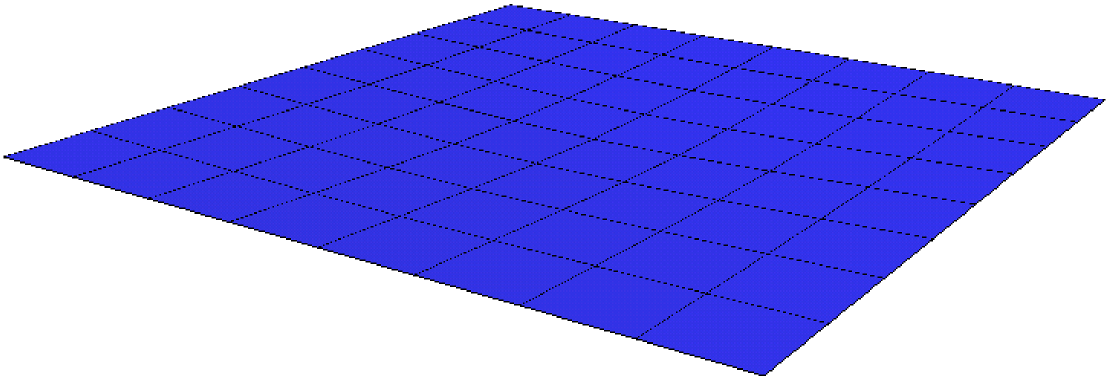

Figure 3.30: Deformed Shape for Simply-Supported Plate (No Hourglass Stiffness)

The deformed shape reveals that this problem does not require any hourglass stiffness. The computed center deflection (w_{center} = 0.008566 m) of the plate is within 0.6% of the 8x8 element solution provided by Zienkiewicz and Taylor (2005), which uses Kirchhoff theory.

3.4 Numerical Integration

3.4.1 Time Integration Scheme

The Hilber-Hughes-Taylor α-method (Hilber et al. 1977) is used together with a predictor/multi-corrector algorithm to integrate the finite element equations. The final form is given by Hughes (1983). Equation 3.20 can be rewritten as follows:

$$Ma_{n+1} + (1+\alpha)Cv_{n+1} - \alpha Cv_n + (1+\alpha)K_p d_{n+1} - \alpha K_p d_n + (1+\alpha)p_{n+1} - \alpha p_n = (1+\alpha)f_{n+1} - \alpha f_n \tag{3.180}$$

The nodal velocity and displacement are given by:

$$v_{n+1} = v_n + [\gamma a_{n+1} + (1-\gamma)a_n]\Delta t \tag{3.181}$$

$$d_{n+1} = d_n + v_n\Delta t + [\beta a_{n+1} + \left(\frac{1}{2} - \beta\right)a_n]\Delta t^2 \tag{3.182}$$

In the α-method, the relationship between acceleration, velocity, and displacement is controlled by the time-integration parameters (α, β, γ). Popescu and Prevost (1993) used α = 0.0, β = 1.0, and γ = 1.5 to calculate consolidation in a dynamic problem. These are the parameters used throughout this work in an attempt to solve the essentially static problems using the dynamic algorithm available within TeraDysac. Substituting these parameters into Equations 3.180-3.182, the following forms emerge:

$$Ma_{n+1} + Cv_{n+1} + K_p d_{n+1} + p_{n+1} = f_{n+1} \tag{3.183}$$

$$v_{n+1} = v_n + [\frac{3}{2}a_{n+1} - \frac{1}{2}a_n]\Delta t \tag{3.184}$$

$$d_{n+1} = d_n + v_n\Delta t + [a_{n+1} - \frac{1}{2}a_n]\Delta t^2 \tag{3.185}$$

The iterative time-marching scheme is given by the following equations (i is the iteration counter). Note: this is the scheme after setting α = 0.0, β = 1.0, and γ = 1.5. The general scheme for dynamic problems can be found in Muraleetharan et al. (1994).

Step 1: Initialize iteration counter i to zero

Step 2: Predictor

$$d_{n+1}^{(i)} = \bar{d}_{n+1} = d_n + v_n\Delta t - \frac{1}{2}a_n\Delta t^2 \tag{3.186}$$

$$v_{n+1}^{(i)} = \bar{v}_{n+1} = v_n - \frac{1}{2}a_n\Delta t \tag{3.187}$$

$$a_{n+1}^{(i)} = 0 \tag{3.188}$$

Step 3:

$$\psi^{(i)} = f_{n+1} - Ma_{n+1}^{(i)} - Cv_{n+1}^{(i)} - K_p d_{n+1}^{(i)} - p_{n+1}^{(i)} \tag{3.189}$$

Step 4:

$$M_{eff}^{(i)} = M + \frac{3}{2}\Delta tC + \Delta t^2 K_p + \Delta t^2 K_T^{(i)} \tag{3.190}$$

where

$$K_T = \frac{\partial p_{n+1}}{\partial d_{n+1}} = \text{global tangent stiffness matrix} \tag{3.191}$$

Step 5: Solve

$$M_{eff}^{(i)} \Delta a^{(\mathrm{i}+1)} = \psi^{(i)} \tag{3.192}$$

for the incremental acceleration $\Delta a^{(\mathrm{i}+1)}$

Step 6: Corrector

$$a_{n+1}^{(i+1)} = a_{n+1}^{(i)} + \Delta a^{(i+1)} \tag{3.193}$$

$$v_{n+1}^{(i+1)} = \bar{v}_{n+1} + \frac{3}{2} a_{n+1}^{(i+1)} \Delta t \tag{3.194}$$

$$d_{n+1}^{(i+1)} = \bar{d}_{n+1} + a_{n+1}^{(i+1)} \Delta t^2 \tag{3.195}$$

Step 7:

$$\psi^{(i+1)} = f_{n+1} - Ma_{n+1}^{(i+1)} - Cv_{n+1}^{(i+1)} - K_p d_{n+1}^{(i+1)} - p_{n+1}^{(i+1)} \tag{3.196}$$

Step 8: Convergence check. If

$$\frac{\|\Delta a^{(i+1)}\|}{\left\|a_{n+1}^{(i+1)}\right\|} \leq \varepsilon \tag{3.197}$$

where ε is a small number (~0.01), then go to the next time step. Else set $i = i + 1$ and go to Step 4.

The user controls the damping for the structural elements (Rayleigh damping) directly. For the static problems solved in this work, there was no damping applied to the structural elements (beams and plates). Although only static problems were solved in this work, the structural elements developed can be used for dynamic problems by introducing damping and changing the time-integration parameters.

3.4.2 Ramped Loading

The amount of load applied to a finite element mesh at any time step is controlled by the user. The use of a ramped loading (see Figure 3.31) was found to be an effective way to apply loads.

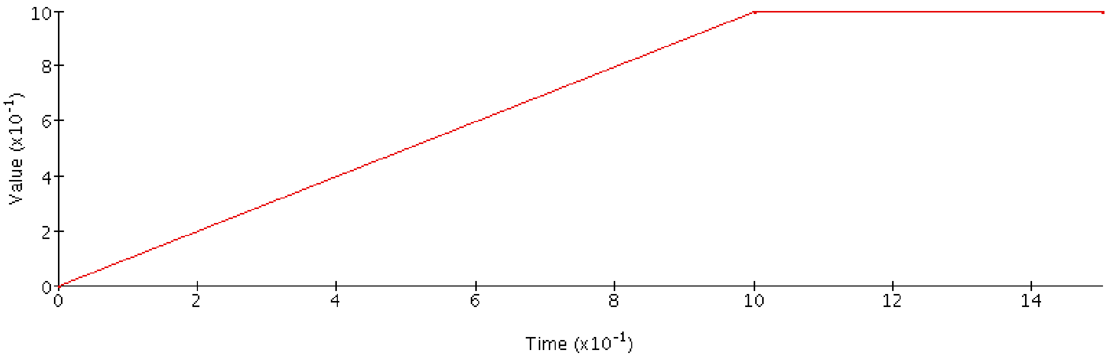

Figure 3.31: Ramped Loading

The x-axis is the time in seconds and the y-axis is the portion of the load applied at a given time. Therefore, for the ramp shown in Figure 3.31, the analysis would begin with no applied load and at 1.0 s, the full load would be applied. The ramp is held constant value for a period of time after the full value of the loading has been reached to allow any solution oscillation to end. Checking the nodal displacement histories upon analysis completion is important to confirm the solution has fully developed. Two analyses which both use the ramped loading shown in Figure 3.31 illustrate oscillation in the dynamic solution.

The cantilever beam problem shown in Figure 3.32 was found to only exhibit minor solution oscillation after the ramp leveled off (i.e. the full load was developed).

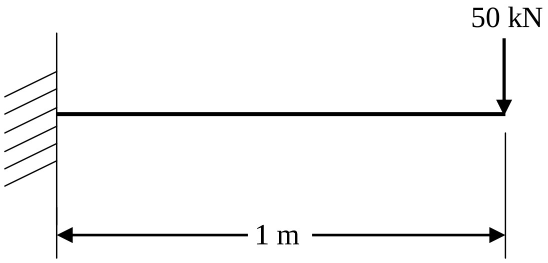

Figure 3.32: Cantilever Beam Problem Demonstrating Minor Oscillation

The beam properties are given here:

A = 0.196 m^2
I = 3.07 * 10^{-3} m^4
E = 3 * 10^7 kPa
ν = 0.3
k = 5/6
ρ = 2.4 Mg/m^3

Figure 3.33 shows the nodal displacement-time history of the beam node directly under the point of load application.

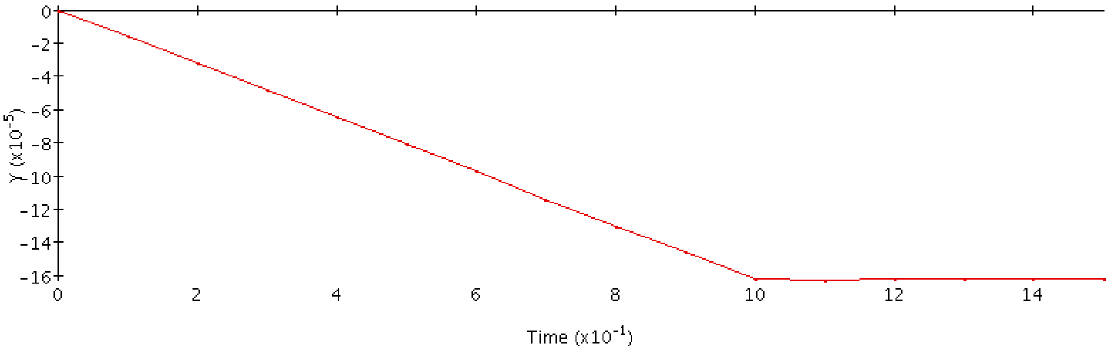

Figure 3.33: Nodal Displacement-Time History for Cantilever Beam Tip

It is apparent that the displacement solution has fully developed at 1.5 s. There was miniscule oscillation after the ramp terminated, but it quickly ended. Successive tip displacements after 1.3 s are identical.

An example exhibiting more solution oscillation is the soil-structure interaction problem described in Figure 3.34.

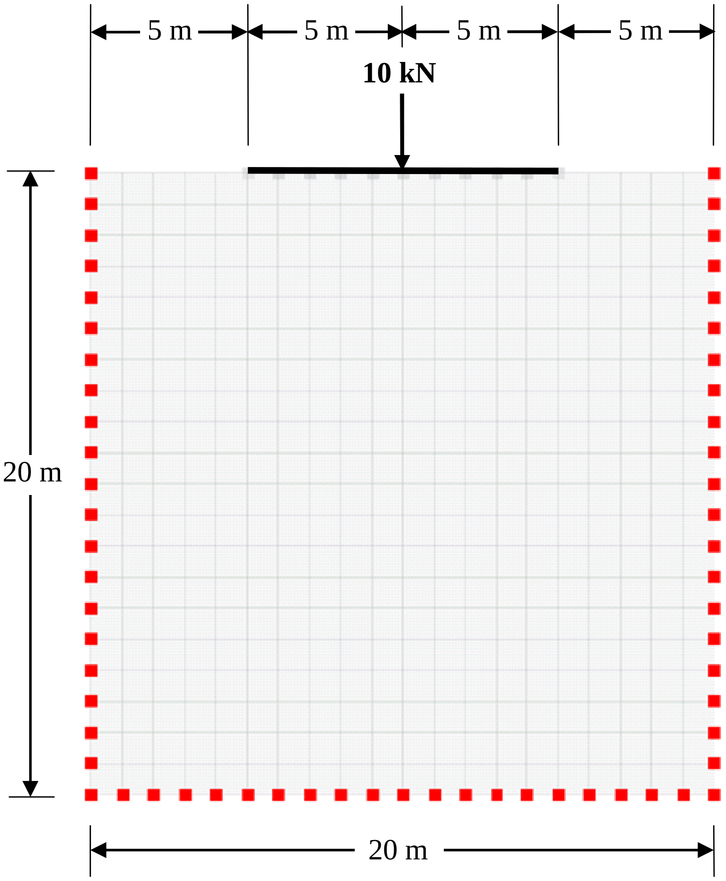

Figure 3.34: Soil-Structure Interaction Problem Demonstrating Oscillation

The soil properties are given here:

$E = 15{,}000$ kPa
$\nu = 0.3$
$\rho_s = 2.67$ Mg/m^3
$\rho_f = 1.0$ Mg/m^3
$\Gamma = 0.0$ kPa

The beam in the problem has the same properties used in the preceding cantilever example. Figure 3.35 shows the displacement-time history of the beam node under the point load.

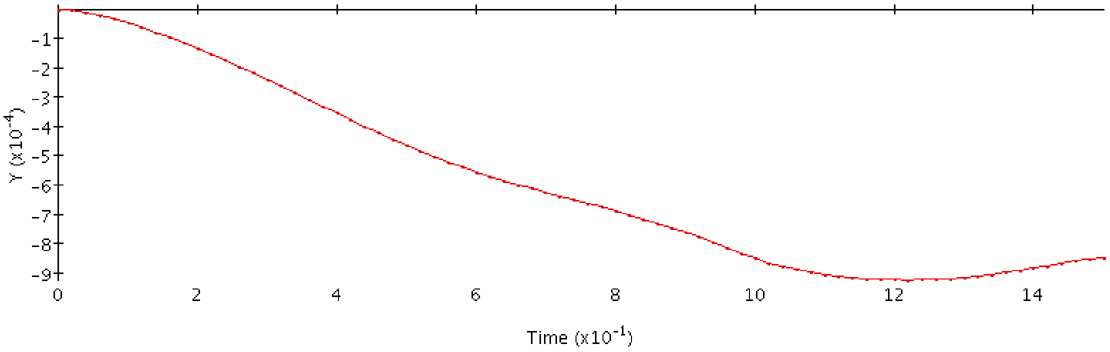

Figure 3.35: Nodal Displacement-Time History (Full Mass)

It is apparent that the nodal displacement has not settled on a final value. To find the true displacement of the node, the loading needs held constant for a longer period of time to allow the oscillation to end. Figure 3.36 shows the displacement history for an analysis where the load is ramped up over 1 s (similar to Figure 3.31), but held constant for another 7 s.

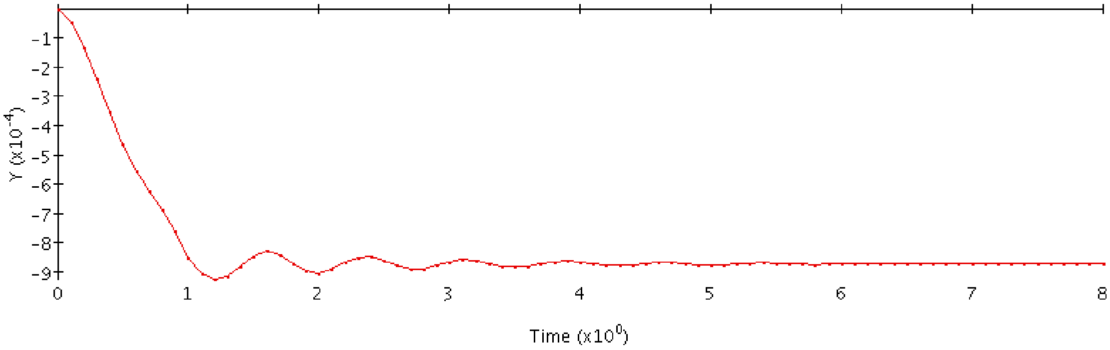

Figure 3.36: Nodal Displacement-Time History (Full Mass, Extended Ramp)

There is oscillation in the solution after the ramp-up ends at 1 s. After about 6 s, the solution oscillation ends and the true displacement solution is reached. In the study of various problems, it was discovered that reducing the mass of the element blocks lead to less oscillation in some cases. Figures 3.37 and 3.38 are the nodal displacement-histories for meshes with 10% mass and zero mass, respectively.

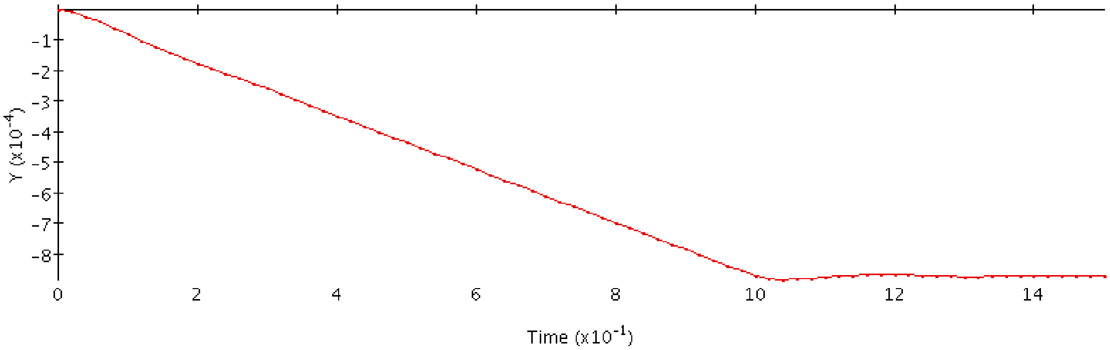

Figure 3.37: Nodal Displacement-Time History (10% Mass)

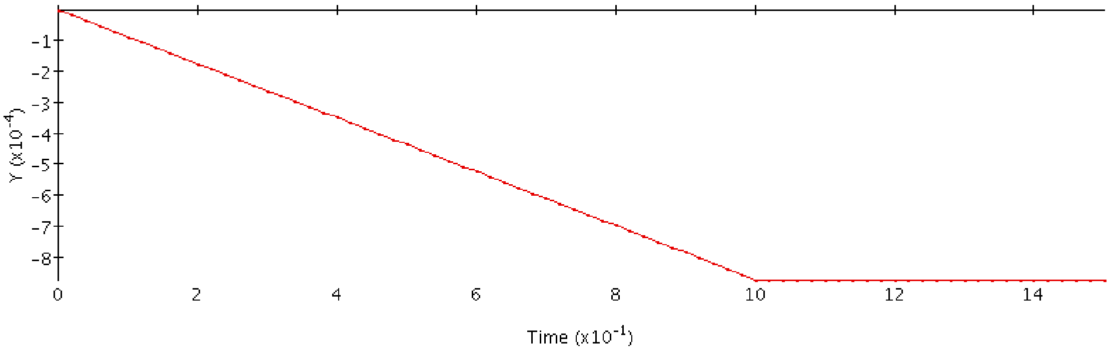

Figure 3.38: Nodal Displacement-Time History (Zero Mass)

For the problem in question, reducing the mass by 90% has significantly trimmed the solution oscillation. Setting the mass to zero has essentially provided the static solution to the problem. Figure 3.38 shows no oscillation in the solution. The obtained solution (after all oscillation dies), is the same for all three analyses (Figure 3.36-3.38), as expected.

As the load is ramped up, there is acceleration of the spatial nodes. Once the ramp tapers off, the load is held constant and the true static solution will eventually develop. In the predictor, specifically Equation 3.190, M_{eff} is calculated. M is contained in this equation, therefore the mass of the model is affecting the problem solution as the load is being ramped up. The incremental acceleration $\Delta a^{(i+1)}$ (see Equation 3.192) is dependent on the value of M_{eff}. Once the full load has been developed and the nodal displacements become constant, the nodal accelerations go to zero.

Reducing the element block mass was found to reduce solution oscillation. However, the mass in the problems should not be reduced without proper cause. Displacement-time histories should be consulted to see if significant solution oscillation is occurring. In some problems, such as gravity loading, the element mass is integral to the solution, so it can not be reduced. An unreduced mass matrix may also be important for stability issues (i.e. solution convergence at each time step), especially in 3D problems and problems utilizing the bounding surface soil model. For these problems, reducing the mass also required increasing the number of time steps. So there is some trade-off involved in reducing the mass which trims oscillation, yet may require more time steps. The right combination of element mass and time step should be selected based on the needs of the individual analysis and the exhibited solution behavior. Yet to be implemented in TeraDysac is a true static procedure, which would be ideal for solving the problems discussed in this work.

4. Soil-Structure Interaction

4.1 Linear Problems

4.1.1 Beams on Elastic Foundation

The theory for beams on elastic foundations began with the work of Winkler (1867). Winkler theory assumes an infinitely long linear elastic beam is resting on an elastic foundation under a uniformly distributed load (see Figure 4.1).

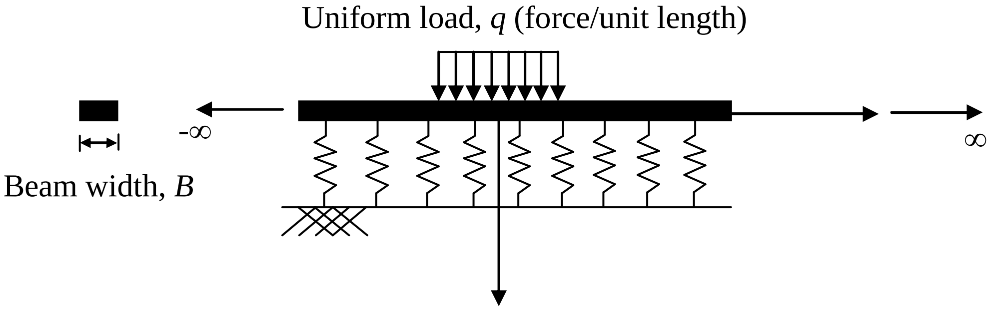

Figure 4.1: Beam on Elastic Foundation

The soil is modeled with an infinite number of discrete elastic springs. The displacement (y) at any given position along the beam (x) is assumed to only depend on the load at that point. The spring force per unit length is given by:

$$p = Bky \tag{4.1}$$

where k is the modulus of subgrade reaction (units of FL^{-3})

Equation 4.2 is the governing fourth-order differential equation in Winkler theory.

$$EI\frac{d^4y}{dx^4} + Bky - q = 0 \tag{4.2}$$

where:

E = Young's modulus for the beam
I = area moment of inertia for the beam

The governing differential equation has a general solution given by:

$$y = e^{\lambda x}(A_1 \cos \lambda x + A_2 \sin \lambda x) + e^{-\lambda x}(A_3 \cos \lambda x + A_4 \sin \lambda x) + y_p \quad (4.3)$$

where:

$$\lambda = \left(\frac{Bk}{4EI}\right)^{\frac{1}{4}} \quad (4.4)$$

A_1, A_2, A_3, A_4 are integration constants to be determined from boundary conditions and y_p is the particular solution for the given loading

Solutions according to Winkler theory can be developed for distributed loads, point loads, concentrated moments, and combinations thereof. Solutions for “short” or non-infinite beams can also be developed.

4.1.2 Linear SSI Example Problem

A soil-structure interaction example is considered here with a concentrated moment applied at the center of an infinitely long beam (see Figure 4.2).

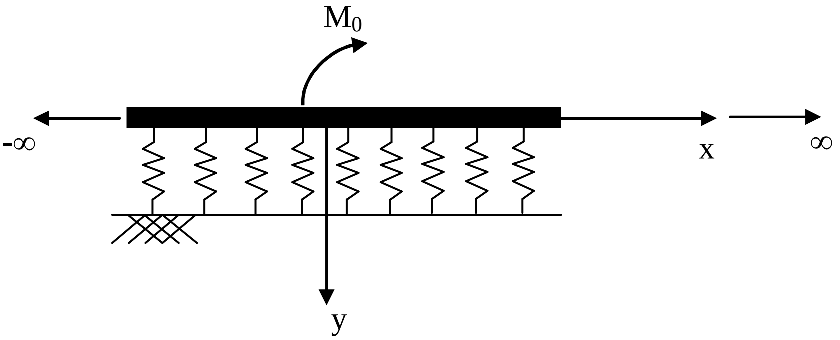

Figure 4.2: Problem Set-Up

The relevant problem parameters are given here:

B = 0.3 m
EI = 948.27 kN-m^2
k = 30,093.93 kN/m^3

The analytical solutions for the Winkler theory (x > 0) are given here:

$$y = \frac{M_0\lambda^2}{Bk} e^{-\lambda x}(sin\ \lambda x) \quad (4.5)$$

$$\theta = \frac{M_0\lambda^3}{Bk} e^{-\lambda x}(\cos \lambda x - sin\ \lambda x) \quad (4.6)$$

$$V = \frac{-M_0\lambda}{2}\, e^{-\lambda x}(\cos \lambda x + sin\, \lambda x) \tag{4.7}$$

$$M = \frac{M_0}{2} e^{-\lambda x}(cos\, \lambda x) \tag{4.8}$$

where:
  y = deflection
  θ = rotation
  V = shear force
  M = bending moment
  M_0 = applied concentrated moment

A concentrated moment problem was selected for the example because the soil boundary conditions had minimal effect on the finite element solution. The soil elements do not have rotation as a nodal variable. Therefore, the beam takes a majority of the loading and the soil in the far field does not influence the results adjacent to the beam. In the finite element analysis of a point load applied to the beam, as expected for this linear elastic case, the soil boundary was shown to have a significant effect on the results. The displacement at the point of load application increased as the depth of the soil stratum increased, therefore the solution did not converge. Just as the deformation of an axial bar (Equation 4.9) is a function of bar length, the displacement solution for the point load is a function of the soil depth.

$$\delta = \frac{PL}{EA} \tag{4.9}$$

where:
  δ = deformation
  P = point load
  L = bar length
  E = Young's modulus
  A = bar area

In studying equation 4.9, for a given P, E, and A, as L increases so too does the deformation. Comparing Figures 4.3 and 4.4, the relationship between the two problems is apparent.

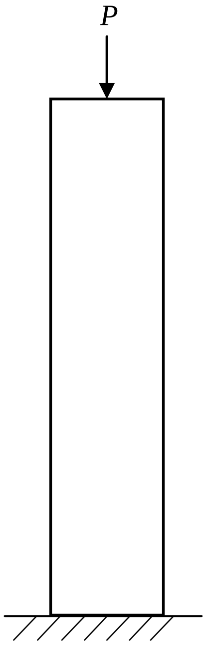

Figure 4.3: Point Load Applied to Axial Bar

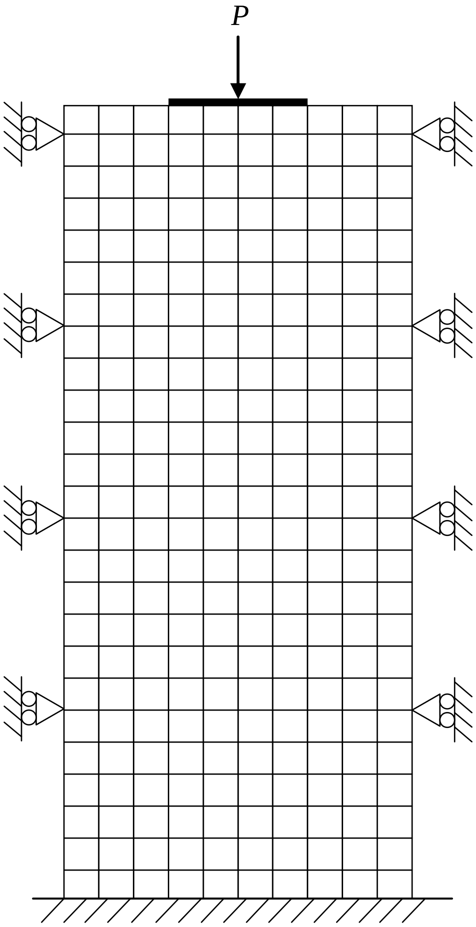

Figure 4.4: Finite Element Set-Up for Point Load Analysis

Convergence for the problem illustrated in Figure 4.4 will occur for a nonlinear constitutive soil model. For a big enough mesh, the bounding surface model will eventually provide a solution that does not have an influence from the soil boundaries.

In a finite element analysis of a beam on a continuum, the subgrade modulus, k, is not used directly. Instead, Young's modulus of the soil, E_s, has to be related to the subgrade modulus. Two forms of an equation relating these two properties are presented by Biot (1937) and Vesic (1961). Biot developed the analytical solution of an infinite beam on an elastic foundation subjected to a point load. By equating the maximum bending moments obtained from his solution and the solution presented by Winkler, he expressed k as a function of the soil and beam properties. Vesic extended the work of Biot by developing complete solutions for elastic beams resting on isotropic elastic solid continuum subjected to both point loads and concentrated moments. Vesic also developed a relationship between k and E_s which matches all solution components (displacement, rotation, bending moment, and shear force) reasonably well. The equation developed by Vesic is given by:

$$k = \frac{0.65\, E_s}{(1-\nu)^2\, B} \left(\frac{E_s\, B^4}{EI}\right)^{\frac{1}{12}} \qquad (4.10)$$

Assuming a Poisson's ratio for the soil of 0.3, Equation 4.10 sets E_s to 15,000 kPa for the example problem. Figures 4.5-4.8 show the comparison of the Winkler and Vesic solutions for M_0 = 100 kN-m.

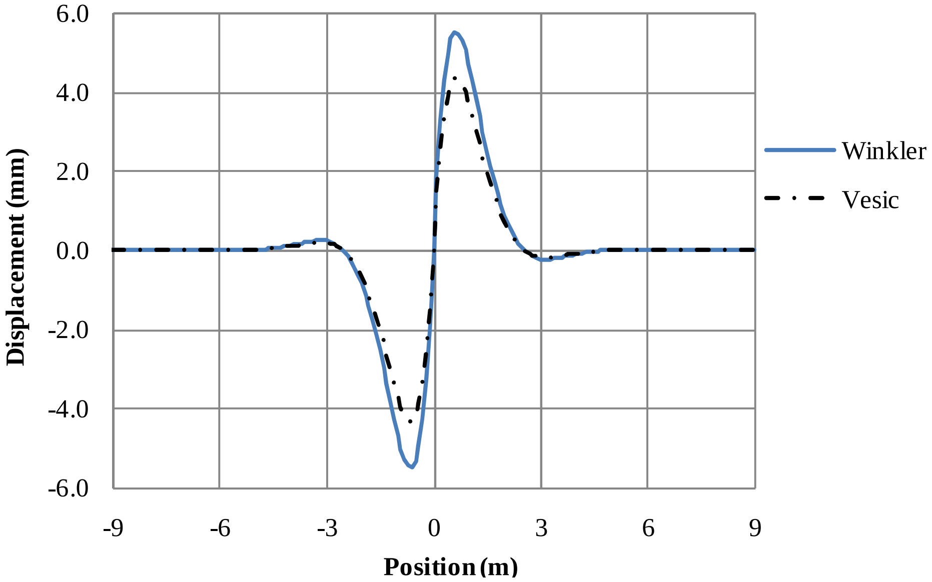

Figure 4.5: Beam Displacement (Winkler vs. Vesic)

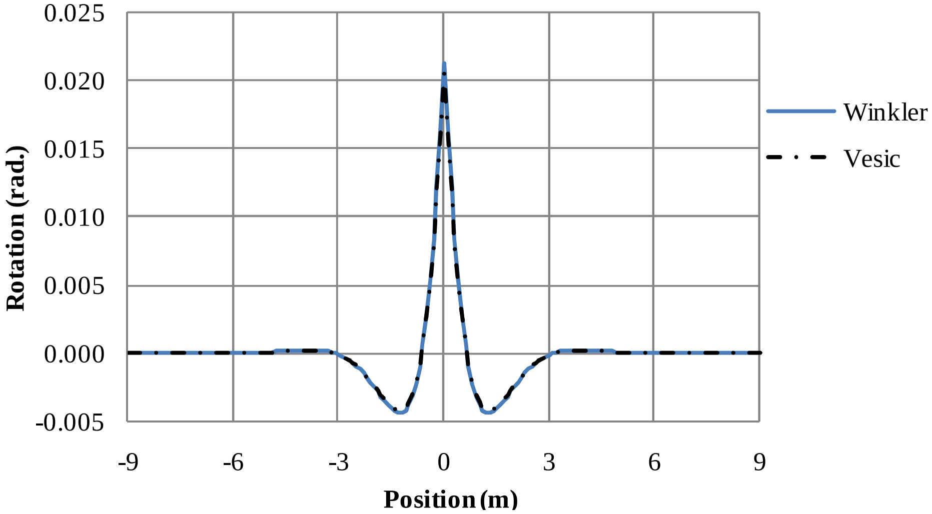

Figure 4.6: Beam Rotation (Winkler vs. Vesic)

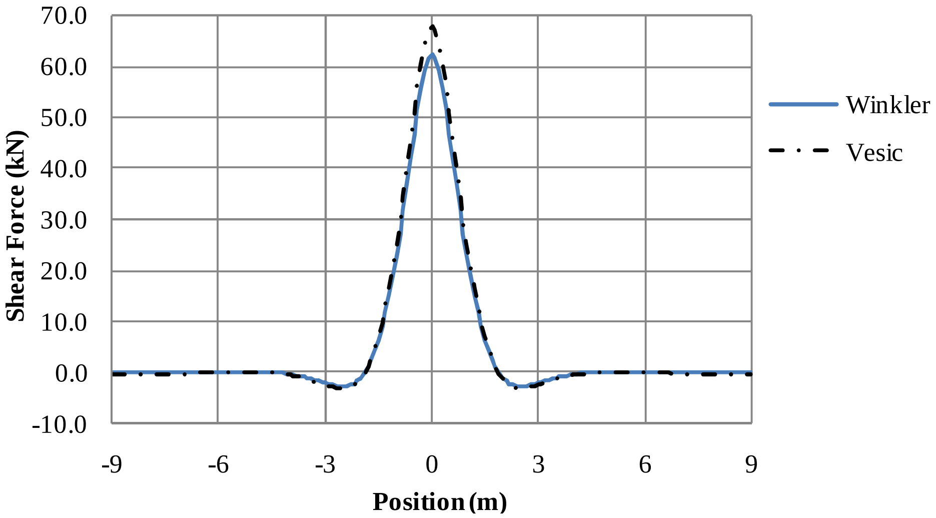

Figure 4.7: Beam Shear Force (Winkler vs. Vesic)

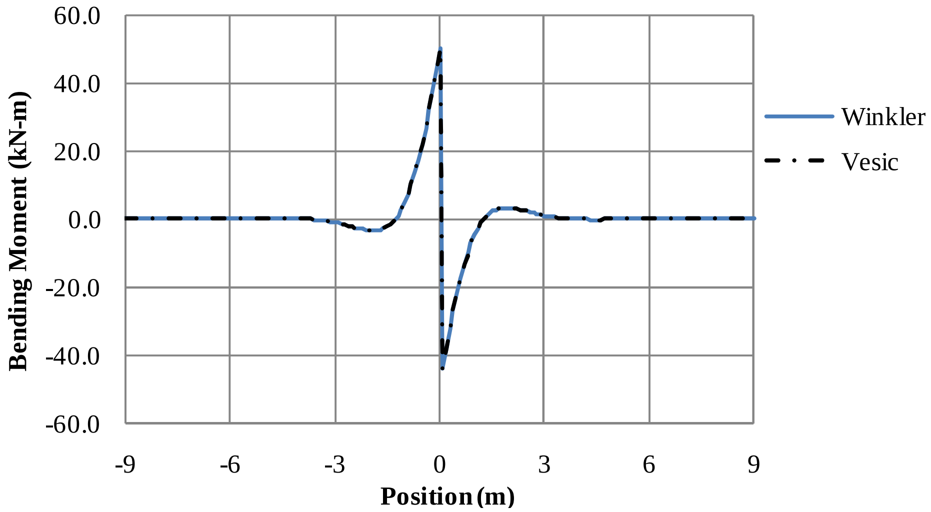

Figure 4.8: Beam Bending Moment (Winkler vs. Vesic)

The curves are in good agreement, but there are slight differences between the Winkler and Vesic solutions. The error between the two solutions depends on the relative stiffness of the beam (Vesic 1961).

The beam theory embedded in the Vesic solution is Euler-Bernoulli. Timoshenko beams are implemented in TeraDysac, so before the soil-structure interaction problem was run, an elastic analysis was performed on the beam only to verify convergence to the Euler-Bernoulli solution for the given beam properties and mesh size. A simply-supported beam with identical properties to the example beam (A = 0.15 m^2, E = 303,446.55 kPa, I = 0.003125 m^4, ν = 0.3, k = 5/6) was analyzed. Explicit equations can be written for the displacement and rotation of the beam shown in Figure 4.9 using Euler-Bernoulli beam theory.

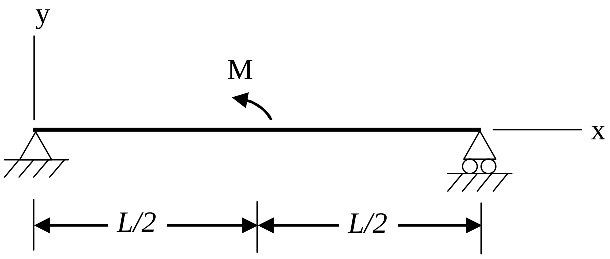

Figure 4.9: Elastic Beam Analysis Set-Up

The elastic curves are given by:

For $0 \le x \le \frac{L}{2}$,

$$EI\ y(x) = \frac{Mx^3}{6L} - \frac{MLx}{24} \tag{4.11}$$

$$EI\ \theta(x) = \frac{Mx^2}{2L} - \frac{ML}{24} \tag{4.12}$$

For $\frac{L}{2} \le x \le L$,

$$EI\ y(x) = \frac{Mx^3}{6L} - \frac{Mx^2}{2} + \frac{11MLx}{24} - \frac{3ML^2}{24} \tag{4.13}$$

$$EI\ \theta(x) = \frac{Mx^2}{2L} - Mx + \frac{11ML}{24} \tag{4.14}$$

Letting M = 100 kN-m and L = 18 m, the comparison between the curves provided by Equations 4.11 – 4.14 and the TeraDysac analysis is shown in Figures 4.10 and 4.11.

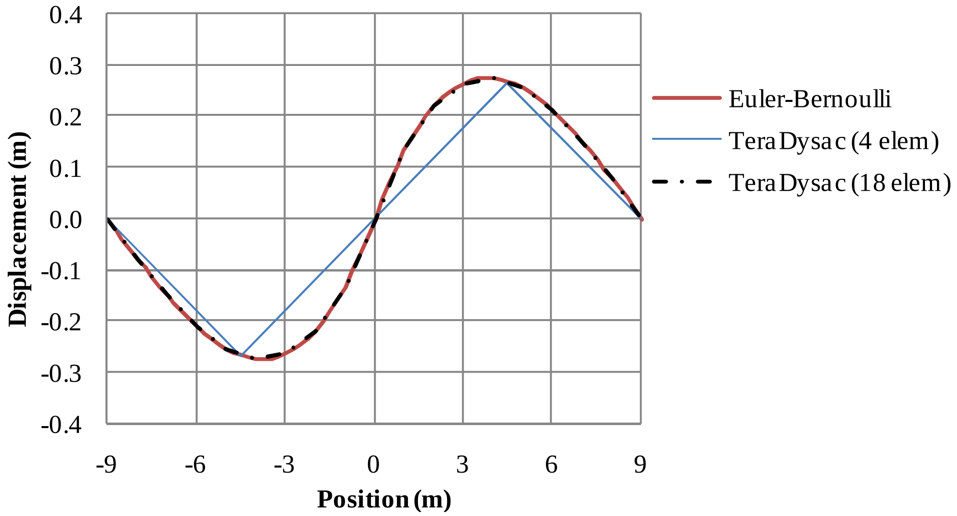

Figure 4.10: Euler-Bernoulli Beam Displacement Comparison

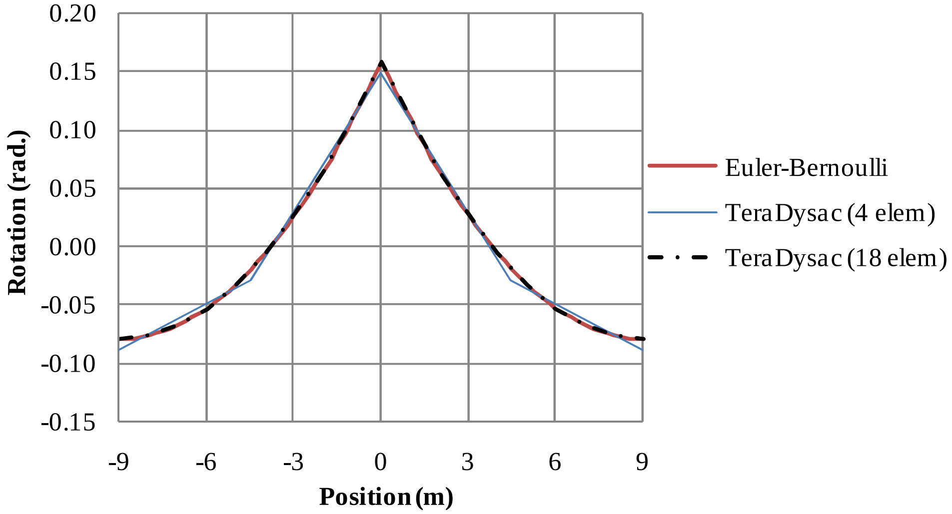

Figure 4.11: Euler-Bernoulli Beam Rotation Comparison

Figures 4.10 and 4.11 reveal that an 18 element mesh (i.e. 1 m beam elements) is sufficient for the beam to converge to the Euler-Bernoulli solution for this particular problem. Therefore, 1 m elements were used as the starting point for the soil-structure interaction analysis. Soil nodes were fixed at the base in all directions and in the horizontal direction only on the sides. Pore water pressure was suppressed by setting Γ = 0.0 kPa (see Equation 3.31). Ultimately, 0.25 m beam elements were used to get a smooth displacement shape. Figure 4.12 shows the finite element mesh and the loading condition. All beam nodes are tied to soil nodes at the top of the mesh. In the vertical direction, there is a gradient of elements with the finer elements near the beam.

To validate the soil-structure interaction capabilities in TeraDysac, the finite element solution was compared to the analytical solution presented by Vesic. Figures 4.5-4.8 reveal that displacement, rotation, shear force, and bending moment all become negligible at a beam length of 18 m. Thus, an 18 m beam finite element solution can reasonably be compared to the infinite beam solution presented by Vesic.

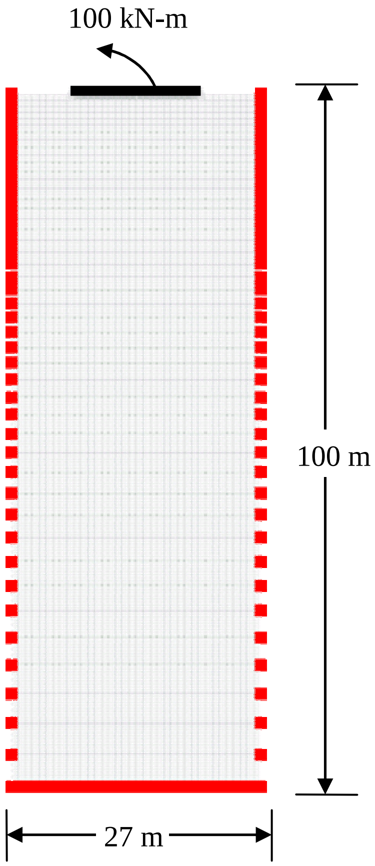

Figure 4.12: Finite Element Model Set-Up for Linear Soil-Structure Analysis

Figures 4.13-4.16 show the results from the TeraDysac analysis compared with the analytical solution presented by Vesic.

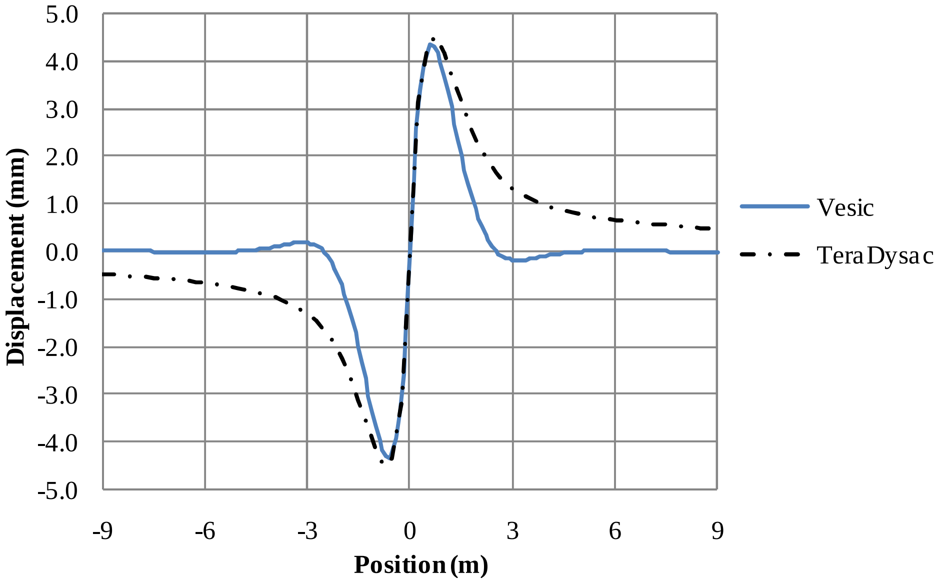

Figure 4.13: Beam Displacement (Vesic vs. TeraDysac)

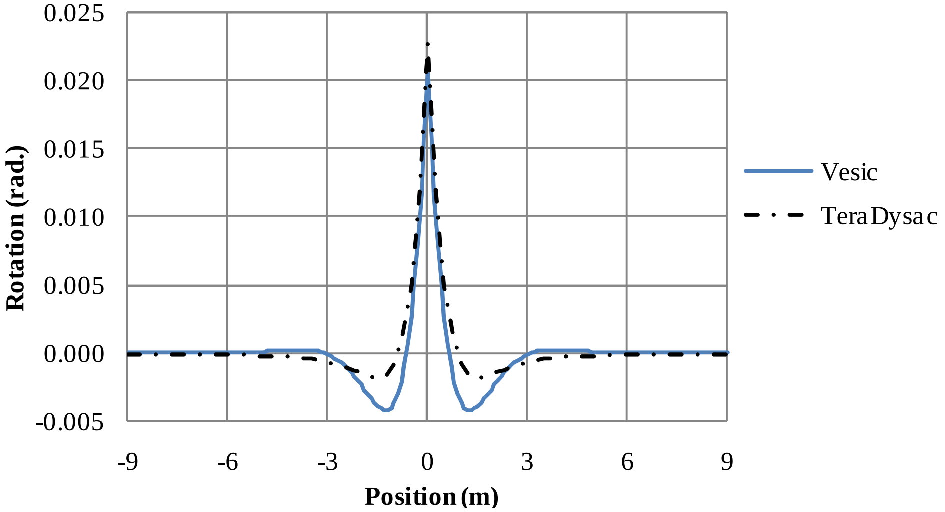

Figure 4.14: Beam Rotation (Vesic vs. TeraDysac)

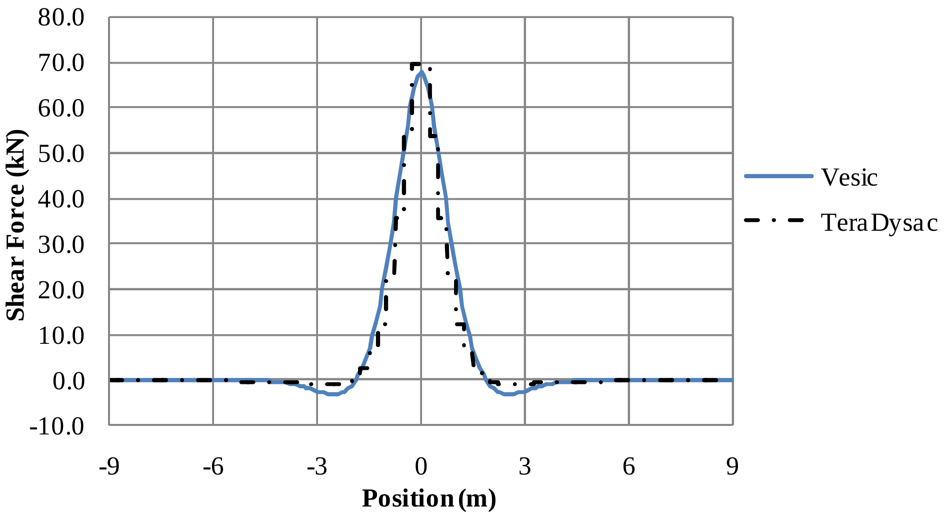

Figure 4.15: Beam Shear Force (Vesic vs. TeraDysac)

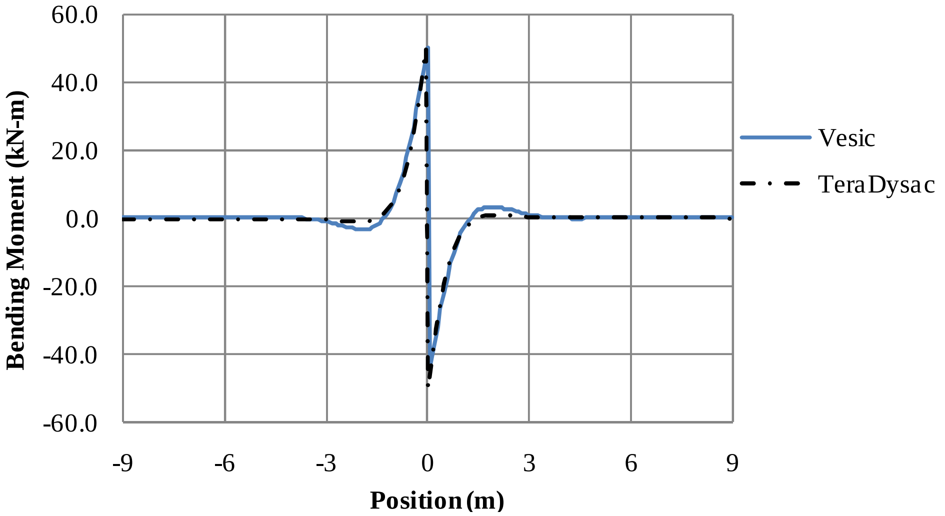

Figure 4.16: Beam Bending Moment (Vesic vs. TeraDysac)

Figure 4.17 shows the displaced shape. The Uniform Gradient formulation is used for the soil elements, so it is important to check the deformed shape to confirm that no hourglassing has taken place in the analysis. The figure zooms in on the beam center and magnifies the displacement by 20. It is apparent that no hourglassing has occurred and the deformed shape of the beam is smooth.

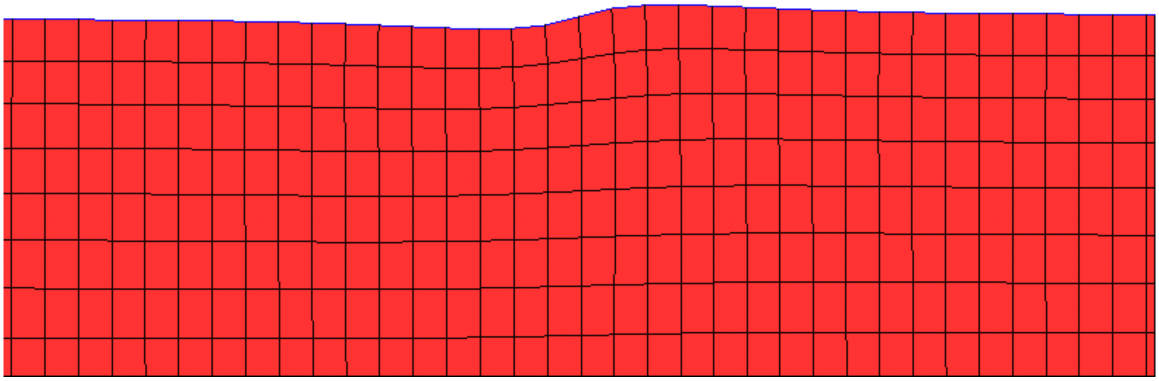

Figure 4.17: TeraDysac Linear SSI Analysis Deformed Shape

The beam shear force and bending moment curves are in concurrence with the Vesic solution. While the TeraDysac solution for displacement and rotation show good agreement near the point of load application, the beam displacement is slow to diminish in the finite element solution. The rotation subsequently has deviation from the Vesic solution after the displacement reaches a maximum (about 0.6 m from the beam midpoint). It is important to note that the Vesic solution presented is for a 3D elastic foundation. Therefore, a 3D mesh (extruded 18 m in the z-direction) was also analyzed. A fine mesh in 3D was not investigated because of the tremendous amount of computational effort necessary for an analysis. A course mesh (1 m beam elements) analysis provided enough insight to draw the conclusion that a 3D finite element solution will converge to the Vesic solution. Figures 4.18-4.21 show the 3D analysis compared with the Vesic solution.

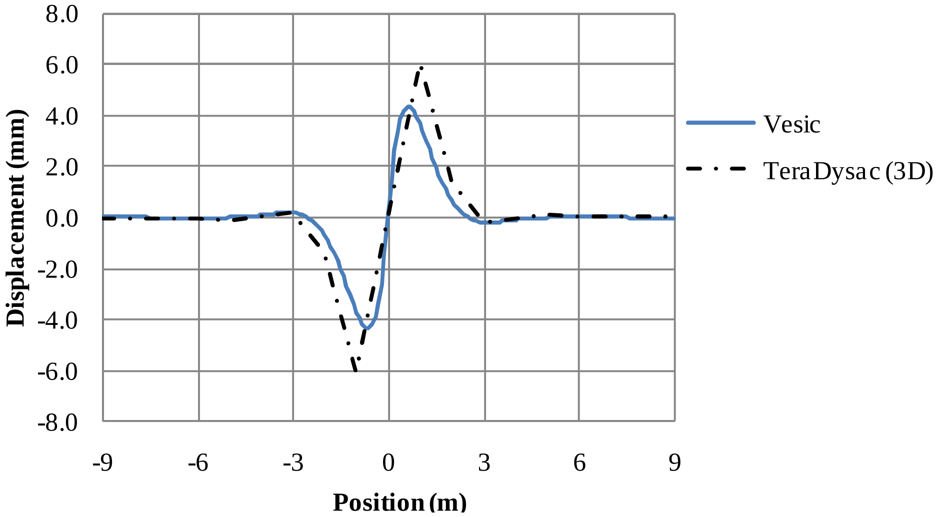

Figure 4.18: Beam Displacement (Vesic vs. TeraDysac – 3D)

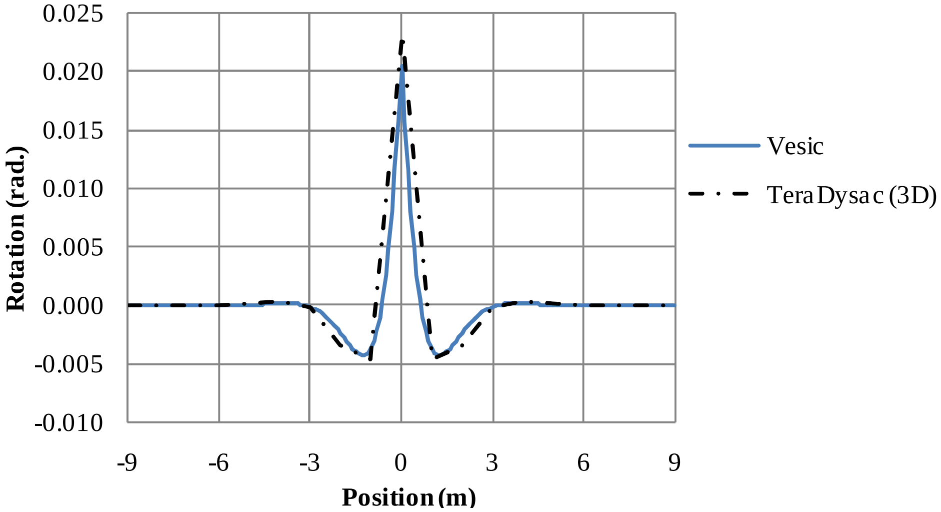

Figure 4.19: Beam Rotation (Vesic vs. TeraDysac – 3D)

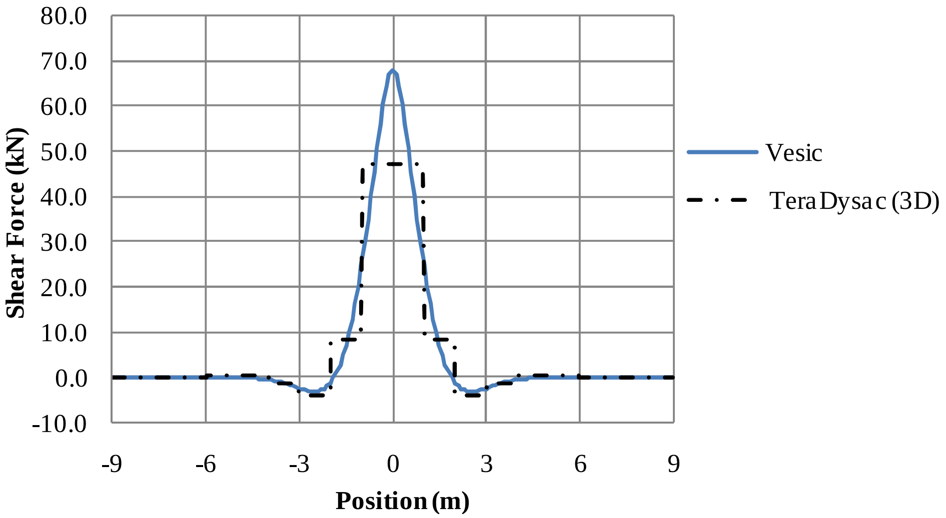

Figure 4.20: Beam Shear Force (Vesic vs. TeraDysac – 3D)

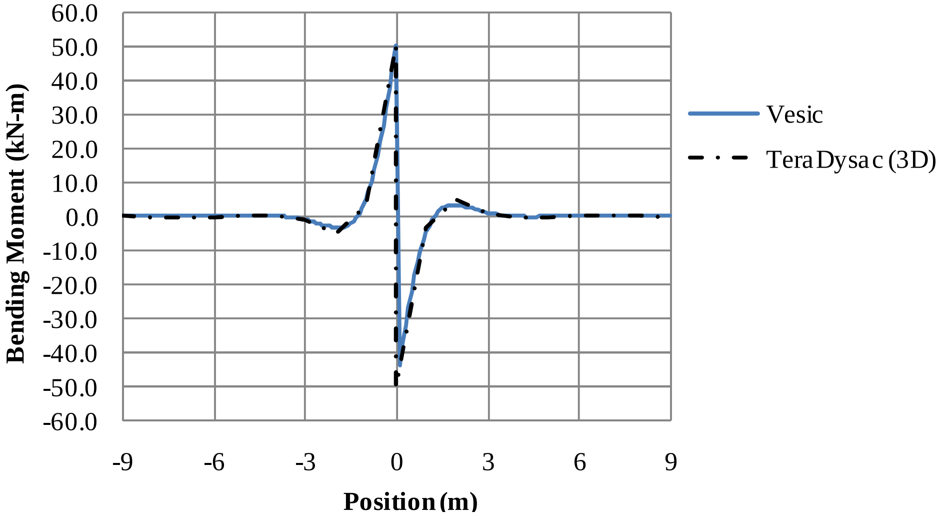

Figure 4.21: Beam Bending Moment (Vesic vs. TeraDysac – 3D)

Figures 4.18 and 4.19 show the 3D displacement and rotation solutions diminish much quicker after the maximum displacement is reached than the 2D solutions. For this particular problem, the 2D (plane strain) solutions were slow to diminish. It is believed that the zero strain condition on the soil in the z-direction is responsible for this departure from the true solution.

4.2 Soil-Pile Interaction in a Soft Clay

More interesting (and realistic) soil-structure interaction problems are the ones where the nonlinear constitutive properties of the soil are considered. In practice, advanced analyses use the $p - y$ method with a program like LPILE (ENSOFT 2007). In LPILE, the user is allowed to manually input $p - y$ curves or use program-furnished curves based on soil type. The program-furnished curves are empirical curves obtained using limited full-scale cyclic loading of piles. In TeraDysac, clays are analyzed using the bounding surface model developed by Dafalias and Herrmann (1982, 1986). This model was discussed in Chapter 3.

4.2.1 Nonlinear SSI Example Problem

To evaluate TeraDysac capabilities for nonlinear soil-structure interaction problems, a soil-pile analysis was performed using saturated soft clay. The pore pressure effects are considered by setting $\Gamma = 2.2 * 10^6$ kPa. Figure 4.22 depicts the problem set-up.

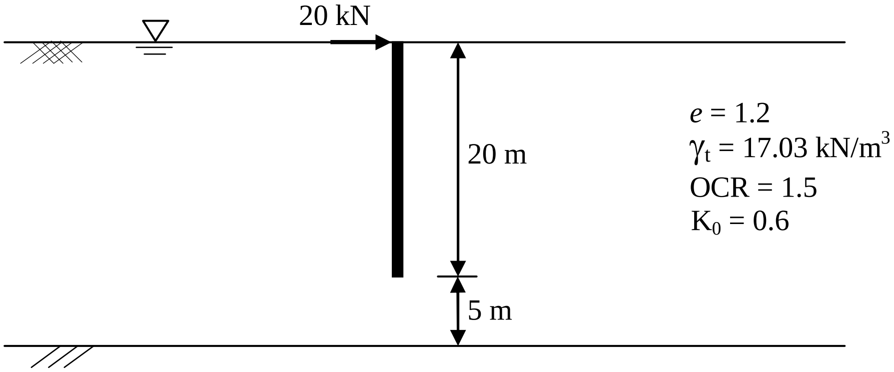

Figure 4.22: Nonlinear SSI Example Set-Up

The bounding surface parameters for Speswhite Kaolin (see Chapter 3) are those recommended by Muraleetharan et al. (1994).

The beam properties are given here:

$E = 30 * 10^6$ kPa
$A = 0.1963$ m^2
$I = 0.003068$ m^4
$\nu = 0.2$
$k = 0.8475$

Figures 4.23 and 4.24 show the TeraDysac analysis set-up.

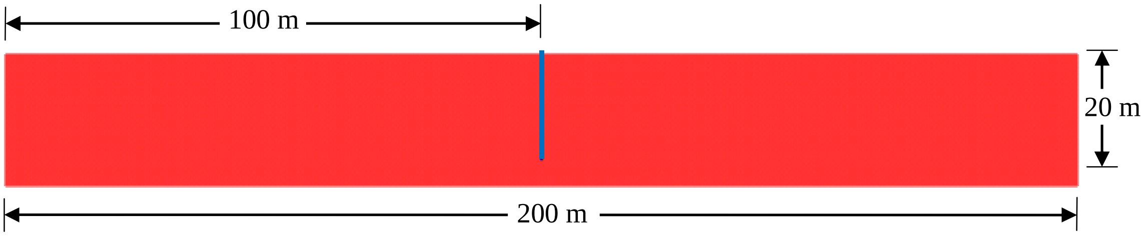

Figure 4.23: Problem Set-Up for Nonlinear SSI TeraDysac Analysis

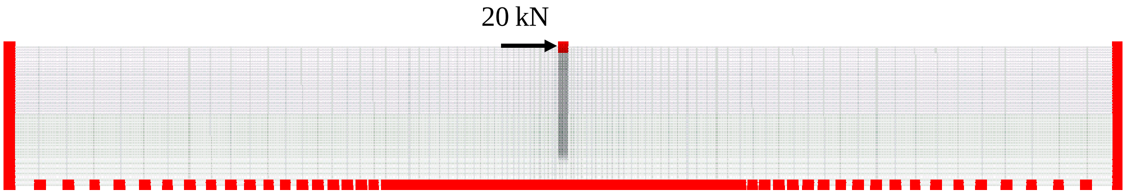

Figure 4.24: Loading and Node Sets for Nonlinear SSI TeraDysac Analysis

In the analysis of soft clay, the initial stress state is important. TeraDysac allows the initial stress state to be specified. The initial stress state was calculated as follows:

$$\sigma'_y = \gamma' h \tag{4.15}$$

$$\sigma'_x = \sigma'_z = K_0 \sigma'_y \tag{4.16}$$

$$\sigma'_{xy} = \sigma'_{yz} = \sigma'_{zx} = 0 \tag{4.17}$$

where γ' is the effective unit weight of the soil and h is the depth below the soil surface.

Figure 4.25 shows the initial vertical effective stress state for the pile loading problem.

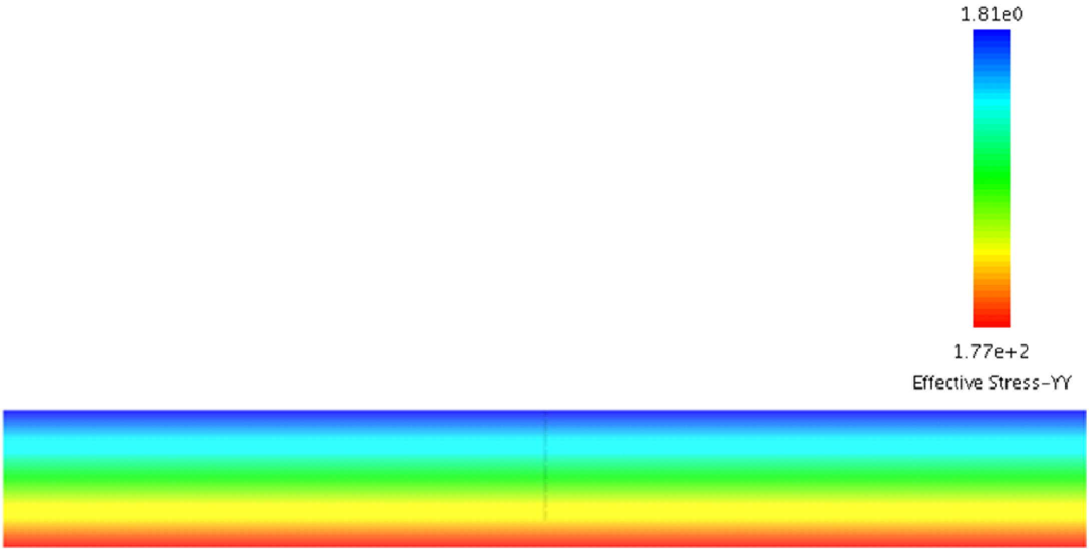

Figure 4.25: Initial Vertical Stress State Contours (kPa)

The TeraDysac analysis results were then compared with results from LPILE. LPILE allows the user to enter $p-y$ curves for soil layers or use program furnished $p-y$ curves based on the soil type (soft clay in the presence of free water, sands, etc). In addition to $p-y$ information, LPILE requires the user to input the strain corresponding to one-half the maximum principle stress difference (ε_{50}) and the shear strength of the clay. A single element computer code (EVALK) utilizing the same bounding surface model implemented in TeraDysac was used to determine the shear strength of the clay. The single element program simulates an undrained triaxial test to determine the strength of the soil. The user is allowed to specify the initial stress state, OCR, and loading type. At a depth of 20 m for the example problem, the EVALK results are given in Figures 4.26 and 4.27.

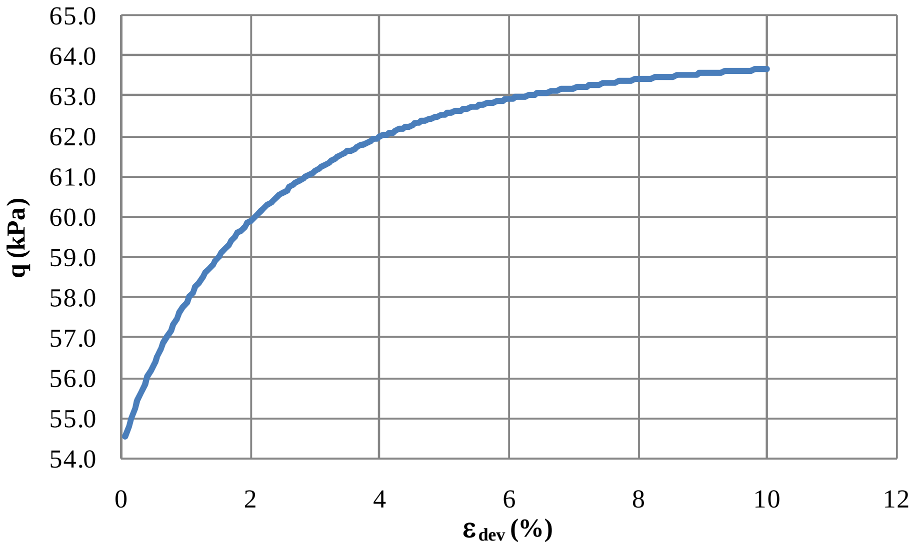

Figure 4.26: Deviator Stress-Strain Curve at 20 m Depth

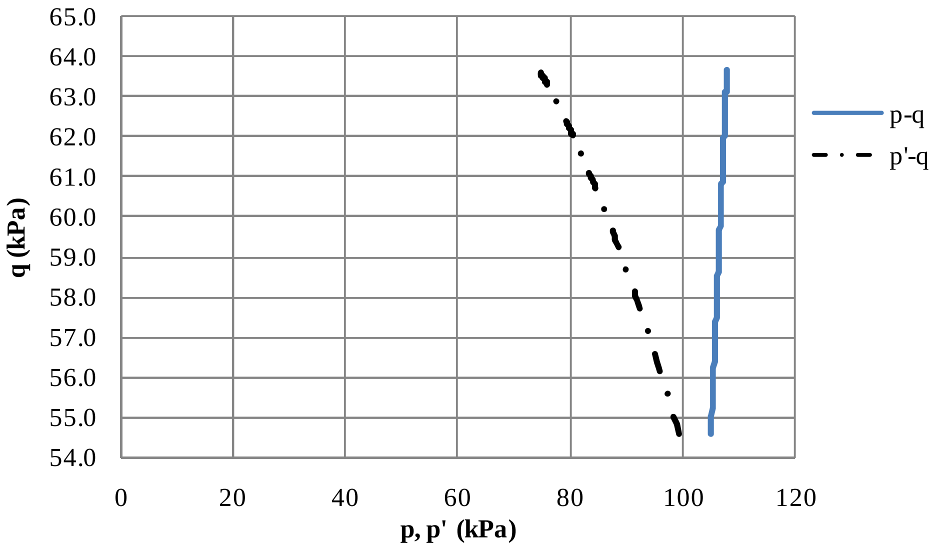

Figure 4.27: Stress Paths at 20 m Depth

The value of ϵ_{50} used was 0.02, which was recommended in the LPILE technical manual (ENSOFT 2004). However, ϵ_{50} can be determined from EVALK analysis results. According to Figure 4.26, the strain corresponding to one-half the principal stress difference is 1.55% (ϵ_{50} = 0.0155). This is sufficiently close to the recommended value of 0.02, which was used at all soil depths in the subsequent analyses.

Note that p' and q follow the Cambridge notation where:

$$p' = \frac{\sigma_1' + 2\sigma_3'}{3} \tag{4.18}$$

$$q = \sigma_1' - \sigma_3' \tag{4.19}$$

The shear strength input to LPILE was one-half the final q values obtained from EVALK. In the first LPILE analysis, the obtained value of soil strength at a depth of 10 m was used for the entire stratum. This is comparable to a design firm having only one triaxial test to describe the soil stratum. The second LPILE analysis uses EVALK-obtained strength values at 1 m increments through the soil depth. This is representative of a highly tested field site. In both of these analyses, the LPILE-furnished $p-y$ curves for soft clay in the presence of free water (Matlock 1970) were used. Figure 4.28 shows the LPILE-generated $p-y$ curves for the first analysis (single value of shear strength).

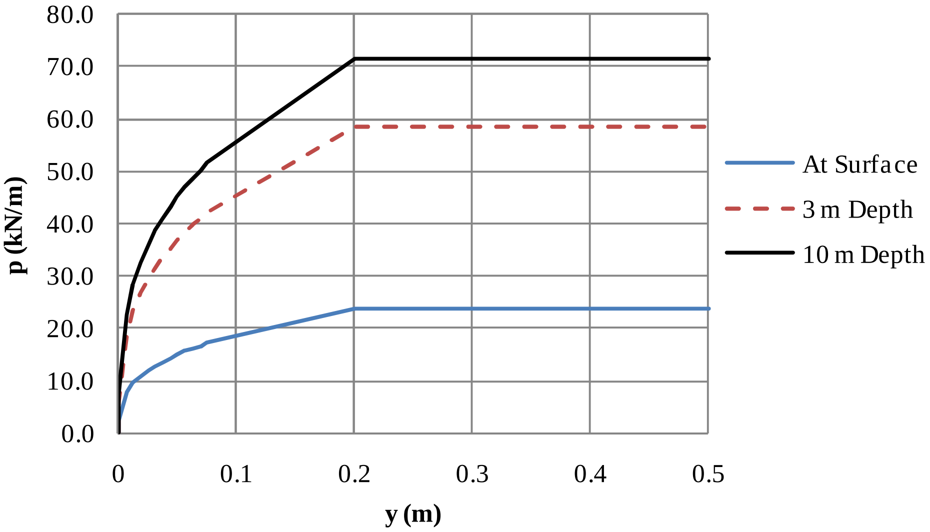

Figure 4.28: p-y Curves Obtained from LPILE

In the third and final LPILE analysis, $p-y$ curves obtained from TeraDysac were furnished to LPILE. To construct $p-y$ curves from TeraDysac output, the beam shear force-time histories and displacement-time histories must be used in conjunction. Because beam nodes are tied into the soil mesh, the equilibrium of each node mandates that the shared forces between the two adjoining beam elements and the soil reaction from the four connecting soil elements must combine to produce no net force. Figure

4.29 illustrates the four soil elements which have a contribution to the soil reaction at a node. Figure 4.30 shows a free-body-diagram of the center node in Figure 4.29.

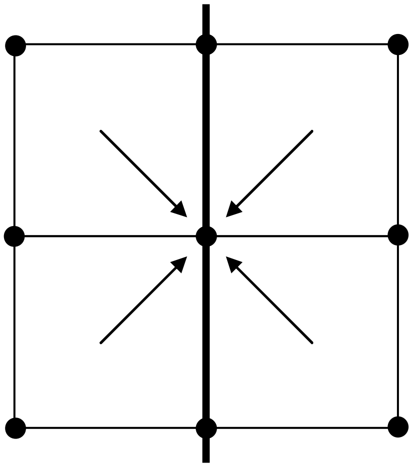

Figure 4.29: Soil Contribution to Nodal Force

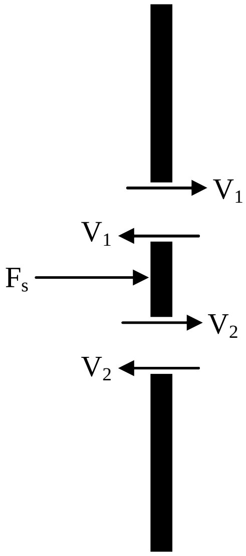

Figure 4.30: Free Body Diagram of the Center Node

If a beam is analyzed alone, the shear forces of the connecting beam elements are of equal magnitude and opposite direction. However, in soil-structure interaction problems, $|V_1| \neq |V_2|$. The difference between the two is the contribution from the soil reaction. This force is denoted by F_s. p, by definition is a force per unit length. p is be found by dividing F_s by the beam element length. y is nodal displacement obtained directly from the displacement-time history. Figure 4.31 shows the $p-y$ curves generated from the TeraDysac analysis.

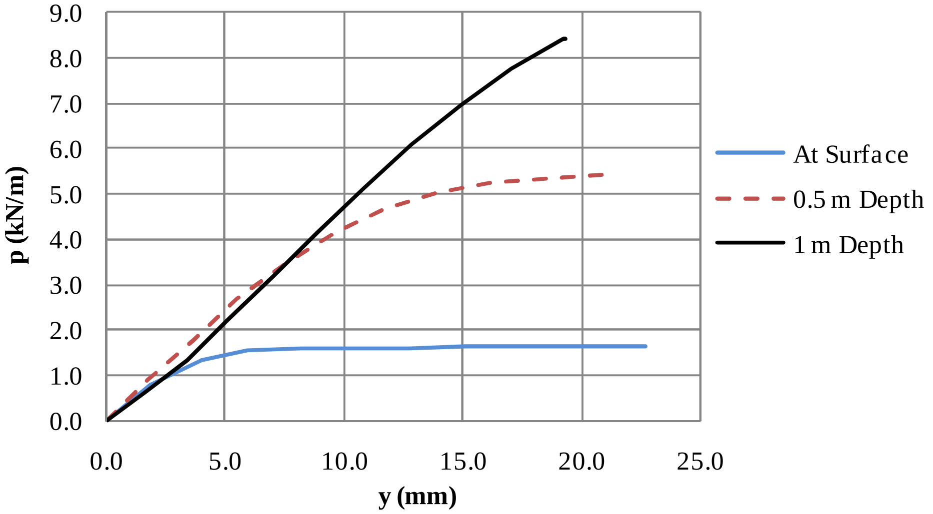

Figure 4.31: p-y Curves Obtained from TeraDysac

Because the $p-y$ curves from LPILE are empirical, there will not be complete agreement with the curves obtained from TeraDysac. Figure 4.32 compares the empirical LPILE $p-y$ curves and the $p-y$ curve obtained from TeraDysac at a depth of 2 m.

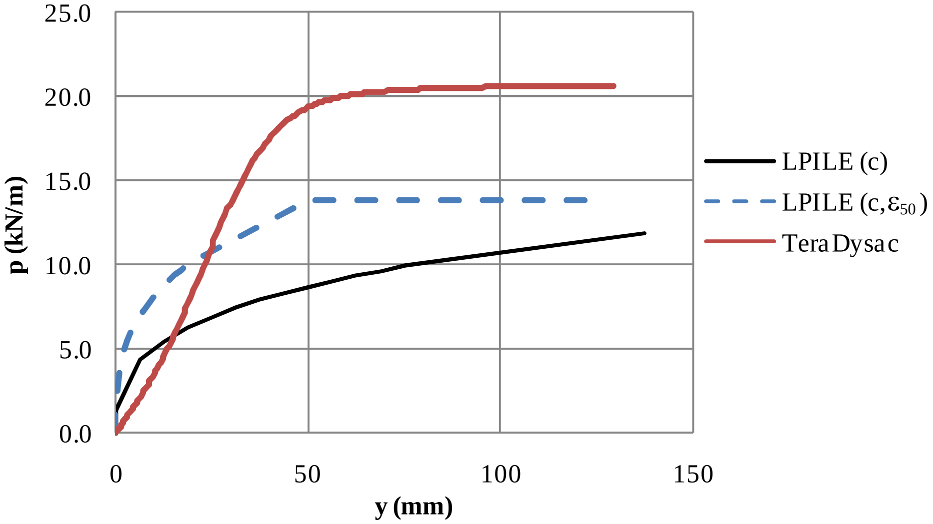

Figure 4.32: p-y Curve Comparison

The black line is the empirical curve using the recommended value of ε_{50} and the accurate value of shear strength (c) obtained from EVALK. The dotted blue line uses both the accurate shear strength and ε_{50} values obtained from EVALK. It is apparent that furnishing accurate c and ε_{50} values to LPILE produces a curve more closely representing the TeraDysac curve. However, both LPILE curves show the soil to be stiffer initially and softer ultimately than what the TeraDysac curve shows.

Figures 4.33-4.36 show the combined results from the soil-pile interaction analysis. The curves are identified in the legend by:

- LPILE – Single: a single value of soil shear strength (obtained at a depth of 10 m) was assumed throughout the depth
- LPILE – Multi: shear strength values at 1 m depth increments were used
- TeraDysac: the results from the TeraDysac analysis
- LPILE $-p-y$: the $p-y$ curves obtained from the TeraDysac analysis were furnished to LPILE

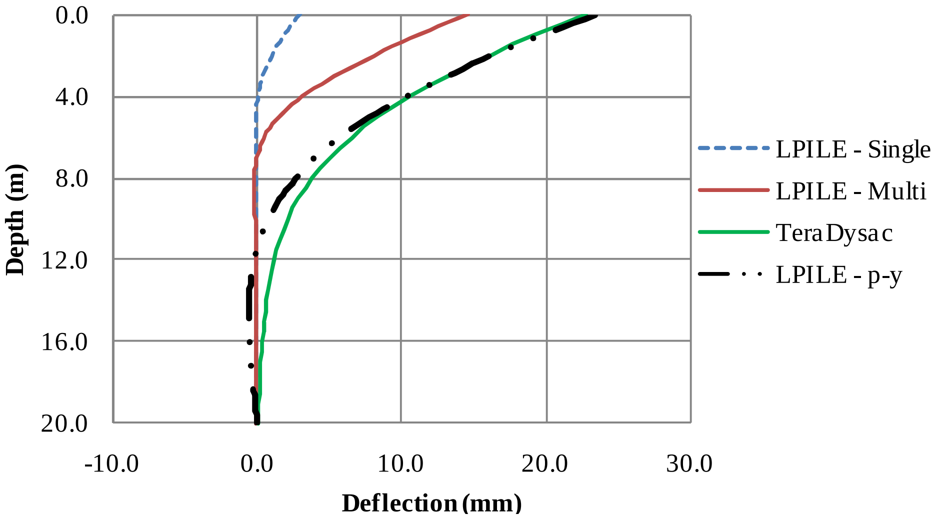

Figure 4.33: Pile Deflection Comparison for Nonlinear SSI Analysis

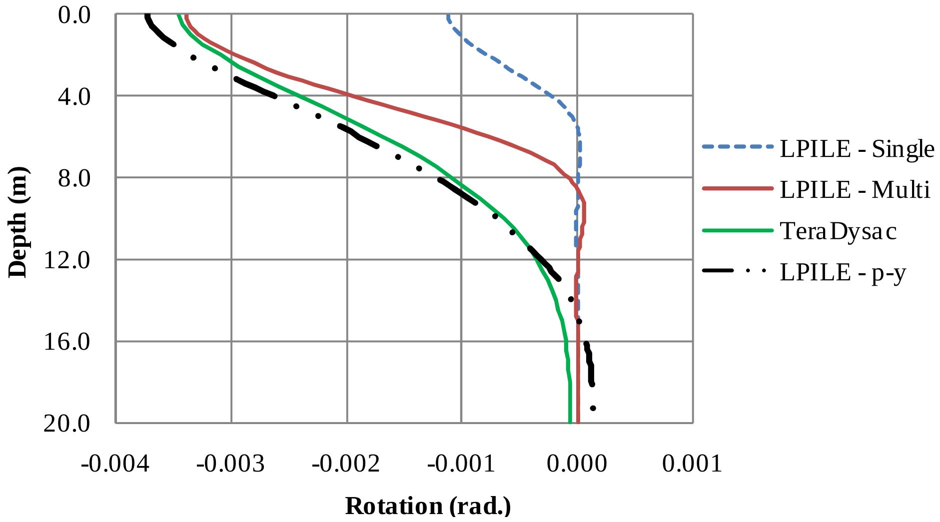

Figure 4.34: Pile Rotation Comparison for Nonlinear SSI Analysis

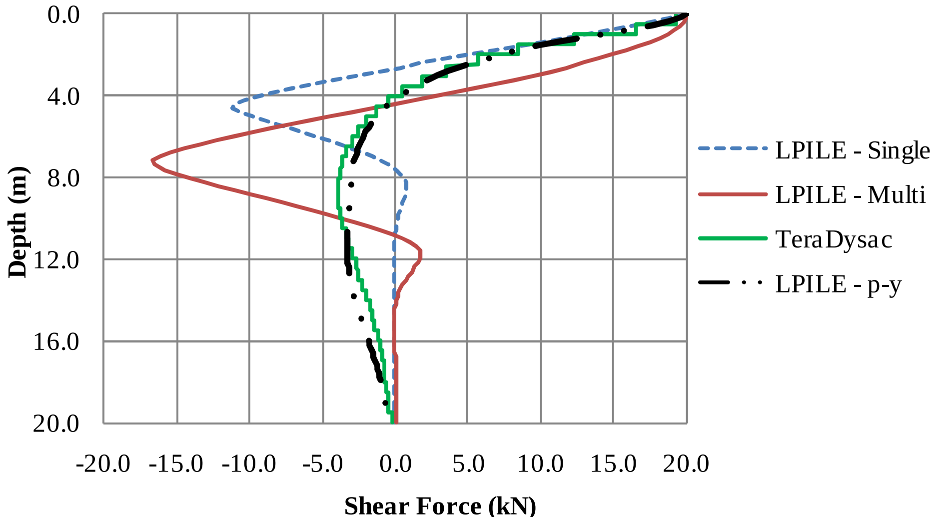

Figure 4.35: Pile Shear Force Comparison for Nonlinear SSI Analysis

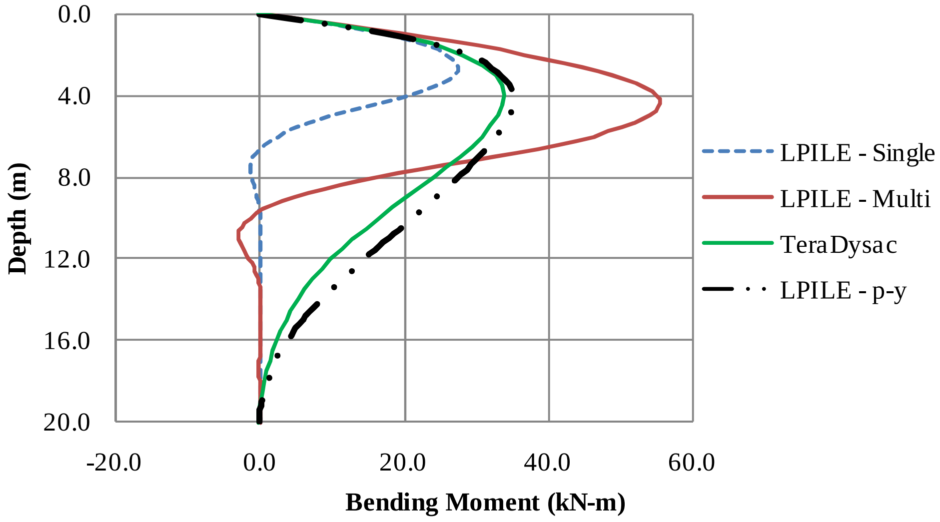

Figure 4.36: Pile Bending Moment Comparison for Nonlinear SSI Analysis

Looking at the first three curves (LPILE – Single, LPILE – Multi, and TeraDysac), it is apparent that there is disparity between the results. Considering the accurate portrayal of shear strength in the LPILE – Multi analysis, results were expected to be closer to that of TeraDysac. The observed differences can be attributed to the LPILE $p-y$ curves. The empirical curves and the bounding surface elastoplasticity models disagree. Note that the bounding surface model parameters were calibrated against laboratory test results (Muraleetharan et al. 1994) and therefore the bounding surface elastoplastic model can be expected to represent the stress-strain response of this soil better. Comparing the last two curves (TeraDysac and LPILE – $p-y$), the results are much more agreeable. Because the bounding surface model was used to obtain the shear strength at various depths and the $p-y$ curves were developed from the TeraDysac analysis, one would expect the results to concur. As this analysis illustrates, the empirical LPILE $p-y$ curves may not be suitable for the analysis of all soft clays. In addition to information on the beam (displacement, rotation, shear force, and bending moment), TeraDysac also provides output on the soil. The pore water pressure contours at the end of the analysis are shown in Figure 4.37. Figure 4.38 is the pore water pressure-time history for the element adjacent to the point of load application.

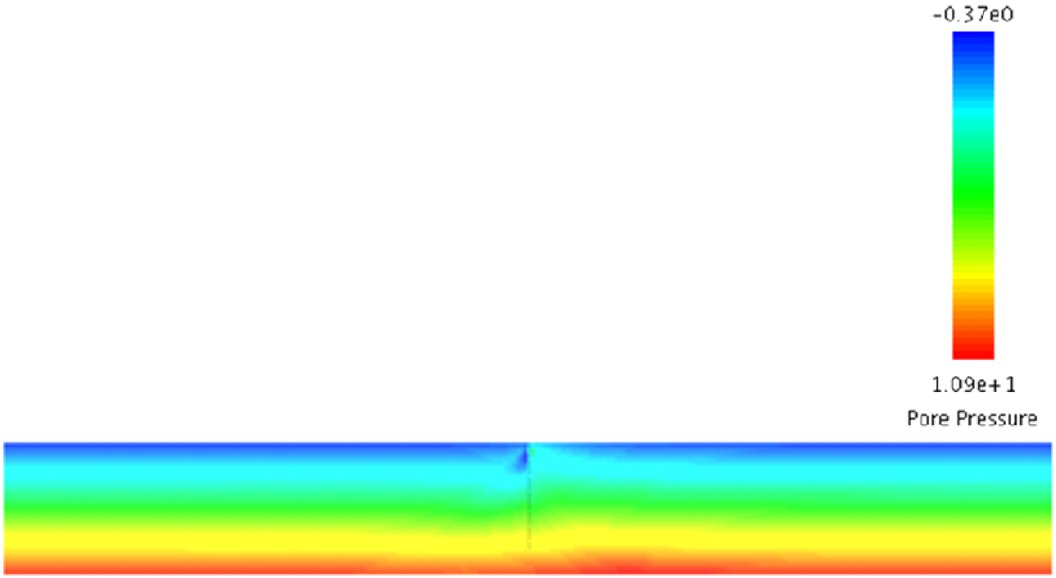

Figure 4.37: Pore Water Pressure Contours (kPa)

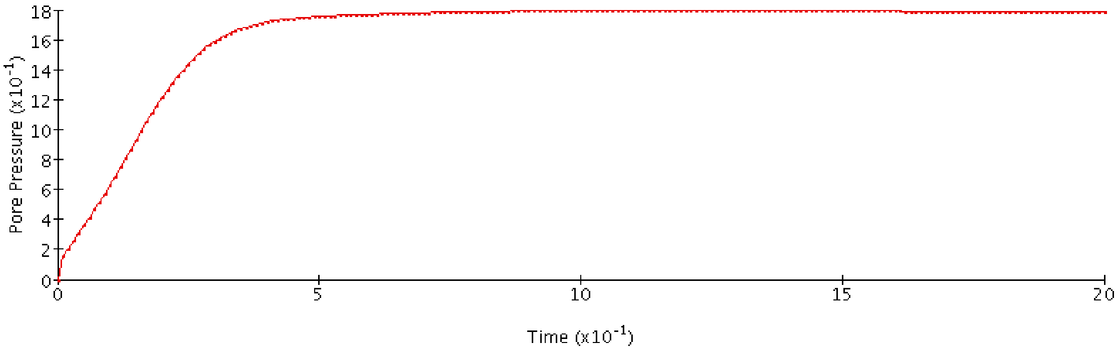

Figure 4.38: Pore Water Pressure-Time History (kPa, s)

Figure 4.37 reveals an accumulation of positive pore water pressure near the pile on the side being compressed. Pore water pressure may not be important for all loading cases, but when analyzing saturated soil, the capability to monitor pore water pressure is a desirable feature. Although the magnitude of the pore pressure shown in Figure 4.38 is small (maximum value of only 1.8 kPa), pore pressures can accumulate during cyclic loading to larger values in clays. The obtained pore pressure is a function of the load duration. In this example, the load was ramped up over 1.0 s and held constant for an additional 2.0 s.

5. Thermal Modeling

The thermal loads for the structural elements are calculated numerically and are discussed in detail in Chapter 3. Several examples illustrating the thermal analysis capabilities in TeraDysac are presented here.

5.1 Linear Temperature Distribution

Instrumentation projects have shown that the temperature varies through the superstructure (e.g. Huang et al. 2004). If no gradient is allowed in the formulation, beam and plate curvature due to temperature can not be captured; all of the thermal-induced deformation will be in the plane of the element local axis (see Figure 5.1). The thermal loading feature implemented in TeraDysac allows a temperature change on the top and bottom of the structure elements with a linear distribution between the two. The difference between the top and bottom temperature changes controls the element curvature. Figures 5.2 and 5.3 illustrate the curvature possibilities. The dotted lines represent the deformed shape due to the thermal effects.

Figure 5.1: Deformed Shape (No Gradient)

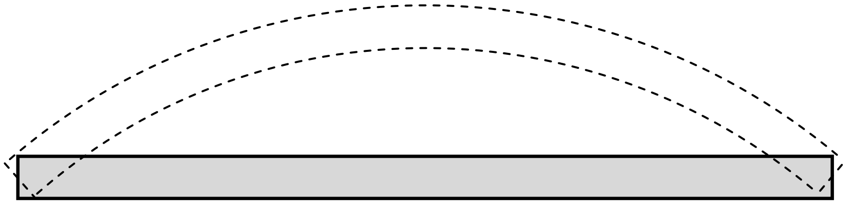

Figure 5.2: Curvature Depiction (Positive Gradient)

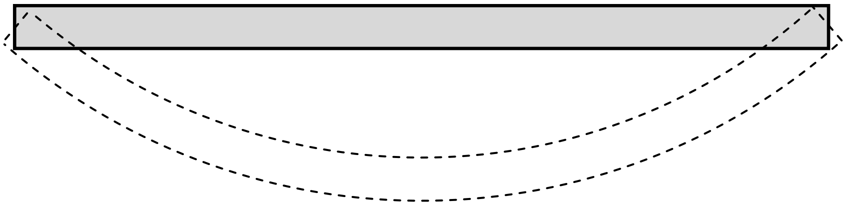

Figure 5.3: Curvature Depiction (Negative Gradient)

For plate elements, thermally induced curvature occurs in two directions (the local x- and y-axes of the element). The following problem is meant to illustrate the capabilities that having a temperature distribution through the element depth will allow. Figures 5.4 shows the finite element setup. The 300 element steel plate is pinned at the corner nodes and subjected to a temperature difference between the top and bottom surface of 10° F ($\Delta T_{top} > \Delta T_{bottom}$).

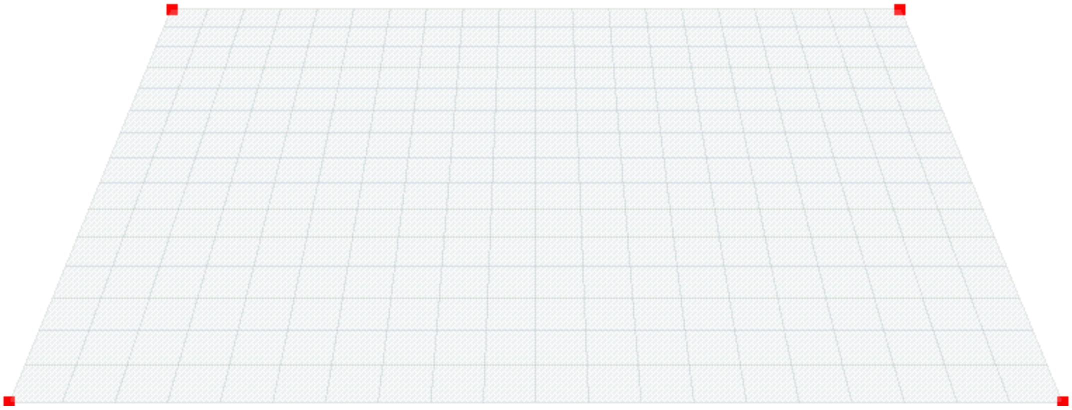

Figure 5.4: Finite Element Mesh for Gradient Analysis

The plate measurements are 2 m x 1.5 m x 20 mm. The other relevant parameters are as follows: E = 200 * 10^6 kPa, ν = 0.3, $\alpha = 6*10^{-6}/°\text{F}$, ρ = 7.85 Mg/m^3. Figure 5.5 shows the deformed shape (displacements magnified by 100).

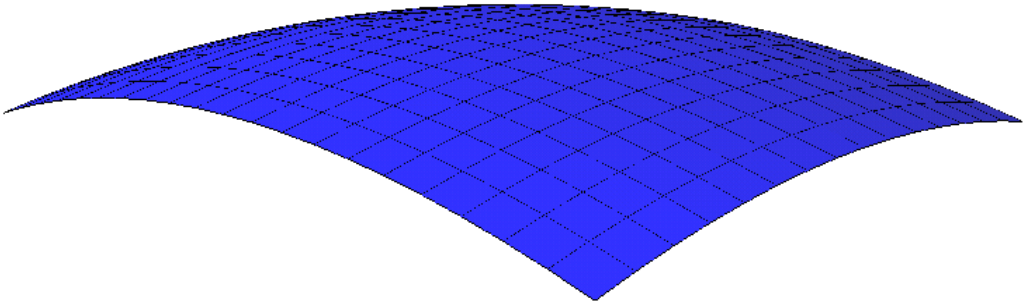

Figure 5.5: Deformed Shape for Gradient Analysis

It is apparent that the plate has taken a dome-like shape with curvature occurring in both the local x- and y-axes. This is exactly what one would expect the deformed shape to look like. As the top fibers of the plate are heated to a higher extent than the bottom fibers, the plate develops curvatures in two directions.

5.2 Skewed Plates Subjected to Thermal Loading

In skewed IAB bridges, instrumental results have shown that the backfill pressure is not uniform behind the abutments (e.g. Sandford and Elgaaly 1993). To study this phenomenon, a series of single element thermal analyses were carried out in TeraDysac. The plate is used to simulate the deck of an IAB. The steel plate parameters are given by: $E = 200 * 10^6$ kPa, $\nu = 0.3$, $\alpha = 6*10^{-6}/°F$, $\rho = 7.85$ Mg/m^3. The plate thickness in all the cases that follow is 30 mm. The four corner nodes are pinned. The global temperature change (uniform through the plate thickness) is 1°F. Only the dimensions in the plane of the element are changing from problem to problem.

Square Plate

Consider a square plate measuring 0.5 m x 0.5 m (see Figure 5.6).

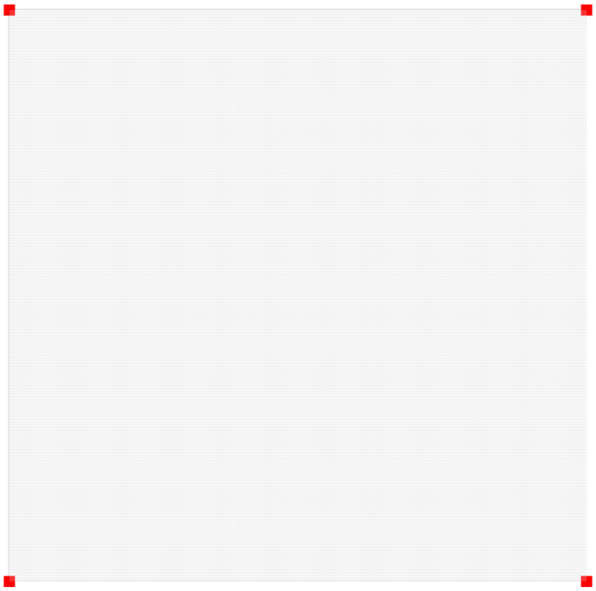

Figure 5.6: Square Test Plate Set-Up

The corner nodes are pinned so forces develop in the plate corners. A depiction of the plate forces is presented in Figure 5.7.

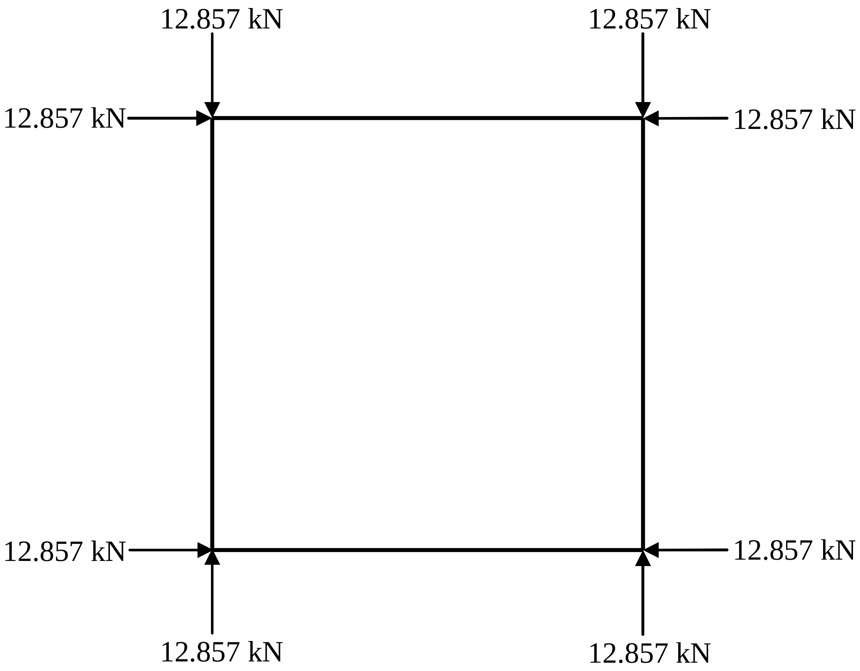

Figure 5.7: Square Plate Corner Forces

The plate geometry and loading are symmetric. The forces developed in the corners are also symmetric as one would expect.

Skewed Plate (Rhombus)

In the first single-element analysis of a skewed plate, the top two nodes from the square plate were each translated 0.1 m to the right (see Figure 5.8). The plate is 0.5 m high, the top and bottom widths are still 0.5 m, but the plate is now skewed.

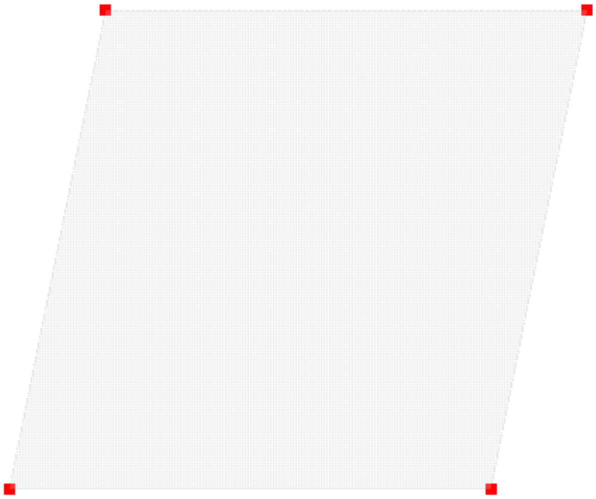

Figure 5.8: Rhombus Plate Set-Up

The plate forces developed in the thermal analysis are shown in Figure 5.9.

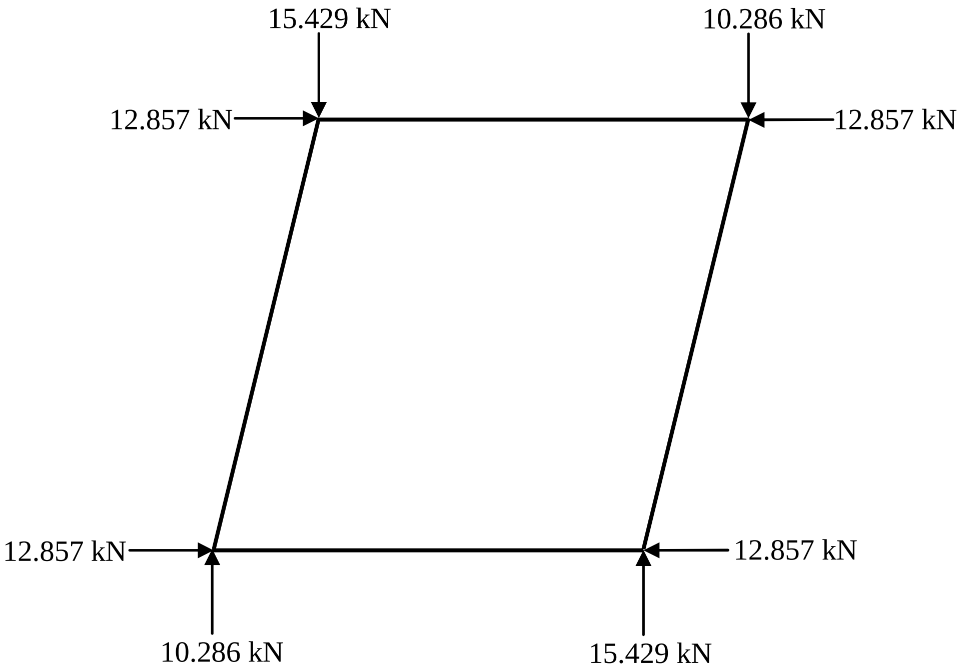

Figure 5.9: Rhombus Plate Corner Forces

The vertical forces in the plate corners are not identical to each other after the skew has been introduced. The element is still in equilibrium (summation of forces in each direction and summation of moments about a point equal zero), but there is an imbalance between the vertical forces on the top and bottom of the plate. The vertical forces developed in obtuse corners are higher than those in the acute corners.

Rectangular Plate

The thermal load vector is calculated numerically at the elemental level (see Chapter 3), so the element layout controls the loading. The element shown in Figure 5.10 is 0.25 m wide and 0.5 m high and has the same boundary conditions, properties, and loading as the previous two examples.

Figure 5.10. Rectangular Plate Set-Up

The plate forces developed in the thermal analysis are shown in Figure 5.11.

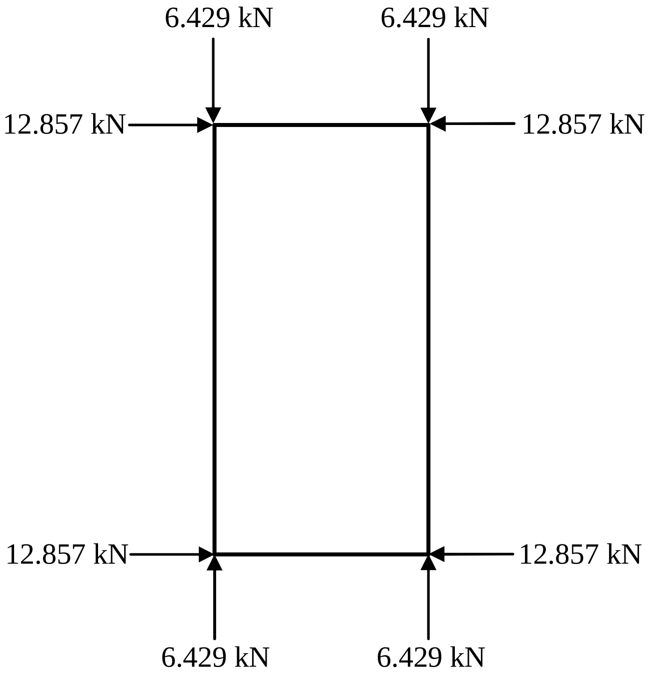

Figure 5.11: Rectangular Plate Corner Forces

If there were no corner restraints, the strain in the plate would be:

$$\epsilon = \alpha\Delta T = 6 * 10^{-6}/°\text{F} * 1°\text{F} = 6\ \mu\epsilon \tag{5.1}$$

and the plate edge deformations would be:

$$\Delta width = \alpha\Delta T * width = 6 * 10^{-6} * 0.25\ \text{m} = 0.0015\ \text{mm} \tag{5.2}$$

and

$$\Delta height = \alpha\Delta T * height = 6 * 10^{-6} * 0.5\ \text{m} = 0.003\ \text{mm} \tag{5.3}$$

Figure 5.12 shows the deformed shape of the rectangular plate if it were free to expand.

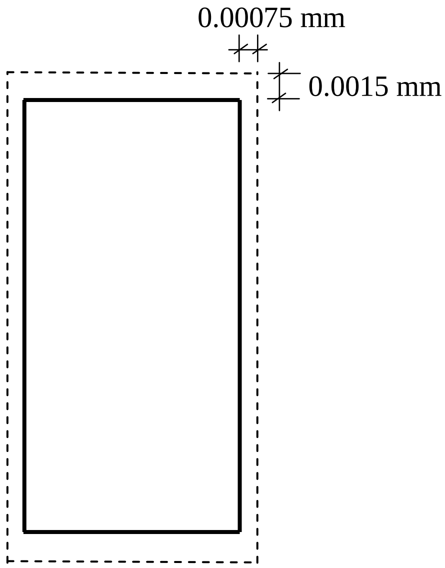

Figure 5.12: Rectangular Plate (Deformed Shape)

It is apparent that the displacement in the horizontal direction is one-half of the displacement in the vertical direction. Looking at the plate dimensions, this makes sense as there is twice as much material length along the vertical axis to expand compared with the horizontal axis. The corner forces (see Figure 5.11) developed when the plate is restrained however show a reversal. The horizontal forces are twice that of the vertical forces. This is because the cross-section in horizontal direction is double the cross-section in the vertical direction. Intuitively, there is twice as much material to create a force in the horizontal direction as there is in the vertical direction; hence, twice the force.

Skewed Plate (Parallelogram)

In the second single-element analysis of a skewed plate, the top two nodes from the rectangular plate were each translated 0.15 m to the right (see Figure 5.13). The plate is 0.5 m high, the top and bottom widths are still 0.25 m, but the plate is now skewed.

Figure 5.13: Parallelogram Plate Set-Up

The plate forces developed in the thermal analysis are shown in Figure 5.14. The vertical forces in the plate corners are again unequal with higher force in the obtuse corners.

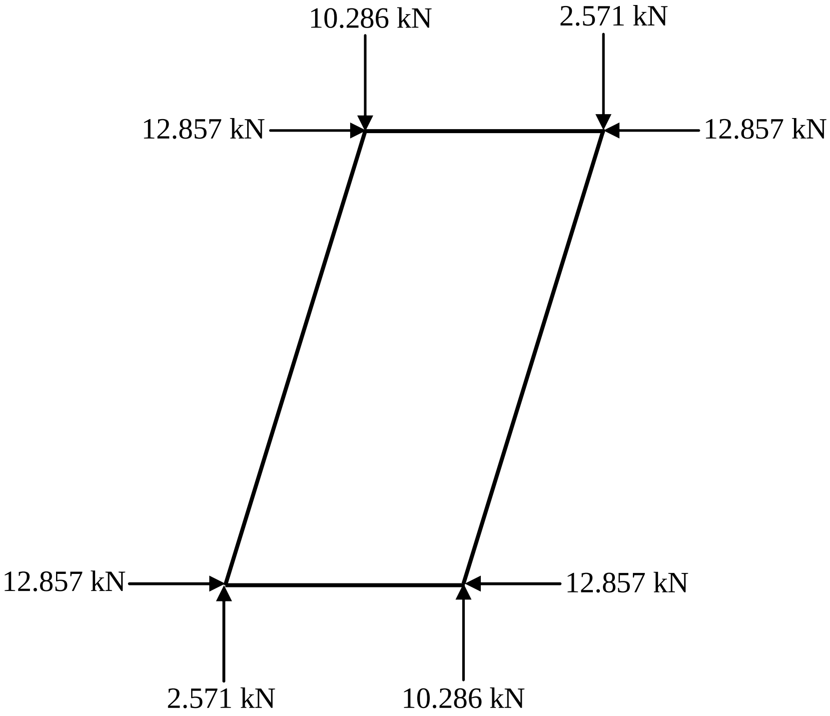

Figure 5.14: Parallelogram Plate Corner Forces

The parallelogram plate was analyzed because its shape is similar to a skewed IAB deck. Figure 5.15 depicts an idealization of a skewed IAB deck with corner forces highlighted based on the results of the parallelogram plate analysis. The results of the single element analyses are in agreement with published reports of the higher stresses in the obtuse corners. For example, the monitoring study conducted by Sandford and Elgaaly (1993) on an IAB with a skew angle of 20° showed backfill pressures behind the obtuse corners to be nearly three times the pressures in the acute corners when the bridge was experiencing maximum expansion.

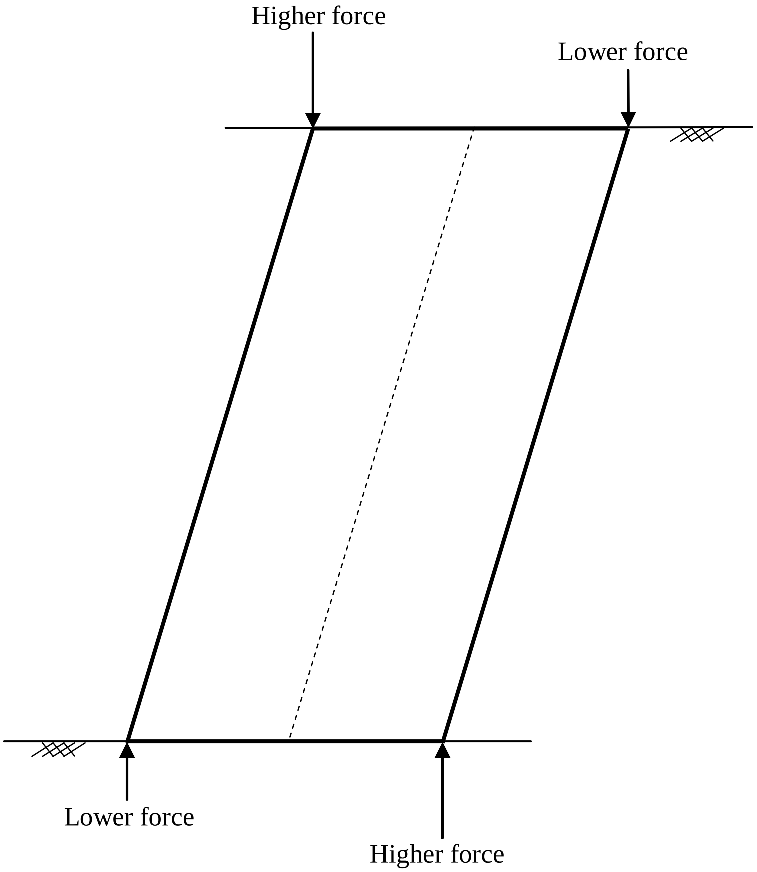

Figure 5.15: Skewed IAB Deck Idealization Highlighting Corner Forces

Mechanics of Skewed Plate Loading

A skewed bridge deck mainly carries load between the obtuse corners, i.e. the shortest path between supports (Hartmann and Katz 2004). The single element in-plane thermal tests agree with this. The forces developed in the obtuse plate corners were higher than those in the acute corners. In attempting to visualize why this force imbalance emerges in skewed plates, a sketch is helpful. Figure 5.16 shows a skewed bridge deck with idealized beams connecting the obtuse corners and the acute corners.

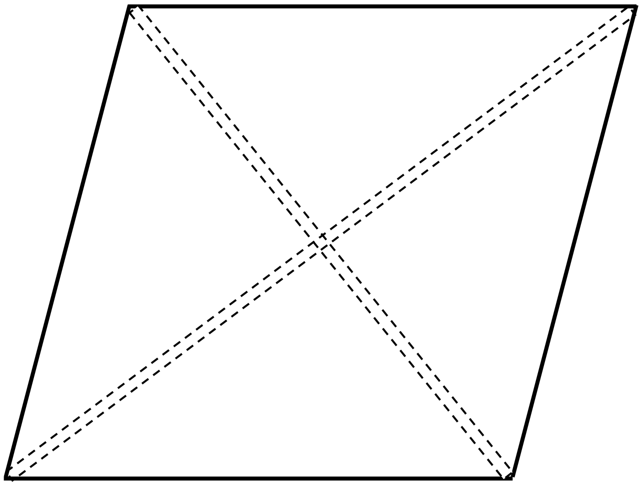

Figure 5.16: Skewed Plate with Corner Connections

It is apparent that the distance between the obtuse corners is less than the distance between the acute corners. Figure 5.17 shows the two beams each subjected to the same axial load, P.

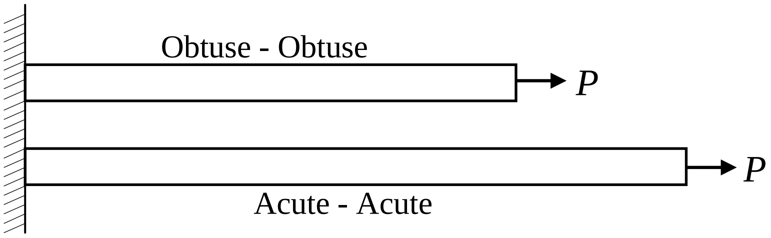

Figure 5.17: Corner-Connecting Beams

The beam connecting the acute corners (Acute-Acute) is longer than the beam connecting the obtuse corners (Obtuse-Obtuse). Assuming each beam has the same cross section (A) and Young's modulus (E), the elongation of each beam is given by:

$$\delta = \frac{PL}{EA} \tag{5.4}$$

Note the beam length (L) is in the numerator of Equation 5.4. So for equivalent point loads, the elongation of the Acute-Acute beam is greater than the elongation of the Obtuse-Obtuse beam. Relative to the beam connecting the acute corners, the beam connecting the obtuse corners is stiffer and will subsequently carry more load. This manifests as higher support reactions in the obtuse corners than in the acute corners of skewed bridge decks.

5.3 Assemblies of Elements

Using the technology available in the TeraDysac mesher, element blocks can be assembled together. For example, beams can be assembled together with a plate. Figure 5.18 shows a 10 x 10 element mesh of a square plate measuring 1 m x 1 m. Figure 5.19 is a 10 element mesh of a 1 m beam.

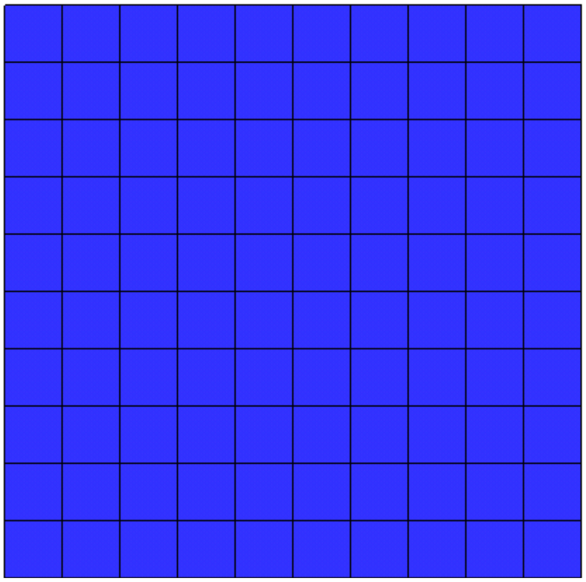

Figure 5.18: 100 Element Plate for Mesh Assembly

Figure 5.19: 10 Element Beam for Mesh Assembly

In the mesher, there is an option to merge out nodes from different element blocks that exist within a user-supplied equivalence tolerance (usually a small number, ~10^{-6}). In the plate, there are 11 nodes in each direction. The beam element also has 11 nodes at a spacing equivalent to the plate mesh. Therefore, any beam lined up vertically with the plate and at any position horizontally incremented by 0.1 m from the left edge of the plate will have 11 equivalence nodes. An assembly of the plate and five beams is shown in Figure 5.20.

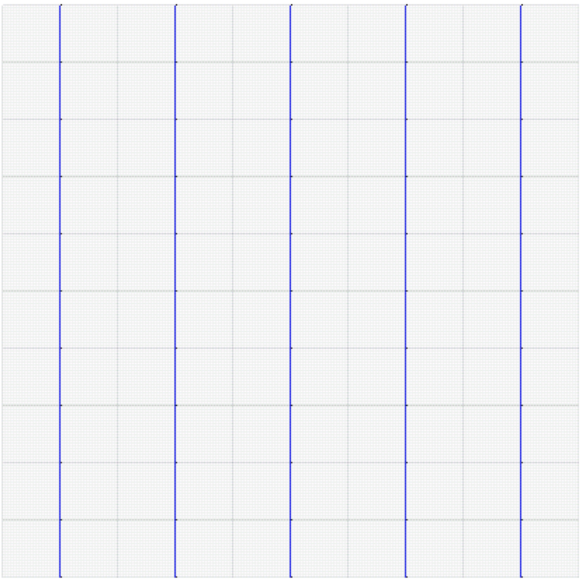

Figure 5.20: Beam and Plate Mesh Assembly

The mesher outputs the results from any node set equivalence. In the example described, there are 55 equivalence nodes (5 beams with 11 each). After the successful meshing, the beams are tied into the plate. Mesh assemblies are key to setting up the bridge models used in this work.

The thermal loading is applied by element block in TeraDysac. When thermal loads are applied to assemblies of structural elements, there is interaction between the two element blocks. A few thermal analyses of the plate-beam assembly illustrate this interaction effect. Both element blocks are steel: E = 200 * 10^6 kPa, ν = 0.3, $\alpha = 6*10^{-6}/°\text{F}$, ρ = 7.85 Mg/m^3. The beams are 0.1 m wide and both the beams and the plate are 0.1 m thick. The temperature loading for the following three cases is a uniform temperature increase of 10° F. To illustrate the interaction between the element blocks, three analyses were carried out. In the first analysis, the entire assembly is heated. In the second analysis, only the plate is heated and in the final analysis, only the beams are heated. The deformed shapes are shown in Figures 5.21-5.23. The magnification factor in all three figures is 1500.

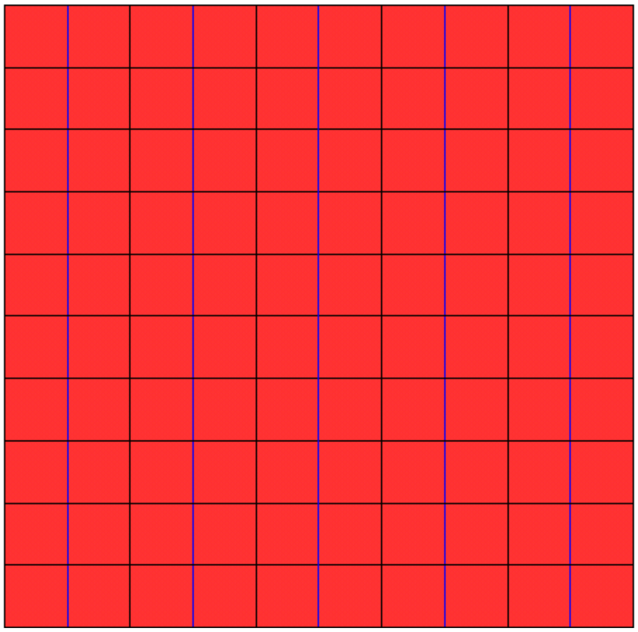

Figure 5.21: Deformed Shape (Both Element Blocks Heated)

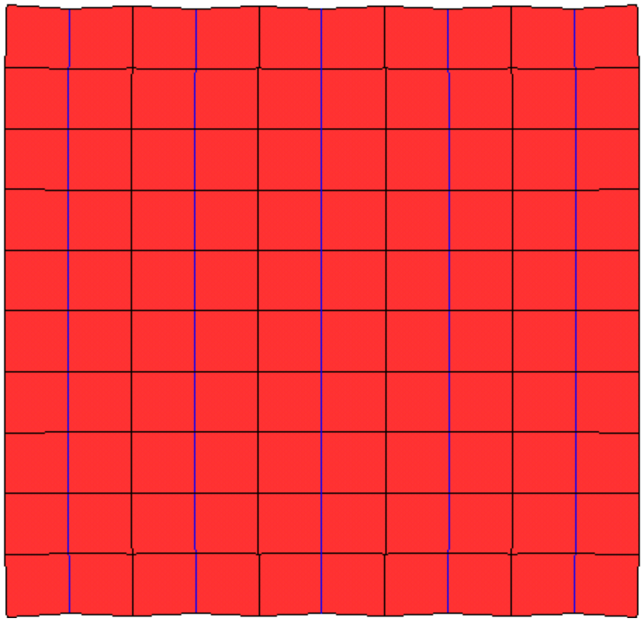

Figure 5.22: Deformed Shape (Plate Element Block Heated Only)

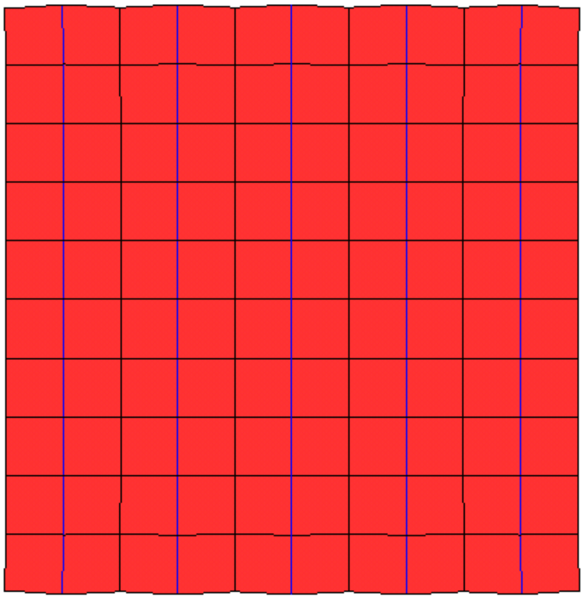

Figure 5.23: Deformed Shape (Beam Element Block Heated Only)

It is apparent that when both element blocks are heated together, the uniform expansion across the beams and plate does not lead to any contortion in the deformed shape (see Figure 5.21). The nodal displacement-histories for the beam ends are identical to those of the plate edges. No forces or moments develop in either element block. The second analysis heats only the plate. The beams restrain the plate expansion as depicted in Figure 5.22. The reverse is true when only the beams are heated (see Figure 5.23). This element block interaction is important in regions like the bridge deck where three sections (deck, girders, and pier caps) are all tied together and being thermally loaded.

6. TeraGrande Modeling

6.1 General

The structural elements implemented in TeraDysac are low order linear elastic elements. To validate the use of these elements, several thorough analyses of the superstructure were performed using the finite element application TeraGrande (ANATECH 2005). The program considers all the material nonlinearity applicable to reinforced concrete modeling. In addition to stress and deformation outputs, concrete cracking can be monitored. The purpose of this section of the dissertation is to illustrate that although cracking does occur during the thermal loading cycles, the cracking is only minimal and therefore linear elements are acceptable for IAB analysis in TeraDysac. The instrumented Minnesota bridge is used as an example. The TeraGrande User's Manual (ANATECH 2005) should be consulted for a full description of the features available in and theory behind the TeraGrande computer program. A cursory explanation of the pertinent details to this work is presented in the following five sections.

6.1.1 Explicit Dynamics

This work uses the explicit dynamics procedure for all analyses. The equations of motion of a body are integrated through time using an explicit central difference integration rule given by the following:

$$\ddot{u}_i = P_i - I_i \tag{6.1}$$

$$\dot{u}_{i+\frac{1}{2}} = \dot{u}_{i-\frac{1}{2}} + \frac{(\Delta t_i + \Delta t_{i+1})}{2}\ddot{u}_i \tag{6.2}$$

$$u_{i+1} = u_i + \Delta t \dot{u}_{i+\frac{1}{2}} \tag{6.3}$$

where u_i are the nodal displacements at time increment i, $\dot{u}_{i+\frac{1}{2}}$ are the nodal mean velocities at the mid-increment, $\ddot{u}_i$ are the nodal accelerations at time increment i, P_i are the external applied loads, and I_i are the internal forces (due to stresses) at time increment i. The time increment, Δt_i, changes as the body deforms and is governed by the damped Courant stability limit of the mesh given by:

$$\Delta t_{cr} \leq \frac{2}{\omega_{max}}\left(\sqrt{1+\xi^2}-\xi\right) \tag{6.4}$$

where ω_{max} is the highest natural frequency of the mesh and ξ is the fraction of critical damping in the highest mode. The time steps in the various analysis runs in this work were quite small. Analysis times of 0.5 seconds (or thereabouts) required hundreds of thousands of time steps.

6.1.2 ANATECH Concrete Model

The smeared-crack finite element technology used in the model was developed by the founder of ANATECH Corp., Dr. Y.R. Rashid (Rashid 1968). The compressive strength of concrete (f_c') is the only input required from the user for the concrete constitutive model. All other model parameters are obtained using correlations to f_c'. This nonlinear model has been shown to accurately predict laboratory tests of reinforced concrete bridge components, capturing cracking, plasticity, and hysteresis among other phenomena (Dunham et al. 1991, Dameron and Dunham 1992). For f_c' = 40.68 * 10^3 kPa (5900 psi), the generated curves representing the concrete constitutive behavior are given Figures 6.1 and 6.2. This is the value of compressive strength at the time of prestress transfer for the example that follows.

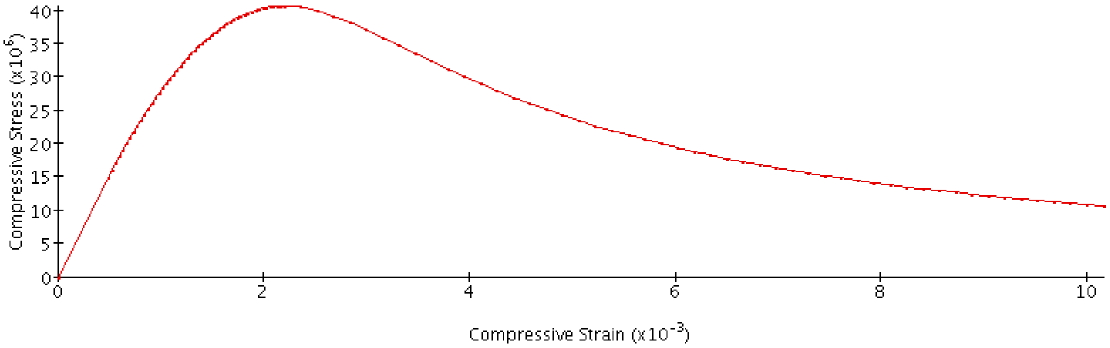

Figure 6.1: Compressive Stress-Strain Curve (Pa)

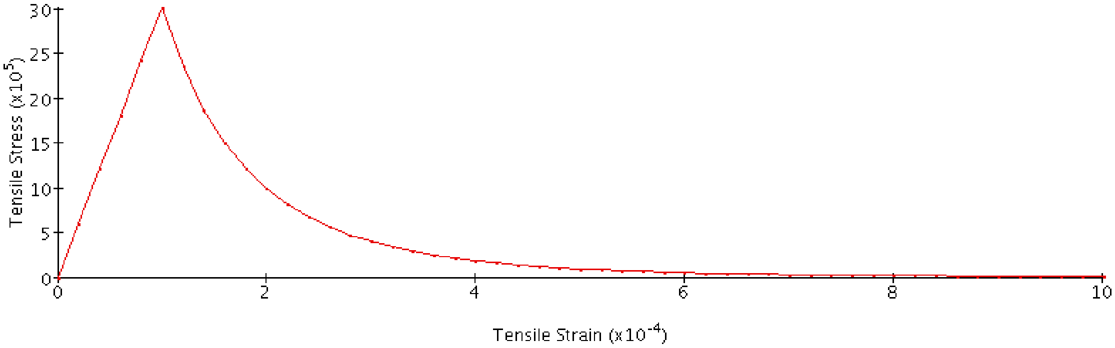

Figure 6.2: Tensile Stress-Strain Curve (Pa)

6.1.3 Concrete Cracking

The Young's modulus for the concrete is computed in the TeraGrande input file, although a user-furnished Young's modulus option is available. The value of Young's modulus for the concrete is computed using Equation 6.5 in accordance with ACI 318-02.

$$E = 57000\sqrt{f_c'} \tag{6.5}$$

where the units of f_c' and E are psi.

The girder concrete compressive strength was given in the bridge plans (f_c' = 5900 psi). Therefore,

$$E = 57000\sqrt{5900} = 4.378 * 10^6 \text{ psi} = 30.19 * 10^6 \text{ kPa}$$

The tensile cracking strain is specified in the input file as 10^{-4}. The tensile cracking stress is determined using Young's modulus (see Figure 6.3).

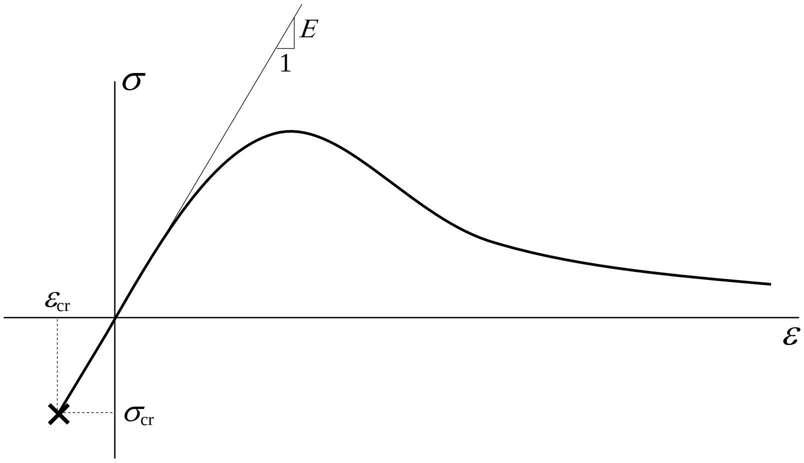

Figure 6.3: Concrete Stress-Strain Diagram

The initial slope of the concrete stress-strain curve is Young's modulus. The cracking stress occurs at the specified tensile cracking strain following the slope of the curve. The concrete cracking stress is given by:

$$\sigma_{cr} = E\epsilon_{cr} = 30.19 * 10^6 \text{ kPa} * 10^{-4} = 3.019 * 10^3 \text{ kPa}$$

This value of cracking stress agrees with the figure furnished by TeraGrande (Figure 6.2). The tensile strength of the concrete quickly diminishes after the cracking stress is reached. Cracking behavior is treated at the element integration stations using the smeared crack model. Cracks are assumed to form perpendicular to the directions of largest tensile strains which exceed the cracking strain. The crack direction remains fixed although the crack can close, resist compression, and re-open under load reversal (ANATECH 2005).

6.1.4 Reinforcement Modeling

TeraGrande allows the user to model individual rebar strands. Uniaxial rebar strands (2D line elements) pierce the concrete elements (3D hexagonal 8-node bricks). Figure 6.4 shows the finite element mesh of one of the bridge girders.

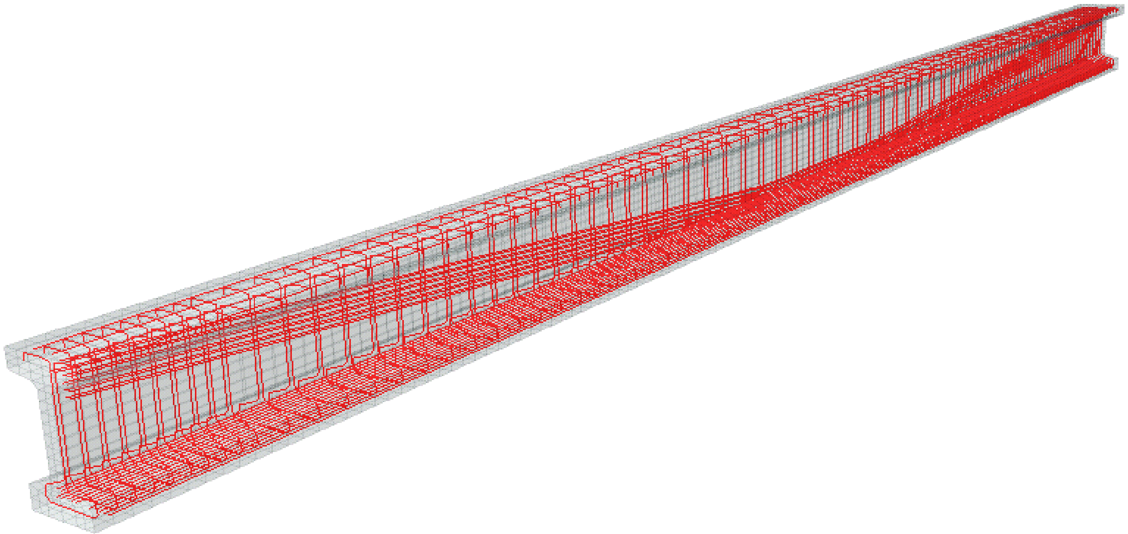

Figure 6.4: Bridge Girder Mesh

Figure 6.4 illustrates that the rebar can be accurately modeled in TeraGrande. The stirrups, prestressed rebar strands, and longitudinal reinforcement (no prestress) are all shown in the beam.

6.1.5 Tied Contact

The bridge model is built by connecting 3D mesh instances. An instance is an individual component of the bridge (i.e. a girder or a bent cap). When rebar is connecting instances (i.e. the girder connection to the deck), tied contact is used between the instances. A simple example of tied contact is shown in Figure 6.5. Three instances (two flat blocks and a bar) are connected using tied contact. The red nodes are shared nodes between instances. When the problem gets meshed, a set of shared node sets on each side of the bar is merged out and three mesh instances become one mesh assembly.

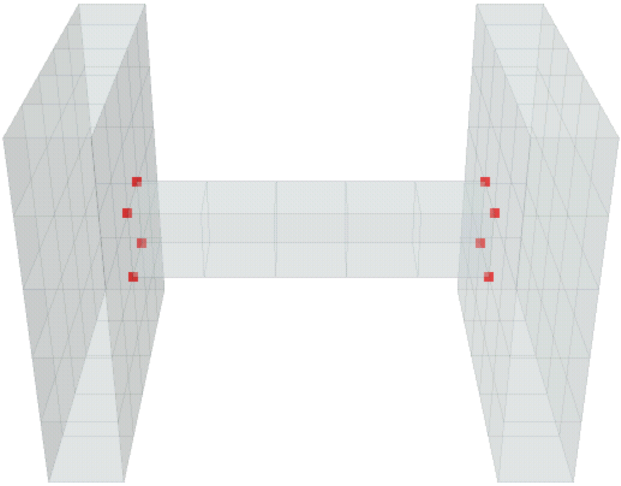

Figure 6.5: Tied Contact Between Mesh Instances

6.2 Prestressed Girder Modeling

To show the accuracy that a reinforced concrete analysis in TeraGrande yields, the analysis of a prestressed girder from the bridge model is presented here. Figure 6.6 shows the tendons subjected to prestressing. The draped strands are located in the girder web.

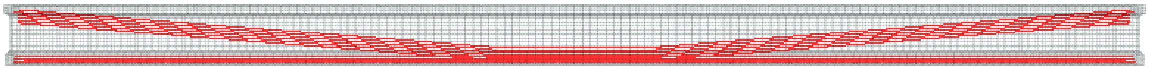

Figure 6.6: Prestressed Tendons in Bridge Girder

A set of plans was available from the IAB project. In addition to the design details (rebar layout, section geometry, etc), the plans provided design strengths, prestress loading magnitude, and camber information. The compressive strength at the time of the transfer of prestress (f_c') was 40.68 * 10^3 kPa. 12.7 mm steel plates were merged on to the girder ends (see Figure 6.7). The plates help support elements near the girder ends as the prestress load develops.

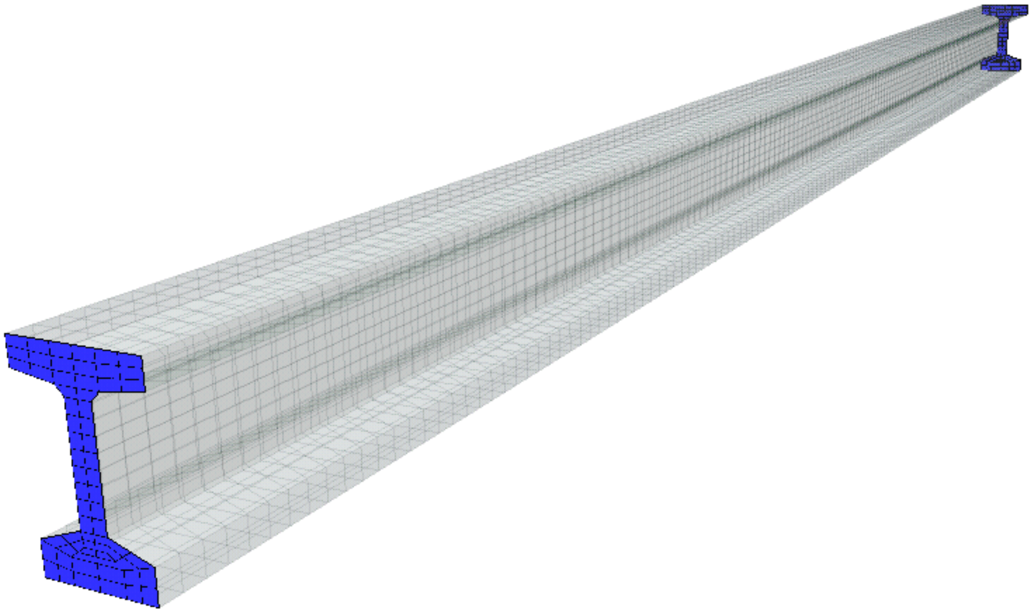

Figure 6.7: Girder End Caps

An explicit dynamics analysis was performed on the girder with two procedures. The prestress was added to mesh followed by the self-weight of the girder. The loading scheme is presented in Figure 6.8.

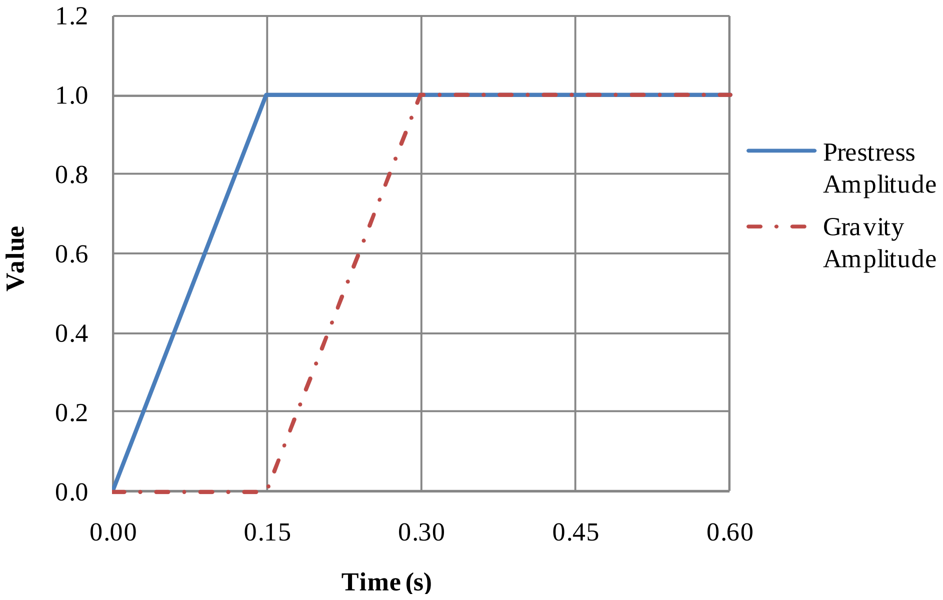

Figure 6.8: Loading Amplitudes for Girder Analysis

The y-axis value in Figure 6.8 is a portion of the loading magnitude. Therefore, when the value is 0.0 there is no load and when it is 1.0, the load is applied fully. It is apparent that the loads are each ramped up over 0.15 seconds. The first procedure (prestressing) lasts for 0.15 s. Immediately after the prestress amplitude reaches its full value, this procedure ends and the gravity procedure begins. TeraGrande allows procedures to import mechanical states from other procedures. So at 0.15 s, the gravity loading begins with the full prestress load already developed in the girder. The gravity ramps up and reaches its full value at 0.3 s. The loads are then held at their full values for another 0.3 s. Figure 6.9 shows the node sets pertinent to the analysis. The boundary nodes on the left are fixed in both the vertical and longitudinal direction of the girder and the nodes on the right are fixed in the vertical direction only. The middle node shown is at the girder midspan on the top of the girder. A nodal displacement-time history was written for this node.

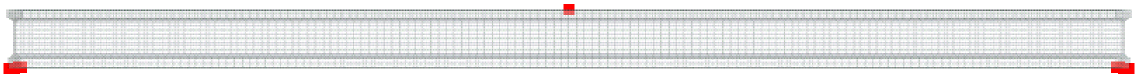

Figure 6.9: Important Node Sets for Girder Analysis

The cracking pattern was tracked during the analysis. Figures 6.10 and 6.11 show the cracked girder at 0.15 s and 0.6 s, respectively. A red marking indicates there is an open tension crack. A blue marking indicates that a once open tension crack is now closed in compression. The displacement is magnified by a factor of 5.

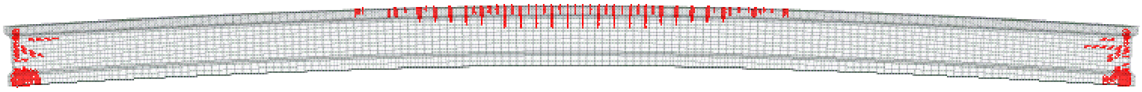

Figure 6.10: Crack Pattern at 0.15 s

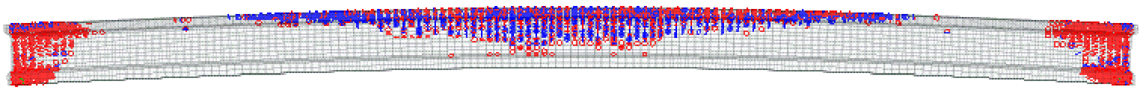

Figure 6.11: Crack Pattern at 0.6 s

It is apparent that there is significant cracking near the beam ends. Focusing on the cracking away from the beam ends, the crack pattern agrees with intuition. There are open tension cracks at the end of the prestressing. The gravity loading subsequently closes most of these cracks, as indicated by the blue markings. Although the cracking pattern looks ominous, it is important to realize that the red makers simply mean the cracking strain has been reached in the concrete. As over a 5200 kN (1.1 million lbs.) of prestress force and 215 kN (24.2 tons) of self-weight are transferred to the beam, cracking is expected. An important check on the validity of the results is found with a nodal displacement-time history. A nodal displacement history of a node at the top-center of the beam at midspan reveals information about the beam deflection and residual camber. According to the bridge plans, the residual camber in the beam is about 6 cm. Figure 6.12 shows the displacement-time history.

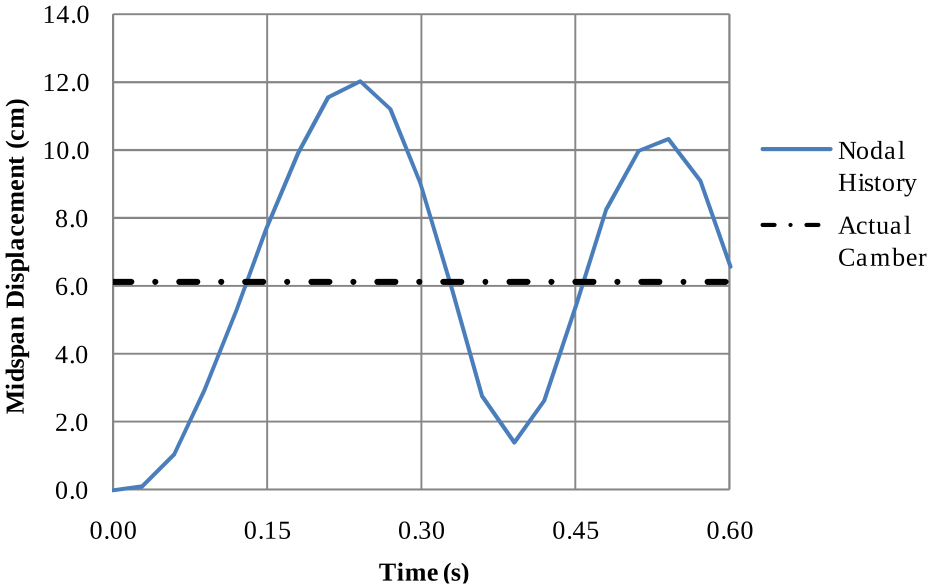

Figure 6.12: Midspan Displacement-Time History from Girder Analysis

Although there is still some oscillation left to occur in the girder, it is apparent that the midspan deflection is converging to the residual camber specified by the bridge plans. This analysis is an excellent check on the reinforced concrete analysis in TeraGrande. Considering the mesh size (9216 concrete elements, 9820 rebar elements), the model complexity, and the load magnitude, it is a very encouraging result to have the nodal displacement so close to the actual camber observed in the field.

6.3 Superstructure Model

A full 3D model of the Minnesota bridge was created in TeraGrande (see Figure 6.13). However, the model was reduced to only the superstructure (girders and deck) for several reasons. Mainly, the analysis was designed to only study the superstructure response to abutment movements. As the girder ends sit on elastomeric bearing pads, abutment movement does not elicit any appreciable response in the piers and pier piles.

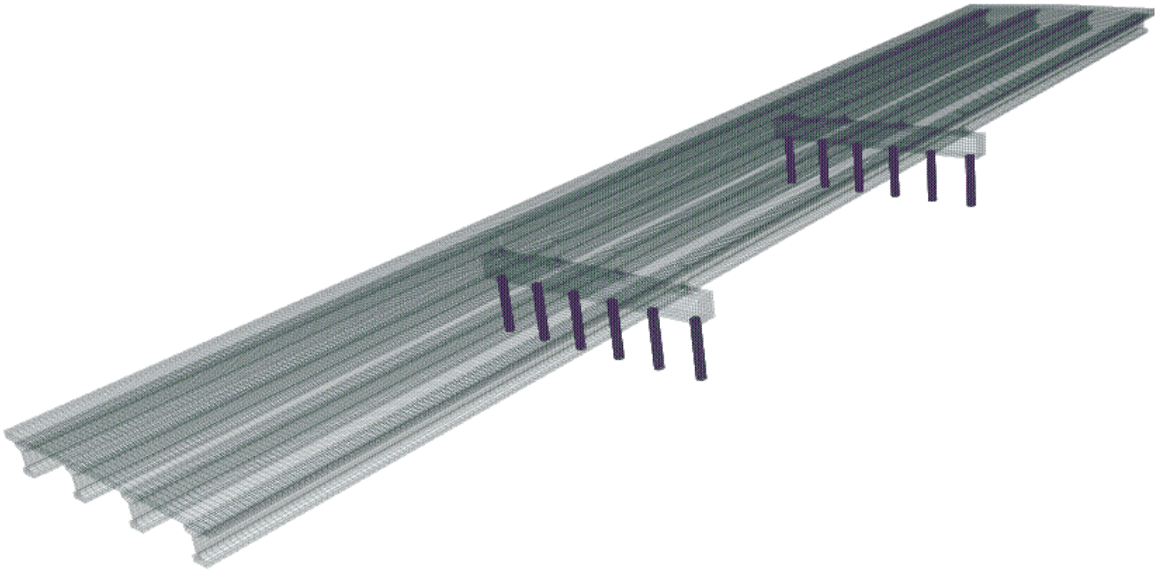

Figure 6.13: Minnesota IAB Model (Piers and Pier Piles Included)

Also, some of the elements in the pier piles above grade had very poor aspect ratios. Figure 6.14 shows a 2D view of the cross section. The red element block is steel and the blue element block is concrete. The thin steel casing around the piles and the piles themselves are quite thin (~10 mm). To make reasonable element aspect ratios for these elements would make the model size grow significantly.

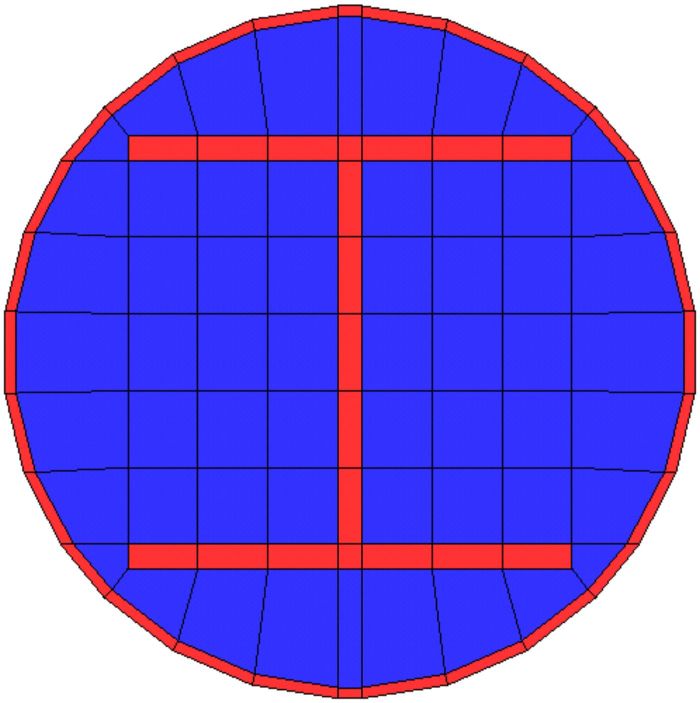

Figure 6.14: Pier Piles (Above Grade) Mesh

Removing the pier caps and the pier piles above grade resulted in a superstructure model with 366,272 elements. The element count includes 193,908 uniaxial rebar elements (see Figure 6.15).

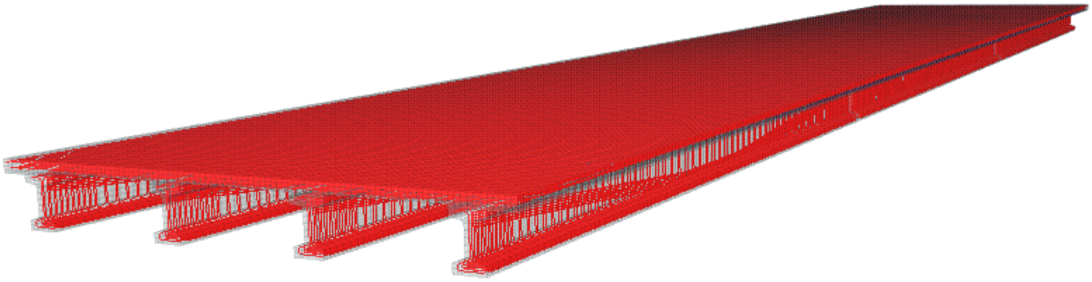

Figure 6.15: Minnesota IAB Superstructure Model (Rebar Shown)

The important regions for boundary condition application in the superstructure model include the locations of the bearing pads and the abutments in the field. A node set is created at the girder ends on the superstructure interior (see Figure 6.16). These nodes are fixed in the vertical direction only to simulate resting on bearing pads. Translation in the longitudinal direction of the bridge is allowed.

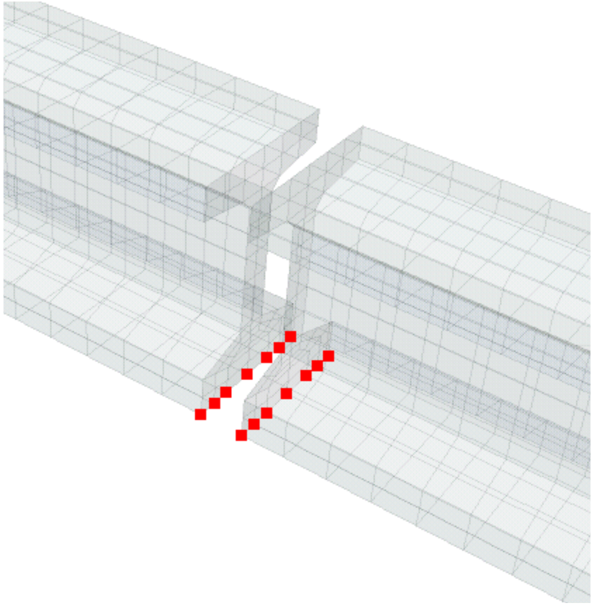

Figure 6.16: Superstructure Interior Nodes

The girder ends and deck are cast integrally into the bridge abutments. Because of the rigidity in this region, the abutment boundary conditions can be applied directly to the ends of the superstructure model. A portion of the superstructure end node set is shown in Figure 6.17.

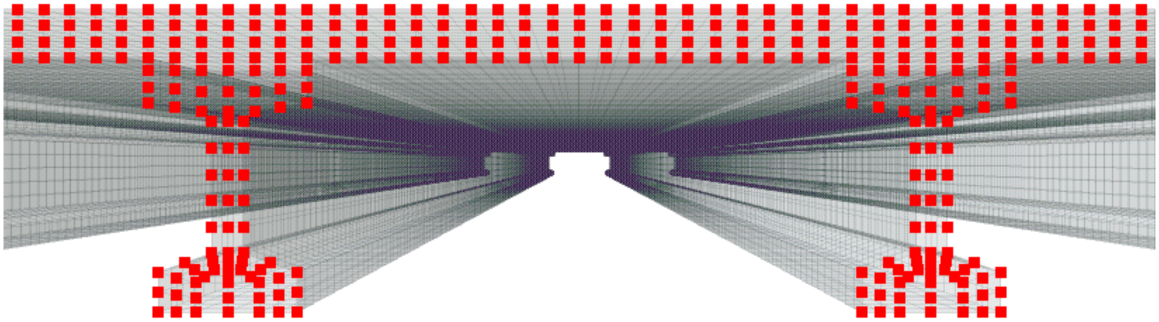

Figure 6.17: Superstructure End Node Set

The ultimate goal of the TeraGrande modeling in this work is to show that significant nonlinear behavior (e.g. concrete cracking) is not occurring during the thermal loading of the IAB. This section is meant to show that the linear structural elements developed for TeraDysac are acceptable for the thermal analysis of IABs.

6.4 Thermal Analysis

Because the abutment movements due to the thermal loading are known from the instrumentation, a thermal analysis does not need to be performed on the superstructure. Instead the measured abutment displacements can be applied directly to the node sets on the ends of the superstructure.

6.4.1 Temperature Increase

A 10° F increase in the bridge temperature induced abutment translations of 2 mm at each abutment. This displacement was applied to each superstructure end to simulate the thermal event used for the TeraDysac validation. These histories were applied to a pristine bridge model. A model with no cracks or residual stress is used so that the observed stress, strain, cracks, etc are all due to the loading in question. Figures 6.18 and 6.19 show the crack pattern in the bridge deck and the bridge girders at the end of the loading.

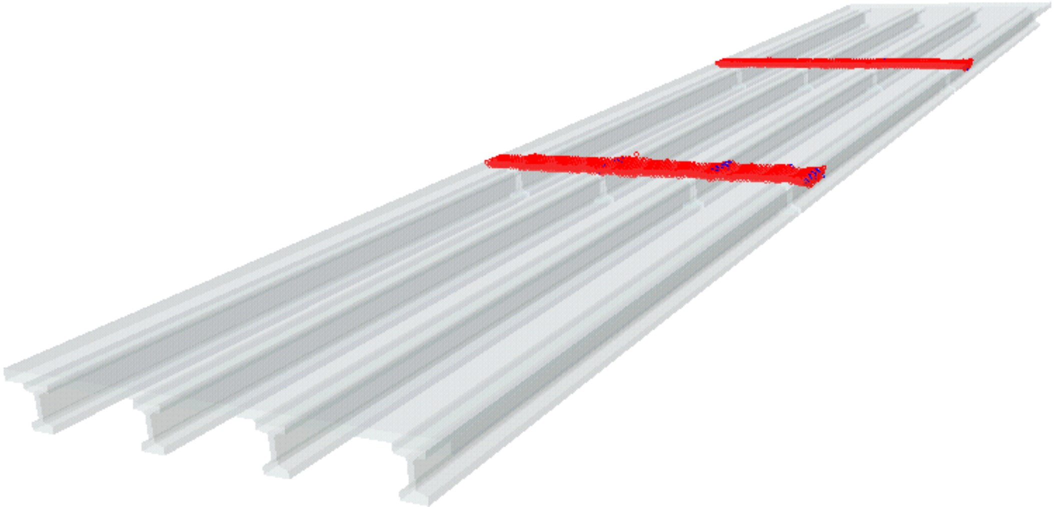

Figure 6.18: Superstructure Crack Pattern for Temperature Increase

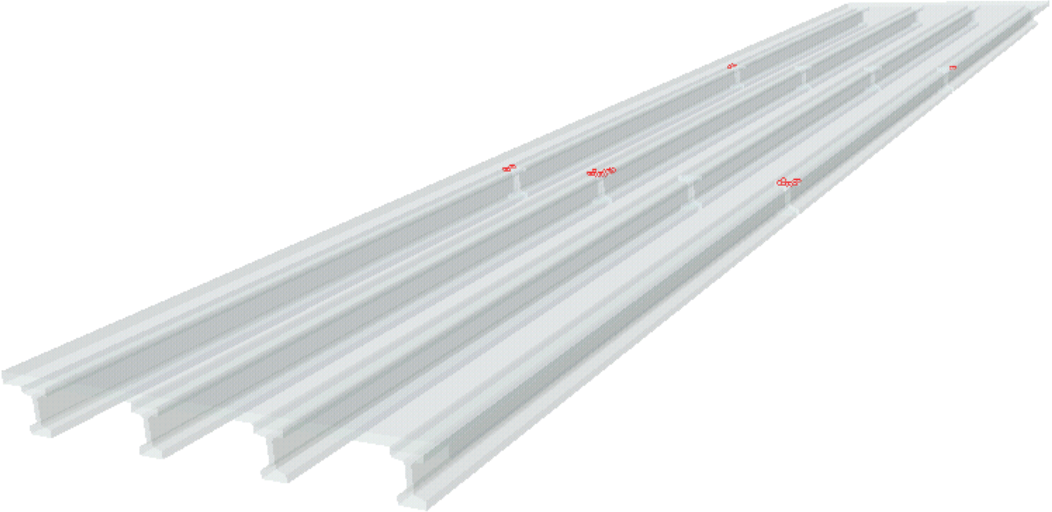

Figure 6.19: Girder Crack Pattern for Temperature Increase

There is negligible cracking in the bridge girders. As these girders are free to translate in the longitudinal direction (their interior ends are resting on bearing pads), there is relatively no induced tensile strain. The applied displacement boundary conditions have led to tension cracks at the locations of the bridge pier caps. Intuitively, crack accumulation here makes sense because the section is reduced at these locations because the girder ends are separated. The strain contours in the superstructure (longitudinal direction, ZZ) are shown in Figures 6.20 and 6.21.

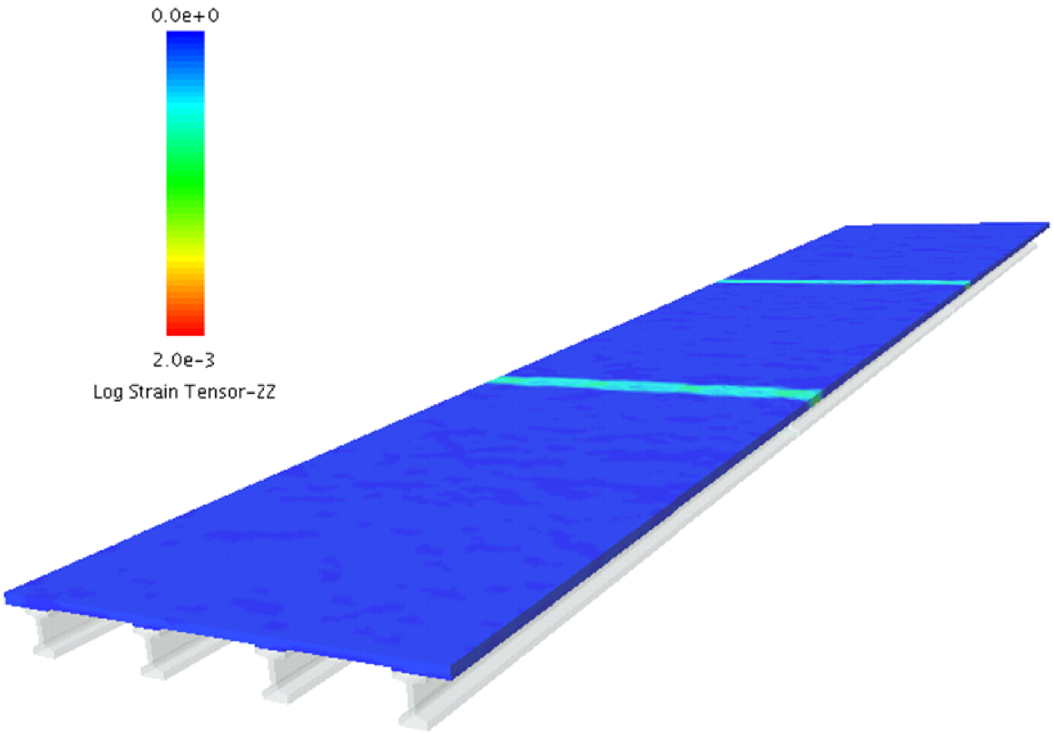

Figure 6.20: Strain Contours for Temperature Increase

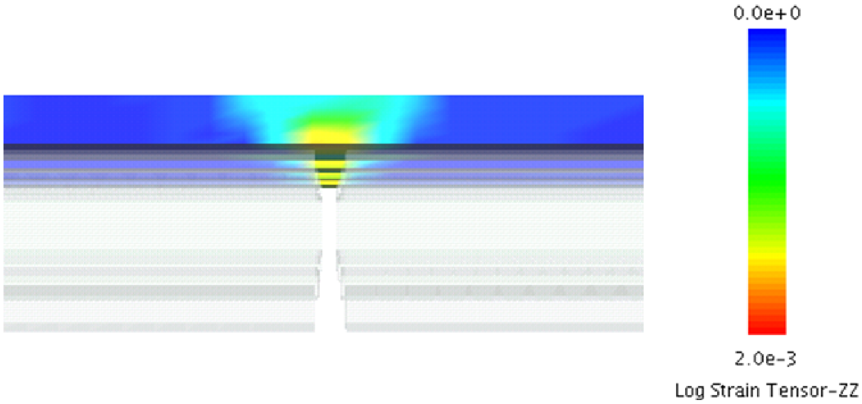

Figure 6.21: Strain Contours for Temperature Increase (Close-Up)

It is apparent that in the three spans of the superstructure, the tensile strain has not been reached. This is evident because there are no red markers in main spans and the strain contours show the tensile strain to be low. The crack pattern and strain contours illustrated in Figures 6.18-6.21 are conservative. The finite element model of the deck is continuous and uniform across the gap between the bridge girders. In the field, a saw cut and a V-joint are used at the piers (see Figure 6.22).

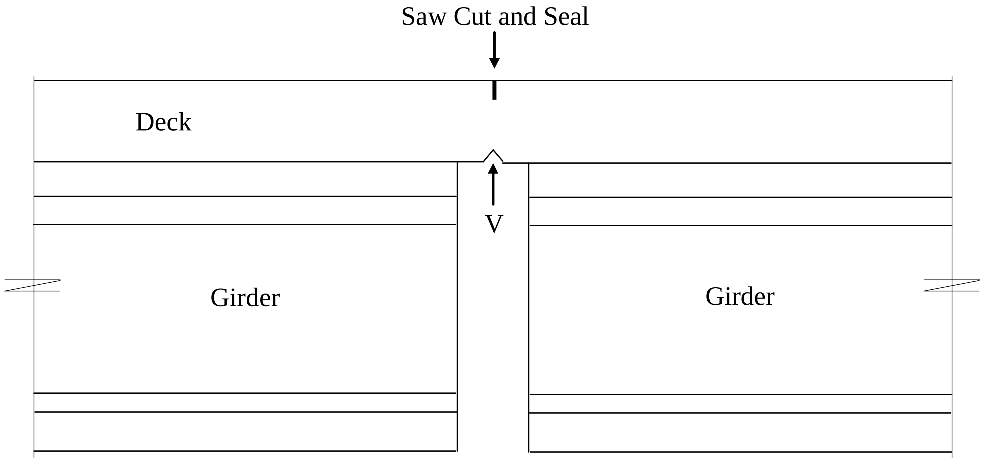

Figure 6.22: Deck Schematic at Pier Locations

Reducing the section even further with the joints will ensure that any cracking in the deck will occur under the saw cut and because it is sealed, there will be little trouble with degradation (water tightness, de-icing salts seeping into the deck). If the saw cut and V-joint were modeled in the TeraGrande analysis, the width of the crack pattern shown in Figure 6.18 would be trimmed. Considering the crack-free main spans of the bridge deck and conservative crack portrayal at the pier locations, it is concluded that the superstructure is not experiencing severe nonlinear behavior. However, this is only the case for the displacement-time history applied at the superstructure ends, which directly relates to an actual temperature change, in this case a temperature increase of 10°F. For a temperature increase of this magnitude (or less), the linear elements developed for TeraDysac should be satisfactory.

6.4.2 Temperature Decrease

A temperature drop at the bridge site was also investigated. In a two-week period in January 1998, the bridge temperature dropped by 8°F. The resulting abutment movements measured by the horizontal extensometers (1.6 mm) were applied to the superstructure end node sets (similar to the bridge heating analysis). Again, a pristine model was used. The stress contours (longitudinal, ZZ) are shown in Figures 6.23 and 6.24.

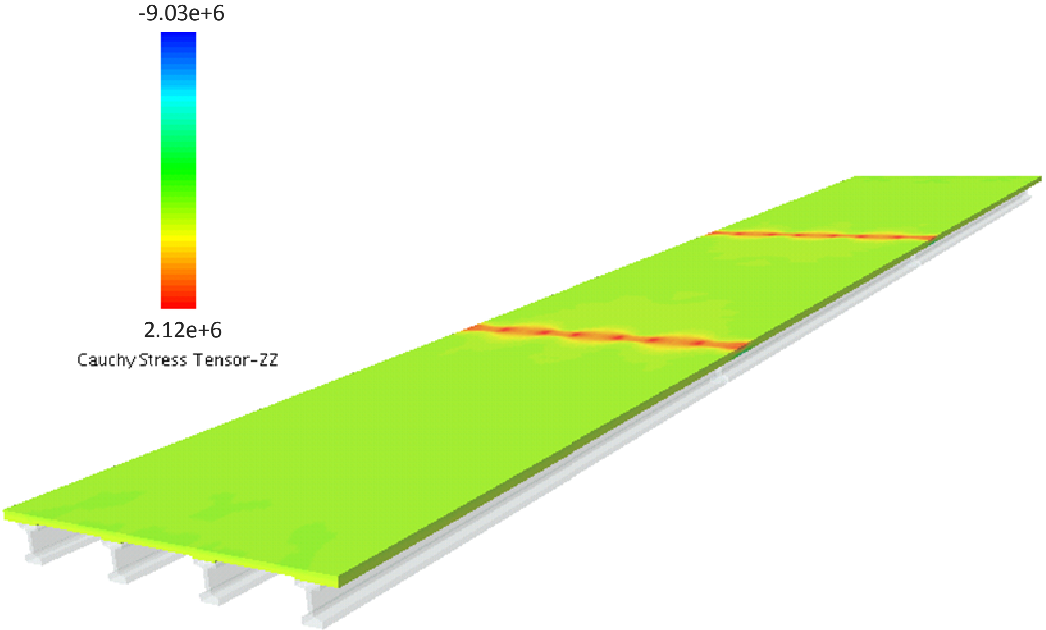

Figure 6.23: Bridge Deck Stress (Pa) Contours for Temperature Decrease

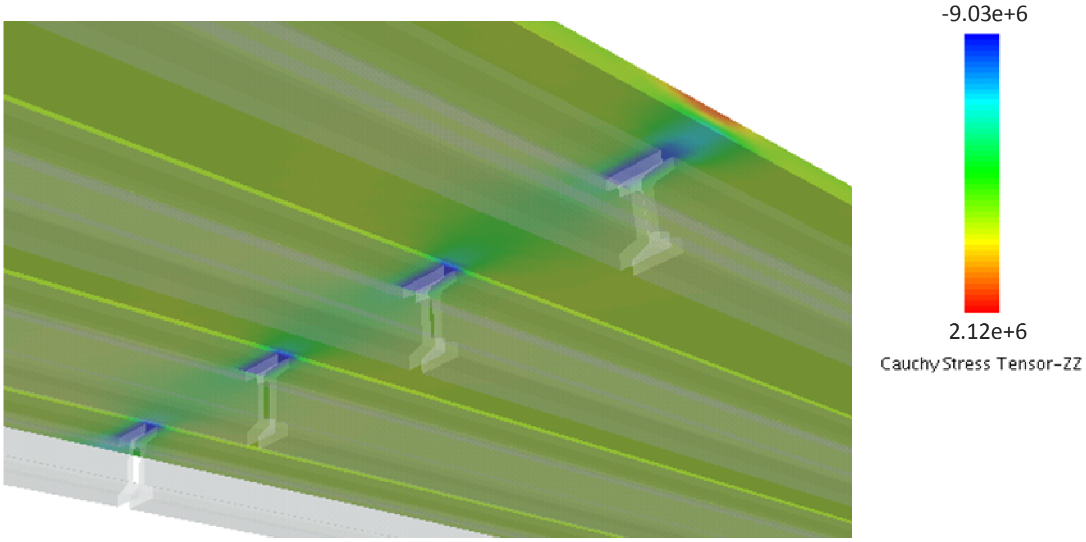

Figure 6.24: Stress (Pa) Contours Viewed from Beneath Bridge

Again, the response is quite uniform in the main spans and there are some stress concentrations in the pier regions. Figure 6.24 shows a view from below the superstructure which reveals the highest regions of compression are on the bottom side of the deck between girder ends. A small tension zone exists on the top side of the deck in this region. This minor tension resulted in a crack pattern shown in Figure 6.25.

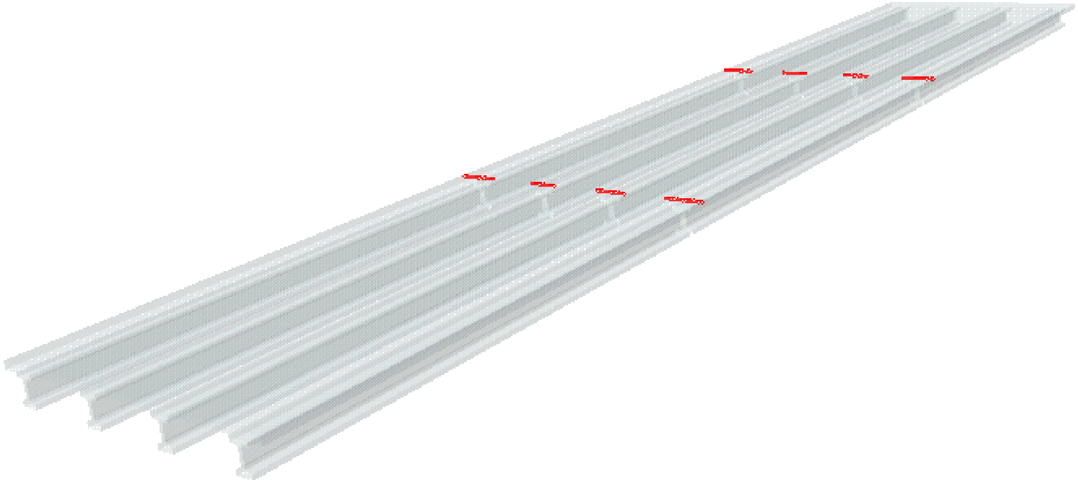

Figure 6.25: Deck Crack Pattern for Temperature Decrease

The compressive strength of the deck concrete (f'_c) is 39.99 MPa (5800 psi). The ANATECH generated compressive stress-strain curve is given in Figure 6.26. Added to the curve are two indicators: the ∇ marks the maximum compressive stress in the deck and the × marks the compressive stress in the deck as indicated by the lime coloring in Figures 6.23 and 6.24.

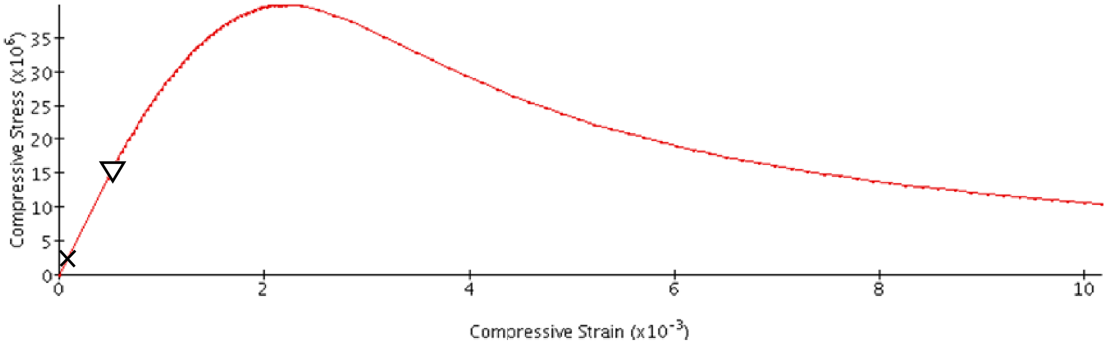

Figure 6.26: Deck Compressive Stress-Strain Curve (Pa)

Figure 6.26 illustrates that for the cooling modeled, the compressive stress in the deck does not enter the nonlinear range (i.e. it is consistent with the slope Young's modulus provides on the stress-strain curve). A majority of the compressive stress in the superstructure is quite small when compared with the compressive strength of the concrete. The compressive stress in the superstructure as indicated by the lime coloring is around 1.9 MPa (about 275 psi). Upon studying the stress-strain curve for the deck concrete and knowing the cooling-induced compressive stresses, it is concluded that the linear plate element developed in TeraDysac is acceptable to model the superstructure in this temperature range. For the temperature drop of 8°F to be modeled in TeraDysac, the developed linear elements should be satisfactory.

6.4.3 Blast Loading

It has been concluded that using linear elements in the superstructure is acceptable for the temperature loading modeled previously. Depending on the analysis, more advanced elements may be necessary. To illustrate one instance of such an analysis, a blast loading event was simulated using the superstructure model. A 3D moving pressure loading feature is available in TeraGrande. A surface blast was initiated on the deck top at the center of the middle span. Again, a pristine model was used. The superstructure end node sets and the girder end node sets were restrained in the vertical direction only. The user is allowed to control the peak overpressure, wave speed, and how the blast pressure diminishes with time and distance. The applied blast has a peak overpressure of 413.68 kPa (60 psi) and a wave speed of 762 m/s (30000 in/s). Figure 6.27 shows the pressure as a function of time at increasing distances from the propagation center. Figure 6.28 shows pressure as a function of distance from the propagation center at increasing times. This is a significant blast event, albeit a fictitious one, that is modeled for illustrative purposes only.

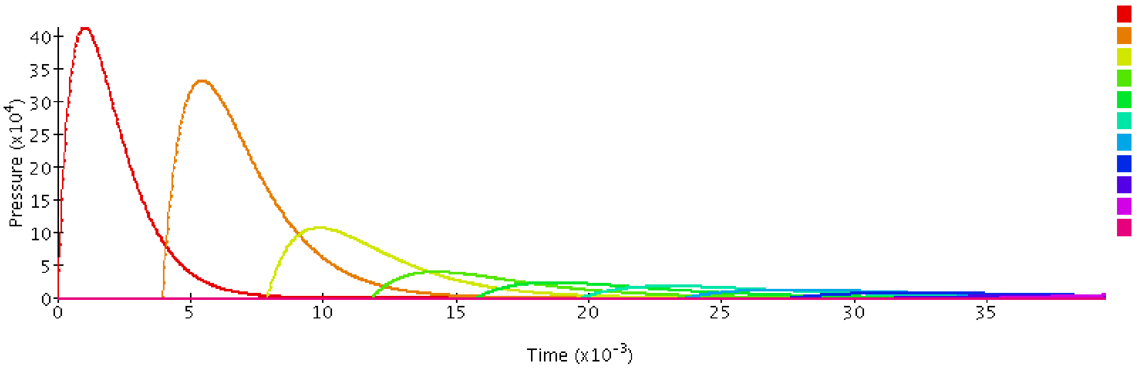

Figure 6.27: Blast Pressure (Pa) vs. Time (s)

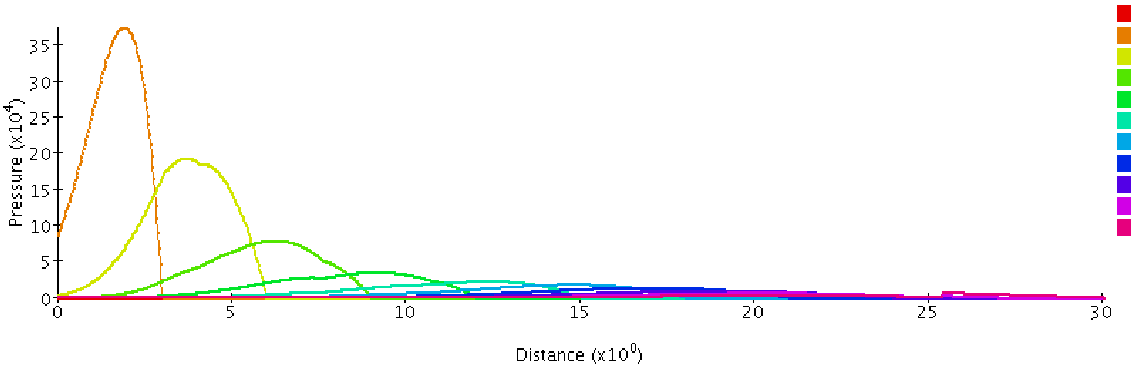

Figure 6.28: Blast Pressure (Pa) vs. Distance (m)

The pressure on the bridge deck 6 ms after the blast load initiation is shown in Figure 6.29.

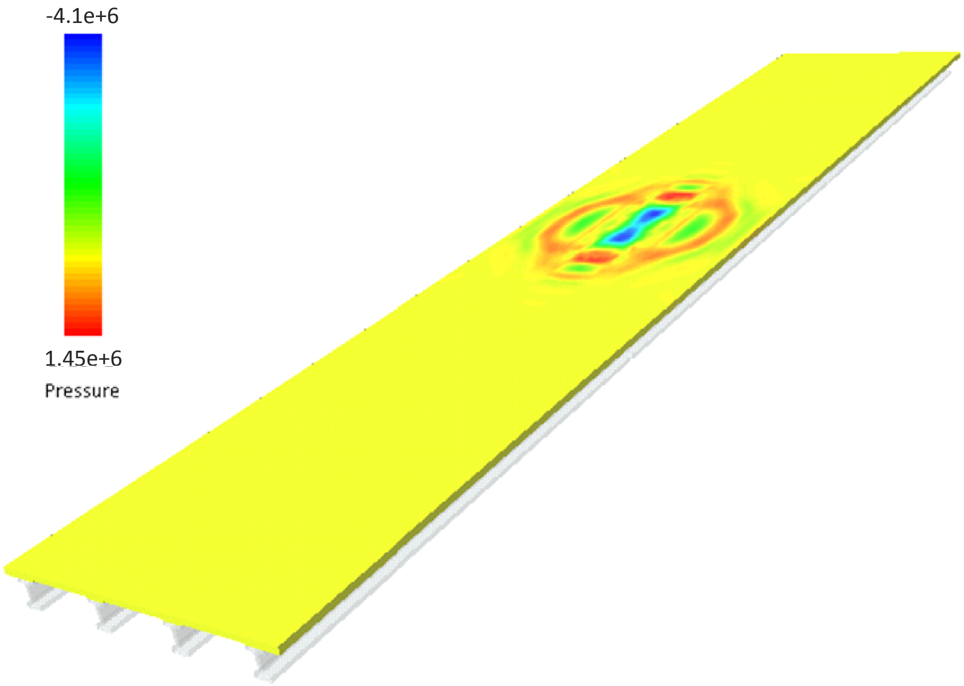

Figure 6.29: Superstructure Pressure (Pa) 6 ms After Blast Initiation

The deformed shape of the bridge 0.15 s after the blast initiation is shown in Figure 6.30. The peak displacement in the vertical direction at this time is 7.29 cm.

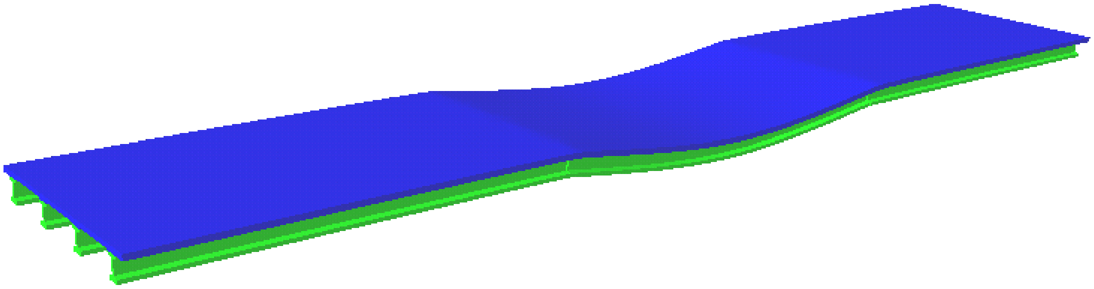

Figure 6.30: Superstructure Deformed Shape at 0.15 s (Magnified by 15)

Figures 6.31 and 6.32 show the crack pattern in the bridge deck and the bridge girders, respectively.

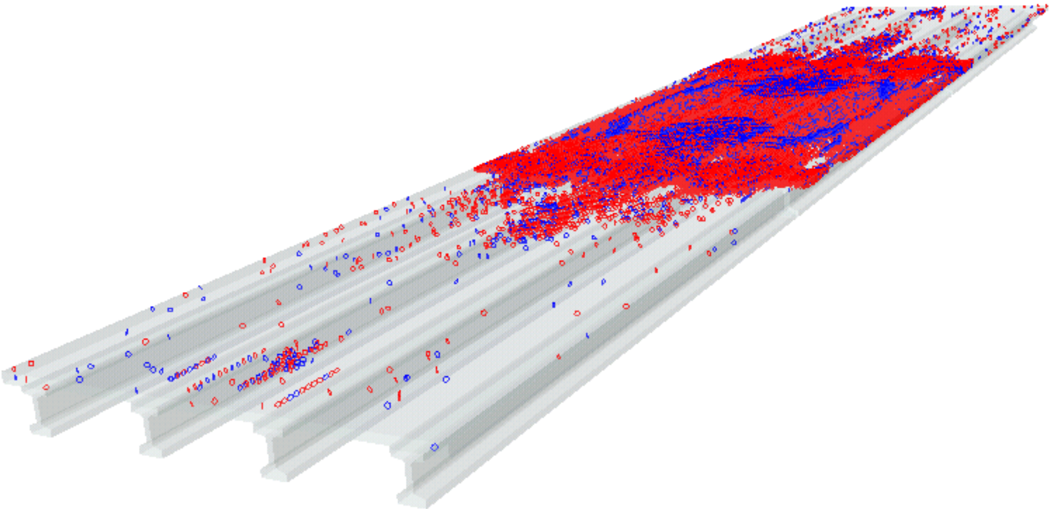

Figure 6.31: Bridge Deck Crack Pattern

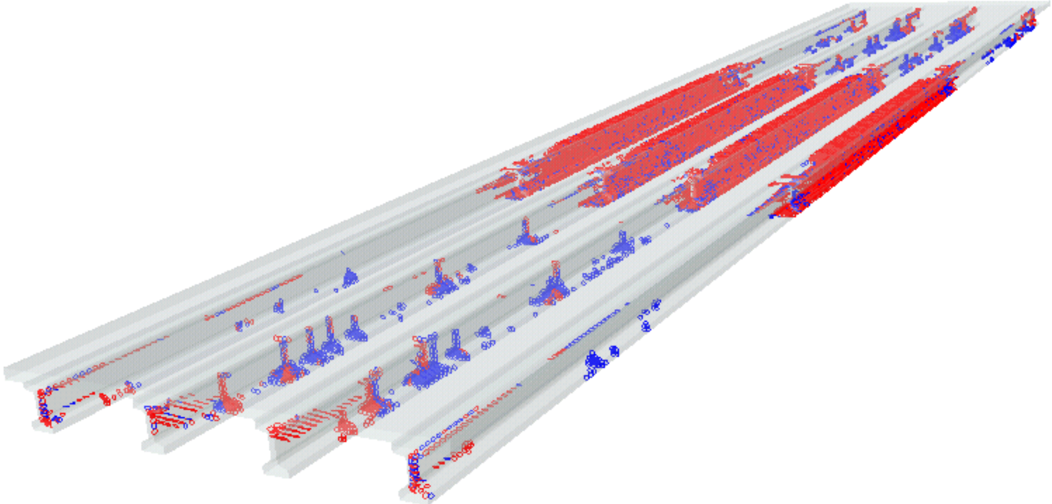

Figure 6.32: Bridge Girders Crack Pattern

It is apparent that the bridge has suffered serious damage due to the blast load. Open tension cracks (in very high density) throughout both the deck and girders indicate that the bridge has been destroyed. This is a severe loading event and any soil-structure interaction analysis will require nonlinear structural elements.

7. TeraDysac Modeling

7.1 Problem Description

To validate the developed technology in TeraDysac, results from a project conducted at the University of Minnesota (see Huang et al. 2004) were used. The published report provided a detailed description of the bridge site, soil testing results, and numerous instrumentation results. Bridge #55555, located in Rochester, Minnesota is a reinforced concrete IAB with no skew angle and prestressed girders. Figures 7.1-7.3 describe the bridge.

Figure 7.1: Concrete IAB (Photo Courtesy of Huang et al. 2004)

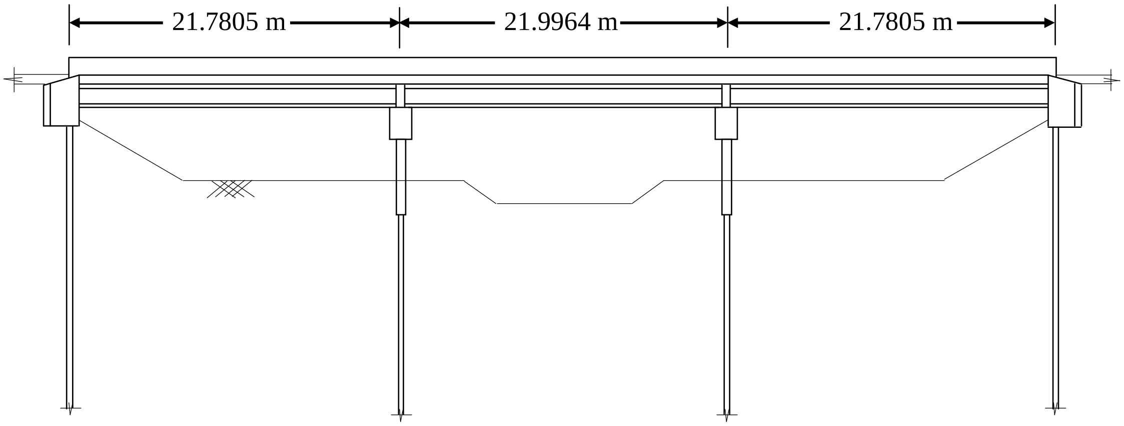

Figure 7.2: Elevation View of Minnesota IAB

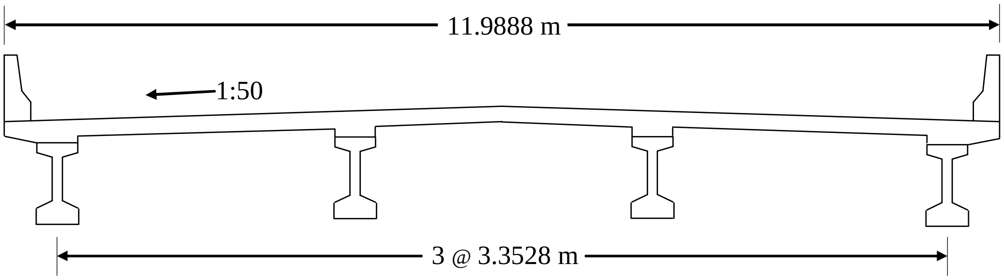

Figure 7.3: Transverse Section (Through Deck)

The monitoring effort was carried on from bridge construction in 1996 to 2004. Report-furnished air temperature, abutment translation, abutment rotation, and abutment pile curvature from the year 1998 were used in the validation of the proposed modeling scheme. The used instrumentation results came from a weather station, horizontal extensometers, tiltmeters, and vibrating wire strain gages, respectively. The report also included the soil testing results from the bridge site which provided stratigraphy information and standard penetration test (SPT) results. A set of bridge plans was also obtained from the Minnesota Department of Transportation (Mn/DOT). The bridge is built over the Zumbro River in southeastern Minnesota. The water table is located about 4.5 m below the abutments, but the soils are assumed to be saturated in this work.

7.2 Soil Properties

Two sets of analyses were carried out in 2D. The first assumes all of the soil is linear elastic. The second uses a combination of a bounding surface clay model and a sand model. In the 3D analyses (skewed vs. zero skew), only linear elastic soil properties are used. The soil exploration reported the blows per foot (BPF) from the SPT. For the linear elastic problems, only Young's modulus and Poisson's ratio are required. Poisson's ratio was set to 0.3 for all soils. Young's modulus was computed in accordance with the method described in the Naval Facilities Engineering Command design manual (NAVFAC 1986). With the exception of the two relatively thin clay layers at the site, the soils are loose and poorly graded sands. The method described in the design manual provides Young's modulus (E) as a function of N-value, where the units of E are tsf.

Table 7.1: Young's Modulus as a Function of N-Value (NAVFAC 1986)

Soil Type	$\boldsymbol{E/N}$
Silts, sandy silts, slightly cohesive silt-sand mixtures	4
Clean, fine to medium sands and slightly silty sands	7
Coarse sands and sands with little gravel	10
Sandy gravels and gravel	12

Figure 7.4 shows the stratigraphy at the bridge site with the values of E/N used in the linear elastic analysis. In both the linear elastic and the bounding surface analysis, pore pressure effects were captured by setting $\Gamma = 2.2 * 10^6$ kPa.

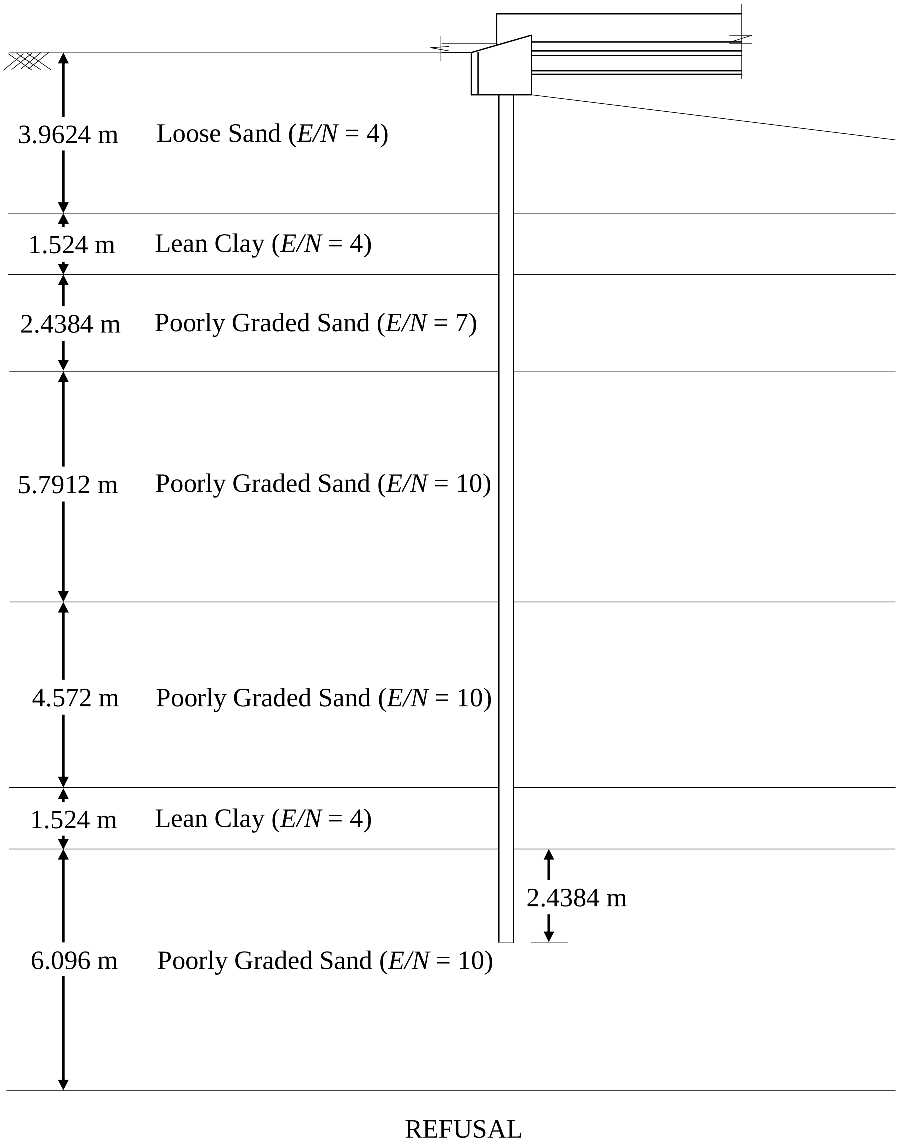

Figure 7.4: Soil Stratigraphy with Used E/N Ratios

7.3 Structural Properties

The bridge deck, bridge girders, abutments, pier caps, and the pier piles above grade are all combinations of concrete and steel. The bridge deck, girders, abutments, and pier caps are made of reinforced concrete. The pier piles above grade and to a depth of about 1.524 m below grade are encased in concrete and steel pipes. Because these components consist of two materials, a weighted average approach was used to obtain the material properties input for the beam and plate elements.

7.3.1 Weighted Average Example

The piles supporting the piers are HP 10 x 57 sections in strong-axis bending surrounded by concrete and steel shells (see Figure 7.5). At about 1.5 m below the ground surface, the concrete and shells end and only the piles continue to significant depth.

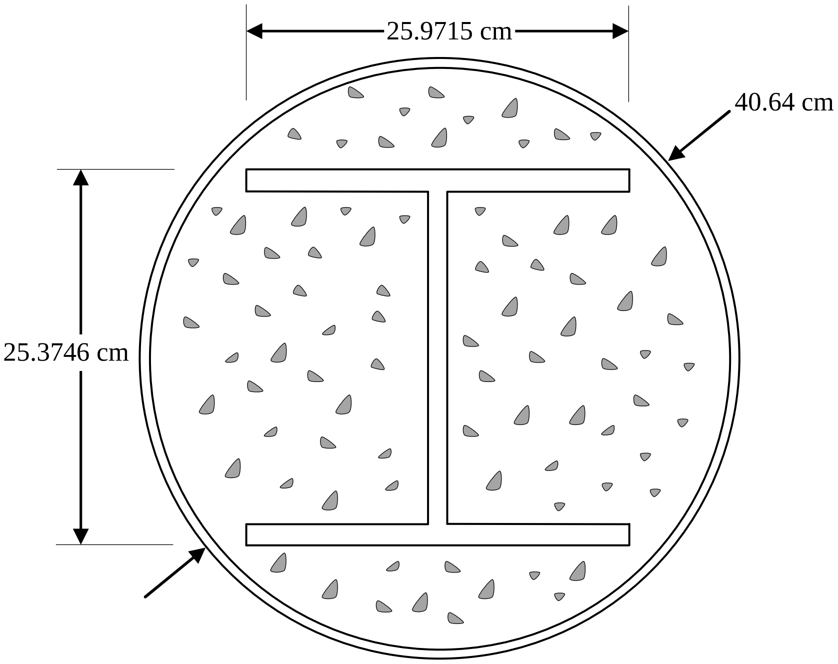

Figure 7.5: Cross-Section Pier Piles Above Grade

The required beam element properties for the TeraDysac input include Young's modulus (E), Poisson's ratio (ν), area (A), strong axis moment of inertia (I_x), weak axis moment of inertia (I_y), and the coefficient of thermal expansion (α).

These properties were obtained as follows:

The modulus of concrete and the coefficients of thermal expansion for the steel and concrete at the site were reported in the Huang et al. (2004) study. The subscripts c, s, and t designate concrete, steel, and total respectively.

To calculated the composite properties, the following are used: $E_c = 30.3 * 10^6$ kPa, $E_s = 200 * 10^6$ kPa, $A_c = 1110.52$ cm^2, $A_s = 186.65$ cm^2, $\rho_c = 2.4$ Mg/m^3, $\rho_s = 7.85$ Mg/m^3, $\nu_c = 0.2$, $\nu_s = 0.3$, $\alpha_c = 6.15 * 10^{-6}/°\mathrm{F}$, $\alpha_s = 6.7 * 10^{-6}/°\mathrm{F}$. The bending stiffness EI is different in the strong and weak axis directions.

$$(EI)_x = (E_s I_{pile})_x + (E_s I_{shell})_x + (E_c I_c)_x = 88{,}150.75 \text{ kN-m}^2$$

$$(EI)_y = (E_s I_{pile})_y + (E_s I_{shell})_y + (E_c I_c)_y = 74{,}819.71 \text{ kN-m}^2$$

$$E_t = \frac{E_s A_s + E_c A_c}{A_t} = 54.72 * 10^6 \text{ kPa}$$

$$I_x = \frac{(EI)_x}{E} = 0.00161 \text{ m}^4$$

$$I_y = \frac{(EI)_y}{E} = 0.00137 \text{ m}^4$$

The composite beam density, Poisson's ratio, and coefficient of thermal expansion were also found using this weighted average approach. The obtained values are given by:

$$\rho_t = 3.18 \text{ Mg/m}^3$$

$$\nu_t = 0.214$$

$$\alpha_t = 6.23 * 10^{-6}/°\mathrm{F}$$

7.3.2 Set-Up for Plane Strain Analysis

The obtained properties described in the above example are input directly for the beams and plates in the 3D analyses. In the 2D analyses, another calculation is needed. The 2D version of TeraDysac uses plane strain theory for the soil elements. Across the width of the bridge, there are four girders and six piles at each abutment and bent. Because the soil is represented by a unit width, the section properties (A and I) for the girders and piles are spread over the bridge width. For example, the moment of inertia for an abutment pile was found to be $5.218 * 10^{-6}$ m^4. Across the bridge width, the six abutment piles combined have a total moment of inertia equal to 6 * 5.218 * 10^{-6} m^4 = 3.131 * 10^{-6} m^4. To find an approximate value of this moment of inertia over a unit width, the value is divided by the bridge width (3.131 * 10^{-6} m^4 / 11.9888 m = 2.611 * 10^{-5} m^4/m). In the 2D model, the ‘Deck/Girder’ element block (see Figures 7.11 and 7.12 and Table 7.2) is a weighted average combination of the roadway and the four girders which support it. The abutments are uniform across the bridge width, so the abutment section properties are based a unit width.

7.3.3 Set-Up for 3D Analysis

Significant reinforcement is used to connect the girders to the bridge deck. In the 3D bridge model, the girder elements are meshed directly into the deck via tied contact. The bent cap is also merged into the plane of the deck. This is not entirely accurate because the girder ends are sitting on elastomeric bearing pads which rest on the pier caps (see Figure 7.6). The diaphragms which connect the girder webs at midspan were neglected in the model. This work is concerned with the thermal response of the bridge, especially behind the abutments so unnecessary elements were not modeled. The parapet wall (concrete railing) on either side of the roadway was also neglected. The railing is divided into roughly 6 m sections with cork deflection joints. This rail was deemed to only marginally influence the response of the bridge deck. The meshed superstructure is shown if Figure 7.7.

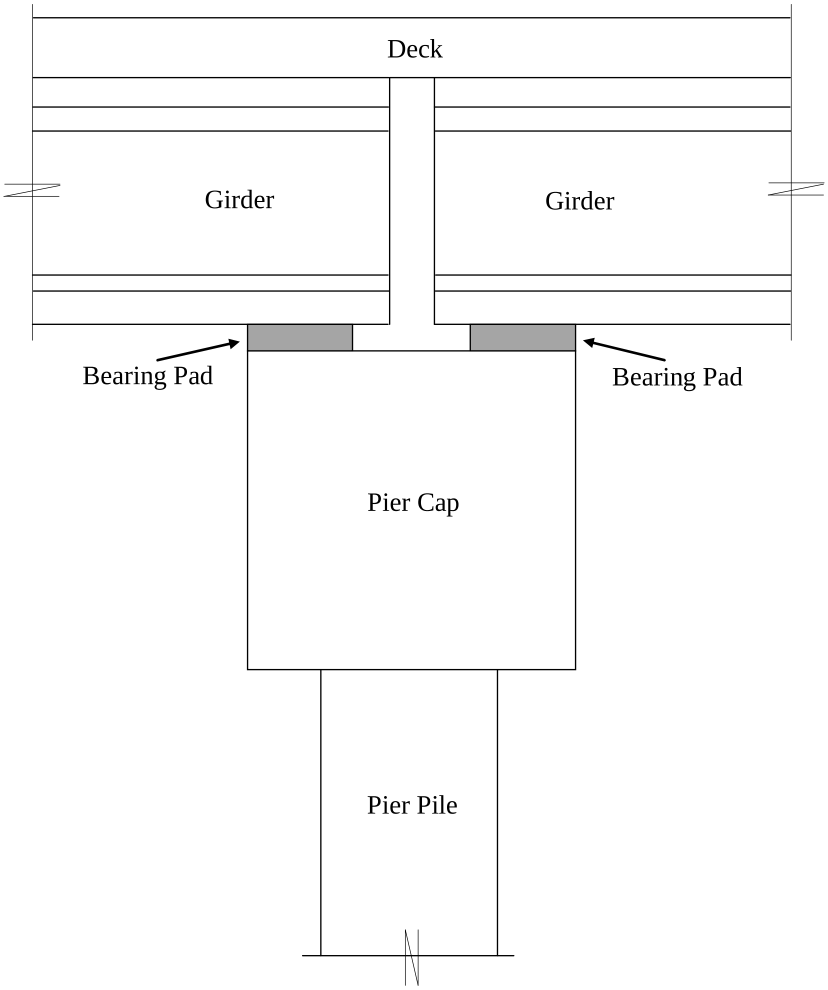

Figure 7.6: Bridge Details at Pier Locations

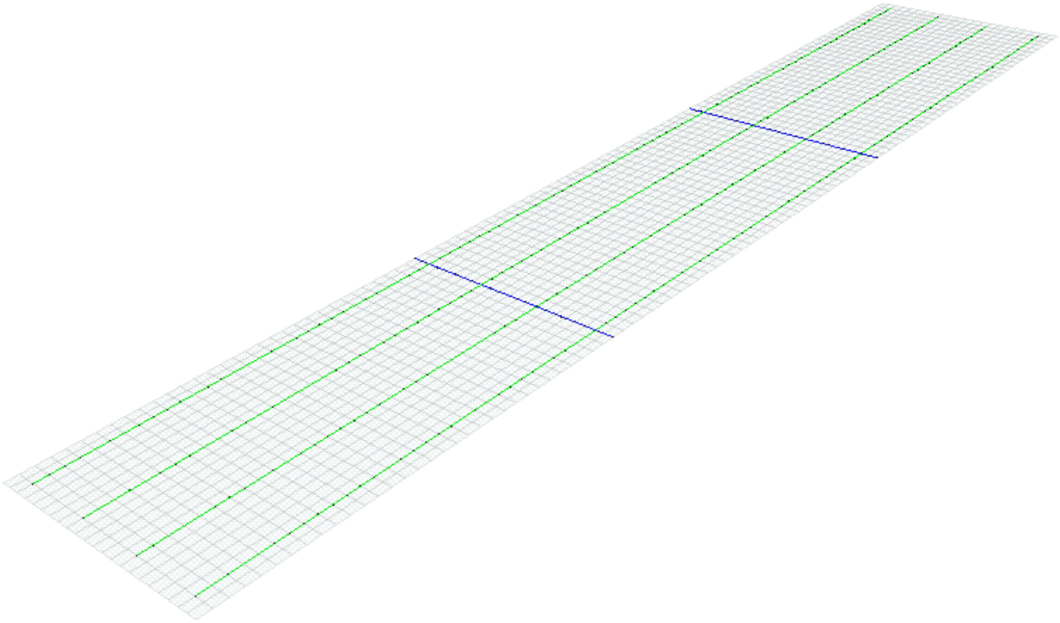

Figure 7.7: 3D TeraDysac Superstructure Model

In the above figure, the girders are colored in green and the bent caps are colored in blue. The three element blocks (deck, girders, and bent caps) are meshed together via tied contact.

7.4 Applied Thermal Loading

In the study conducted by Huang et al. (2004), thermocouples were installed in the superstructure cross-section to develop temperature profiles through the deck and girders. Figures 7.8 and 7.9 show the temperature profiles for a sunny summer day and a cloudy winter day, respectively. The figures were obtained from an electronic version of the Minnesota report (Huang et al. 2004).

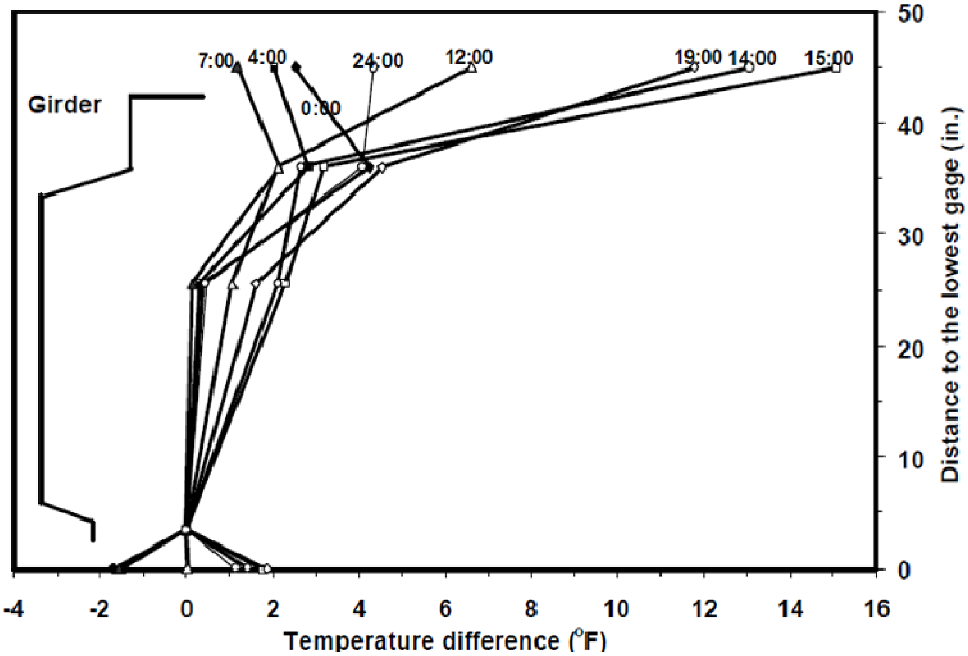

Figure 7.8: Temperature Gradient (Sunny Summer Day, After Huang et al. 2004)

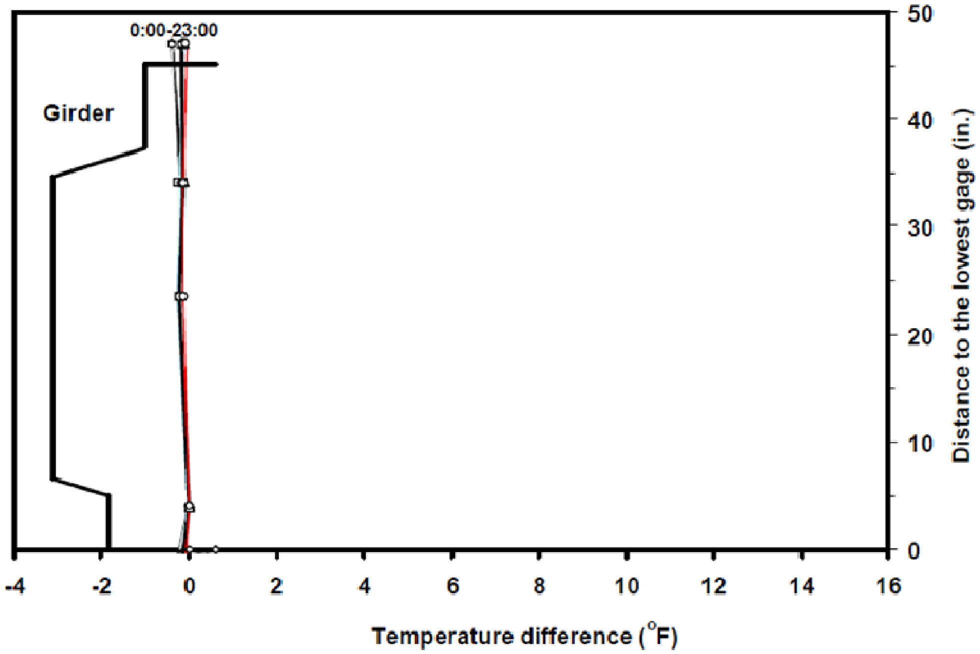

Figure 7.9: Temperature Gradient (Cloudy Winter Day, After Huang et al. 2004)

It is apparent that on sunny summer days there is an appreciable temperature difference through the superstructure, especially in the afternoon. Included in the instrumentation plan on the Minnesota bridge were pyranometers used to measure solar radiation. On the two days in question (Figures 7.8 and 7.9), solar radiation was high in the afternoon on the summer day and relatively minimal throughout the winter day.

7.4.1 Validation Technique

For the results comparison, temperature loading was applied to the TeraDysac models and the abutment rotation, displacement, and pile curvature were compared to the instrumental data from the Minnesota report. Abutment movement was reported in two week intervals from horizontal rod extensometers during the year 1998. The bridge temperature, abutment rotation, and pile curvature were reported on a more frequent basis (every 6 hours) through the use of data loggers and a computer. A two-week period in

June was selected for the temperature increase TeraDysac analysis and a two-week period in January was selected for the temperature decrease analysis.

In the summer analysis, a temperature gradient was applied through the superstructure. The bridge temperature change from the beginning to the end of the two weeks (10°F) was applied at the mid-depth of the composite superstructure. The exact temperature distribution during this time was not reported, so the gradient was estimated based on the observed temperature distribution during similar times of the year (see Figure 7.8). The temperature loading input to TeraDysac is shown in Figure 7.10.

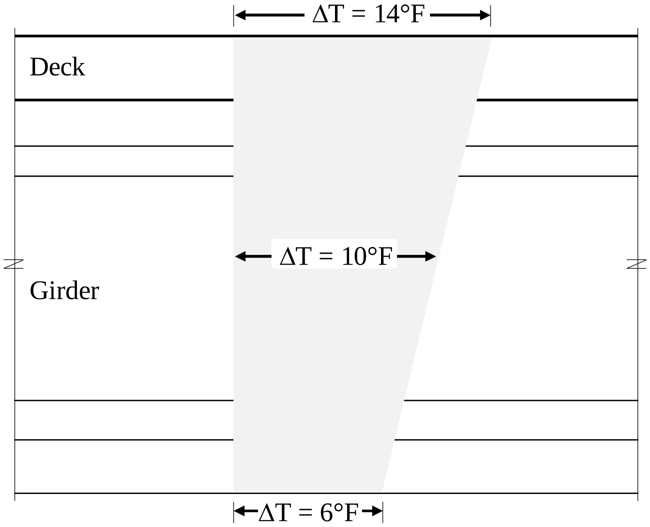

Figure 7.10: Superstructure Temperature Input (Heating)

In the temperature drop analysis, the bridge temperature change from the beginning to the end of the two weeks (8°F) was applied throughout the superstructure. Consistent with Figure 7.9, no thermal gradient was used. The thermal loading was ramped up over 1.0 s and then held to allow any oscillations in the solution to level off. Note that the obtained pore water pressure contours presented for the subsequent analyses are a function of the load duration. As a two-week event is simulated over 1.0 s of problem time, the obtained pore water pressures may not reflect field values. The ability to track pore water pressure generation is a nice feature of TeraDysac and the results are presented to provide insight into what soil regions may experience a gains or losses in pore water pressure during the simulated event. The obtained abutment displacement, abutment rotation, and pile curvature from the TeraDysac analysis were compared with the respective values incurred over the two weeks of analysis.

7.5 Linear Elastic Analysis

The first analysis performed on the bridge model uses the calculated Young's modulus values in a linear elastic saturated soil model. Several analyses were used to ensure the mesh has a minimum size (spatially) with minimal effect from the soil boundaries. The finite element model is shown in Figure 7.11. There are 316 line elements (structure) and 7302 quadrilateral elements (soil) in the mesh.

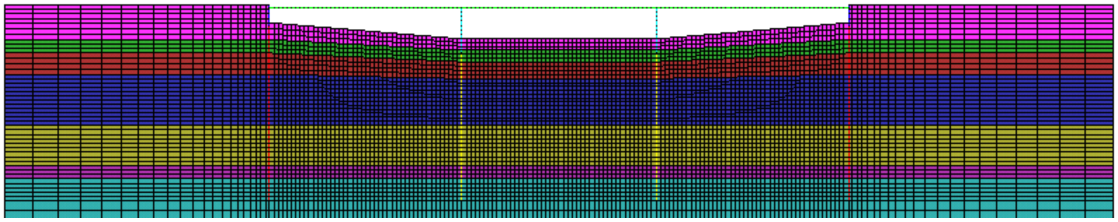

Figure 7.11: 2D IAB Finite Element Model

A gradient is applied away from the abutments on each side to reduce the model size without sacrificing accuracy near the bridge. Figure 7.12 shows a zoomed in view of the bridge with the various element blocks colored.

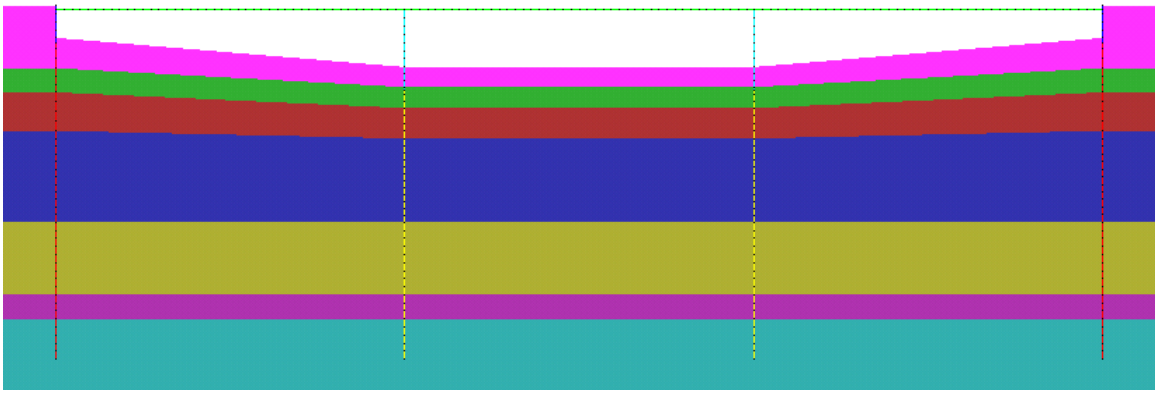

Figure 7.12: Element Block View

The various colors in Figures 7.11 and 7.12 represent the following element blocks:

Table 7.2: Element Blocks by Color.

Soil	
Color	*Element Block*
Pink	Fill / Loose Sand
Green	Lean Clay
Maroon	Poorly Graded Sand
Blue	Poorly Graded Sand
Gold	Poorly Graded Sand
Purple	Lean Clay
Turquoise	Poorly Graded Sand
Structure	
Color	*Element Block*
Green	Deck/Girder
Blue	Abutment
Red	Abutment Pile
Aqua	Pier Piles (Above Grade)
Yellow	Pier Piles (Below Grade)

The various poorly graded sand layers are differentiated by locations where the SPT values changed significantly in the soil exploration. The nodal equivalence scheme allows for two nodes at the same location to be merged together. The deck is merged into the abutment and the pile sections change at locations away from soil nodes (see Figure 7.13).

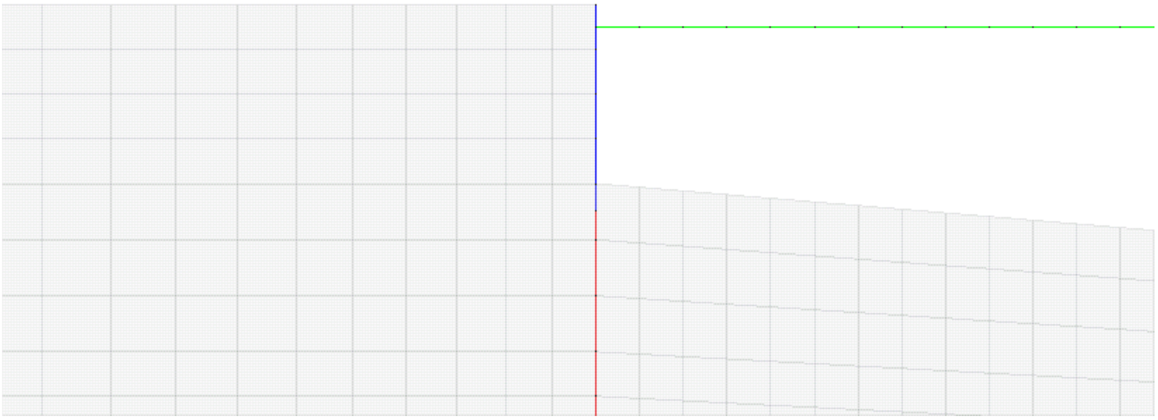

Figure 7.13: Structure Assembly at Abutment

Ideally the deck should be merged into the abutment at the top of the abutment element block. However, because a soil node is already tied to the abutment at this location, merging a deck node at this location is not allowed. This situation does provide the possibility of some analysis problems. Because the junction of the deck and the abutment is not located at a soil node, the junction node can deviate from the soil displacement (linear between soil nodes). Figure 7.14 illustrates this phenomenon.

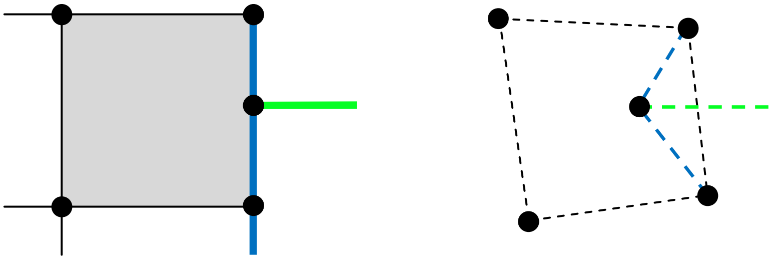

Figure 7.14: Junction Undeformed and Deformed Shapes

The deformed shape in Figure 7.14 is grossly exaggerated. The actual deformed shape in this region on the bridge models is much more agreeable with the soil element edge displacement because of the huge stiffness of the abutment relative to the soil.

The entire soil stratum is assumed to be saturated. The applied boundary conditions for the model include fixing the solid and fluid displacement in both the horizontal and vertical directions on the bottom soil nodes and in the horizontal direction only on the side soil nodes. Figure 7.15 highlights the boundary nodes.

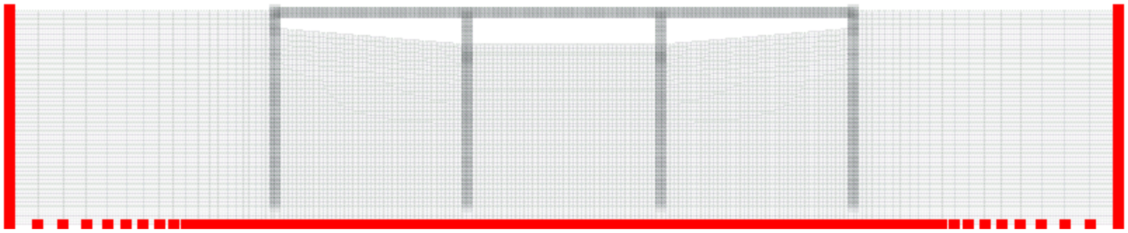

Figure 7.15: Boundary Nodes for 2D Analysis

7.5.1 Temperature Increase

The first linear elastic analysis considers the temperature raise measured during a two-week period in the summer of 1998. Figure 7.16 shows the deformed shape of the bridge (magnified by 100). No hourglassing has taken place in the soil elements (Uniform Gradient formulation).

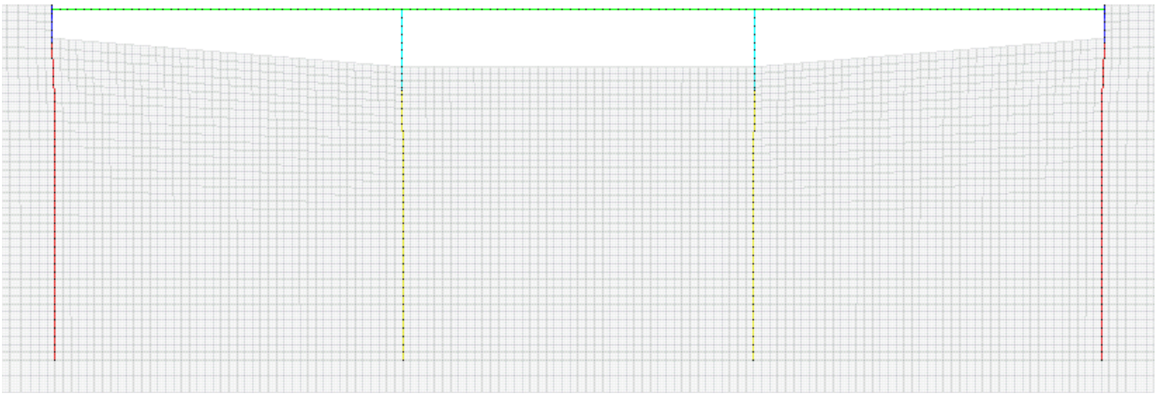

Figure 7.16: IAB Deformed Shape for Temperature Increase

A more accurate depiction of the abutment and abutment pile deformation is presented in Figure 7.17. During the two weeks of temperature variation at the IAB site, the horizontal extensometers revealed an abutment movement of about 2 mm. Figure 7.17 shows the TeraDysac displacement results to be in good agreement this value.

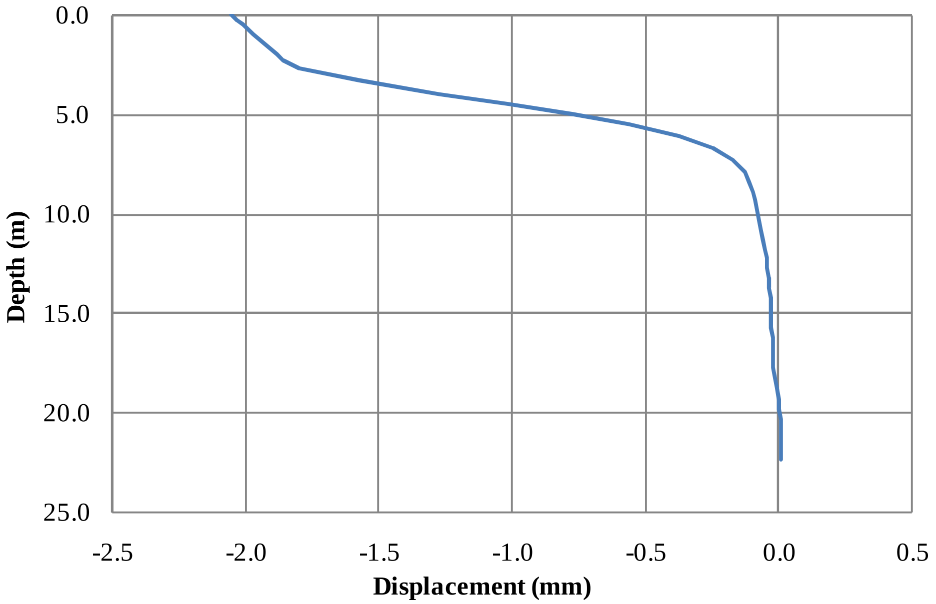

Figure 7.17: Abutment and Abutment Pile Displacement for Temperature Increase

The transition from the abutment to the abutment pile occurs at a depth of 2.35 m. The abutment is moving as a rigid unit and the behavior illustrated in Figure 7.14 is not occurring. Knowing the length of the bridge deck in the model, the coefficient of thermal expansion, and the applied temperature change, a free expansion calculation revealed an abutment displacement of about 2 mm. It is apparent the relatively high stiffness of the composite superstructure (deck and girder) to the soil stiffness allows the abutment movement to approach a free expansion. A free expansion would lead to a stress-free superstructure and a fully restrained loading (zero abutment movement) would lead to maximum thermal superstructure stresses, with the field behavior residing somewhere between the two. As the field response is much closer to a free expansion, the thermal superstructure stresses are low.

In addition to the abutment displacement, abutment rotation was checked against tiltmeter-measured abutment rotation in the field. The abutment rotated away from the river by 0.014° over the two week period. Because the abutment is comprised of beam elements, there is a nodal rotation output for each node. The values of nodal rotation for the seven abutment nodes ranged from 0.0046° to 0.0050°. As Figure 7.17 illustrates, there appears to be no significant bending in the abutment (it rotated as a unit), so these rotation values are expected to be very close. Another approach to obtain the abutment rotation is to treat the abutment as a straight line that has deviated from vertical by some angle. This angle, which can be easily calculated, is the abutment rotation. Using the top and the bottom of the abutment as the line endpoints, the calculated abutment rotation is 0.0048°.

The Minnesota study also reported the abutment pile curvatures. After the piles were driven, arc-weldable strain gages were installed at depths of 15 cm and 91 cm below the bottom of the abutment. The bending moment value for each abutment pile node was obtained in the analysis. Using Equation 7.1, the pile curvature at various locations can be calculated.

$$\frac{M}{\phi} = EI \tag{7.1}$$

The reported pile curvature change over the two weeks was 866 $\mu\varepsilon$/m. Using Equation 7.1, the curvature immediately below the abutment was found to be 552 $\mu\varepsilon$/m. Considering the assumptions made (linear elastic soil and structure) and techniques used (weighted average approach for structural properties, SPT values to obtain Young's modulus), the results from the linear elastic analysis are encouraging. The obtained abutment translations agree with the field values. The abutment rotation and abutment pile curvature are both under-estimated.

In addition to the results already discussed, one of the main advantages of using TeraDysac is that the pore water pressure development during loading can be captured.

Figure 7.18 shows the pore pressure contours at the end of the analysis run. As the bridge deck is heated, it expands pushing the abutments into the backfill soil. This loading creates a positive pore pressure buildup in the backfill soils. On the interior sides of the abutments, negative pore pressure has developed. This stems from the tied contact between the soil and structure elements. The pore pressure variations are small, with range of only about 0.9 kPa.

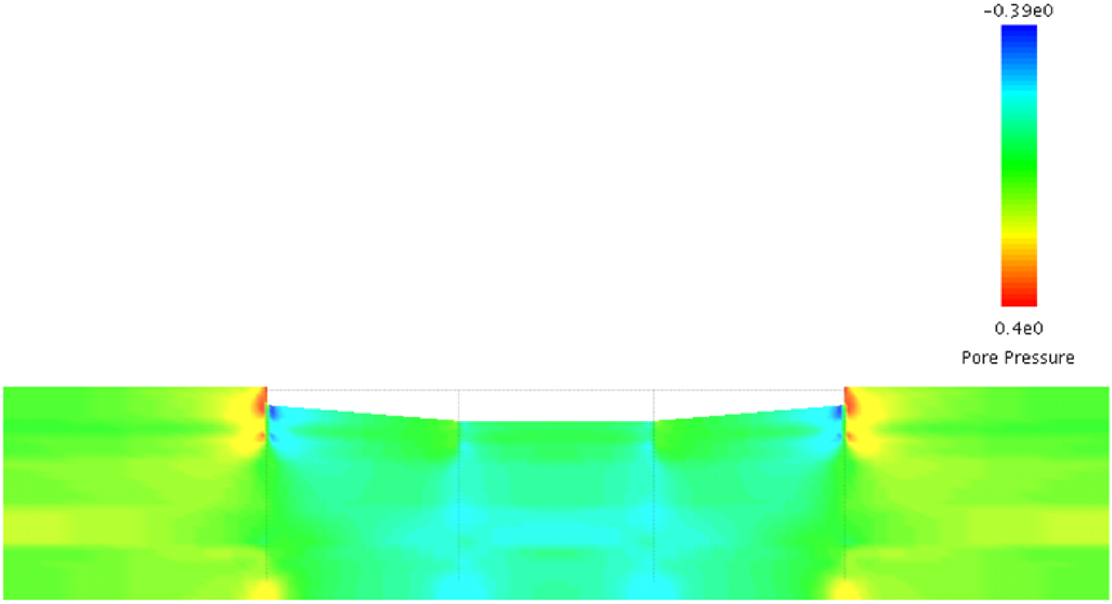

Figure 7.18: Developed Pore Water Pressure (kPa) During Temperature Increase

7.5.2 Temperature Decrease

The second linear elastic analysis considers the bridge temperature drop measured during a two-week period in the winter of 1998. Figure 7.19 shows the deformed shape of the bridge (magnified by 100).

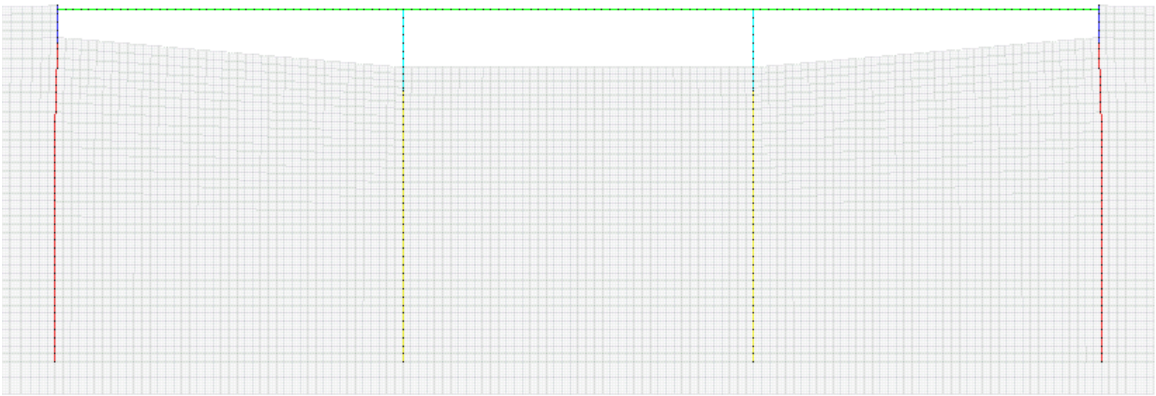

Figure 7.19: IAB Deformed Shape for Temperature Decrease

A more accurate depiction of the abutment and abutment pile deformation is presented in Figure 7.20. During the two weeks of temperature variation at the IAB site, the horizontal extensometers revealed an abutment movement of about 1.6 mm. Figure 7.20 shows the TeraDysac displacement results to be in good agreement this value.

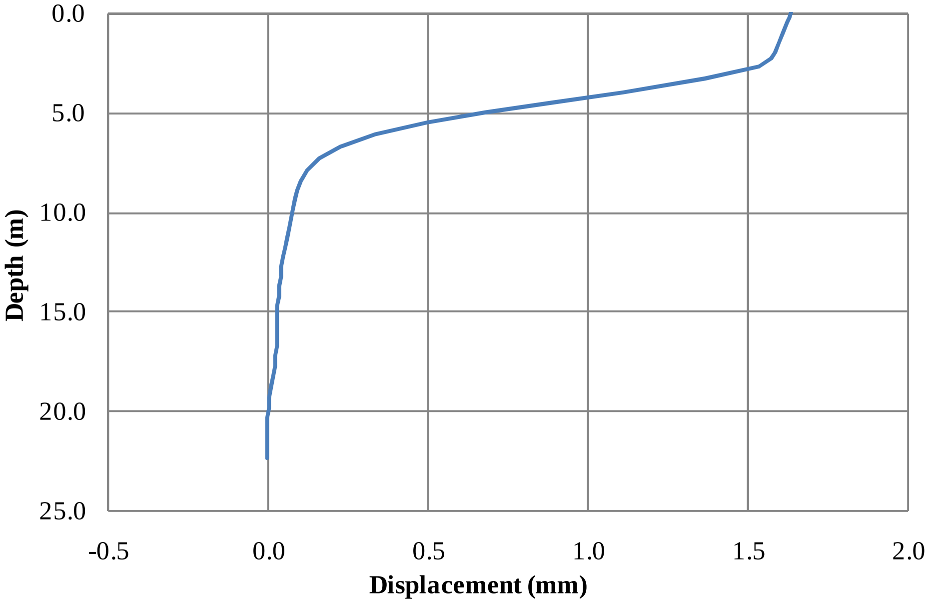

Figure 7.20: Abutment and Abutment Pile Displacement for Temperature Decrease

In addition to the abutment displacement, abutment rotation was checked against tiltmeter-measured abutment rotation in the field. The abutment rotated toward the river by about 0.01° over the two week period. As Figure 7.20 illustrates there appears to be no significant bending in the abutment (it rotated as a unit). The abutment rotation using the top and the bottom of the abutment as the endpoints of straight line, the calculated abutment rotation is 0.0015°. The reported pile curvature change over the two weeks was 709 με/m. Using Equation 7.1, the curvature immediately below the abutment was found to be 515 με/m. Again, the linear elastic analysis results are encouraging. The obtained abutment translations agree with the field values. The abutment rotation is still under-estimated, but the calculated pile curvature is closer to the measured curvature than in the heating analysis. This could be attributable to the uncertainty in the gradient applied in the heating analysis. Gradients are low in the winter (for this analysis, no gradient was used) so the guesswork is reduced.

Figure 7.21 shows the pore pressure contours at the end of the analysis run. As the bridge deck is cooled, it contracts pulling the abutments toward the river. This loading creates a negative pore pressure buildup in the backfill soils and positive pore pressure on the interior sides of the abutments.

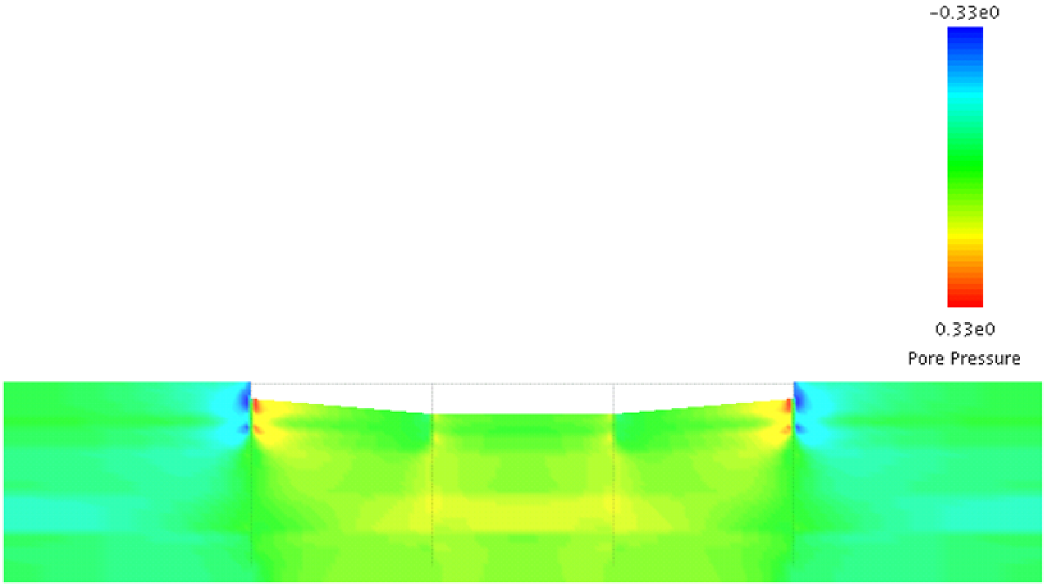

Figure 7.21: Developed Pore Water Pressure (kPa) During Temperature Decrease

7.6 Bounding Surface Analysis

7.6.1 Bounding Surface Properties

The soil stratum at the bridge site consists of two relatively thin layers of soft clay, but is mostly comprised of loose and poorly graded sands (see Figures 7.4 and 7.12). The soil exploration revealed the soil classification and the SPT N-values. Lab testing of the site soils would have provided more detailed information and made determining the bounding surface model parameters easier. But as this was not the case, some engineering judgment was used to determine what bounding surface properties to input for the data model. The clay at the bridge site was soft based on low N-values. The parameters for Speswhite Kaolin, a soft clay with calibrated parameters (see Muraleetharan 1994 and Table 3.1) were used in the finite element model. The N-values in the sand layers were used to determine the relative densities using the method outlined in Tokimatsu and Seed (1986). The calibrated bounding surface properties for Nevada Sand with relative densities of 40 and 60% are available (see Muraleetharan 1995). The sand at the bridge site was assumed to be Nevada Sand and the bounding surface properties for the respective layers were set based on the relative densities for the sand layers at the bridge site. Bounding surface model parameters for the denser sand layers (D_r = 82% and 84%) were estimated based on the calibrated values of Nevada Sand (D_r = 40% and 60%). Figure 7.22 shows the soil stratum with the obtained relative densities for the sand layers. The OCRs used in the analysis for the clay layers are also shown. The OCR sets the initial bounding surface size which controls the soil response. A higher OCR corresponds to a stiffer clay. The top clay layer was softer than the layer at depth, so it was assumed to be slightly less over-consolidated than the deep layer.

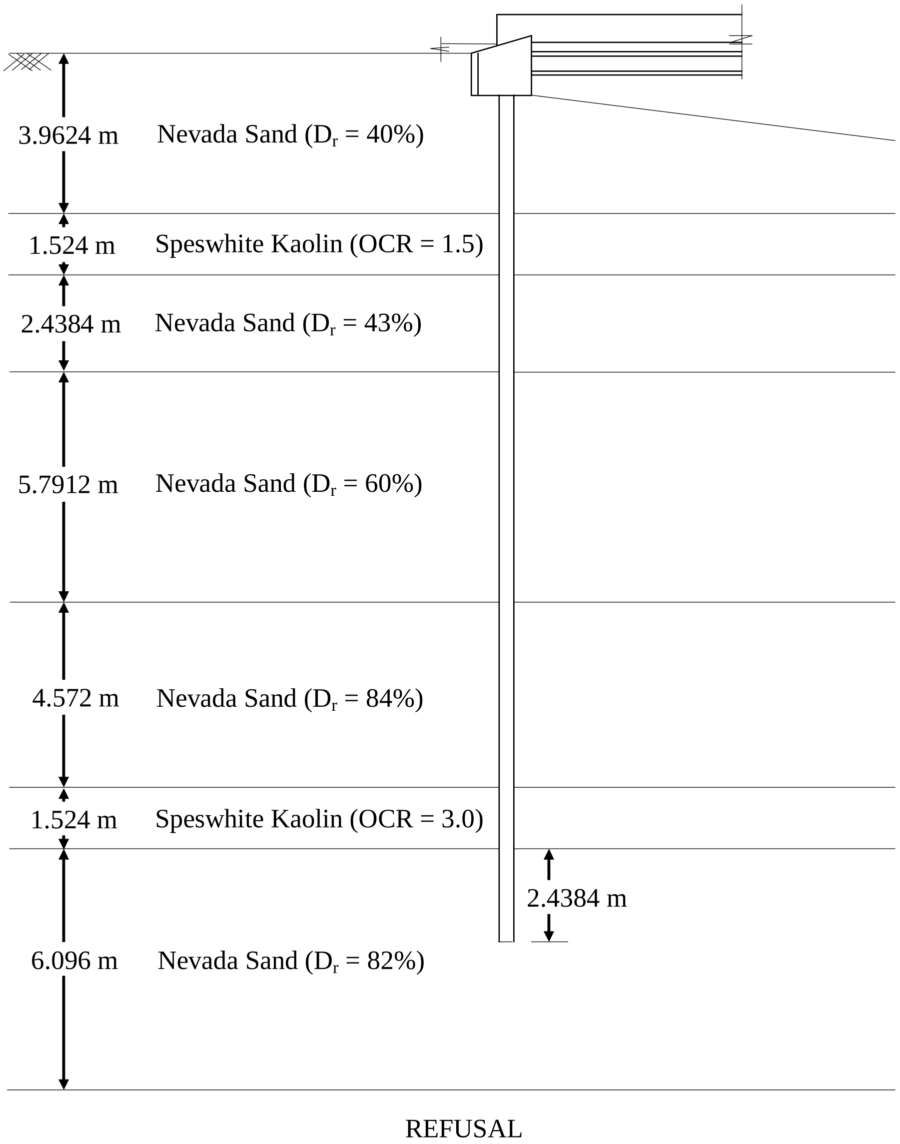

Figure 7.22: Soil Profile Composition (Nevada Sand and Speswhite Kaolin)

The five sand layers break into three distinct groups with relative densities near 40, 60, and 80%. The calibrated bounding surface properties for 40 and 60% relative density were used directly and the values for 80% relative density were estimated. The bounding surface properties for the sand layers are given in Table 7.3.

Table 7.3: Bounding Surface Properties for Sand Layers

		Nevada Sand (D_r = 40%)	Nevada Sand (D_r = 60%)	Nevada Sand (D_r = 80%)
Traditional Model Parameters				
Slope of isotropic consolidation line on $e - \ln p'$ plot	λ	0.017	0.009	0.007
Slope of elastic rebound line on $e - \ln p'$ plot	κ	0.003	0.002	0.0014
Bounding Surface Configuration Parameters				
Slope of line OA (Fig. 3) in $q - p'$ space (compression)	M_c	0.89	0.89	0.89
Ratio of extension to compression value of M	M_e/M_c	0.61	0.61	0.61
Value of R in triaxial compression	R_c	1.5	1.5	1.5
Related to gradient of ellipse 2 on I-axis	α	5.0	5.0	5.0
Parameter defining the initial size of the bounding surface	I_0/I	1.5	1.5	2.5
Plastic Potential Surface Configuration Parameter				
Slope of critical state line (compression) in $q - p'$ space	$(M_u)_c$	1.33	1.44	1.55
Hardening Parameters During Loading				
Shape hardening parameter in triaxial compression	h_c	2.0	2.0	2.0
Ratio of triaxial extension to triaxial compression value of h	h_e/h_c	0.05	0.05	0.05
Deviatoric hardening parameter	β_1	0.5	0.4	0.4
Hardening Parameters During Unloading				
Unloading hardening parameter	H_u	0.2	0.2	0.2

Notes:

e = void ratio, $p' = (\sigma_1' + 2\sigma_3')/3$, $q = \sigma_1' - \sigma_3'$

The initial stress state is important when using the bounding surface models. The initial stress state provides the starting location inside the bounding surface. Assuming a saturated soil stratum and using the soil unit weights, the initial stress state was calculated by hand. After the mesh was created, the mid-element depths were used to find the effective stresses. A K_0 value of 0.5 was assumed. Figure 7.23 shows the initial effective stress in the vertical direction.

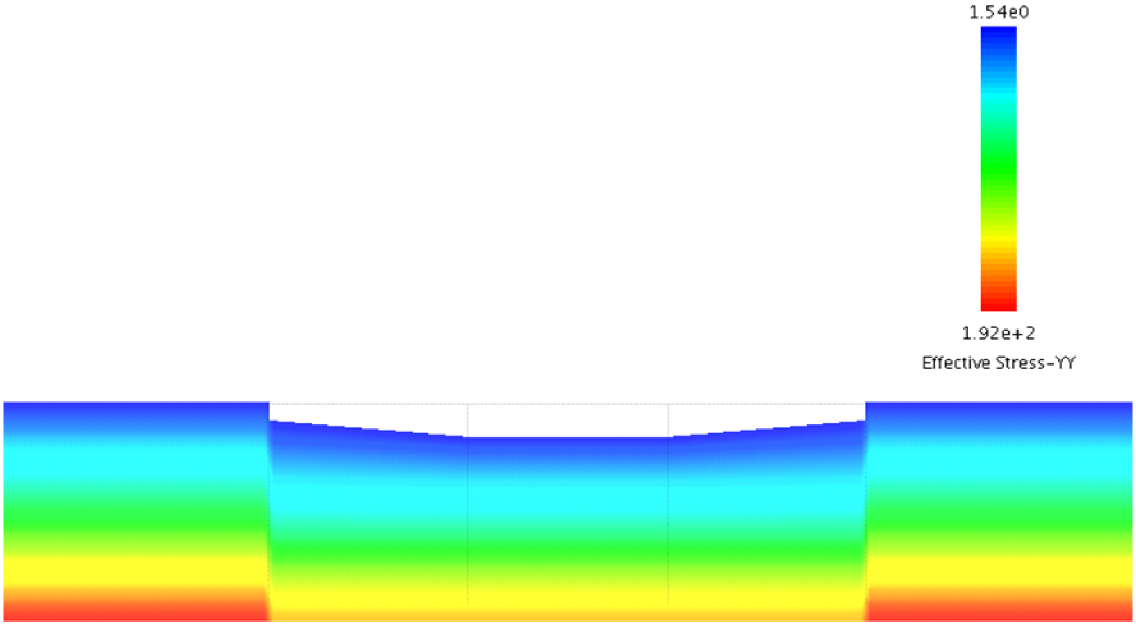

Figure 7.23: Initial Stress State (kPa) for Bounding Surface Analysis

To set up the initial stress state, a spreadsheet was used to calculate the stresses by element group. The data was then imported to the TeraDysac input file.

7.6.2 Temperature Increase

The temperature increase was also applied to the bounding surface model. A comparison between the abutment and abutment pile deformations in the two analyses (linear elastic and bounding surface soils) is given in Figure 7.24. The abutment translation in the two analyses is nearly the same. The superstructure is very stiff compared with the backfill soil that when it is thermally loaded, it is almost expanding as it would in a free expansion. The more important behavior to study in Figure 7.24 is the abutment rotation and the pile response. Knowing the soil stratigraphy (see Figure 7.22), the results from the bounding surface model agree with expected pile behavior at depth. The clay layer (highlighted in Figure 7.24) is located between depths of 3.96 m and 5.49 m, with sand on either side. As the pile transitions from the soft clay layer to the sand layer, one would expect the pile deformation to markedly decrease. This is the case in the bounding surface model, but in the linear elastic model, the transition is not distinguishable.

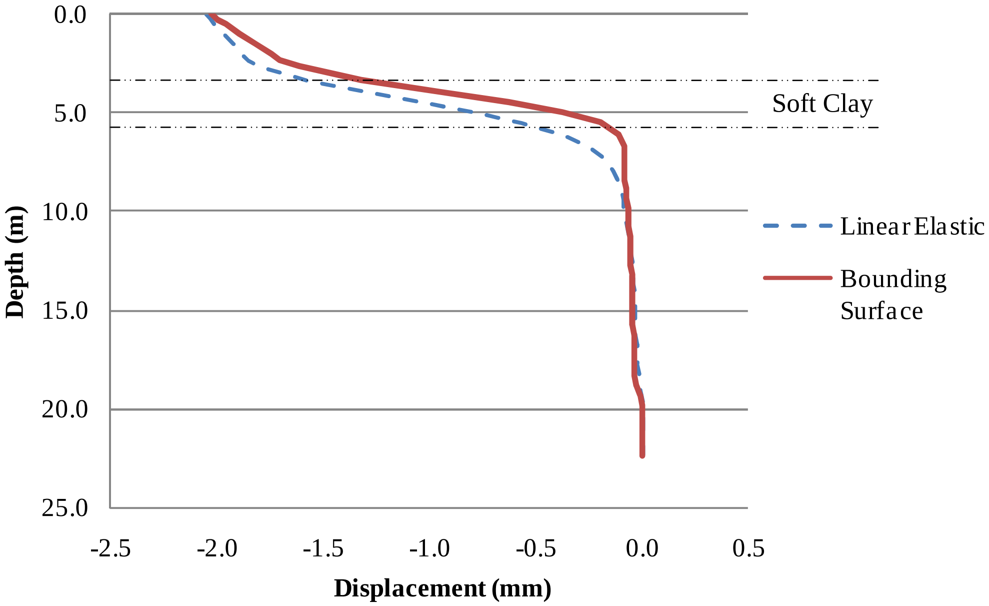

Figure 7.24: Abutment and Abutment Pile Deformation Comparison

The abutment displacements from both the linear elastic and bounding surface analysis are essentially the same. The superstructure in both cases was found to almost have a free expansion. The values of abutment rotation and pile curvature under the abutment were provided by the instrumentation study (Huang et al. 2004). The error magnitudes of the respective analyses are given in Table 7.4.

Table 7.4: Results and Error Estimates for Heating Analysis

	True	Linear Elastic	% Error	Bounding Surface	% Error
Rotation (°)	0.014	0.0048	65.7	0.0079	43.6
Pile Curvature ($\mu\epsilon/m$)	866	552	36.3	784	9.5

The error calculations show the bounding surface analysis to be more accurate. The pore pressure developed during the loading is shown in Figure 7.25. The noticeable band of pore pressure is the clay layer. Part of the pore pressure developed in this layer is from the specified K_0 condition and OCR. The specified OCR (1.5) in this layer forms a relatively small initial bounding surface and as the initial stress state is brought into the bounding surface there is pore water pressure development. In the deep clay layer (OCR = 3), the pore pressure development is not nearly as defined as in the top layer.

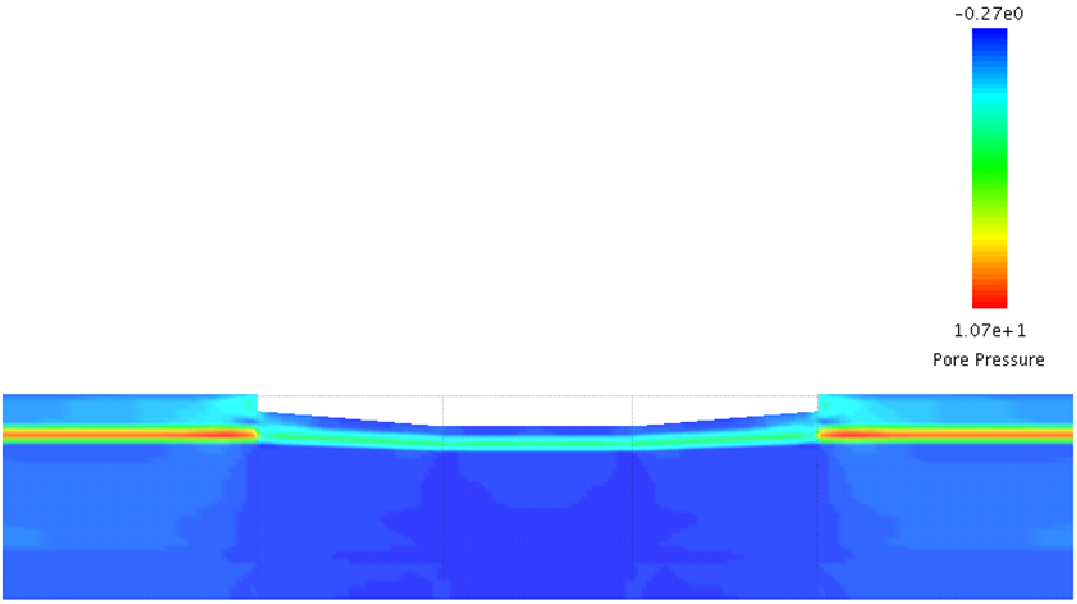

Figure 7.25: Bounding Surface Pore Pressure Development (kPa)

7.6.3 Temperature Decrease

The temperature decrease was also applied to the bounding surface model. A comparison between the abutment and abutment pile deformations in the two analyses (linear elastic and bounding surface soils) is given in Figure 7.26. Again, the abutment translation in the two analyses is nearly the same.

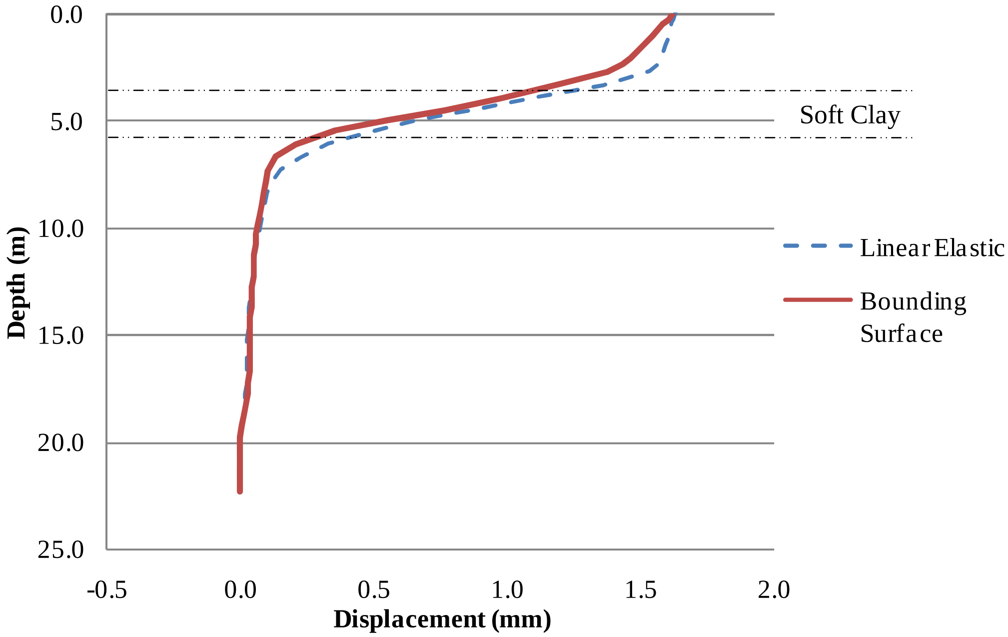

Figure 7.26: Abutment and Abutment Pile Deformation Comparison

The results comparison and error values are given in Table 7.5.

Table 7.5: Results and Error Estimates for Cooling Analysis

	True	Linear Elastic	% Error	Bounding Surface	% Error
Rotation (°)	0.01	0.0015	85.0	0.0045	55.0
Pile Curvature ($\mu\epsilon/m$)	709	515	27.4	687	3.1

The error calculations show the bounding surface analysis to be more accurate.

7.7 Three-Dimensional Analysis

Full 3D models of the Minnesota bridge and 15° skewed version of it were made in TeraDysac. However, the analysis of these models is not possible until a new solver has been implemented. Therefore, to illustrate the developed technology, these models were reduced to a size capable of running on a single processor machine. By removing the piles from the models, a substantial number of elements in the vertical direction could be eliminated. And because the bridge girders rest on elastomeric pads over the piers, no elements were modeled in the pier regions either. These models consist only of the superstructure (girders and deck), the abutments, and the top two soil layers. They are small enough to be analyzed on a single processor in a feasible amount of time. The meshes have 918 quadrilateral elements (deck and abutments), 256 line elements (girders), and 1344 hexagonal elements (soil), for a total of 2518 elements. The soil was modeled with the linear elastic elements and Γ was set to zero. Setting $\Gamma = 0.0$ kPa does not allow pore water pressure generation, but it permits a larger time step (and subsequently less computational effort). The 3D model (non-skewed) is shown in Figure 7.27.

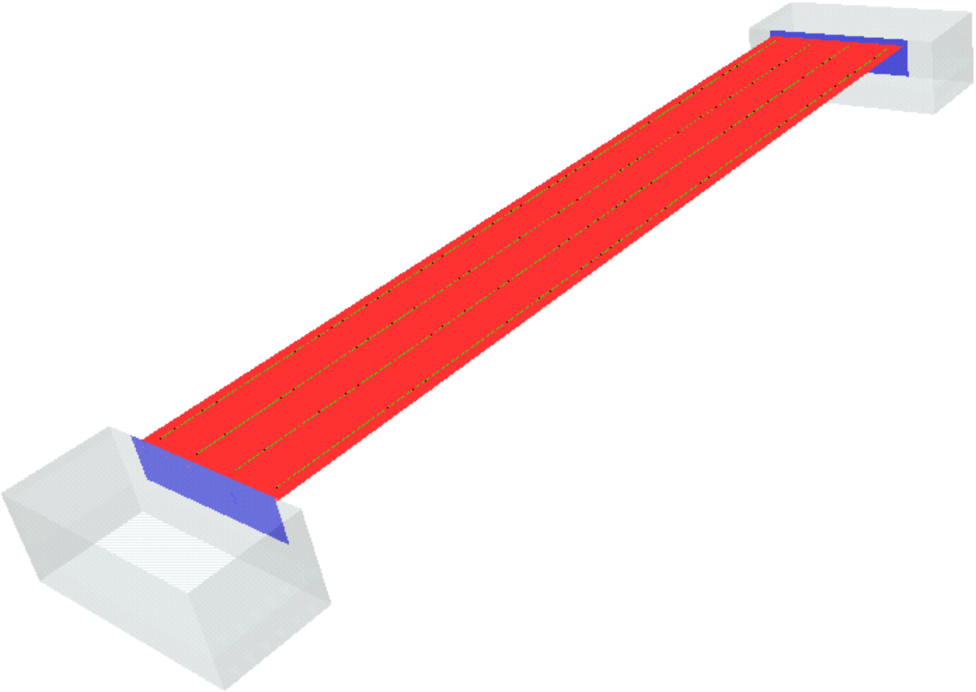

Figure 7.27: 3D Superstructure Model (Non-Skewed)

A plan view of the two 3D models is shown in Figure 7.28.

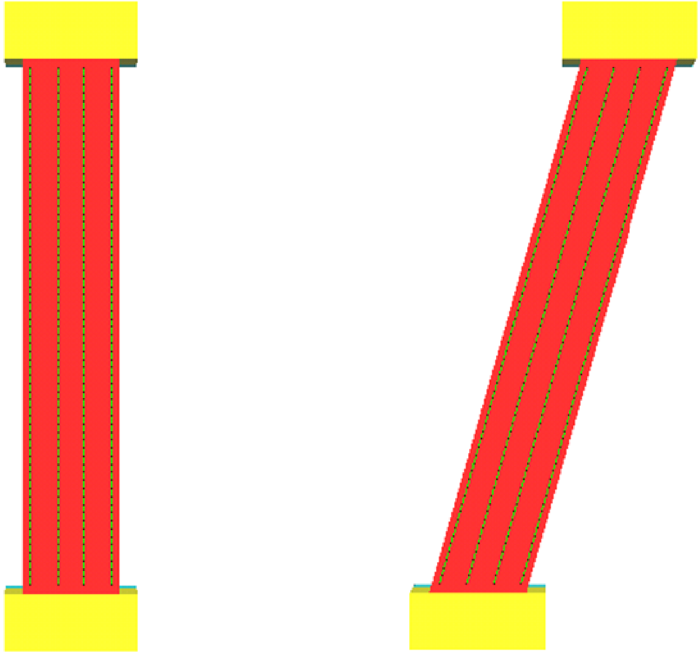

Figure 7.28: Plan View of 3D Superstructure Models

The bridges are both 66.0 m long and have a linear coefficient of thermal expansion of $6.162 * 10^{-6} / {}^\circ F$. The coefficient of thermal expansion was calculated using the weighted average approach described earlier. Both models were subjected to uniform temperature increase of $10^\circ F$. In addition to heating the superstructure, the abutments were also heated by the global temperature increase. This was done to strip away any interaction between the deck and the abutments (see Section 5.3). A plot showing the deformed shapes of the abutments is given in Figure 7.29. The line of nodes at the deck-abutment connection is used for the plot. The displacements correspond to the abutments at the top of Figure 7.28. Therefore, for the skewed bridge the obtuse corner is at a 'Position' of 0.0 m.

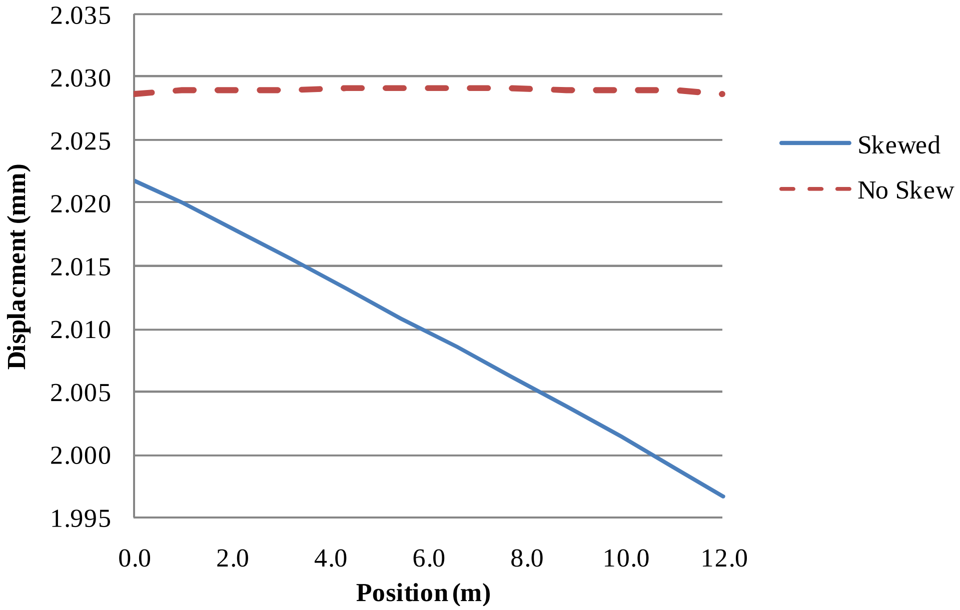

Figure 7.29: Abutment Deformations from 3D Analyses

A hand calculation of a free expansion of the non-skewed superstructure reveals abutment displacements of 2.03 mm, so it is evident that the implemented finite element technology and thermal loading scheme are working properly. It is also apparent that the backfill soils are not providing significant resistance, similar to what was observed in the 2D analyses. In studying Figure 7.29, it is clear that the bridge with no skew has a uniform displacement into the backfill soil. There is variation between the abutment corners in the skewed case though. The obtuse corner (‘Position’ = 0.0 m), is pushed farther into the backfill than the acute corner. The difference between the two corners is minor for this particular case, but the results provide insight into the general behavior of skewed IABs. In the obtuse corner, where the abutment has more displacement, the backfill pressure and stress in the superstructure will all be higher than in the acute corner. Figure 7.30 shows the forces at the abutment corners obtained from the analysis.

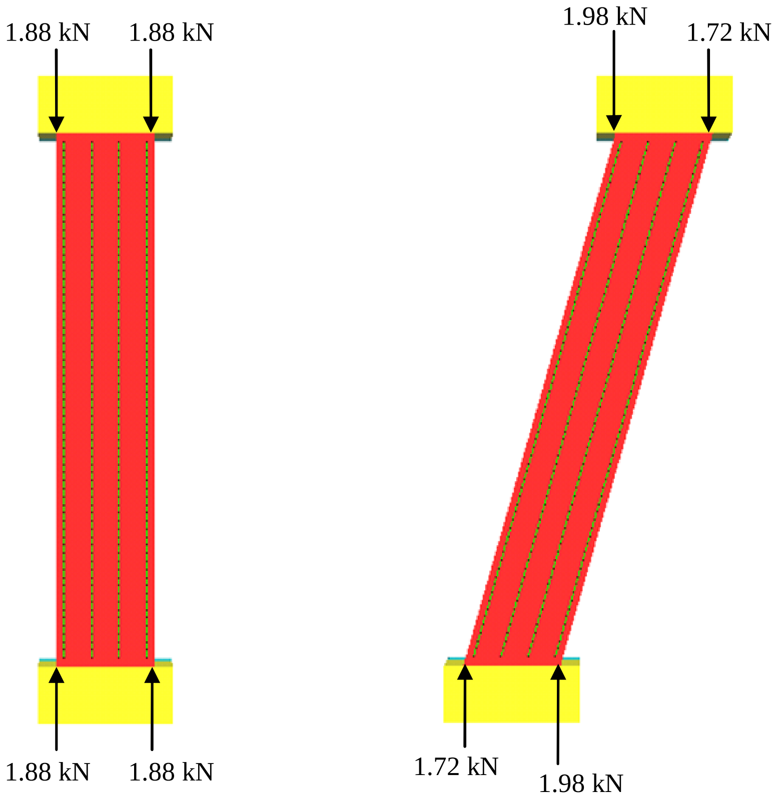

Figure 7.30: 3D Superstructure Corner Forces

The corner forces are equal in the non-skewed superstructure. In the skewed version, the forces in the obtuse corners are higher than the forces in the acute corners. This agrees with expected results and previous instrumentation results (e.g. Sandford and Elgaaly 1993).

8. Conclusions

8.1 General

Beam and plate elements have been developed and implemented in the TeraDysac computer code (Muraleetharan et al. 2003, Ravichandran 2005). The low order elements are computationally efficient and have compatibility with the soil 2D quadrilaterals and 3D hexagonal brick edges. Numerous problems involving plates, beams, and soils have been successfully run. The goal in the development of these elements was to analyze IABs subjected to thermal events. To do so, thermal loading capability has also been added to TeraDysac. The available thermal applications allows for a linear temperature distribution through structural sections. In structures where thermal radiation is a factor, being able to account for a temperature gradient is a required feature. The user is allowed to specify the temperature change on both sides of the structural elements which can allow thermal curvature in beams and plates.

A study of soil-structure interaction has been presented. For beams on elastic foundations, comparisons have been made between analytical solutions presented by Winkler (1867) and the continuum solutions presented by Vesic (1961). The Vesic solutions have also been compared with the finite element solutions obtained from a TeraDysac finite element analysis. The program-obtained solutions showed good agreement with the Vesic solutions, which serves as validation of the soil-structure interaction capabilities for linear problems. In soil-structure interaction, more realistic and interesting problems are ones where soil nonlinearity is considered. Solutions of a pile in soft clay were presented and compared with solutions obtained from the $p-y$ program LPILE (ENSOFT 2007). The user-input soil strengths were obtained using the same bounding surface algorithm implemented in TeraDysac. A series of analyses were performed, including one where the $p-y$ curves furnished to LPILE were obtained from the TeraDysac analysis. The results between the two were in good agreement. A method for extracting the $p-y$ information from the finite element analysis was also presented. The empirical $p-y$ curves in LPILE may not be accurate for all soils.

In the analysis of IABs, the capability to capture the nonlinear bending stiffness of the abutment piles may be important. These piles may experience high stress near the abutments and some yielding may occur. A nonlinear EI application has been written for TeraDysac. The algorithm uses the equation relating moment, curvature, and bending stiffness to find the bending stiffness as a function of bending moment. Prior to yield, EI is constant but when the pile begins to yield the bending stiffness diminishes. As a plastic hinge forms, the bending stiffness goes to zero. An example was presented on how to obtain the Moment-Curvature relationship for a rectangular steel section. The example section was analyzed using the nonlinear EI application and the results were discussed.

A series of finite element analyses of the Minnesota IAB superstructure were performed using the program TeraGrande (ANATECH 2005). The advanced reinforced concrete analyses which model rebar accurately and use a smeared crack model to study nonlinear concrete behavior showed that for the deformations experienced during the thermal loading modeled in this work, the linear structural elements developed for TeraDysac are adequate. Significant concrete cracking was not observed in the superstructure and stresses and strains were low enough that the linear elastic assumptions embedded in beam and plate formulations are acceptable. To illustrate when more advanced structural elements are necessary, a blast loading simulation was also performed on the Minnesota IAB superstructure.

The Minnesota IAB has no skew angle. Because the bridge abutment translates and rotates uniformly across the bridge width, a 2D analysis can approximate the field behavior. The 2D soil analysis in TeraDysac uses a plane strain assumption for the soil elements. A procedure for obtaining structural properties (area and moment of inertia) based on a unit width of bride was presented. The structural components of the bridge consist of steel and concrete. Using a weighted-average approach, material parameters such as Young's modulus, linear coefficient of thermal expansion, and Poisson's ratio were determined. The series of 2D TeraDysac analyses showed reasonable agreement with the instrumented results. There were four analyses performed: a temperature increase and decrease using linear elastic and bounding surface soils. In each loading case, the bounding surface models provided more accurate results. The results for the temperature decrease analysis were generally better than for the heating analysis. This is attributed to the fact that in the winter (January in this case), thermal gradients are minimal through the superstructure depth. Therefore, the deck temperature change can be applied directly to the model without having to estimate what the thermal gradient might be (as was done in the summer heating analysis).

Full 3D models of the Minnesota IAB and a skewed version of it were developed. These models were not analyzed in their entirety, but reduced models considering the superstructures and the top two soil layers were studied. Each model was subjected to a uniform temperature increase and the behavior at the abutments was observed. In the non-skewed bridge, the abutment deformation was uniform across its width. The skewed superstructure (15°) had a non-symmetric response at the abutments. The deformation at the obtuse corner was greater than at the acute corner. The difference was minor, but the analysis revealed that the abutment deformation and subsequently the developed pore water pressure and earth pressure behind the abutments will be varied. For small skew angles, a 2D approach may be acceptable. Not capturing the variation in response behind the abutments may be worth the computational savings. A 3D model is more demanding computationally and requires more effort to build, but is required for accurate results, especially for large skew angles in IABs.

8.2 Recommendations

Full versions of the Minnesota IAB (and its 15° skew counterpart) have been created (see Figures 8.1 and 8.2). Although these models were not analyzed due to the current solver capabilities, reduced models were successfully studied (see Section 7.7). The 3D analyses, although simplified, show that the plate, beam, and soil element assemblies and the thermal loading application are working properly. In anticipation of solving the full models, some thought has been given on how to set up the meshes. When studying IAB response to thermal events the meshes need to be large enough spatially that the soil boundaries are not influencing the results severely, yet are not unnecessarily large to waste computational effort. A series of analyses can be performed with different dimensions of backfill behind the abutments to reveal an appropriate mesh size. Studying the deformed shape of the abutments and abutment piles between the analyses will help to find an appropriate model size. It is recommended to start with large amount of soil behind the abutments (~one-half the bridge length). Then plot the deformed shape of the abutment and abutment piles. Next increase the dimension of backfill soil and re-plot the deformed shape. If the plots are identical, then the first mesh is large enough and can be trimmed. Begin to decrease the backfill dimension until a departure is noticed between the deformed shapes. The smallest mesh providing the true displacement results is the one that will minimize computational effort. For loading events of the magnitude used for the analysis or less, the mesh size will be adequate. For more severe loading, the soil boundaries may be influencing the results and this must be investigated. This procedure was used in preparing the 2D models used throughout this work.

In preparing the full 3D models, some thought has been given on how to minimize computational effort on the skewed models. Figure 8.1 shows the 3D model with no skew. There are a total of 56,112 elements in this mesh. When building the skewed models, as the skew angle increases, so too does the mesh size. A bigger skew angle requires a bigger mesh extrusion in the transverse direction to the bridge. Figure 8.2 shows the skewed IAB model. There are 95,712 elements in the mesh, which is a sizeable increase from the model with no skew.

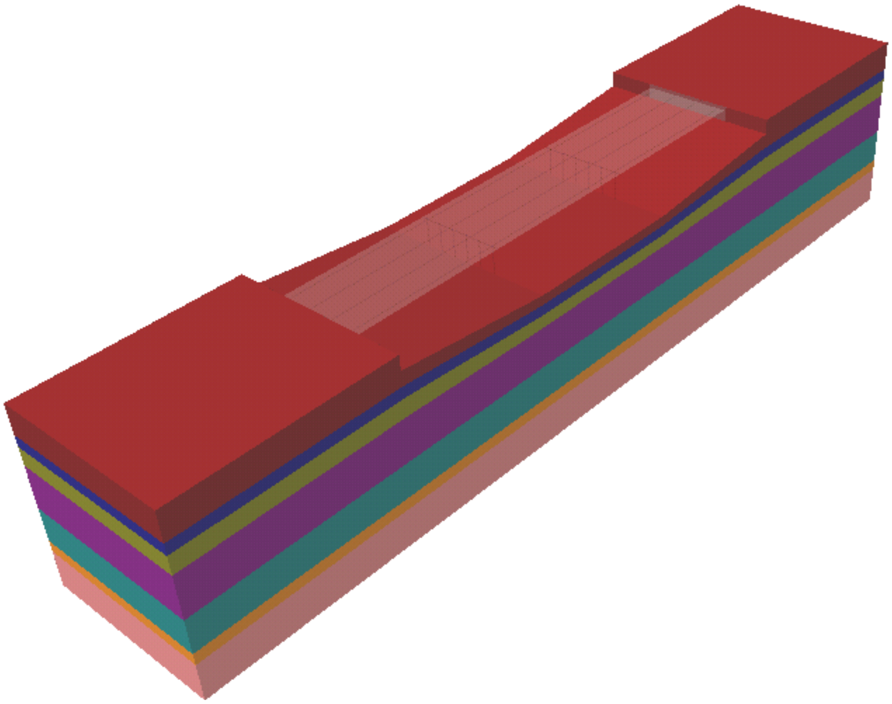

Figure 8.1: Full 3D Minnesota IAB Model

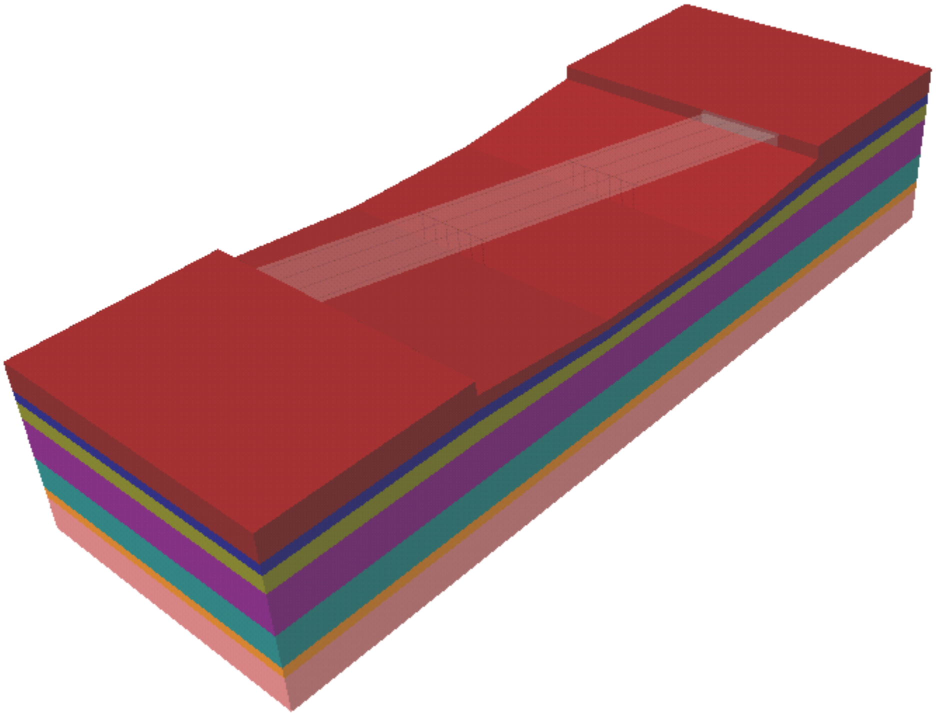

Figure 8.2: Full 3D Minnesota Bridge Model (Skewed)

Studying Figure 8.2 shows a large number of soil elements which do not have a major contribution to the solution are located in the two mesh corners away from the abutments.

A plan for building the skewed models in a more efficient manner is illustrated in Figure 8.3.

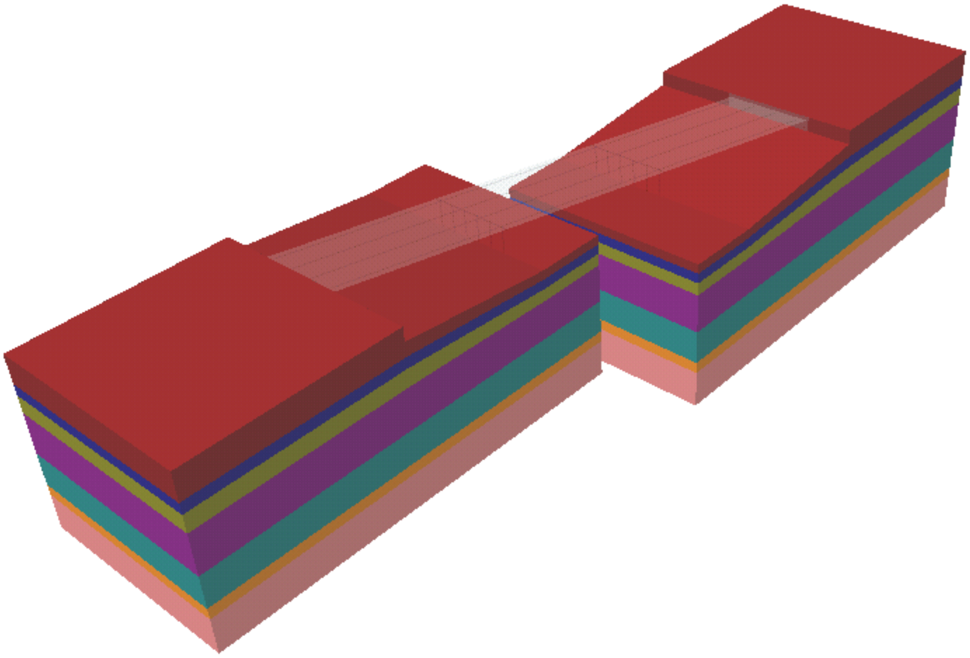

Figure 8.3: 3D Reduced Model (Skewed IAB)

Figure 8.4 shows the elevation view of the mesh. A single row of elements at the bridge centerline has been removed. Doing so allows the soil stratum to be modeled with two separate blocks which makes the model size significantly smaller.

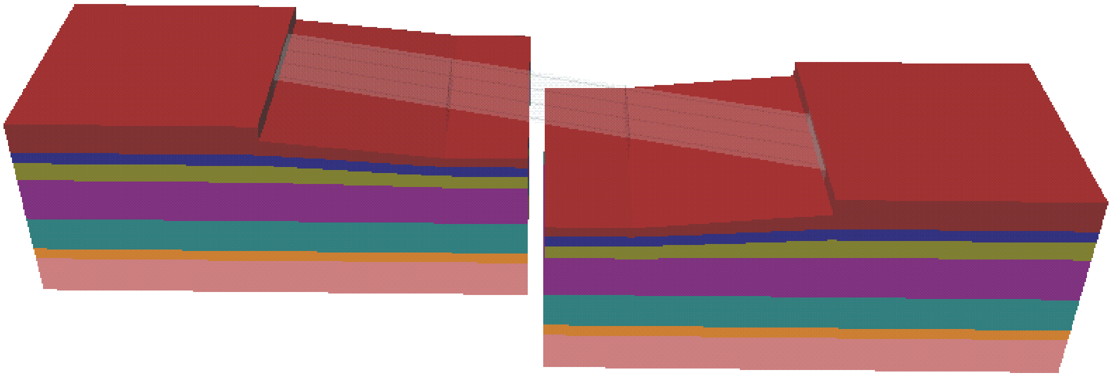

Figure 8.4: Elevation View of 3D Reduced Model (Skewed IAB)

The model shown in Figures 8.3 and 8.4 has 65,952 elements, a reduction in mesh size of about 30%. The viability of the proposed scheme needs to be investigated, but it is anticipated that the reduced models will give accurate results because the soil element removal takes place only in areas that see minimal load during the thermal events (i.e. the bridge centerline and in the corners away from the abutments).

The nonlinear EI application developed in this work needs further refinement. Currently, the maximum bending moment in the beam element block is used to determine the value of bending stiffness for the entire element block. Ideally, the bending stiffness should be calculated for each element in the beam mesh and the provided stiffness should be applied only to that element. This is important in abutment piles near the ground surface where they might go into the yielding range. It is incorrect to apply the reduced stiffness throughout the pile depth. This problem can be circumnavigated by breaking the pile into separate element blocks, putting a high density in regions where nonlinear behavior may be anticipated. Figure 8.5 illustrates this concept. The different shading in the abutment pile shows the different element blocks used to comprise the pile. There are several small pile pieces near the abutment where the possibility of yielding is the highest. In regions where the pile is not expected to yield, larger pieces can be used.

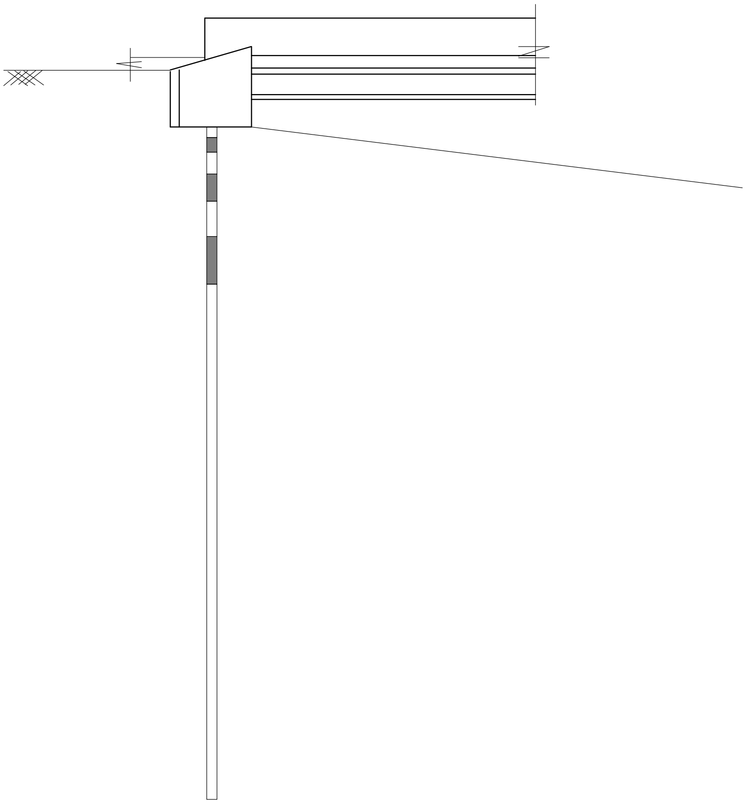

Figure 8.5: Element Block Composition for Nonlinear Pile Analysis

In addition to changing the bending stiffness from a datum to a field for the beam elements, a predictor algorithm needs to be written for the nonlinear EI application. In its current form, the Moment-Curvature curve alone is furnished to the program and iteration is allowed until the bending moment and curvature are in agreement. A method for increasing the convergence rate needs to be developed.

A discussion has been presented on how to handle static problems using the dynamic time-marching scheme implemented in TeraDysac. In the future, a true static algorithm should be developed for solving thermal loading problems (among others). Reducing the element block mass and holding the load at a constant value has been shown to yield the static solution in an approximate sense. In the bounding surface soil analyses, the full element mass was used. A reduced mass decreased the time step and adversely affected the convergence. Therefore, the bounding surface results presented, especially in regions away from point of load application (the deck-abutment connection) exhibited some oscillatory behavior. In the linear elastic analyses, zero model mass was successfully used to obtain solutions.

The use of the Uniform Gradient formulation for the linear elastic and bounding surface clay soil elements showed good behavior in all problems analyzed in this work. However, severe hourglassing was observed when the Uniform Gradient formulation was used for the sand elements. Therefore, the 2D IAB bounding surface analyses were carried out using Gauss-Quadrature (2x2) integration. This adds a significant amount of computation time. Further work needs to be done to allow the use of the Uniform Gradient formulation in the bounding surface sand models. The hourglass stiffness parameter may need to be adjusted for the sand model, but this was not investigated.

Bounding surface elements for saturated and unsaturated clays and sands are currently available in TeraDysac. Structural elements (low order beams and plates) have also been developed. Tied contact has been shown to give fairly accurate results for the problems solved in this work. Naturally, the next evolution in using TeraDysac for soil-structure interaction is the development of an interface element. The accurate capture of behavior at the interface between soils and structures would be a nice addition to the computer program. This is a sizeable task because of the fluid flow that will emerge when there is separation at the interface, but it is certainly a worthwhile endeavor. In the solution of dynamic problems (e.g. earthquakes) an interface element would be very desirable.

The bounding surface soil models in TeraDysac can capture nonlinear soil behavior and pore pressure generation in soil-structure interaction problems. But the structural elements developed in this work are limited because of the embedded linear elastic assumption. The structural element technology in TeraGrande is superior because it models reinforced concrete and rebar prestressing accurately. The combination of the bounding surface soil models in TeraDysac, the structural element technology in TeraGrande, and an interface element would make a supreme tool for modeling civil engineering systems accurately.

REFERENCES

American Concrete Institute. Building Code Requirements for Structural Concrete (ACI 318-02) and Commentary (ACI 318R-02). Page 318/318R-89.

ANATECH Corporation (formerly TeraScale, LLC). TeraGrande: A multi-physics finite element program. Albuquerque, NM. 2005.

ANATECH Corporation (formerly TeraScale, LLC). TeraGrande User's Manual, Version 1.0. Albuquerque, NM. 2005.

ANATECH Corporation (formerly TeraScale, LLC). The TeraScale Framework. Albuquerque, NM. 2001.

ANSYS, Inc. Computer program ANSYS Release 11.0. 2007.

Alampalli, S. and Yannotti, A.P. In-service performance of integral bridges and jointless decks. Transportation Research Record 1624. 1998. Pages 1-7.

Arockiasamy, M., Butrieng, N., and Sivakumar, M. State-of-the-art of integral abutment bridges: design and practice. Journal of Bridge Engineering (ASCE) 9 n5. 2004. Pages 497-506.

Bathe, K.J. Finite Element Procedures in Engineering Analysis. Prentice-Hall, Inc. 1982. Pages 251-255.

Beer, G. An isoparametric joint/interface element for finite element analysis. International Journal for Numerical Methods in Engineering 21. 1985. Pages 585-600.

Belytschko, T. and Tsay, C-S. A stabilization procedure for the quadrilateral plate element with one-point quadrature. International Journal for Numerical Methods in Engineering 19. 1983. Pages 405-419.

Biot, M.A. Bending of an infinite beam on an elastic foundation. American Society of Mechanical Engineers – Transactions. Journal of Applied Mechanics 4 n1. March 1937. Pages A-1-7.

Comstock, L. and Dagher, H. Physical testing of two R/C skewed slab bridges with integral wall abutments. Structural Engineering in Natural Hazards Mitigation. Proceedings of Papers Presented at the Structures Congress '93. Volume 2. 1993. Pages 969-974.

Dafalias, Y.F., and Herrmann, L.R. Bounding surface formulation of soil plasticity. Soil Mechanics – Transient and Cyclic Loads (in G.N. Pande and O.C. Zienkiewicz eds). Wiley. Chichester, England. 1982. Pages 253-282.

Dafalias, Y.F., and Herrmann, L.R. Bounding surface plasticity II: application to isotropic cohesive soils. Journal of Engineering Mechanics 112 n12. December 1986. Pages 1263-1291.

Dafalias, Y.F., and Popov, E.P. Plastic internal variables formalism of cyclic plasticity. Journal of Applied Mechanics 98 n4. 1976. Pages 645-650.

Dameron, R.A. and Dunham, R.S. Continuum F.E. analyses of concrete bridge outrigger cyclic loading tests with a new rebar bond-slip model. Report to the Third NSF Workshop on Bridge Engineering Research in Progress. November 16-17, 1992.

Day, R.A., and Potts, D.M. Zero thickness interface elements – numerical stability and application. International Journal for Numerical and Analytical Methods in Geomechanics 18. 1994. Pages 689-708.

Desai, C.S., Zaman, M.M., Lightner, J.G. and Siriwardane, H.J. Thin-layer elements for interfaces and joints. International Journal for Numerical and Analytical Methods in Geomechanics 8. 1984. Pages 19-43.

Dunham, R.S. et al. Predictive analysis of outrigger knee-joint hysteresis tests: a torsion/flexure test at UCB and two flexure tests at UCSD. Caltrans First Annual Seismic Research Workshop. November 1991.

ENSOFT, Inc. Computer program LPILE^{PLUS} 5.0 for Windows. Austin, TX. 2007.

ENSOFT, Inc. LPILE^{PLUS} 5.0 for Windows Technical Manual. Austin, TX. July 2004. Page 3-33.

Fennema, J.L., Laman, J.A., and Linzell, D.G. Predicted and measured response of an integral abutment bridge. Journal of Bridge Engineering (ASCE) 10 n6. 2005. Pages 666-677.

Goodman, R.E., Taylor, R.L. and Brekke, T.L. A model for the mechanics of jointed rock. Journal of the Soil Mechanics and Foundations Division, ASCE 94. May 1968. Pages 637-659.

Greimann, L.F., Wolfe-Tinsae, A.M., and Yang, P.S. Skewed bridges with integral abutments. Transportation Research Record 903. 1983. Pages 64-72.

Hartmann, F. and Katz, C. Structural Analysis with Finite Elements. Springer. 2004. Page 341.

Hassiotis, S., and Roman, E.K. A survey of current issues on the use of integral abutment bridges. Bridge Structures 1 n2. June 2005. Pages 81-101.

Hilber, H.M., Hughes, T.J.R., and Taylor, R.L. Improved numerical dissipation for time integration algorithms in structural dynamics. Earthquake Engineering and Structural Dynamics 5. 1977. Pages 283-292.

Horvath, J.S. Integral-abutment bridges: a complex soil-structure interaction challenge. Geotechnical Special Publication, n 126 I, Geotechnical Engineering for Transportation Projects: Proceedings of Geo-Trans 2004. 2004. Pages 460-469.

Huang, J., French, C.E., and Shield, C.K. Behavior of concrete integral abutment bridges: final report. November 2004.

Hughes, T.J.R. Analysis of transient algorithms with particular reference to stability behavior. Computational Methods for Transient Analysis (T. Belytschko and T.J.R. Hughes eds). Elsevier. Amsterdam. 1983. Pages 67-155.

Jorgenson, J.L. Behavior of abutment piles in an integral abutment in response to bridge movements. Transportation Research Record: Journal of the Transportation Research Board 903. 1983. Pages 72-79.

Kirchhoff, G.R. Über das gleichgewicht und die bewegung elastischen scheibe. Crelles Journal 40. 1850. Pages 51-88.

Kunin, J. and Alampalli, S. Integral abutment bridges: current practice in United States and Canada. Journal of Performance of Constructed Facilities 14 n3. August 2000. Pages 104-111.

Lai, J.Y., and Booker, J.R. A residual force finite element approach to soil-structure interaction analysis. International Journal for Numerical and Analytical Methods in Geomechanics 15. 1991. Pages 181-203.

Matlock, H. Correlations for design of laterally loaded piles in soft clay. Proceedings, Offshore Technology Conference, Houston, Texas. Volume I, Paper No. 1204. 1970. Pages 577-594.

Mindlin, R.D. Influence of rotary inertia and shear on flexural motions of isotropic, elastic plates. Journal of Applied Mechanics 18. 1951. Pages 31-38.

Muraleetharan, K.K. VELACS extension project: constitutive model calibration and predictions. Research report. October 1995.

Muraleetharan, K.K., Mish, K.D., and Arulanandan, K. A fully coupled non-linear dynamic analysis procedure and its verification using centrifuge results. International Journal for Numerical and Analytical Methods in Geomechanics 18. 1994. Pages 305-325.

Muraleetharan, K.K., Ravichandran, N., and Taylor, L.M. TeraDysac: TeraScale Dynamic Soil Analysis Code. Computer Code. School of Civil Engineering and Environmental Science, University of Oklahoma. Norman, Oklahoma. 2003.

Naval Facilities Engineering Command. Design Manual 7.01. 1986. Page 7.1-220.

Nickerson, R.L. Jointless steel bridges design and retrofit. Proceedings of Structures Congress XIV 1. 1996. Pages 313-320.

Paul, M., Laman, J.A., and Linzell, D.G. Thermally induced superstructure stresses in prestressed girder integral abutment bridges. Transportation Research Record: Journal of the Transportation Research Board. 6th International Bridge Engineering Conference. 2005. Pages 287-297.

Popescu, R. and Prevost, J.H. Numerical class 'A' predictions for Models Nos 1, 2, 3, 4a, 4b, 6, 7, 11 & 12. Proceedings of the International Conference on the Verification of Numerical Procedures for the Analysis of Soil Liquefaction Problems (K. Arulanandan and R.F. eds). Davis, California. October 17-20, 1993. Pages 1105-1207.

Przemieniecki, J.S. Theory of Matrix Structural Analysis. McGraw-Hill, Inc. 1968.

Rashid, Y.R. Ultimate strength analysis of prestressed concrete pressure vessels. Nuclear Engineering and Design 7. 1968. Pages 334-344.

Ravichandran, N. A framework-based finite element approach for solving large deformation problems in multi-phase porous media. Ph.D. dissertation, University of Oklahoma, Norman, OK. 2005.

Reissner, E. The effect of transverse shear deformation on the bending of elastic plates. Journal of Applied Mechanics 67. 1945. Page A-69.

Sandford, T.C., and Elgaaly, M. Skew effects on backfill pressures at frame bridge abutments. Transportation Research Record: Journal of the Transportation Research Board 1415. 1993. Pages 1-11.

Sandford, T.C., Davids, W.G., Hartt, S.L., and DeLano, J.G. Construction-induced stresses in H-piles supporting an integral abutment bridge. Transportation Research Record: Journal of the Transportation Research Board 1975. 2006. Pages 39-48.

Steinberg, E., Sargand, S.M., and Bettinger, C. Forces in wingwalls of skewed semi-integral bridges. Journal of Bridge Engineering 9 n6. November/December 2004. Pages 563-571.

Timoshenko, S.P. On the correction for shear of the differential equation for transverse vibrations of bars of uniform cross-section. Philosophical Magazine 41. 1921. Pages 744-746.

Tokimatsu, K. and Seed, H.B. Evaluation of settlements in sands due to earthquake shaking. ASCE Journal of Geotechnical Engineering 113 n8. August 1987. Pages 861-878.

Vesic, A.B. Bending of beams resting on isotropic elastic solid. ASCE Journal of the Engineering Mechanics Division - Proceedings, v 87, n EM2, Part 1. April 1961. Pages 35-53.

Winkler, E. Die Lehre von der Elastizität und Festigkeit. Prague. 1867. Page 182.

Wolde-Tinsae, A.M., and Greimann, L.F. General design details for integral abutment bridges. Civil Engineering Practice 3 n2. 1988. Pages 7-20.

Yang, P.S., Wolde-Tinsae, A.M., and Greimann, L.F. Effects of Predrilling and Layered Soils on Piles. Journal of Geotechnical Engineering 111 n1. 1985. Pages 18-31.

Yogachandran, C. Numerical and centrifugal modeling of seismically induced flow failures. Ph.D. dissertation. University of California, Davis. 1991.

Zienkiewicz, O.C. and Taylor, R.L. The Finite Element for Solid and Structural Mechanics, 6th ed. Elsevier Butterworth-Heinemann. 2005. Page 349.